Imperial College London

A theoretical study of the stability of Zr-Al-C and Ti-Al-C MAX phases

A thesis submitted in partial fulfilment of
the requirements for the degree of
Doctor of Philosophy
–
Department of Materials

Angeliki Poulou

Principal Supervisor
Prof. Mike Finnis

August 15, 2021

Statement of Originality

I, Angeliki Poulou, declare that the work presented in this thesis is my own and that work or contributions by others are properly acknowledged and cited. Contents of the paper that I have published with title 'Stability of Zr-Al-C and Ti-Al-C MAX phases: A theoretical study' in Physical Review Materials, Volume 5, Issue 3 (2021), page 033608, ©2021 American Physical Society, have been included in this thesis, with the main results of the paper presented in Chapter 4.

Copyright Declaration

Abstract

MAX phases have garnered considerable research attention due to their unusual combination of metallic and ceramic properties that make them desirable materials especially in applications requiring extreme operating conditions. Zr-Al-C MAX phases specifically, are of particular interest in the nuclear industry where their low neutron absorption make them compelling candidates for fuel cladding materials. The synthesis of Zr-Al-C MAX phases, however, has been challenging, with the presence of impurities suggested as necessary to stabilise them [1, 2, 3] and secondary phases considered unavoidable in the reported successful synthesis of Zr_2AlC [4] and Zr_3AlC_2 [5]. This has led to questions as to whether the composition of MAX phases in this system is likely to change when in service.

Addressing these uncertainties has been the main objective of this thesis, making the theoretical study of the thermodynamic stability of $Zr_{n+1}AlC_n$ of central importance. The stability of the $Zr_{n+1}AlC_n$ and closely related $Ti_{n+1}AlC_n$ MAX phases in the context of the M-A-X ternary phase diagrams and competing binary and ternary compounds, as a function of temperature, was calculated by applying density functional theory (DFT) within the quasiharmonic approximation. We found that the Zr-based MAX phases are thermodynamically unstable at room temperature, although Zr_3AlC_2 becomes stable above 500 K. Ti-based MAX phases on the other hand, show higher thermodynamic stability, with Ti_2AlC in particular, having the lowest formation energy of the MAX phases on the Ti-Al-C convex hull and appearing stable at all temperatures, in agreement with its reported success in synthesis. In the course of this work we also attempted to identify trends and similarities in predicted structural, elastic, thermophysical and electronic properties as well as the chemical bonding within the MAX phases in the two systems. Chemical bonding differences between the two systems, though, were not found to explain their differences in stability. Based on phonon calculations, Raman-active mode frequencies of Zr-based MAX phases and their most competing phases were also predicted, to assist in identifying phases present in a Zr_3AlC_2 synthesised sample [6]. Our predicted Zr_3AlC_2 frequencies of Raman-active modes were within 2% of peaks in the experimental Raman spectra recently measured by Lyons [6].

Acknowledgements

I would like to express my sincerest gratitude to my supervisor, Mike Finnis, for his continuous and invaluable guidance, encouragement, support and patience throughout my Ph.D. I would also like to extend my gratefulness to Tom Mellan who worked as a post-doc in our group, for his huge help and encouragement. Finally, I must thank Max and my family for their support and love.

Contents

List of Tables

List of Figures

Chapter 1

Introduction

MAX phases are a class of compounds that follow the formula $M_{n+1}AX_n$, with 'M' being an early transition metal, 'A' an element in groups 13–16 of the periodic table, 'X' being either C or N and with $n = 1$, 2 or 3 resulting in MAX phase subgroups with stoichiometries of 211, 312 and 413 respectively. They are characterised by their layered hexagonal structure belonging to space group $P6_3/mmc$, with two formula units per unit cell. In the unit cell, thin layers of rock-salt structured MX forming $[M_6X]$ M-atom octahedra, with both faces M-terminated, alternate with single atomic layers of graphene-structured A in $[M_6A]$ trigonal triangular prisms. The stacks of $[M_6X]$ octahedra between the layers of A-elements increase according to the stoichiometries denoted by n as shown in Fig. 1.1. In this structure a combination of anisotropic bonding types exist, such as strong directional covalent bonds, or ionic bonds, between M-X and M-A atoms, and metallic bonding along the basal axis in the A-layer [25, 26].

Many of the MAX phases known of today were experimentally discovered quite soon after the first MAX phase was synthesised in the 60s, with a large number of them being reported in the review by Nowotny in 1970 [27]. Around this time some of the most studied phases, and some of particular interest to this study, were also synthesised. These include 211 phases such as Ti_2AlC [28], Ti_2AlN [29] and Cr_2AlC [30] as well as some 312 phases such as Ti_3SiC_2 [31], Ti_3GeC_2 [32] and Ti_3AlC_2 [33]. The synthesis of the first 413 MAX phase, Ti_4AlN_3 [34], was also soon followed by more phases of this type including Ta_4AlC_3 [35] and Nb_4AlC_3 [36].

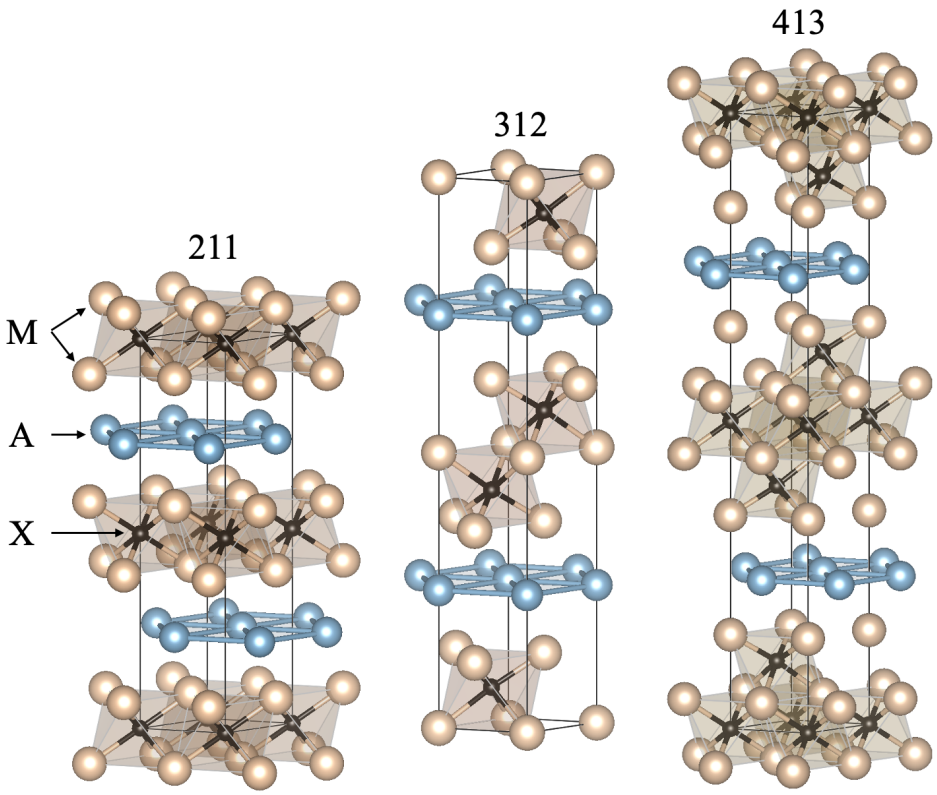

Figure 1.1: The crystal structure for MAX phases with $n = 1$, 2 and 3.

Particular research attention was drawn to these types of materials after the phases Ti_3SiC_2, Ti_3AlC_2 and Ti_2AlC were investigated, finding promising combinations of properties [37, 38]. As a result, many studies focused on the synthesis of new MAX phases, with a large number of Ti, V, Ta and Nb based phases being synthesised since 2004 [39]. Regarding the Zr-Al-C system, which is of central interest in this study, the first MAX phases synthesised were by Lapauw *et al.* with Zr_3AlC_2 [5] and Zr_2AlC [4], though not in pure form. The synthesis of such materials has however been a challenge, with many attempts having been reported [1, 2]. Other relatively recent efforts at MAX phase synthesis have focused on higher values of n and on ways of tailoring the properties of existing phases, e.g. by partial substitutions of M and A sites, thus expanding the possible combinations significantly. For example, quaternary phases have been explored such as in the V-Cr-Al-C system [40], in $(Zr,M)_2AlC$ and $Zr_2(Al,A)C$ with M being Cr, Ti or Mo and A being S, As, Sn, Sb or Pb [2], in $(Zr_{1-x}Ti_x)_3AlC_2$ [1] or double solutions such as $(Zr, Ti)_2(Al, Sn)C$ [3] and $(Zr, Nb)_2(Al, Sn)C$ [41]. Other systems that were explored by fine-tuning their stoichiometry by modifying their stacking sequences were MAX-like phases with layered structures, such as $Ti_5Al_2C_3$, which was studied by Lane *et al.* [42] and composed with

a structure of alternating layers of Ti_2AlC and Ti_3AlC_2. Aside from the experimental efforts, theoretical research such as density functional theory (DFT) calculations has also considerably assisted the discovery of new phases [43, 44, 45]. This significant research interest in the synthesis and discovery of new MAX phases is due to the interesting combination of properties of both metals and ceramics that these materials were predicted and found to exhibit, which make them very compelling for a range of applications, especially those requiring extreme operating conditions such as in the nuclear industry.

The development of efficient and safe nuclear reactor components, such as fuel cladding materials, has been a great challenge in nuclear reactor engineering. Materials in such applications need to withstand oxidising environments, high operating temperatures and high levels of irradiation, without sustaining enough damage to compromise the safety and efficiency of the reactor. For the last few decades Zr-based alloys have had the monopoly as materials used in key components of nuclear reactors and especially in Light Water Reactor (LWR) fuel cladding. The focus on Zr-based alloys is due to their low neutron absorption, balanced with adequate mechanical properties. Extensive research has been conducted toward the improvement of their performance and especially their oxidation resistance at high temperatures. This research focused on modifying their composition by substituting elements such as Fe, Cr, Ni, and U into the alloy. Alloys based on the UO_2/Zr system (e.g. Zircaloy-4) have been optimised for performance under normal operating conditions, characterised by temperatures of approximately 300℃ [46]. However, these cladding materials suffer from corrosion which becomes very relevant in accident scenarios such as loss-of-coolant accidents (LOCA), which involve coolant leaking from the reactor making the cladding and fuel vulnerable to overheating. In such accidents, Zr oxidation becomes significant at temperatures above 1200℃ leading to release of hydrogen that can be absorbed in the cladding material potentially resulting in the production of hydride precipitates in the alloys which can cause embrittlement of the cladding material and eventual material rupture [46].

As a result of these problems there is a need for nuclear fuel systems with enhanced accident tolerance [47]. Such systems, compared with the currently used alloys, are characterised by their ability to sustain reactor function for long periods during loss of active cooling while at

the same time maintaining, or even improving, general reactor performance. Basic features required for the sustainability of such nuclear systems are increased oxidation resistance at elevated temperatures and decreased H production —which limit the core's lifetime. To support efficient fission product behaviour, improved thermodynamic and mechanical properties are also required. An approach for enhanced accident tolerance is the use of coated cladding materials based on nanolaminated ternary carbides such as MAX phases. This approach is considered promising due to the available near-term technology, as it is based on a Zr-alloy coating with years of development and optimisation already available on the base material.

Research in MAX phases in the Ti-Al-C and Ti-Si-C systems has also shown features that make such phases viable for nuclear applications, such as their ability to self-annihilate radiation-induced defects at elevated temperatures and to self-heal cracks in oxidising environments representative of accident scenarios. Examples such as Ti_3SiC_2 and Ti_2AlC exhibit good creep and fatigue resistance as well as sustaining their strength at high temperatures. Additionally, studies on Ti_3SiC_2 also verified the enhanced irradiation resistance compared to the highly damaged binary TiC secondary phases in the material. This is attributed to the existence of the A-layers in the MAX phases which accommodate or annihilate point defects produced during irradiation, as they act as defect sinks due to the low defect formation energy requirements in the A-layers [48]. Phases in these systems were found to be light-weight and oxidation resistant as well as self-healing in oxidising environments [49]. Formation of layers of Al_2O_3 and SiO_2 were found to be beneficial for resistance against oxidation, as these dense, protective layers result in lower oxidation kinetics at the material's grains. Such layers also support an oxidation based healing process as Al near the cracking area can react with oxygen to form Al_2O_3, which fills the crack space, especially in the case of Ti_2AlC whose fracture strength was found to recover almost completely [50]. Moreover, compared with their corresponding binary phases, such as TiC, Ti_2AlC and Ti_3AlC_2 exhibit enhancement in properties like electrical and thermal conductivity, oxidation resistance, and fracture toughness [49].

Building on the above, an important part of the motivation behind considering phases in the Zr-Al-C system originates from the low neutron cross section of Zr which contributes to improvements over the other systems in reactor performance and cost-effectiveness. Furthermore,

Zr-based phases are expected to benefit from the compatibility with the Zr-alloy cladding materials that are currently widely used. For the A layer, Al and Si could be considered natural choices for oxidation resistance enhancement, as they would typically be expected to form the previously noted passivating layers of Al_2O_3 and SiO_2 oxides around the grains. Additionally, in two recently reported MAX phases Zr_2AlC and Zr_3AlC_2 [4, 5], oxidation resistance is suspected to be higher in the case of the 211 compared to the 312 phase, as Al could have an increased likelihood to diffuse out to form the Al_2O_3 protective layer at high temperatures due to the 211 phase's higher content in A-layers per unit cell. Regarding the choice of the X atom in the MAX phase formula, C is preferred over N as it does not lead to radiotoxic oxidation products in the same way that N does.

Therefore, MAX phases in the Zr-Al-C system, especially the Zr_2AlC phase, have represented a potentially fundamental step towards further improvement in accident tolerance and efficiency in nuclear reactors. However, the synthesis of such materials has been a challenge, as also mentioned previously, with the purity of the produced phases being difficult to efficiently improve and impurities having non-negligible effects on the properties of the alloy. In the case of Zr_3AlC_2, two other phases, ZrC and $ZrAl_2$, where found to be present in 31 mol% and 8 mol% amounts respectively [5], whereas in the Zr_2AlC system, the final material was composed of 72 vol% Zr_2AlC and 28 vol% ZrC phases [4]. Secondary phases can result in early degradation of the cladding material under neutron irradiation as the alloys are more prone to differential swelling and cracking along the grain boundaries, while in the Ti-Al-C or Ti-Si-C systems the presence of secondary phases has been linked to problematic behavior of the materials [48]. Studies of the Ti_3SiC_2 phase revealed the appearance of irradiation-induced defects in the form of denuded zones on the grain boundaries of the MAX phase [48]. Additionally, an increased proportion of secondary phases, like TiC, were found to be detrimental to the overall irradiation resistance of the material as a higher number of defects and dislocations are produced in them compared to the MAX phase grains.

An important aspect of MAX phases is that they enable tailoring their properties by applying partial substitutions at A and M sites at different compositions, which can help them effectively fit the requirements of nuclear cladding applications. Recent studies on Zr-based MAX phases

focus on tailoring their thermal stability and oxidation resistance while preserving the neutron absorption levels of Zr. Investigations of (Nb, Zr)$_4$AlC$_3$, confirmed an improved thermal stability examined with respect to the temperature-dependent elastic constants and Young's modulus, compared to the Nb$_4$AlC$_3$ phase [51]. Additionally, in the case of Zr$_2$AlC, partial substitution of the M-sites with Ti is suspected to improve the oxidation resistance [52]. For the same parent MAX phase oxidation resistance is suspected to improve with partial substitutions of the A-site with Si as is indicated by studies in the Zr-Al-C system where high oxidation resistance for solid solutions Zr$_2$(Al,Si)$_4$C$_5$, as well as Ti-doped Zr$_2$[Al(Si)]$_4$C$_5$ and Zr$_3$[Al(Si)]$_4$C$_6$ was observed [53, 54]. In the reverse case, partial substitution of Zr in the Ti$_3$(Al,Si)C$_2$ solid solution, was found to improve stiffness at high temperatures [55], up to 1200°C, as the presence of Zr can strengthen the bonding between the Si and Ti–C layers at elevated temperatures.

Regarding phase purity issues reported for the Zr-Al-C MAX phase synthesis, experimental studies suggest improvement to the stability of such phases through the inclusion of impurities in the form of partial substitutions. Such suggestions are based on studies that show the purity of the final MAX phase was improved by Si additions to the initial reaction powder mixes in Ti$_3$AlC$_2$ synthesis. The synthesis of Zr$_3$(Al$_{1-x}$Si$_x$)C$_2$ MAX phases that has been reported, suggests further investigation for quality improvement based on the same mechanism applied in the Ti-Al-C system [55]. Additionally to this composition-based approach, the final purity of the material has been experimentally reported to considerably depend on the selection of the appropriate starting powder mixtures [51] as well as the synthesis methodology, as alternatively to hot-pressing, pressureless sintering resulted in higher purity MAX phases [52].

It is worth noting that although the main application of MAX phases discussed so far has been in the nuclear industry, MAX phases are, as mentioned previously, also considered promising for a wide range of other applications that require similarly high temperature operating conditions, high mechanical strength, while at the same time, machinability, high fracture toughness and oxidation tolerance. Such applications can be in the form of protective coatings for high temperature turbine components such as turbine disks, used in jet aircraft, oil and gas drilling tools, and high-efficiency engines indicatively used in ships, trains, and tanks. In aerospace applications, high stresses during operation lead to turbine disk failure which poses a signifi-

cant threat to engine safety. Under normal operating conditions the disks and blades must also tolerate corrosive gases and temperatures exceeding 700℃. In the case of turbine environments, with such high temperature and high load requirements, MAX phases, such as Ti_2AlC [56] show potential. Tailoring the properties and optimising the production for high-purity MAX phases is therefore not only significant to improving the safety and efficiency of nuclear reactors, but could have wider utility in other oxidising, high temperature environments.

Given everything we have discussed so far, undoubtedly, Zr-based MAX phases have a strong potential to be valuable materials for industrial applications, especially in the nuclear industry. The difficulties faced in their synthesis and the importance of their higher quality pure form, however, raise concerns as to whether their composition would be stable in service. The main objective of this thesis therefore, was to address these concerns by providing an improved understanding of the MAX phases in the Zr-Al-C system with a specific focus on their thermodynamic stability. Thus this research focused on the understanding of their mechanical, elastic and thermodynamic properties at high temperatures as well as predicting their thermodynamic stability and comparing them with the closely resembling phases in the Ti-Al-C system, to better explain their stability differences and the very different options necessitated for their synthesis despite their very close chemical and structural resemblance. Given this main objective, this thesis is structured as follows:

Chapter 2 presents the primary concepts underlying the theoretical background applied in our computational study. This includes the description of first principle calculations, particularly Density Functional Theory (DFT), bonding analysis methodologies, harmonic lattice dynamics, thermodynamic concepts and free energy calculations to derive the thermophysical properties of interest in this study.

Chapters 3–6 present the main results:

Chapter 3 includes the prediction of the thermophysical and structural properties of the $Zr_{n+1}AlC_n$ and $Ti_{n+1}AlC_n$ MAX phases, with a focus on Zr_2AlC, within the DFT framework with the lattice vibrations being treated within the quasiharmonic approximation and contributions of electron excitations also being accounted for for Zr_2AlC. Investigation of anisotropy and the

approximation of the introduced c/a ratio constraint to the energy and thermal expansion is also included.

Chapter 4 presents the predictions of the thermodynamic stability of MAX phases in the Zr-Al-C system against the formation of other secondary phases in the system. Thermodynamic stability was calculated via convex hull construction and the effect of temperature on stability was evaluated within the quasiharmonic approximation. Part of the results presented are concerned with the comparison of this system with the Ti-Al-C system, with similar convex hull calculations for the known stoichiometric phases in that system being performed as well. An investigation of geometric distortions in the MAX phases in both systems is included at the end of the chapter.

Chapter 5 is focused on the understanding of the electronic structure and type of chemical bonding in the two closely related $Zr_{n+1}AlC_n$ and $Ti_{n+1}AlC_n$ phases and draws comparisons between the chemical environments of the two systems with the aim to provide a probable explanation for their difference in thermodynamic stability. Different methodologies of bonding analysis and charge partitioning were applied and their different trends were also discussed.

Chapter 6 is focused on harmonic phonon calculations for the $Zr_{n+1}AlC_n$ and $Ti_{n+1}AlC_n$ MAX phases, with the main characteristics of the phonon band structure and DOS of these phases being identified. A particular aim was to identify phases present in experimental samples of Zr_3AlC_2 with a focus on the non-stoichiometric Zr carbides. For this reason the frequencies of the Raman-active modes of Zr-based MAX phases and their possibly competing phases in the system were predicted and their corresponding mode symmetries were identified.

Chapter 7 summarises the main conclusions drawn from each chapter in this thesis and proposes areas of potential future research.

Before moving on to the Chapters defined in the outline above, the rest of this introductory chapter aims to provide some further context regarding relevant research, by providing a more detailed review of the available literature on experimental and theoretical studies on the properties of MAX phases, with a specific focus on the MAX phases in the two systems of interest,

Zr-Al-C and Ti-Al-C.

1.1 Overview of MAX phase properties

It is the aforementioned, unusual, often unique, combination of ceramic and metallic properties characterising MAX phases that initially sparked and continues to drive the particular research interest in these materials [57]. In common with the closely-related and more familiar MX binary compounds, MAX phases are elastically stiff, good thermal and electrical conductors and corrosion resistant, while in contrast, MAX phases are more easily deformed plastically, resistant to thermal shock and more tolerant to radiation damage. Many specific examples and trends of MAX phases have been reported in reviews by Barsoum *et al.* [57, 58, 59] that considered measured properties from a large number of the to date synthesised MAX phases. For example, MAX phases have demonstrated lower hardness values than their MX counterparts though higher values than metals, with their Vickers hardness noted within the range of 2–8 GPa [57]. The MAX phase Ti_3SiC_2 was reportedly able to recover its form from being compressed with up to 1 GPa stress at room temperature, while absorbing roughly 25% of the applied mechanical energy [58]. In terms of room temperature elastic stiffness, MAX phases have also been found to have shear and Young's moduli in the ranges of 80–142 GPa and 178–362 GPa respectively. These are combined with low densities of around 4–5 g/cm which in some cases can result in specific stiffness values up to three times larger than titanium [57]. Thermal and electrical conductivity at room temperature in MAX phases has also been found to be in the ranges of 12–60 W/(m·K) and 1.4×10^9–5.0×10^9 mS/m respectively, which are comparable ranges to metals such as titanium, with the Ti_3SiC_2 and Ti_3AlC_2 MAX phases even reported to be better conductors than titanium [59] whose thermal and electrical conductivity is 16 (W/mK) and 1.9×10^9–2.4×10^9 mS/m respectively [60]. Additionally, MAX phases have a relatively low thermal expansion coefficient, within the range of 5–10 μK^{-1} [59]. MAX phases with magnetic properties have also been reported and are mainly based on Cr or Mn [61]. Another important aspect of the usefulness of MAX phases in industrial applications is their resilience to oxidation. Reports have shown that the Ti_3AlC_2, Ti_2AlC and Cr_2AlC phases are

particularly resistant [62]. Cr_2AlC in particular, was found to begin oxidation resistance 400°C higher than other Al-containing carbides at 800°C [63], while the Ti_2AlC phase showed the highest oxidation resistance overall with high resilience to thermal cycling at 1350°C [59]. The mechanism that results in this high tolerance in Al-containing MAX phases is the protective Al_2O_3-rich layer, noted previously, that develops under both high-temperature oxidation and hot corrosion [63, 62]. However, it is worth noting that although enhanced corrosion resistance due to the above mechanism is observed in some Al-containing MAX phases and had been suspected to also apply for Zr-based MAX phases, recent experimental studies considering their potential in nuclear fuel cladding applications have shown that MAX phases in the Zr-Al-C system in fact suffer from poor corrosion resistance, specifically assessed when in contact with advanced nuclear reactor coolants, such as heavy liquid metals (e.g. LBE=lead-bismuth eutectic) [64, 65]. Despite Zr-based MAX phases showing greater interaction with liquid LBE compared to other assessed MAX phases, such as Ti-based ones [64, 65], they have still been found to outperform stainless steels in liquid LBE environments [66].

1.2 Elastic and thermal properties

Numerous studies of MAX phases based on DFT calculations at $T = 0\,\mathrm{K}$ have been performed to investigate ground-state properties such as mechanical and elastic properties as well as stability and electronic structure that give a good predictive picture of the MAX phases' thermodynamics. In particular, several high throughput surveys have covered a wide range of structures with the aim of capturing trends in the properties. The DFT framework was selected in these studies for its combination of sufficiently accurate and robust calculations, uniformly applied for all phases, with the required computational efficiency to support the large number of phases screened. Sufficient accuracy in this case might not be enough to capture subtleties in the properties, however this can be an acceptable trade-off given the large number of phases [67, 68, 69]. In the study by Cover *et al.* [67], such a computational survey was conducted for 240 elemental combinations of M_2AX phases with an aim to understand trends in elastic properties between those materials. In the same study [67] calculation errors and uncertainties were investigated

and the impact of the choice between the stress-strain relationship approach and the energy method to calculate the elastic constants was discussed; with the energy method being applied by Taylor expanding the free energy up to the second order in terms of the two strains ϵ_1 and ϵ_3 along the a and c lattice constants as expressed later in Eq. 2.68. In the same study the role of M and A elements was highlighted as affecting the compressibility in the c axis. Another DFT study that considered a large number of MAX phases [68] focused on M_3AlC_2 phases, with M being an early transition metal from $3d$ to $5d$, and examined the effect of the choice of M on elastic and structural properties. The same study also noted that the bulk modulus increases with n, which is a trend that is also indicated by experimental evidence [70, 71]. Another systematic study [69] examined a large number of Al-containing MAX phases, $M_{n+1}AlC_n$ with $n = 1$–3, with a focus on compressibility and, in particular, the effect of varying levels of pressure on the bond stiffness and c/a ratio. Apart from these studies that consider wide ranges of phases, most studies focus on specific systems or sub-groups of the MAX phase family. For the $Zr_{n+1}AlC_n$ and $Ti_{n+1}AlC_n$ MAX phases in particular, an extensive number of studies of elastic and mechanical properties at $T = 0\,\mathrm{K}$ [69, 68, 72, 7, 73, 74, 75, 19, 76, 77, 67, 78, 79, 80] exist. For the Zr_2AlC phase the pressure effect on the elastic constants has been investigated [18, 80] but predictions at finite temperature have not yet been reported nor experimental measurements of the elastic constants been found.

Thermal properties are simulated by taking into account lattice vibrations with the lowest level of approximation being the quasiharmonic approximation (QHA) in which the vibrational free energy, F_{vib}, is described by the harmonic expression 2.57, where the phonon normal modes are functions of the unit cell volume and the total free energy is calculated by adding the ground state DFT enthalpy to F_{vib}. As explained in the following chapter, for structures with hexagonal symmetry, like the MAX phases, the free energy surface is minimised on a 2D strain mesh corresponding to the a and c lattice parameters in order to take into account their anisotropy. Reported studies on MAX phases that treated the lattice vibrations within the QHA assumed that the c/a ratio is kept fixed, therefore the free energy was minimised in only one dimension, indicating an isotropic change in volume. Such examples include studies of Sc_2AlC [81] and Cr_3AlB_4 [82] that calculated the phonon dispersion curve and predicted

the dynamical stability of the phases. For the $Zr_{n+1}AlC_n$ and $Ti_{n+1}AlC_n$ MAX phases studies using QHA exist [83, 84, 73, 85, 86] that predict the thermal expansion, heat capacities and temperature dependent bulk moduli of the phases.

A higher level of lattice vibration approximation that has been extensively used in the literature to predict thermal properties is the quasiharmonic Debye model which only takes into account acoustic modes with linear dispersion from the Γ point up to a Debye frequency, Θ_D, thus treating the crystal as an isotropic elastic medium. Studies using this approximation have been conducted for phases such as Sc_3SnX (X = B, C) [87] and Cr_2AlB_2 [88] as well as for the $Zr_{n+1}AlC_n$ and $Ti_{n+1}AlC_n$ MAX phases [82, 7, 18, 89, 90, 91, 19]. The quasiharmonic Debye model can be considered one of the simplest approximations [92] and it can often show a good accuracy for chemically and structurally simple materials such as some metals. However, it generally has good reliability for temperatures up to a few hundreds of degrees Kelvin, after which its accuracy is noticeably reduced. Relatively large discrepancies have been noted between predicted properties using the quasiharmonic Debye model and experimental measurements, which are improved when QHA is applied instead, as also noted in the study by Wang *et al.* [83] particularly for the thermal expansion in Ti_2AlC. This can be explained by the fact that, unlike QHA, the Debye approach takes no account of zero-point energy, nor of the higher frequency optical phonons associated e.g. with carbon atoms in the structure of MAX phases.

Further corrections to the free energy were applied by a number of studies by taking into account electronic excitations [73, 83] and anharmonic effects [85]. At high temperature the electronic corrections were found to increase the heat capacity by almost the same amount as the quasiharmonic contribution, resulting in a better agreement with experiment for Ti_2AX (A = Al or Ga and X = C or N) phases [73].

Although a number of experimental studies in the literature focus on the anisotropic thermal expansion of MAX phases, there are fewer theoretical studies investigating the topic, with predictions usually considering MAX phases as isotropic mediums. The study by Wang *et al.* [83] conducted experimental measurements and DFT calculations to understand the isotropic thermal expansion in Ti_2AlC and Cr_2AlC. Although there is a lack of relevant experimental research

on Zr-based MAX phases, for the Ti-based MAX phases such as Ti_2AlC and Ti_3AlC_2, a number of experimental studies have been reported focusing on thermal expansion and anisotropy [93, 94, 95, 96, 97, 83, 98].

1.3 Chemical bonding

The large interest in MAX phases is mainly driven by their combination of metallic and ceramic characteristics, which is closely related to their structural and electronic properties. Their unusual features mostly stem from their layered structure where strong directional covalent M-X bonding exists in the carbide layers alternating with weaker M-A bonds between the carbide slabs. The metallic nature of MAX phases can be explained by their non-vanishing electron density at the Fermi level governed by the M atoms. These general chemical bonding characteristics are found to be consistent for all studied MAX phases, as a recent review on electronic structure and bonding analysis suggests [99], indicating that a combination of metallic-covalent and ionic bonding exists. These main features have also been confirmed experimentally for a number of MAX phases as noted in the review by Magnuson *et al.* [100]. As an example, for Ti-based 312 MAX phases [99] a very good agreement was found between experiment, using X-ray emission spectroscopy, and theory, where the full potential linearised augmented plane wave (FPLAPW) method was used. Due to the importance of understanding the electronic structure of such materials, extensive theoretical research has focused on the topic, with many studies specifically focused on the Zr and Ti based MAX phases [78, 76, 77, 74, 75, 101, 100, 102] which are of particular interest in this study. Many studies focused on the electronic structure and bonding analysis to draw conclusions on how M elements affect the bond strength in MAX phases and how their stability and mechanical property trends could be explained from an electronic point of view. A connection between mechanical properties and electronic structure was made, linking the relatively weak M-Al interaction to properties such as high thermal shock resistance, high fracture toughness, elasticity and bulk modulus [68, 103, 72, 104, 105]. Site substitutions on M or A sites could be used to tailor MAX phase properties such as conductivity, mechanical properties and elastic anisotropy [77, 74]. Indicatively, the inclusion of Ti

in Zr sites was found to increase the strength of covalent bonding, thus improving mechanical properties [74]. In the study by Dahlqvist *et al.* [43] a trend was noted for the $M_{n+1}AX_n$ phases with M = Sc, Ti, V, Cr, or Mn, A = Al, and X = C or N, between the M transition metal as it varied across the 3*d* series in the periodic table and the stability of the MAX phases. In the study by Bai *et al.* [102], where a number of $M_{n+1}AlC_n$ phases with $n = 1$–3 and M including Zr and Ti were studied, increasing valence electron concentration (VEC) was found to lower the energy range of M-Al and M-C bond hybridisation states. Apart from the effect of the VEC number on stability, the effect of varying the *d*-electron shell number when VEC = 4 on the energy range of hybridisation states of M-C and M-A was also studied in [102], finding however no indication or link between thermodynamic stability and M atoms with different numbers of *d*-electron shells while keeping the VEC number fixed.

1.4 Thermodynamic stability

A useful approach to the study and prediction of stable crystalline materials is to generate a high-throughput set of calculations, wide-ranging and automated, to create a database in which several properties are calculated for hundreds or even many thousands of different materials, many of which will turn out to be unstable, either thermodynamically or mechanically. Such a database can then be used to reject hypothetical materials or to identify candidates for possible synthesis and testing, which can save the time and cost of experimental attempts at synthesis. One might also seek correlations of desired properties with simple quantitative characteristics of the elements, either by inspection or with more sophisticated machine-learning approaches. Studies of this kind have been made on the MAX phase structures by Aryal *et al.* [44] and Ohmer *et al.* [45]. Ref. [44] included density functional theory (DFT) calculations of elastic constants and electronic structure for 792 real or hypothetical MAX phase materials, eliminating those that were mechanically unstable and of the remainder retaining only those whose heats of formation were negative or at the most +53 meV/atom. The small positive value was to admit borderline cases, that might actually prove to be thermodynamically stable in a more exact theory than DFT. For example they might have been incorrectly filtered out because

the calculations assumed temperature $T = 0\,\mathrm{K}$, with no contributions to the free energy from phonons or electronic excitations. This left 665 candidates, for which the data was mined to discover correlations that might predict the stability and properties of potential new compounds. Several correlations were documented [44], but the difference in stability between Zr and Ti MAX phases could not be distinguished. Ref. [45] also reports a set of high-throughput calculations, which again serve well to highlight the contrasting and complementary findings of our more detailed comparison of the Zr-Al-C and Ti-Al-C systems. Whereas in ref. [44], heats of formation were calculated, ref. [45] included the more relevant criterion of thermodynamic stability against decomposition into competing phases, which requires calculation of a *convex hull*.

As mentioned earlier in the chapter, while two particular MAX phases in the $Ti_{n+1}AlC_n$ family have been known since the mid seventies, namely Ti_2AlC [28] and Ti_3AlC_2 [33], their cousins in the $Zr_{n+1}AlC_n$ family are a relatively recent discovery, and have not yet been synthesised in such a pure phase. Successful synthesis was achieved in recent studies by Lapauw *et al.* [3] and Tunca *et al.* [41], by using Zr-hydrides as precursor materials. These authors introduced techniques to improve the phase purity by means of partial site-substitutions, achieving purity above 98 wt%. This relative difficulty in synthesising the Zr-based compared to the Ti-based MAX phases could not have been foreseen from the reported high-throughput studies.

DFT calculations for some selected M-Al-C phases have been published by several authors. Music *et al.* [106] studied the 0 K energy of the $Ta_{n+1}AlC_n$ series for $n = 1$–3 as a function of pressure, and the free energy as a function of temperature, within the harmonic approximation. They observed a structural phase transition to occur in MAX phase α-Ta_3AlC_2 to β-Ta_3AlC_2 at above ∼1000 K. Dahlqvist *et al.* [43] studied a wide range of M-Al-X compounds with DFT, and compared their energies with competing binary compounds. They used a simple linear optimisation technique, which in effect, although they did not refer explicitly to convex hulls, discovered whether the MAX phase was on or above the hull, with a quantitative estimate of its relative stability or instability at 0 K. These studies did not include the Zr-Al-C MAX phases, which are the focus of our study. Besides the aforementioned high-throughput study [44], DFT calculations of MAX phases in Zr-Al-C have been reported by several other groups.

Chapter 2

Theoretical background

This Chapter contains a brief description of the theoretical concepts that are behind the calculation of the free energies of crystals.

2.1 Density Functional Theory

In this section I describe the basis of all the calculations of total energy and forces on atoms on which my free-energy calculations are based. It is also the basis for evaluating the properties of chemical bonds.

2.1.1 Born–Oppenheimer approximation

Given a system of N nuclei and M electrons, an electronic state is entirely described by the many-body wavefunction which is an exact solution of the time-independent Schrödinger equation:

$$\hat{\mathcal{H}}\Psi(\boldsymbol{R},\boldsymbol{r}) = E\Psi(\boldsymbol{R},\boldsymbol{r}) \tag{2.1}$$

where $\hat{\mathcal{H}}$ is the Hamiltonian in the Hilbert space where the many-body wavefunction $\Psi(\boldsymbol{R},\boldsymbol{r})$ is defined, which describes the probability of possible configurations of electrons, at coordinates

$\{\boldsymbol{r}\}$ and of nuclei, at coordinates $\{\boldsymbol{R}\}$. Due to the considerably larger mass of the atomic nuclei compared to the electrons, we can assume that any displacements of the nuclei would result in instant relaxation of the electrons. Therefore, by treating the electrons in a static ionic potential (Born-Oppenheimer approximation), the solution of Eq. 2.1 can be made more tractable by decoupling the sets of electron and nuclei coordinates:

$$\hat{H}\Psi(\boldsymbol{r}) = E\Psi(\boldsymbol{r}) \tag{2.2}$$

The Hamiltonian $\hat{H}$ in the above equation consists of the sum of the kinetic $\hat{T} = -\sum_i \frac{1}{2}\nabla_i^2$ and potential $\hat{V}$ energy operators. The nucleus-nucleus potential energy and the kinetic energies of the nuclei, which were included in Eq. 2.1, are omitted in 2.2 and 2.3, because they can be included in the total energy as required after the electronic part of the total energy has been dealt with. The potential energy operator $\hat{V}$ consists of electrostatic terms involving the Coulomb interactions between the electrons and the interactions between the electrons and the nuclei V_{ext}. In atomic units, the Hamiltonian $\hat{H}$ is therefore given as:

$$\hat{H} = -\sum_i \frac{1}{2}\nabla_i^2 + \frac{1}{2}\sum_{j\neq i} \frac{1}{|\boldsymbol{r}_i - \boldsymbol{r}_j|} + \sum_i V_{\text{ext}}(\boldsymbol{r}_i; \boldsymbol{R}_1, \boldsymbol{R}_2, ..., \boldsymbol{R}_N) \tag{2.3}$$

Although the degrees of freedom of the solution under the Born-Oppenheimer approximation have been reduced, solving this for the majority of systems remains too computationally demanding due to the $3M$ dimensions involved.

2.1.2 Hohenberg–Kohn theorems

The core concept behind the Kohn and Sham (KS) DFT method is based on the two Hohenberg–Kohn (HK) theorems [107]. The first HK theorem proves there is a unique external potential $V_{\text{ext}}(\boldsymbol{r})$ corresponding to the ground state electron density $\rho_0(\boldsymbol{r})$. The second HK theorem describes the variational principle, stating that the ground state energy for a given external potential can be found variationally by minimising the total energy with respect to the electron density. The ground state energy of the system can therefore be obtained based

on the expression:

$$E_0 = F[\rho_0(\boldsymbol{r})] = \min_{\rho} F[\rho(\boldsymbol{r})] \tag{2.4}$$

The total energy functional, $F[\rho(\boldsymbol{r})]$, can be expressed as the expectation value of the Hamiltonian $\hat{H}$ based on Eq. 2.3, with T and W below corresponding to the kinetic energy and the Coulomb interactions between electrons respectively:

$$\begin{aligned} F[\rho(\boldsymbol{r})] &= \langle\Psi| - \sum_i \frac{1}{2}\nabla_i^2 |\Psi\rangle + \langle\Psi| \frac{1}{2} \sum_{j\neq i} \frac{1}{|\boldsymbol{r}_i - \boldsymbol{r}_j|} |\Psi\rangle + \int \rho(\boldsymbol{r}) V_{\text{ext}} \mathrm{d}\boldsymbol{r} \\ &= T + W + \int \rho(\boldsymbol{r}) V_{\text{ext}} \mathrm{d}\boldsymbol{r} \end{aligned} \tag{2.5}$$

Expressing the energy functional of the electronic density $\rho_0(\boldsymbol{r})$ does not however reduce the complexity of the many-body wavefunction corresponding to Eq. 2.2 and the dimensions of the problem remain $3M$. Kohn and Sham subsequently published an ingenious way of reducing the dimensionality of the problem, using ideas familiar from the simple mean-field Hartree model of electronic structure, in which the electronic wavefunction is a determinant constructed from single-electron wavefunctions. The determinant function ensures antisymmetry of the wavefunction with respect to exchange of a pair of electrons. To appreciate how Kohn and Sham could achieve this, I first summarise the Hartree model and the ideas of antisymmetry, exchange and correlation.

2.1.3 Hartree model and Hartree–Fock theory

Considering the complexity of solving a many-body problem, one approach to its simplification could be to represent the system based on a set of single-electron equations. One of the earliest and simplest such approximations, to separate the electronic variables based on approximating the electron-electron interactions within the system, was the Hartree approximation (mean field approximation). Within the Hartree method each electron in the system is treated independently and their only interaction with one another considered, is through a mean field Coulomb potential produced by all of the electrons in the system. In the Hartree model, the many-body

wavefunction could initially be described by the product of single-particle wavefunctions:

$$\Psi(\boldsymbol{r}_1, \boldsymbol{r}_2, ..., \boldsymbol{r}_N) = \psi_1(\boldsymbol{r}_1)\psi_2(\boldsymbol{r}_2)..\psi_N(\boldsymbol{r}_N) \tag{2.6}$$

and the Hamiltonian is expressed as the sum of the system's single-electron Hamiltonians $\hat{H}_i$:

$$\left(\sum_i \hat{H}_i\right)\Psi = E\Psi \tag{2.7}$$

with each Hamiltonian $\hat{H}_i$ being defined as:

$$\left[-\frac{\nabla_i^2}{2} + V_{\mathrm{H}}(\boldsymbol{r}) + V_{\mathrm{ext}}(\boldsymbol{r})\right]\psi_i^{\mathrm{H}}(\boldsymbol{r}) = \epsilon_i^{\mathrm{H}}\psi_i^{\mathrm{H}}(\boldsymbol{r}) \tag{2.8}$$

where the V_{H} term corresponds to the Hartree potential that accounts for the effect of the mean field of all electrons in the system on each electron i. Within the Hartree approximation the total energy functional $F^{\mathrm{S}}[\rho(\boldsymbol{r})]$ is then expressed as:

$$\begin{aligned} F^{\mathrm{S}}[\rho(\boldsymbol{r})] &= T_{\mathrm{S}} + W_{\mathrm{S}} + \int \rho(\boldsymbol{r})V_{\mathrm{ext}}(\boldsymbol{r})\mathrm{d}\boldsymbol{r} \\ &= \sum_i \langle\psi_i| - \frac{\nabla_i^2}{2}|\psi_i\rangle + \frac{1}{2}\int\int \frac{\rho(\boldsymbol{r})\rho(\boldsymbol{r'})}{|\boldsymbol{r}-\boldsymbol{r'}|}\mathrm{d}\boldsymbol{r}\mathrm{d}\boldsymbol{r'} + \int \rho(\boldsymbol{r})V_{\mathrm{ext}}(\boldsymbol{r})\mathrm{d}\boldsymbol{r} \end{aligned} \tag{2.9}$$

with the second term, W_{S} corresponding to the classical electrostatic self-energy of the charge density ρ, now called the Hartree energy.

Therefore through this mean field approximation, the $3M$ many-body problem is reduced to a series of coupled 3D equations. However, the main drawback of the Hartree model is that it relies on an incomplete picture of the real system that does not capture exchange and correlation effects. In particular, the original Hartree method does not factor in the Pauli exclusion principle which requires an anti-symmetric many-body wavefunction when two electrons are interchanged. The Hartree-Fock method [108] improves on the Hartree method by expressing the multi-electron wavefunction as a Slater determinant and thus approximates the exchange between the electrons with the simplest possible antisymmetrised wavefunction. However, the main drawback of the Hartree-Fock model is that the exchange potential is non-local and cor-

relation, a shorthand term for the effect on the wavefunction of Coulomb repulsion between electrons, is not accounted for. Overall Hartree-Fock is computationally more expensive than Kohn–Sham DFT, given the non-local expression of the exchange energy, usually gives results with lower accuracy and is inapplicable for metallic systems. For example for jellium, Hartree-Fock predicts zero density of states at the Fermi level, so that simplest of model metals appears to be insulating.

As we shall see in the next section, Kohn–Sham DFT differs from Hartree-Fock in that the exchange potential is local, depending explicitly on the charge density, and that it accounts for the correlation energy of the system.

2.1.4 Kohn–Sham DFT

Kohn and Sham made use of the Hartree model referring to a system of non-interacting electrons, with a single-determinant wavefunction, moving in a mean-field potential, which comprises the Hartree potential, just as described in Eq. 2.9, but including an additional local potential to represent the exchange and correlation energies. They had the insight that such an effective potential exists, which uniquely determines the exact ground-state charge density. The only change required to the functional (2.9) is the addition of a so-called exchange-correlation functional. Besides the direct Coulomb energy of exchange and correlation effects, the functional implicitly includes the deviation of the kinetic energy, which is induced by exchange and correlation, from its value T_{S}:

$$\begin{aligned} F[\rho(\boldsymbol{r})] &= T_{\mathrm{S}} + W_{\mathrm{S}} + \int \rho(\boldsymbol{r}) V_{\mathrm{ext}}(\boldsymbol{r}) \mathrm{d}\boldsymbol{r} + E_{\mathrm{XC}}[\rho(\boldsymbol{r})] \\ &= F^{\mathrm{S}}[\rho(\boldsymbol{r})] + E_{\mathrm{XC}}[\rho(\boldsymbol{r})] \end{aligned} \tag{2.10}$$

Therefore the exchange correlation term includes the discrepancies occurring between the real system of electrons and the Hartree model. The minimisation of this energy functional $F[\rho(\boldsymbol{r})]$

by varying the electronic density of the system is performed under the constraint:

$$\int \rho(\boldsymbol{r})\mathrm{d}\boldsymbol{r} = M \tag{2.11}$$

and can be formulated as the following differential equation:

$$\frac{\delta}{\delta\rho(\boldsymbol{r})}\left[F[\rho(\boldsymbol{r})] - \mu\left(\int \rho(\boldsymbol{r})\mathrm{d}\boldsymbol{r} - M\right)\right] = 0 \tag{2.12}$$

resulting in the Euler-Lagrange equality with μ representing the Lagrange multiplier:

$$\left.\frac{\delta F[\rho(\boldsymbol{r})]}{\delta\rho(\boldsymbol{r})}\right|_{\rho_0} = \frac{\delta F^{\mathrm{S}}[\rho(\boldsymbol{r})]}{\delta\rho(\boldsymbol{r})} + \frac{\delta E_{\mathrm{XC}}[\rho(\boldsymbol{r})]}{\delta\rho(\boldsymbol{r})} = \mu \tag{2.13}$$

The Kohn and Sham effective potential $V_{\mathrm{KS}} = V_{\mathrm{H}} + V_{\mathrm{XC}} + V_{\mathrm{ext}}$ is the mean field potential in the assumed system of nuclei and non-interacting electrons. The single-electron equation describing this system as defined by Kohn and Sham is then:

$$\left[-\frac{\nabla_i^2}{2} + V_{\mathrm{H}}[\rho(\boldsymbol{r})](\boldsymbol{r}) + V_{\mathrm{ext}}(\boldsymbol{r}) + V_{\mathrm{XC}}[\rho(\boldsymbol{r})](\boldsymbol{r})\right]\psi^{\mathrm{KS}}(\boldsymbol{r}) = \epsilon_i^{\mathrm{KS}}\psi_i^{\mathrm{KS}}(\boldsymbol{r}) \tag{2.14}$$

the total ground state energy can then be expressed as the sum over the KS eigenvalues of the occupied states resulting from Eq. 2.14 with the second and third terms subtracted to correct for the double counting of the electron-electron interaction since the Hartree and exchange-correlation potentials already appear in the Hamiltonian term and the exchange-correlation energy, E_{XC}, is added in the forth term.

$$E_0 = \sum_i \epsilon_i^{\mathrm{KS}} - W_{\mathrm{S}} - \int \rho(\boldsymbol{r})V_{\mathrm{XC}}(\boldsymbol{r})\mathrm{d}\boldsymbol{r} + E_{\mathrm{XC}} \tag{2.15}$$

The solution of this single-particle Kohn-Sham equation is based on a self-consistent scheme. The initial step in this process is to determine a starting value for the charge density, which can usually be chosen to be the superposition of the charge densities of each atom in the system. The Hartree potential V_{H} can then be calculated from this initial charge density, as can V_{XC} via exchange-correlation approximations (e.g. GGA, LDA, etc). The Kohn-Sham effective

potential is then constructed by adding these calculated V_{H} and V_{XC} potentials to the external potential and is used to solve Eq. 2.14 to produce a set of eigenstates $\{\psi_i^{\mathrm{KS}}(\boldsymbol{r})\}$ based on which the Kohn-Sham energy is evaluated (Eq. 2.15). The aforementioned steps are then repeated using the output charge density mixed with the input density to provide an input for the next iteration until a reasonable level of convergence has been reached. The converged eigenfunctions $\{\psi_i^{\mathrm{KS}}(\boldsymbol{r})\}$ are called the Kohn–Sham eigenstates and the corresponding energy is the ground state energy of the system.

2.1.5 Exchange–Correlation Functionals

The Kohn–Sham eigenstates from Eq. 2.10 correspond, in principle, to the ground state energy of the real system providing that the form of the exchange and correlation (XC) functional $E_{\mathrm{XC}}[\rho]$ is known. However, $E_{\mathrm{XC}}[\rho]$ can, so far, only be approximated although many such approaches have been developed since KS DFT was first introduced involving various levels of theory and empirical adjustments often made for different classes of materials. The exchange and correlation approximation is one of the most important in the DFT framework as it can determine the overall level of accuracy of the DFT calculations.

One of the first and simplest XC approximations is the Local Density Approximation (LDA) [109], whose main concept is based on the idealised case of free electron gas (FEG). LDA treats the electron density locally by subdividing the 3D space into small volumes wherein electron density is assumed to be approximately constant, as in FEG. The XC energy within LDA, expressed based on the local electron density at $\boldsymbol{r}$, $\rho(\boldsymbol{r})$, and the energy eigenvalues of the homogeneous electron gas system is given by:

$$E_{\mathrm{XC}}^{\mathrm{LDA}}[\rho(\boldsymbol{r})] = \int \mathrm{d}\boldsymbol{r}\rho(\boldsymbol{r})\epsilon_{\mathrm{XC}}^{\mathrm{FEG}}[\rho(\boldsymbol{r})] \tag{2.16}$$

The energy of a FEG at density ρ has been obtained by Ceperley and Alder [110] using accurate quantum Monte Carlo simulations.

The LDA approximation is one of the most widely used exchange correlation functionals in

first-principle studies with surprisingly good accuracy given the degree of inhomogeneity of the electron densities in real systems. Many attempts to improve on the LDA functional have been made with one such being the Generalised Gradient Approximation (GGA) functionals that add correlations to the FEG eigenstates that depend on the gradient of the electron density $\epsilon_{\mathrm{XC}}^{\mathrm{FEG}}[\rho(\boldsymbol{r}), \nabla\rho]$. The default functional used in this study is PBESol [111], which belongs to the GGA functional family.

2.1.6 Periodic boundary conditions - Plane wave basis

In crystalline materials whose structure is characterised by unit cells, the application of periodic boundary conditions on the electronic wavefunction becomes necessary. The expression of a single-electron wavefunction for such systems can be based on Bloch's theorem and thus be written as:

$$\psi_{n\boldsymbol{k}}(\boldsymbol{r}) = e^{i\boldsymbol{k}\cdot\boldsymbol{r}} u_{n\boldsymbol{k}}(\boldsymbol{r}) \tag{2.17}$$

where the $u_{n\boldsymbol{k}}(\boldsymbol{r})$ function shares the lattice's periodicity and n is the band index used to specify the wavefunctions, $\psi_{\boldsymbol{k}}$, denoted by the same wavevector $\boldsymbol{k}$ within the first Brillouin zone. Computationally it can be beneficial to express the wavefunction in a basis of plane waves by writing $u_{n\boldsymbol{k}}(\boldsymbol{r})$ as a Fourier series:

$$u_{n\boldsymbol{k}}(\boldsymbol{r}) = \sum_{\boldsymbol{G}} c_{\boldsymbol{G}}^{n\boldsymbol{k}} e^{i\boldsymbol{G}\cdot\boldsymbol{r}} \tag{2.18}$$

and then the wavefunction from the Eq. 2.17 can be rewritten as:

$$\psi_{n\boldsymbol{k}}(\boldsymbol{r}) = \sum_{\boldsymbol{G}} c_{\boldsymbol{G}}^{n\boldsymbol{k}} e^{i(\boldsymbol{G}+\boldsymbol{k})\cdot\boldsymbol{r}} \tag{2.19}$$

where reciprocal space lattice vectors are denoted $\boldsymbol{G}$.

Expression 2.19 consists of an unlimited number of plane waves. To make it computationally feasible, the expression can be approximated by considering only a finite number of plane waves, leading to the idea of the plane wave cut-off energy, E_{cut}. This cut-off energy sets a limit on

the highest frequency plane waves in the basis set, resulting in the greatest $\boldsymbol{G}$ being used to set the E_{cut}.

$$E_{\text{cut}} = \frac{\boldsymbol{G}_{\text{max}}^2}{2} \tag{2.20}$$

Considering that a basis set with missing plane waves will introduce errors in the calculations (e.g. Pulay stresses), it is important to establish a sufficient description of the system balanced against the processing cost introduced by raising the cut-off energy.

From Bloch's theorem and the resulting equation, Eq. 2.19, the dependence of the wavefunctions on the wavevector $\boldsymbol{k}$ is shown. In practice, apart from the need to determine a finite number of plane waves, k-point sampling within the Brillouin zone is also required. This is implemented based on schemes like Monkhorst-Pack [112], wherein the sampling provides an effective basis for integrating the periodic functions in the first Brillouin zone. Similarly with the case of E_{cut}, it is important that the k-point sampling is sufficiently converged, particularly for electron density of states calculations.

2.1.7 Pseudopotentials

In the Kohn-Sham DFT framework the number of electrons in the system significantly affects the calculation's cost. It is known that it is mainly the valence electrons that are involved in chemical bonding and that contribute to the chemical environment of a system, since the electron densities associated with the core electrons are strongly confined near the nucleus, in contrast with the valence electrons. This gives rise to the development of pseudopotential methods which keep the core electrons frozen compared to the valence ones which are accounted for explicitly within the Kohn-Sham scheme. Different schemes to produce pseudopotentials have been developed, with an important aspect of their applicability depending on how soft or hard they are. A hard pseudopotential depends on many Fourier terms to sufficiently describe it, whereas a soft one requires fewer terms, resulting in quicker convergence but at the cost of transferability between different chemical systems.

2.2 Chemical bonding

This section is mainly concerned with the description of different calculation approaches to chemical bonding and the distribution of charges on atoms. As is known, the amount of charge associated with an atom in a solid is not a measurable quantity in the sense of quantum mechanics, therefore there is no unique way to partition the charge and allocate it to particular atoms. This has led to the development of several partitioning schemes to express the charge transfer, bond orders and bond energies, which may be used to show trends in charge transfer within a class of compounds or elements. Some such approaches that were applied in this work and will be described in the following sections are the Bader analysis [113], the Mulliken analysis [114], the Crystal Orbital Overlap Population (COOP), the Crystal Orbital Hamilton Population (COHP) [115] and the Density Derived Electrostatic and Chemical (DDEC) method [15]. In this work the calculations are based on DFT using a plane waves basis. Plane wave basis sets, however, are not the natural way to describe the bonds between atoms, and normally local orbital (or atomic orbitals) are used in chemical bonding analysis. Based on the DFT planewave framework, the following sections describe methodologies for nevertheless extracting the chemical bonding information based on two main approaches. One approach is based on charge density which is the fundamental output quantity from DFT calculations from which a material's properties are determined. Examples of methodologies based on analysis of the charge density information are the Bader analysis or the more recent DDEC method. An alternative approach is based on the one-electron wavefunctions acquired from the DFT calculations and projected onto a local orbital basis to describe the charge transfer. Examples of such are the Mulliken analysis, COOP and COHP. The amount of charge associated with bonds, quantified as the COOP, and the bond-strength calculated from the COHP can be understood as useful indicators, but they are dependent on projection onto some chosen atom-centred basis functions of the one-electron wavefunctions of Kohn-Sham DFT.

2.2.1 Mulliken analysis and Crystal Orbital Hamilton Populations

Since, as noted previously, planewave basis sets are not the natural way to describe the bonds between atoms, in this section we discuss concepts for describing bonding by projecting the one-electron wavefunctions acquired from the DFT calculations onto local basis functions. The discussion in this section is based on the textbook by Finnis [116] and follows its notation. Across the approaches we are interested in, each of the single particle Kohn-Sham eigenfunctions $|n\rangle$ are expanded on a basis of local functions:

$$|n\rangle = \sum_{I\mu} C^n_{I\mu} |I\mu\rangle \tag{2.21}$$

with $C^n_{I\mu}$ being the expansion coefficients of the local orbitals and μ labeling a particular orbital on a particular atom, I. While local orbitals on each atom are orthonormal, orthogonality between orbitals on different atoms, i.e. atoms I and J where $I \neq J$, is unlikely. Therefore in the case of such non-orthogonal local basis functions, a matrix, S, is introduced to account for the overlap between the orbitals, μ and ν, on the atoms, I and J:

$$S_{I\mu J\nu} = \langle I\mu | J\nu \rangle \tag{2.22}$$

The total number of electrons, N, in the system can then be expressed as the trace of the electron density operator, $\hat{\rho}$:

$$N = \text{Tr } \hat{\rho} = \sum_{n=0}^{\infty} \sum_{I\mu J\nu} f_n C^n_{I\mu} C^{n*}_{J\nu} S_{J\nu I\mu} = \sum_{I\mu J\nu} \rho^{I\mu J\nu} S_{J\nu I\mu} \tag{2.23}$$

where

$$\rho^{I\mu J\nu} = \sum_{n=0}^{\infty} f_n C^n_{I\mu} C^{n*}_{J\nu} \tag{2.24}$$

are the expansion coefficients of the density operator expressed in a local basis, and f_n is the occupancy of each state n. One way to then partition this total number of electrons when a non-orthogonal local basis is used, is into the atom-centered charges, ρ_I, and the bond charges,

ρ_{IJ}:

$$N = \sum_I \rho_I + \frac{1}{2} \sum_{I \neq J} \rho_{IJ} \tag{2.25}$$

Apart from this particular charge partition, it can also be useful to allocate all the charge to individual atoms, even with a non-orthogonal basis set, without any charge being assigned to the bond, since this charge can be indicative of the valency of this atom. One way to define these atomic charges is as Mulliken charges, by adding half of the bond charges of the neighboring atoms, ρ_{IJ}, to each atom, ρ_I:

$$q_I = \rho_I + \frac{1}{2} \sum_J \rho_{IJ} \tag{2.26}$$

Complementary to the on-site Mulliken charges, one can describe chemical bonding between different atomic pairs via the concept of 'bond orders' as defined by Coulson [117] as the off-diagonal expansion coefficients of the density operator, $\hat{\rho}$, expressed on the basis of local orbitals, as shown in Eq. 2.24. These bond orders are commonly used as bond strength indicators.

Other ways to provide a measure of bond strength include the Crystal Orbital Overlap Population, COOP(ϵ), and the later-introduced Crystal Orbital Hamiltonian Population, COHP(ϵ), both of which are a function of the Kohn-Sham single particle energy ϵ. These methods describe the local and energy resolved form of the number of electrons, from the COOP, and the band energy, from the COHP. Published software tools exist that apply these concepts to the output of planewave calculations performed by tools like VASP [118, 119]. One such software implementation used in our study is LOBSTER which was introduced by Maintz *et al.* [120, 121, 122].

Starting our further discussion with the COOP, it can be thought of as an energy-resolved bond order and can be derived by first considering the density operator represented in a local basis:

$$\hat{D} = \sum_{n, I\mu, J\nu} C^n_{I\mu} \left| I\mu \right\rangle \delta(\epsilon - \epsilon_n) C^{n*}_{J\nu} \left\langle J\nu \right| \tag{2.27}$$

The COOP can then be expressed by taking the trace of $\hat{D}$ in the local basis:

$$D(\epsilon) = \mathrm{Tr}\ \hat{D}(\epsilon) = \sum_{I\mu J\nu} D^{I\mu J\nu}(\epsilon) S_{J\nu I\mu} \tag{2.28}$$

which is used to allocate the DOS to particular atoms, orbitals and bonds. Thus for particular terms, the COOP can be expressed as:

$$\mathrm{COOP}(\epsilon, I\mu, J\nu) = \sum_{n=0}^{\infty} C_{I\mu}^{n} \delta(\epsilon - \epsilon_n) C_{J\nu}^{n*} S_{J\nu I\mu} + c.c. \tag{2.29}$$

and specifically for the onsite terms, considering the orbitals on each atom to be orthonormal, we get:

$$\sum_{n=0}^{\infty} C_{I\mu}^{n} \delta(\epsilon - \epsilon_n) C_{I\mu}^{n*} + c.c.$$

Considering that the off-diagonal terms of the COOP expression are included, the COOP describes the energy-resolved values that quantify the local contributions, i.e. of bonds between particular atomic pairs, to the total number of electrons. Similarly, but instead of accounting for local contributions to the number of electrons, the COHP represents the local and energy-resolved form of the band energy. To derive the expression for the COHP, we make use of Eq. 2.24 that describes the density expansion coefficients to express the trace of $\hat{\rho}$ times the Hamiltonian operator, $\hat{H}$, as:

$$\mathrm{Tr}\ \hat{\rho}\hat{H} = \sum_{n,I\mu,J\nu} f_n C_{I\mu}^{n} C_{J\nu}^{n*} H_{J\nu I\mu} \equiv 2 \sum_{I\mu J\nu} \int_{-\infty}^{\infty} d\epsilon f_{\mathrm{F}}(\epsilon) C_{I\mu}^{n} \delta(\epsilon - \epsilon_n) C_{J\nu}^{n*} H_{J\nu I\mu} \tag{2.30}$$

where f_{F} is the Fermi distribution, $f_n = 2f_{\mathrm{F}}(\epsilon_n)$, and $H_{J\nu I\mu}$ is a matrix element of the Hamiltonian. For a particular bond, the COHP therefore can quantify its contribution to the total band energy at a given energy as follows:

$$\mathrm{COHP}(\epsilon, I\mu, J\nu) = 2f_{\mathrm{F}}(\epsilon) C_{I\mu}^{n} \delta(\epsilon - \epsilon_n) C_{J\nu}^{n*} H_{J\nu I\mu} + c.c. \tag{2.31}$$

2.2.2 Bader analysis

Apart from the approaches discussed above based on the one-particle Kohn-Sham equations, as mentioned, other approaches to extract chemical bonding information from a system have been based on charge density, which is a fundamental output quantity of DFT calculations.

The simplest such method is Bader analysis [113]. In Bader analysis charges on atoms are calculated based on topological partitions of the charge density where the charge density is separated into non-overlapping volumes enclosed by zero flux surfaces where $\nabla\rho(\boldsymbol{r}) = 0$.

2.2.3 Density Derived Electrostatic and Chemical Method

A second, but much more complex method using the same approach of depending only on the charge density without direct reference to the wavefunctions is the Density Derived Electrostatic and Chemical (DDEC) method [15]. DDEC is a partitioning method that was applied for these calculations to predict the overlap population, atomic net charges, bond orders (BOs), and sum of bond orders (SBOs) [14, 16]. Bond formation is considered to be based on the electron exchange of two neighbouring atoms with electron densities that overlap. The strength of these bonds can be quantified by the bond order, as it is derived within the DDEC method and is based on the use of the dressed-exchange hole approach [15]. The implementation of the version of this method used in this study, DDEC6, has been done in the CHARGEMOL program [123].

In particular, the dressed-exchange electrons between two atoms I and J, in the reference unit cell and the material respectively, is represented by the $B_{I,J}$ matrix, whose off-diagonal elements quantify the bond order between the two atoms. These off-diagonal elements are calculated by the expression:

$$B_{I,J} = \mathrm{CE}_{I,J} + \Lambda_{I,J} \tag{2.32}$$

where the $\mathrm{CE}_{I,J}$ term describes the electron exchange between atoms I and J in a material. This term is formulated as:

$$\mathrm{CE}_{I,J} = 2 \oint \frac{\boldsymbol{\rho}_I^{\mathrm{avg}}(r_I) \cdot \boldsymbol{\rho}_J^{\mathrm{avg}}(r_J)}{\boldsymbol{\rho}^{\mathrm{avg}}(\boldsymbol{r}) \cdot \boldsymbol{\rho}^{\mathrm{avg}}(\boldsymbol{r})} \rho(\boldsymbol{r}) \mathrm{d}^3\boldsymbol{r} \tag{2.33}$$

where $\rho(\boldsymbol{r})$ is the total electron density at position $\boldsymbol{r}$ and $\rho(\boldsymbol{r}_I)$ is the electron density assigned to atom I with $\boldsymbol{r}_I$ being the vector from the nuclear position of atom I to a position $\boldsymbol{r}$. The vector $\boldsymbol{\rho}_I^{\mathrm{avg}}(r_I)$ (and equivalently $\boldsymbol{\rho}_J^{\mathrm{avg}}(r_J)$) is a spherical average, at distance $r_I = \|\boldsymbol{r}_I\|$ from the center of atom I, of the electronic and spin magnetisation densities, which were acquired

from the DDEC partition method. $\boldsymbol{\rho}^{\text{avg}}(\boldsymbol{r})$ corresponds to the sum over all atomic $\boldsymbol{\rho}_J^{\text{avg}}(r_J)$ in the unit cell. The $\Lambda_{I,J}$ term, describes the delocalisation of the dressed exchange hole, which tailors the degree of contraction or diffusion to obtain accurate BOs. This term takes into account pairwise interactions, the coordination number effects and a constraint on $B_{I,I}$, the density-derived localisation index (DDLI), to ensure it is well behaved.

The diagonal elements $B_{I,I}$ satisfy the expression:

$$B_{I,I} = N_I - \frac{1}{2}\text{SBO}_I \tag{2.34}$$

where N_I is the total number of electrons assigned to atom I, expressed as $N_I = \oint \rho_I(\boldsymbol{r}_I)\text{d}^3\boldsymbol{r}$, and SBO_I is the sum of the bond orders on atom I.

It follows that for a material containing N electrons in the unit cell, the following summation rule is true for the above defined $B_{I,J}$ matrix:

$$N = \frac{1}{2}\left(\sum_I \sum_J B_{I,J} + \sum_I B_{I,I}\right) \tag{2.35}$$

The number of electrons assigned to atom I, N_I, can be expressed as the difference between its nuclear charge z_I and its net atomic charge, q_I:

$$N_I = z_I - q_I \tag{2.36}$$

where N_I is connected to the $B_{I,I}$ by the expression:

$$N_I = B_{I,I} + \frac{1}{2}\sum_{I \neq J} B_{I,J} \tag{2.37}$$

The sum of bond orders is defined as:

$$\text{SBO}_I = \sum_{I \neq J} B_{I,J} \tag{2.38}$$

Given the information of the atomic charge q_I and the SBO_I, $B_{I,I}$ can be expressed using Eq. 2.36 and 2.37 as:

$$B_{I,I} = z_I - q_I - \frac{1}{2}\mathrm{SBO}_I \tag{2.39}$$

Therefore, for an atom I the electrons transferred to bonds or to other ions can be given by the following:

$$z_I - B_{I,I} \tag{2.40}$$

2.3 Harmonic phonons

2.3.1 Harmonic lattice dynamics

The theory of lattice dynamics concerns collective vibrations of atoms in crystalline solids and is central to explaining thermal expansion and other thermophysical properties in such materials. This theory has been described in available textbooks and papers, such as by Wallace [124] and by Togo *et al.* [125], among others. Crystalline solids are represented by lattices of atoms typically described by atomic unit cells infinitely repeated in all directions. We can consider this infinite crystal structure by imposing periodic boundary conditions on a system of n_{cell} unit cells of M atoms each, where n_{cell} is considered to be large enough to avoid interactions of atoms with periodic images of themselves. In this system, we refer to each unit cell and atom within it using the labels k and I, respectively. The potential energy of this crystal is expressed as a function of the atomic displacements $\boldsymbol{u}(kI)$ around the equilibrium positions of its atoms $\boldsymbol{r}(kI)$ and is expanded by applying Taylor expansion about the equilibrium positions of the atoms that correspond to the minimum energy E_0:

$$E = E_0 + \sum_{kI}\sum_{\alpha} \Phi_a(kI)u_\alpha(kI) + \frac{1}{2}\sum_{kk'II'}\sum_{\alpha\beta} \Phi_{\alpha\beta}(kI,k'I')u_\alpha(kI)u_\beta(k'I') + \dots \tag{2.41}$$

where α and β indicate the Cartesian directions of the atomic displacements. Since the expansion in this equation is about the equilibrium positions, where no forces are applied on the atoms, $\Phi_a(kI) = \frac{\partial E}{\partial u_a(kI)}$ will also be zero. The expansion of the crystal energy in Eq. 2.41 has

been approximated up to the second-order expansion, assuming displacements of atoms in the crystal are sufficiently small (harmonic approximation).

For atom kI, that is being displaced by $u_a(kI)$, the force applied on it is determined as follows:

$$F_\alpha(kI) = -\frac{\partial E}{\partial u_a(kI)} \tag{2.42}$$

Considering Eq. 2.42, an element of the second-order force coefficient can then be determined as follows:

$$\Phi_{\alpha\beta} = \frac{\partial^2 E}{\partial u_\alpha(kI)\partial u_\beta(k'I')} = -\frac{\partial F_\beta(k'I')}{\partial u_\alpha(kI)} \tag{2.43}$$

More computational details about the calculation of the force constants follow in Section 2.3.2. Based on the classical equations of motion ($F = -k \cdot u = m \cdot \ddot{u}$), the motion of the system of atoms and how they change over time in a unit cell k, can be expressed as $3M$ coupled equations:

$$F_a(kI) = m_I \frac{\partial^2 u_a(kI)}{\partial t^2} = -\sum_{k'I'} \sum_{\beta} \Phi_{\alpha\beta} u_\beta(k'I') \tag{2.44}$$

where m_I refers to the mass of atom I. The summation of the pairwise interactions between displaced atoms and atom kI along the α direction in the system, yields the net force on that atom.

Considering the periodic potential of the lattice, from the Bloch theorem we could expect the atom displacements to be described by a periodic function with the periodicity of a unit cell and modulated by a plane wave. It can thus be preferable to express Eq. 2.44 in reciprocal space. The dynamical matrix is then expressed in reciprocal space after Fourier transforming the real space force constant matrix $\Phi_{\alpha\beta}(kI, k'I')$.

$$D^{\alpha\beta}_{II'}(\boldsymbol{q}) = \sum_{k'} \frac{\Phi_{\alpha\beta}(0I, k'I')}{\sqrt{m_I m_{I'}}} e^{i\boldsymbol{q}\cdot[\boldsymbol{r}(k'I') - \boldsymbol{r}(0I)]} \tag{2.45}$$

Combining the dynamical matrix Eq. 2.45 with the classical equations of motion Eq. 2.44, leads to an eigenvalue problem that requires the diagonalisation of the $\boldsymbol{D}(\boldsymbol{q})$ dynamical matrix resulting in a set of $\omega_{\boldsymbol{q}j}$ eigenfrequences and $\boldsymbol{e}_{\boldsymbol{q}j}$ eigenvectors at each wavevector $\boldsymbol{q}$ and band

index j:

$$\sum_{\beta I'} D_{II'}^{\alpha\beta}(\boldsymbol{q}) e_{\boldsymbol{q}j}^{\beta I'} = \omega_{\boldsymbol{q}j}^2 e_{\boldsymbol{q}j}^{\alpha I} \tag{2.46}$$

Each $\boldsymbol{e}_{\boldsymbol{q}j}$ eigenvector at a particular wave vector $\boldsymbol{q}$ consists of $3M$ components describing the collective motion of the atoms. The term 'normal modes' is used to describe these collective displacements of the atoms in the crystal. The dependency of the frequency ω of each normal mode on the wavevector $\boldsymbol{q}$ within the first Brillouin zone gives the phonon dispersion of the crystal. At $q = 0$, corresponding to the center of the Brillouin zone (Γ), the displacement wave has an infinite wavelength which describes the in phase movement of symmetrically equivalent atoms in the different unit cells. At the Γ point there are always three acoustic modes, as all the atoms in the unit cells of the crystal are moving in phase as a rigid block towards the three directions of the crystal. These acoustic modes correspond to zero energy as their frequency is zero and for small values of $\boldsymbol{q}$, near zero, they show a linear dispersion. The remaining $3M - 3$ modes at Γ are known as optical modes and involve relative movements between the atoms in each unit cell.

Once the calculation of the phonon dispersion has been completed the phonon DOS is expressed as:

$$g(\omega) = \frac{1}{n_{cell}} \sum_{\boldsymbol{q}j} \delta(\omega - \omega_{\boldsymbol{q}j}) \tag{2.47}$$

when the DOS is integrated over the phonon frequency range and normalised by being divided by the number of unit cells n_{cell}, it equals $3M$. In practise the DOS can be calculated via the smearing method or a linear tetrahedron method [126], which is what was used in this study implemented in PHONOPY [125]. The phonon frequencies are calculated at the $\boldsymbol{q}$ points on a defined $\boldsymbol{q}$ sampling and then Eq. 2.47 is evaluated by integration within tetrahedra defined in the Brillouin zone.

2.3.2 Calculations of phonon eigenmodes and eigenfrequencies

While the previous section covers the theoretical basis of harmonic lattice dynamics and normal phonon modes in crystals, this section describes an outline of how the phonon eigenmodes

and eigenfrequencies are calculated. The first requirement in this process is the evaluation of the force constant matrix, which can be mainly performed using the finite difference method (supercell method) or the linear response method [127]. In the supercell method, which is the method used in this study, finite displacements $\Delta r_\alpha(kI)$ of one atom at a time in the supercell are performed and the resulting forces on each atom can then be calculated. By exploiting the crystal symmetry, not all atoms in the unit cell need to be displaced thus reducing the computational cost. For each supercell arrangement, the forces on each of its atoms are evaluated with DFT calulations, making use of the Hellman-Feynman force method implemented in VASP [118, 119]. The force constants can then be calculated from first-order derivatives of the forces as:

$$\Phi_{\alpha\beta}(kI, k'I') = -\frac{F_\beta(k'I'; \Delta r_\alpha(kI)) - F_\beta(k'I')}{\Delta r_\alpha(kI)} \tag{2.48}$$

which approximates the exact derivative in Eq. 2.43.

The dynamical matrix is then calculated at each wavevector, $\boldsymbol{q}$, defined from the $\boldsymbol{q}$ sampling mesh by applying Fourier transformation on the force constant matrix. The supercell in this case, whose size can be determined by the interaction range between the atoms, must be large enough to allow for a wavelength $\lambda = 2\pi/|\boldsymbol{q}|$. After the evaluation of the $3M \times 3M$ dynamical matrix at each $\boldsymbol{q}$ point, the calculation of the eigenfrequencies and eigenmodes is done by its diagonalisation resulting in $3M$ eigenfrequencies $\omega_{\boldsymbol{q}j}$ and eigenmodes $e^{\alpha k}_{\boldsymbol{q}j}$. Therefore, after the force set evaluation in VASP, the force constants, dynamical matrix, phonon frequencies and eigenvectros at each $\boldsymbol{q}$ point are calculated in PHONOPY. Other dependant values such as the phonon band structure, phonon DOS, thermodynamic properties, thermal properties and characters of irreducible representations of normal modes are also calculated in PHONOPY and are discussed further in the following sections.

2.3.3 Harmonic phonon thermodynamics

In the previous sections the discussion was classical, with the lattice vibrations in a crystal being described in terms of its normal modes. In quantum mechanics, considering the analog

of the quantum harmonic oscillator, the quantitised normal modes are called phonons, with the energy of n quanta in a normal mode s at a wavevector $\boldsymbol{q}$ given as:

$$\epsilon^{(s)}(\boldsymbol{q}) = \left(\frac{1}{2} + n\right)\hbar\omega^{(s)} \tag{2.49}$$

where n is the number of phonons in that normal mode. From this we can see that a non-zero energy ($\hbar\omega/2$) corresponds to the lowest energy state, $n = 0$, indicating that there is some degree of vibrational energy in the system even at 0 K, known as the zero-point energy.

The population $n^{(s)}(\boldsymbol{q}, T)$ of phonons at temperature T is defined based on a Bose-Einstein distribution given that phonons are bosons:

$$n^{(s)}(\boldsymbol{q}, T) = \frac{1}{\exp\left(\frac{\hbar\omega^{(s)}(\boldsymbol{q})}{k_{\mathrm{B}}T}\right) - 1} \tag{2.50}$$

The Helmholtz free energy can be defined based on the canonical partition function, Z, as:

$$F = -k_{\mathrm{B}}T\ \ln Z \tag{2.51}$$

where the harmonic partition function, Z_{har}, for a crystal configuration is calculated as the sum over all energy levels $\epsilon^{(s)}$ of the given system:

$$Z_{\mathrm{har}} = \sum \exp\left(-\frac{\epsilon}{k_{\mathrm{B}}T}\right) \tag{2.52}$$

The phonon Helmholtz free energy within the harmonic approximation for a quantum mechanical solid is then given by the expression [124]:

$$F_{\mathrm{vib}} = \sum_{\boldsymbol{q}j}\left[\frac{\hbar\omega_{\boldsymbol{q}j}}{2} + k_{\mathrm{B}}T\ \ln\left[1 - \exp\left(-\frac{\hbar\omega_{\boldsymbol{q}j}}{k_{\mathrm{B}}T}\right)\right]\right] \tag{2.53}$$

Other thermodynamic values such as entropy S and internal energy U can then be obtained by taking the derivative of the free energy F with respect to the temperature T.

The harmonic phonon entropy is given by [124]:

$$S_{\text{vib}} = \sum_{\boldsymbol{q}j} \left[\frac{\hbar\omega_{\boldsymbol{q}j}}{T\left(\exp\left(\frac{\hbar\omega_{\boldsymbol{q}j}}{k_{\text{B}}T}\right) - 1\right)} - k_{\text{B}} \ln\left(1 - \exp\left(-\frac{\hbar\omega_{\boldsymbol{q}j}}{k_{\text{B}}T}\right)\right)\right] \tag{2.54}$$

Given that the internal energy is:

$$U = F + TS \tag{2.55}$$

then the internal energy is given by [124]:

$$U_{\text{vib}} = F_{\text{vib}} + TS_{\text{vib}} = \sum_{\boldsymbol{q}j} \hbar\omega_{\boldsymbol{q}j} \left(\frac{1}{\exp\left(\frac{\hbar\omega_{\boldsymbol{q}j}}{k_{\text{B}}T}\right) - 1} + \frac{1}{2} \right) \tag{2.56}$$

2.3.4 Quasiharmonic lattice dynamics

There are a number of thermal properties such as thermal expansion, heat capacity, thermal conductivity that are not explained by harmonic approximation, since the effect of unit cell volume changes cannot be described. In quasiharmonic approximation, harmonic approximation is applied for different volumes but the force constants are allowed to change in accordance to the unit cell volume. In that way phonon frequencies are expressed as a function of the volume, also allowing for the calculation of the Grüneisen parameters. A commonly noticed trend is a decrease in phonon frequency as the lattice expands.

Considering the volume dependence of the frequencies, the equations for vibrational free energy 2.53 and entropy 2.54 are written as follows:

$$F_{\text{vib}}(T, V) = \sum_{\boldsymbol{q}j} \left[\frac{\hbar\omega_{\boldsymbol{q}j}(V)}{2} + k_{\text{B}}T \ln\left[1 - \exp\left(-\frac{\hbar\omega_{\boldsymbol{q}j}(V)}{k_{\text{B}}T}\right)\right]\right] \tag{2.57}$$

and

$$S_{\text{vib}}(T, V) = \sum_{\boldsymbol{q}j} \left[\frac{\hbar\omega_{\boldsymbol{q}j}(V)}{T\left(\exp\left(\frac{\hbar\omega_{\boldsymbol{q}j}(V)}{k_{\text{B}}T}\right) - 1\right)} - k_{\text{B}} \ln\left(1 - \exp\left(-\frac{\hbar\omega_{\boldsymbol{q}j}(V)}{k_{\text{B}}T}\right)\right)\right] \tag{2.58}$$

Quasiharmonic approximation is an accurate enough approximation for temperatures generally below about half the melting point.

2.3.5 Raman spectroscopy

Raman spectroscopy relies upon inelastic scattering of light by the material by inducing different types of transitions, such as vibrational, electronic, rotational or a combination of these, to the molecules or atoms of the scattering material. This results in emitted photons from the scattering material having either lower (Stokes lines) or higher (anti-Stokes lines) frequency than that of the incident photon. The most common transition noticed in solids is the vibrational one, where each peak of the Raman spectra corresponds to a different vibrational mode of the crystal. Raman spectroscopy is widely used as a method to identify the scattering material based on its spectra, as the number and position of the peaks are determined uniquely from the Raman-active normal modes allowed by the symmetry of the crystal. The selection rules for these are based on the symmetry of the change of the polarisability in the material induced by the normal mode amplitude.

At an elementary level, the Raman phenomenon can be explained classically based on electromagnetic wave theory by considering a time-dependent electric field $\boldsymbol{E}$ inducing a dipole moment $\boldsymbol{P}$ between atoms of the material whose magnitude is proportional to the incident electric field:

$$\boldsymbol{P} = a\boldsymbol{E} \tag{2.59}$$

with a being the polarisability tensor of the matter, showing the ease with which the electron density between the atoms is distorted due to the presence of the imposed electromagnetic field.

The polarisation, $\boldsymbol{P}$, fluctuates with time with the frequency ω_i of the electromagnetic field inducing it $\boldsymbol{E} = \boldsymbol{E}_0 \sin(\omega_i)$:

$$\boldsymbol{P} = a\boldsymbol{E}_0 \sin(\omega_i) \tag{2.60}$$

emitting electromagnetic radiation at the same frequency ω_i (Rayleigh).

This time dependence of the material's polarisation can be affected by lattice vibrations. Considering a vibrational mode k and its normal coordinate Q_k, vibrating with frequency ω_{01}, $Q_k = Q_{01}\sin(\omega_{01}t)$, then for small nuclear displacements the polarisability is a linear function of nuclear displacements around the atomic equilibrium positions and can be expressed as:

$$a = a_0 + \left.\frac{\partial a}{\partial Q_k}\right|_{Q_k=0} Q_k = a_0 + \frac{\partial a}{\partial Q_k} Q_{01}\sin(\omega_{01}t) \tag{2.61}$$

where a_0 is the polarisability when the atoms are at equilibrium positions. By combining Equations 2.60 and 2.61 the time dependency of the material's polarisation is expressed:

$$\boldsymbol{P} = a_0\boldsymbol{E}_0\sin(\omega t) + \frac{\partial a}{\partial Q_k} Q_{01}\boldsymbol{E}_0\sin(\omega_i t)\sin(\omega_{01}t) \tag{2.62}$$

or equivalently

$$\boldsymbol{P} = a_0\boldsymbol{E}_0\sin(\omega_i t) + \frac{1}{2}\frac{\partial a}{\partial Q_k} Q_{01}\boldsymbol{E}_0\left[\cos(\omega_i - \omega_{01})t - \cos(\omega_i + \omega_{01})t\right] \tag{2.63}$$

Equation 2.63 shows that a non-vanishing differential polarisability $\frac{\partial a}{\partial Q_k}Q_{01}$ is the main condition under which Raman spectra can be observed, and the emitted frequencies are $\omega_i - \omega_{01}$ or $\omega_i + \omega_{01}$.

To determine whether this derivative would be zero or not, group theory can be applied. Normal modes of lattice vibrations can be categorised using group theory based on whether they interact with the incident electromagnetic wave via changes in polarisability (Raman activity) or the dipole moment (infrared activity).

Significant information about the symmetry of a phase can be summarised in the table of character which plays a key role in the selection procedure. A particular point group can be described by a number of representations, since many different basis functions can be used, with each representation's symmetry species being able to be described by a linear combination of the symmetry species corresponding to the point group's irreducible representation. This symmetry species list can then be used to uniquely describe the symmetry of that point group. This information along with the different symmetry operations of the point group and their effect on each particular symmetry species are summarised in the character table.

The eigenvectors of each normal vibrational mode, which express the displacement of atoms in the normal mode coordinates, can serve as a basis function with the mode linked to an irreducible representation. To determine the irreducible representation of each normal mode, the symmetry operations of the point group are applied on each mode's eigenvectors, thus determining the characters based on whether the operations change the direction of atomic displacements for the mode. Given the characters assigned for the different symmetry operations for each mode, the corresponding irreducible representation for that particular point group can be determined based on the character table. A mode can then be characterised to be Raman-active, where the vibration results in a change in polarisability, if the irreducible representation has basis functions which are binary products of x, y and z e.g. x^2, xy, xz, etc. or their linear combinations. On the other hand, irreducible representations with basis functions x, y or z correspond to infrared active modes of vibration.

2.4 Free energy

2.4.1 Combined free energy

The Helmholtz free energy is considered in terms of the following free energy contributions:

$$F(T,V) = U_0(V) + F_{\text{qha}}(T,V) + F_{\text{el}}(T,V) \tag{2.64}$$

where U_0 is the DFT energy at $T = 0\,\text{K}$ without including the zero-point energy, and F_{qha} corresponds to the free energy due to atomic vibrations computed within the quasiharmonic approximation as defined in Eq. 2.57 which includes the zero-point energy $\sum_{\boldsymbol{q}j} \frac{1}{2}\hbar\omega_{\boldsymbol{q}j}(V)$. F_{el} is the electronic contribution to the free energy, calculated using a finite temperature DFT approach based on the Mermin functional [128]. According to this approach, at each finite temperature an exchange-correlation functional is used to determine the free energy due to electronic excitations. In this study we do not consider higher-order anharmonic vibrations nor the impact of lattice vibrations on the electronic free energy, which would be much more

expensive to compute, since we are not concerned with properties above about half the melting point where these contributions would start to become important [129].

In quasiharmonic approximation, as explained in section 2.3.4, the full phonon density of states is calculated at each configuration, considering a set of different unit cell volumes V for the crystal structure, where a volume scaling factor is used to scale the lattice vectors and atomic coordinates of the unit cell requiring a one-dimensional sampling of strains. However, for non-cubic unit cells such as hexagonal or tetragonal unit cells the c/a ratio is not fixed, but $a = b$ at all volumes, therefore in principle a mesh of two defined strains along the a and c directions is needed in such cases, with the strains defined as:

$$\epsilon_1 = \frac{a - a_0}{a_0} \text{ and } \epsilon_3 = \frac{c - c_0}{c_0} \tag{2.65}$$

where a_0 and c_0 are the equilibrium lattice constants at zero temperature and ϵ_2 is always held equal to ϵ_1. The free energy, Eq. 2.64, is then expressed in terms of temperature and the two strains as:

$$F(T, \epsilon_1, \epsilon_3) = U_0(\epsilon_1, \epsilon_3) + F_{\text{qha}}(T, \epsilon_1, \epsilon_3) + F_{\text{el}}(T, \epsilon_1, \epsilon_3) \tag{2.66}$$

Once the free energy expression has been calculated, the Gibbs free energy is then acquired by minimising $F + PV$ with respect to the volume or the strains (ϵ_1, ϵ_3):

$$G(T, P) = \min_V [F + PV] \tag{2.67}$$

2.4.2 c/a constraint

As already mentioned, crystals of hexagonal or tetragonal symmetry exhibit some degree of anisotropic thermal expansion which changes the c/a ratio of the unit cell. However, it can be assumed, as it has been in later chapters, that by keeping the c/a ratio fixed the free energy as a function of temperature and volume is a sufficiently good approximation. This approximation is considerably more computationally efficient since sampling of strains along only one dimension is required instead of a 2D mesh of strains. This is particularly useful in cases where a large

number of phases are being considered such as in Chapter 4. The errors introduced due to this approximation to the free energy and volume for hexagonal or tetragonal unit cells have been derived by Mike Finnis and are described below.

The free energy is expressed with respect to the strains ϵ_1 and ϵ_3, considering the hexagonal symmetry of MAX phases, within the approximation of linear elasticity:

$$F = -2\alpha_1\epsilon_1 - \alpha_3\epsilon_3 + (C_{11} + C_{12})\epsilon_1^2 + \frac{1}{2}C_{33}\epsilon_3^2 + C_{13}\epsilon_1\epsilon_3 \tag{2.68}$$

the coefficients α_1 and α_3 describe the thermal expansion and C_{ij} correspond to the elastic constants, both sets of coefficients are functions of temperature.

The thermal expansions are described by minimising F with respect to the strains, and the equilibrium strains are:

$$\begin{aligned} \epsilon_1 &= \frac{\alpha_1 C_{33} - \alpha_3 C_{13}}{2C_{13}^2 - C_{33}(C_{11} + C_{12})} \\ \epsilon_3 &= \frac{2\alpha_1 C_{13} - \alpha_3(C_{11} + C_{12})}{2C_{13}^2 - C_{33}(C_{11} + C_{12})} \end{aligned} \tag{2.69}$$

and the corresponding unconstrained equilibrium free energy is:

$$F_{\text{unconstrained}} = \frac{\alpha_3^2(C_{11} + C_{12} - 4\alpha_1\alpha_3 C_{13} + 2\alpha_1^2 C_{33})}{4C_{13}^2 - 2C_{33}(C_{11} + C_{12})} \tag{2.70}$$

Similarly, by minimising F but under the constraint that $\epsilon_3 = \epsilon_1$, the equilibrium strain ϵ is:

$$\epsilon = \epsilon_1 = \epsilon_3 = \frac{2\alpha_1 + \alpha_3}{4C_{13} + C_{33} + 2(C_{11} + C_{12})} \tag{2.71}$$

and the corresponding constrained F is:

$$F_{\text{constrained}} = \frac{(2\alpha_1 + \alpha_3)^2}{2(4C_{13} + C_{33} + 2(C_{11} + C_{12}))} \tag{2.72}$$

In order to express both the constrained and unconstrained free energies in terms of strains, we substitute the α_1 and α_3 coefficients with the expressions that result by inverting Equations 2.69.

Therefore, the free energy error expression is defined:

$$F_{\text{error}} = F_{\text{unconstrained}} - F_{\text{constrained}} = -\frac{(-2C_{13}^2 + (C_{11} + C_{12})C_{33})(\epsilon_1 - \epsilon_3)^2}{2C_{11} + 2C_{12} + 4C_{13} + C_{33}} \tag{2.73}$$

Similarly, if we consider that the volume strain under the c/a constraint is 3ϵ ($\epsilon_1 = \epsilon_3$, Eq. 2.71) and without the constraint imposed is $2\epsilon_1 + \epsilon_3$ (Eq. 2.69), then the resulting error in the volume strain is:

$$V_{\text{error}} = \frac{2(C_{11} + C_{12} - C_{13} - C_{33})(\epsilon_1 - \epsilon_3)}{2C_{11} + 2C_{12} + 4C_{13} + C_{33}} \tag{2.74}$$

The error in the free energy shows a quadratic dependence on the strains $(\epsilon_1 - \epsilon_3)$ whereas it is linear for the volume, indicating that it is a good approximation. This is later verified by inserting calculated and experimental numbers for the quantities involved, in Chapter 3.

2.4.3 Thermophysical properties

Having calculated the Helmholtz free energy as a function of temperature and volume $F(T, V)$ and the Gibbs free energy $G(T, P)$ as defined in equations 2.64 and 2.67, many thermophysical properties can be derived such as the thermal expansion coefficient (α_V), the isobaric and isochoric heat capacities (C_P and C_V), the isothermal bulk modulus (B_T) and the mode Grüneisen parameter ($\gamma(\boldsymbol{q}i)$). The macroscopic Grüneisen parameter (γ_{th}) can then be defined based on the previous properties, α_V, B_T and C_V [124].

The thermal expansion coefficient expresses how the crystal volume varies with temperature at constant pressure, and is defines as:

$$\alpha_V = \frac{1}{V}\left(\frac{\partial V}{\partial T}\right)_P \tag{2.75}$$

The isothermal compressibility K_T expresses how the crystal volume changes with pressure and is defined as:

$$K_T = -\frac{1}{V}\left(\frac{\partial V}{\partial P}\right)_T \tag{2.76}$$

The isothermal bulk modulus is expressed as the inverse of the isothermal compressibility K_T:

$$B_T = \frac{1}{K_T} \tag{2.77}$$

The heat capacity expresses how the temperature of the crystal changes in response to a supplied amount of heat. The isochoric heat capacity is expressed by:

$$C_V = -T \left(\frac{\partial^2 F}{\partial T^2} \right)_V \tag{2.78}$$

and the isobaric heat capacity is expressed by:

$$C_P = -T \left(\frac{\partial^2 G}{\partial T^2} \right)_P \tag{2.79}$$

The mode Grüneisen parameter, $\gamma(\boldsymbol{q}i)$, at the wave vector $\boldsymbol{q}$ and band index i is expressed by:

$$\gamma(\boldsymbol{q}i) = -\frac{V}{\omega(\boldsymbol{q}i)} \frac{\partial \omega(\boldsymbol{q}i)}{\partial V} \tag{2.80}$$

which shows the dependence of each frequency mode $\omega(\boldsymbol{q}i)$ upon the unit cell volume. These can be calculated within the quasiharmonic approximation. The thermal or macroscopic formulation of the Grüneisen parameter is given by:

$$\gamma_{\text{th}} = \frac{\beta V B_T}{C_V} \tag{2.81}$$

2.4.3.1 Calculation of elastic constants

Elastic constants are a measure of material's stiffness and are expressed as the constant matrix that connects the stress, σ, and strain, ϵ, tensors describing the crystal's behaviour under deformation within the linear elastic regime. This relationship using Voigt notation is expressed as:

$$\sigma_i = C_{ij} \cdot \epsilon_j \tag{2.82}$$

The elastic constants can be calculated from the stress-strain relationship and also equivalently, as done in this study, as a second derivative of the free energy with respect to the strains. As explained previously in Section 2.4.2, after applying a second order Taylor expansion to the free energy with respect to the strains and exploiting the hexagonal or tetragonal symmetry of the crystal, the free energy can be expressed as a function of the two strains ϵ_1 and ϵ_3 and the elastic constants C_{ij} (Eq. 2.68). The three C_{11}+C_{12}, C_{13} and C_{33} elastic constants used in the free energy expression Eq. 2.68 correspond to crystal deformations along the a and c axes without allowing any shear, preserving the crystal's symmetry. Thus these three are available as a bonus from the data obtained on the 2D mesh used for calculating free energy and volume expansion. There are three more independent elastic constants in hexagonal crystals that we have not investigated, which could only be obtained from further calculations involving shears of the unit cell.

The elastic constants are computed by fitting a polynomial expression to the free energies calculated for each deformation of the crystal defined in a 2D strain mesh ϵ_1 and ϵ_3. The same process but calculating the free energy $F(T, \epsilon_1, \epsilon_3)$ at different temperatures is used to determine the temperature dependence of the elastic constants.

2.4.3.2 Free energy of formation and convex hull

The datasets provided in experimental studies from the literature commonly refer to the standard enthalpies of formation (or heats of formation) for different compounds. DFT studies from the literature usually calculate formation energies based on the DFT energy at 0 K without accounting for any vibrations, this approach is a first approximation to either the enthalpy or the free energy. In this study, the total Gibbs formation energy is calculated based on the first DFT term corrected by the free energy contributions of the vibrations which also include the entropic contribution.

In order to examine the relative stability of a phase against other phases existing in a system its formation energy can be compared against any linear combination of alternative phases via the construction of a convex hull. In the context of this work it will be useful to define three distinct

meanings of convex hull. Convex hull is a term appropriated from geometry, which is widely used in computational materials science to mean the convex hull of formation energies generated in the space of compositions by the calculated minimum energies of crystal structures that are available at each composition. If a well-defined crystal structure lies on this convex hull, for example in the two dimensional space of ternary compositions, it would be deemed to be stable with respect to decomposition into neighbouring crystal structures on the hull. If above the convex hull, it would be unstable to such a decomposition. As mentioned previously it is usual in most DFT studies and in particular in the high-throughput calculations [45, 44], that the energies are calculated for systems at zero absolute temperature, which neglects, besides the effect of temperature itself, the contribution of the zero-point energy of vibration. It is worth recalling that in quantum mechanics every vibrational mode has a certain energy even at zero Kelvin, as described in Eq. 2.49, known as the zero-point energy. We designate such a convex hull, that neglects zero-point energy, by the abbreviation CH0. For the stability of crystals at finite temperature, the relevant energies would be the Gibbs energies, so we distinguish their associated convex hull by the abbreviation CH(T), where T denotes the temperature in degrees Kelvin. Any difference between CH(0) and CH0 is the effect of including the zero-point energy.

The Gibbs energy of formation for each phase is defined as the difference in total Gibbs energy of the compound and the Gibbs energies of its constituent elements in their stable states divided by the number of atoms in the molecular unit. For the ternary Zr-Al-C and Ti-Al-C systems we examine in Chapter 4, the Gibbs energy of formation is then expressed as:

$$\Delta G_{\mathrm{f}}(\mathrm{M}_x\mathrm{Al}_y\mathrm{C}_z) = \frac{1}{x+y+z}(G(\mathrm{M}_x\mathrm{Al}_y\mathrm{C}_z) - xG(\mathrm{M}) - yG(\mathrm{Al}) - zG(\mathrm{C})) \tag{2.83}$$

where M is either Zr or Ti. For this purpose we assume their standard crystal structures for the metals, while for simplicity we assume pure C in the diamond structure. The precise element reference energies are of no practical importance for our conclusions about the stability of ternary MAX phases. The ternary convex hulls we calculate include only fully ordered structures, including the Zr-C and Ti-C systems, and no configurational entropy is associated with the arrangement of structural vacancies in the γ-phase, which we took from low-temperature

calculations of total energy [130, 131].

Chapter 3

Structural and Thermophysical properties of $Zr_{n+1}AlC_n$ and $Ti_{n+1}AlC_n$.

In this chapter the thermophysical and structural properties of the $Zr_{n+1}AlC_n$ and $Ti_{n+1}AlC_n$ MAX phases with a focus on Zr_2AlC were calculated within the DFT framework with the lattice vibrations being treated within the quasiharmonic approximation. For Zr_2AlC the free energy was expressed in terms of strains, $\epsilon_1 = \epsilon_2$ and ϵ_3, and temperature, thus allowing for the calculation of the three independent elastic constants that do not relate to any loss of symmetry. In addition to the lattice vibrations, the electronic excitations were considered and their contribution to the free energy and thermophysical properties was evaluated. The choice of exchange correlation (XC) functional was also discussed, as was the effect of assuming that the coefficient of expansion is isotropic. Apart from considering the choice of computational parameters, such as the XC functional and the error introduced by the different levels of approximation for Zr_2AlC, less computationally-demanding free energy calculations were conducted under the c/a constraint for a larger number of MAX phases in the Zr-Al-C and Ti-Al-C systems. Based on these free energy calculations, thermophysical properties were predicted for these MAX phases and trends between them were discussed.

3.1 Computational details

The following calculations are based on Density Functional Theory (DFT) implemented in the Vienna Ab initio Simulation Package (VASP) [118, 119]. The electron-ion interactions have been treated using a projector augmented wave (PAW) [132] pseudopotential method. The exchange-correlation energy has been calculated using the PBEsol functional (Perdew-Burke-Ernzerhof revised for solids) [111]. The electrons treated as valence were the $4s$ $4p$ $5s^2$ $4d^2$ for Zr, the $3s$ $3p$ $4s^2$ $3d^2$ for Ti, the $2s$ $2p$ $3s^2$ $3p^1$ for Al, and the $2s$ $2p$ for C.

The cut-off kinetic energy used was 760 eV and the k-point meshes were $13 \times 13 \times 3$, $19 \times 19 \times 3$ and $23 \times 23 \times 3$ for the 211, 312 and 413 MAX phases respectively, for which values the total energy was found to be sufficiently converged to better than 1 meV/atom. For certain Zr_2AlC calculations, the strain dependent free energy and resulting thermophysical properties, such as the elastic constants, were calculated using an increased cut-off energy of 820 eV and $23 \times 23 \times 5$ k-points that were found to converge the elastic constants to 1 GPa. This more accurate set of computational parameters was used due to the high sensitivity of this phase's elastic constants calculations.

Accurate structural relaxation was conducted for each phase at a state of zero stress, setting the threshold for the total energy at 10^{-9} eV and for the forces during the ionic relaxation at 10^{-5} eVÅ^{-1}. Phonon spectra were calculated using the small displacement supercell method implemented in PHONOPY [125] by applying finite displacements of 0.01 Å. The supercell for each phase was sufficiently large to converge the phonon free energy to 1 meV/atom. The convergence criterion for the density of Brillouin zone mesh points for sampling the phonons was 1 meV/atom or less, with a q-point sampling of $73 \times 73 \times 12$ for 312 MAX phases, $25 \times 25 \times 5$ for Zr_2AlC and $171 \times 171 \times 38$ for Ti_2AlC. The electronic free energy at finite temperatures was calculated using the Mermin method [128].

In order to obtain the free energy as a function of ($\epsilon_1 = \epsilon_2$, ϵ_3) and temperature T, the internal energy, $U_0(\epsilon_1, \epsilon_3)$, was calculated on a mesh consisting of 49 different strained structures in the $\{\pm\epsilon_1, \pm\epsilon_3\}$ strain domain. The displacements for the mesh started from the center of the

strain domain and ended at a maximum of 0.0075 with a step of 0.0025. The lattice vibrational part of the free energy, $F_{\text{vib}}(\epsilon_1, \epsilon_3, T)$, was calculated at two-degree temperature intervals from 0 to 2000 K for supercells defined by a set of 17 strains on a square mesh of (ϵ_1, ϵ_3) with a maximum strain magnitude of 0.02. The electronic free energy $F_{\text{el}}(\epsilon_1, \epsilon_3, T)$ was calculated for 14 temperatures between 116–2000 K on a similar mesh of 17 strains with a maximum magnitude of 0.01. When the c/a ratio was kept fixed, the free energy was expressed in terms of volume and temperature by fitting the harmonic free energy calculated at temperature intervals of 2 K from 0 to 2000 K, and the internal energy with a 3$^{\text{rd}}$ order polynomial to five volumes. The volume scaling factors used to scale the lattice vectors and atomic coordinates were 0.98, 0.99, 1.0, 1.01, 1.025 for the Zr-based phases, while for the Ti-based phases we used six volumes, scaling as 0.98, 0.99, 1.0, 1.005, 1.015, 1.025.

3.2 Results

3.2.1 Free energy and lattice parameters of Zr_2AlC

The free energy is analysed in terms of its partial contributions:

$$F = U_0(\epsilon_1, \epsilon_3) + F_{\text{qha}}(\epsilon_1, \epsilon_3, T) + F_{\text{el}}(\epsilon_1, \epsilon_3, T) \tag{3.1}$$

where $U_0(\epsilon_1, \epsilon_3)$ is the zero-temperature energy, $F_{\text{qha}}(\epsilon_1, \epsilon_3, T)$ is the vibrational free energy and $F_{\text{el}}(\epsilon_1, \epsilon_3, T)$ is the electronic free energy.

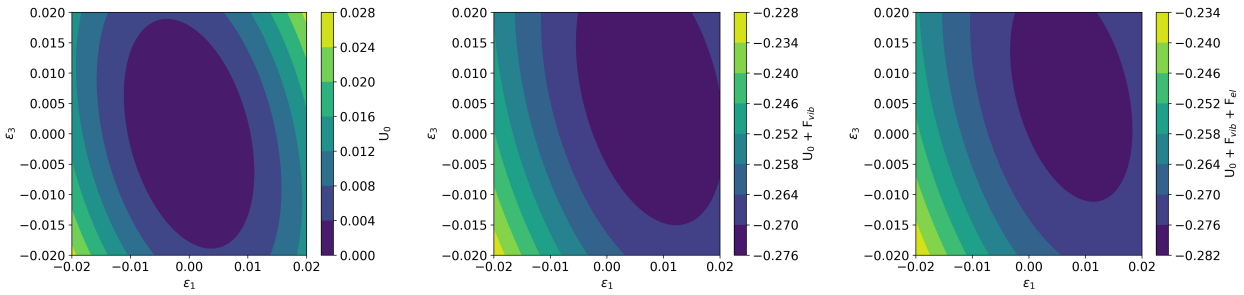

(a) U_0 (b) $U_0 + F_{\text{qha}}$ (c) $U_0 + F_{\text{qha}} + F_{\text{el}}$

Figure 3.1: The energy contours against the strain mesh for the different free energy contributions at 1000 K.

The free energy including the vibrational and electronic contributions is shown in the fitted contours displayed in Figure 3.1 against the two strains (ϵ_1, ϵ_3). Starting from Fig. 3.1a, only the internal energy $U_0(\epsilon_1, \epsilon_3)$, then $U_0(\epsilon_1, \epsilon_3) + F_{\text{qha}}(\epsilon_1, \epsilon_3)$, and finally the free energy $U_0(\epsilon_1, \epsilon_3)$ + $F_{\text{qha}}(\epsilon_1, \epsilon_3)$ + $F_{\text{el}}(\epsilon_1, \epsilon_3)$ at $T = 1000\,\text{K}$ are shown. The shift of the lowest energy point from zero in the case of $U_0(\epsilon_1, \epsilon_3)$ corresponds to the effect of each of the two contributions.

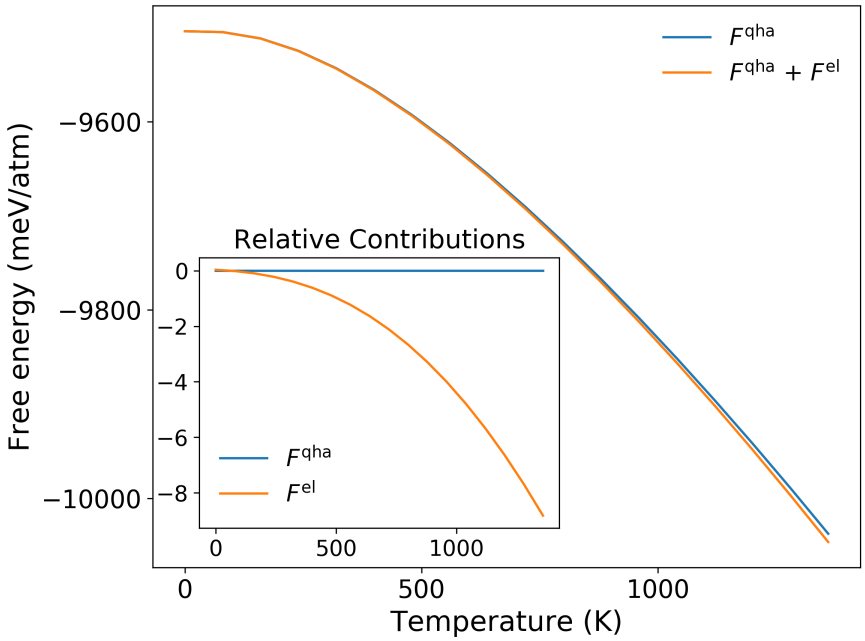

Figure 3.2: The free energy, $U_0 + F_{\text{qha}}$ and $U_0 + F_{\text{qha}} + F_{\text{el}}$, at zero strains as a function of temperature.

The contribution made by electronic excitations is very small as seen in Fig. 3.2. It amounts to 8 meV/atom, contributing less than 1% to the total energy at 1400 K.

Table 3.1 contains the lattice parameters for the Zr_2AlC phase, whose structure is shown in Fig. 3.3, calculated for three different XC functionals, which are compared with other experimental and theoretical studies. The LDA [109] and GGA (Perdew-Wang) [133] functionals are generally believed to bracket the exact value [134] and our choice of PBEsol is a recommended GGA-type functional for solids with improved treatment of the exchange energy [111, 134], which we expect to return values within the range between standard LDA and GGA. For PBEsol the effect of zero point energy on the lattice constants shows an increase by 0.17% and 0.14% for a and c respectively. The effect of the thermal expansion at 300 K increases a and c by 0.3% and 0.2% respectively. For PBEsol at room temperature the lattice constants

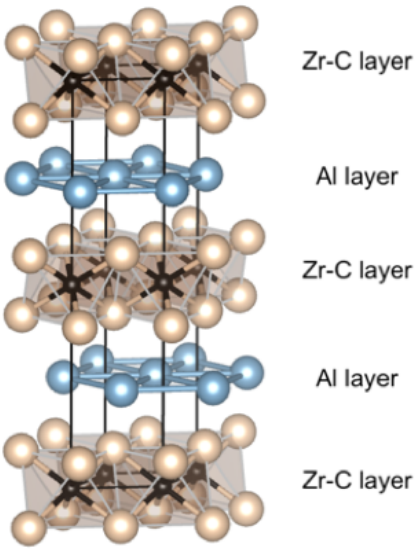

Figure 3.3: The primitive unit cell for the Zr_2AlC phase, consisting of alternating Zr-C and Al layers.

only differ by 0.7% and 0.3% from the experimental values. This is probably within the error bars of any DFT calculation. Equally, such a difference could be explained by the possibility of impurities in the Zr_2AlC phase, elements like Hf and Nb, and in particular Hf due to their very similar chemical behaviour and ionic radii, and electron configurations ($4d^2\ 5s^2$ for Zr and $5d^2\ 6s^2$ for Hf) resulting in complete solubility between each other. Usually even in high purity Zr powder there is some amount of Hf present and specifically, Hf can be present in the final sample in percentages less that 1%, as has been reported in the initial reacting powders used for MAX phases synthesis e.g ZrH_2 contains about 1–2% of Hf in it [135]. Based on the study by Lapauw *et al.* [3] it is reported that 0.1% of Nb changes the a and c lattices by 0.8% and 0.4% respectively. Thus, even less than 1% of Nb could cause differences in the lattice parameters similar to the differences that are shown between the calculations at room temperature and the experimental results. In another study by Lapauw *et al.* [4] the sample of Zr_2AlC phase was reported with the presence of secondary phases such as ZrC and thus the measured lattice constants of the Zr_2AlC phase could have been affected by the resultant internal stresses.

Our calculations show close agreement with other theoretical studies, in particular our GGA (Perdew-Wang) calculations have less than 0.4% difference for the a and c lattice constants with other GGA calculations [19, 77, 18, 84, 136]. Of these studies, closest agreement for both

Zr_2AlC	a (Å)	c (Å)	Z_M
This study			
LDA	3.272	14.407	0.087
GGA	3.322	14.584	0.087
PBEsol	3.290	14.506	0.086
PBEsol (zero point energy)	3.296	14.526	-
PBEsol (T= 300K)	3.300	14.538	-
Experimental studies			
XRD [4]	3.3237	14.5705	0.087
SAED [4]	3.3	14.6	-
NPD [4]	3.3239	14.556	0.0898
Computational studies			
GGA (PBE) [18]	3.3174	14.6304	0.0861
LDA [78]	3.2104	14.2460	-
GGA [136]	3.334	14.600	-
GGA (PBE) [77]	3.319	14.604	0.0864
GGA (PBE) [19]	3.319	14.606	0.0864
GGA (PBE) [84]	3.3186	14.6062	0.0864

Table 3.1: Lattice constants a and c and the z-coordinate of the Zr atoms, Z_M.

lattice constants was noted with [19, 77, 84] where differences with our calculations were less than 0.09% for a and 0.15% for c. These three studies applied the plane wave pseudopotential approach using the GGA (PBE) XC functional and used the same type of ion-electron interaction method, the Vanderbilt-type ultrasoft pseudopotential. The cut-off kinetic energy used was 500 eV and 550 eV for [19, 77] and [84] respectively. This high similarity of the chosen computational details in these studies could explain the negligible differences with each other in their predicted lattice constants. The study by Luo *et al.* [18], which also used the PBE XC functional, like the aforementioned three studies, but a slightly lower cut-off energy at 400 eV, shows a slightly larger difference with our GGA calculations at 0.14% for a and

0.32% for c. Closest agreement for c specifically is shown between our GGA calculations and those by Shang *et al.* [136], who used GGA-based projector augmented wave potentials and a cut-off kinetic energy at 500 eV, with the difference being 0.11% for c, though a higher difference of 0.36% is noted for a. Despite the differences between our GGA calculations and these other GGA studies being small overall, these small differences could also possibly be affected by other choices in computational parameters apart from the use of lower cut-off kinetic energies and different pseudopotentials than our calculations, which used a cut-off of 760 eV and projector augmented-wave (PAW) potentials. Specifically for the three aforementioned studies with closest agreement for both lattice constants, [19, 77, 84], the maximum force threshold for structural relaxation was set to 0.01 eV/Å compared to the 10^{-5} eV/Å in our calculations. The k-points sampling was also quite different between our calculations, which used $23 \times 23 \times 5$, and the sparser sampling by Ali *et al.* [77], Nasir *et al.* [19] and Hadi *et al.* [84] at $10 \times 10 \times 2$ and $12 \times 12 \times 3$ and $19 \times 19 \times 3$ respectively. Overall however, it is difficult to assign a cause to the small differences between the calculated results, since the contributing factors: choice of XC functional, k-point sampling, pseudopotential and cut-off are never the same in different publications.

3.2.2 Elastic moduli of Zr_2AlC

Out of the six elastic constants that correspond to the hexagonal symmetry of the MAX phases, the three that were calculated, C_{11}+C_{12}, C_{13} and C_{33}, correspond to deformations along the $a = b$ and c axis while preserving the hexagonal symmetry. Only these deformations are required for exploring the thermal expansion and heat capacity, which are our main focus in this chapter with regard to the thermophysical properties.

In Fig. 3.4 the three elastic constants are plotted as a function of temperature showing the effect of the electronic contribution. The electronic contribution to the elastic constants is negative for C_{11}+C_{12} and C_{33}, resulting in a 2% decrease at 1400 K, whereas for C_{13} the contribution is positive resulting in an increase of 2%. Overall, the elastic constants were found to decrease with temperature by around 59, 41 and 10 GPa for C_{11}+C_{12}, C_{33} and C_{13} respectively from 0

to 1400 K.

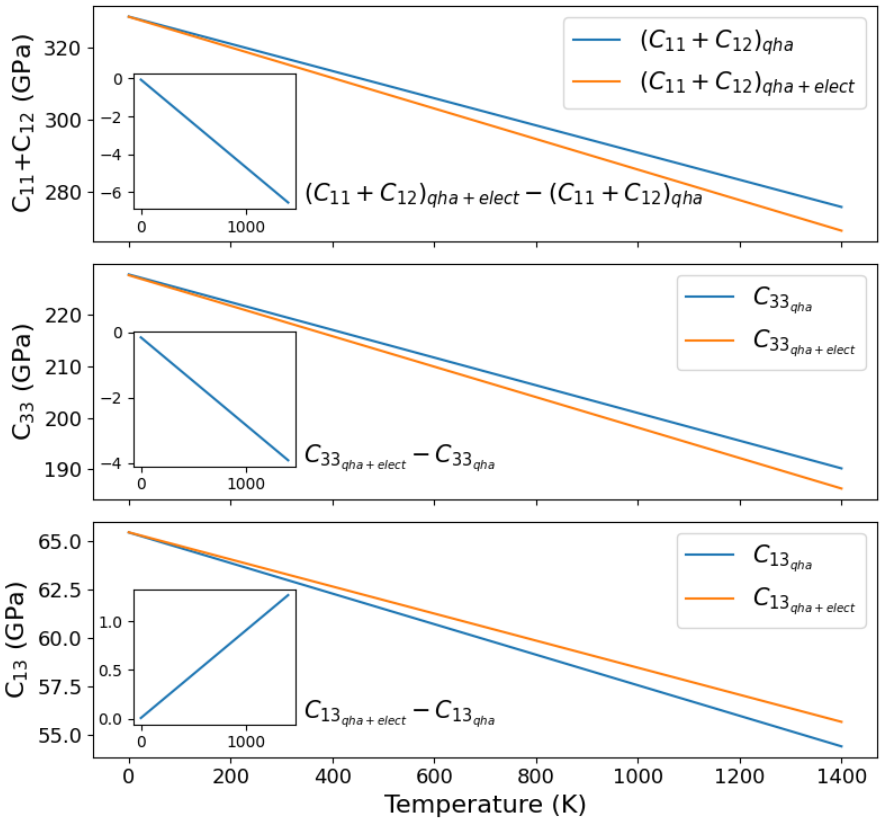

Figure 3.4: The C_{11}+C_{12}, C_{33} and C_{13} elastic constants against temperature.

The values of the elastic constants have been found to be very sensitive to a number of computational parameters including the density and amplitude of the strain mesh used to fit the polynomial to the free energy. Fine-tuning these parameters is important to ensure that the mesh size is small enough to capture the harmonic part. Apart from the method to calculate the elastic constants as applied in this study, other theoretical studies used the stress-strain relationship usually implemented through software packages e.g. VASP or CASTEP [137], where the amplitude of the strains along several strain directions is usually set to a default value which is sometimes inadequate.

In Table 3.2 the calculated elastic constants at different temperatures between 0 and 1400 K, including the electronic contributions to the free energy, are shown as well as the elastic constants from various studies calculated at 0 K. The studies [18, 80] calculated the pressure effect on the elastic constants, but we have not found any published theoretical study predicting temperature dependent elastic constants nor experimental measurements for Zr_2AlC. In the studies

[19, 77, 74, 67, 18, 79] the elastic constants were predicted slightly lower than our results, with a maximum difference of 2.0%, 3.7% and 2.9% for C_{11}+C_{12}, C_{13} and C_{33} respectively. Apart from the computational details related to the method of calculating the elastic constants as explained above, the elastic constants show sensitivity to the cut-off kinetic energy and, as discussed in the computational details, were shown to require a high value. For instance, from the aforementioned studies, the study by Luo *et al.* [18], which shows some of largest differences compared to our results, uses a GGA-PBE XC functional, a cut-off kinetic energy of 400 eV and k-points mesh of $9 \times 9 \times 2$ instead of PBEsol, 820 eV and $23 \times 23 \times 5$ used in this study. Also, the parameters for geometry optimisation were set to a convergence of energy of 10^{-5} eV/atom and a maximum force of 0.03 eV/Å, whereas in this study the values were 10^{-9} eV/atom and

Temp (K)	C_{11}+C_{12} (GPa)	C_{13} (GPa)	C_{33} (GPa)
0	328.43	65.44	227.71
150	326.46	64.76	225.89
500	313.19	62.05	216.19
1000	289.66	58.46	200.09
1200	279.59	57.07	193.25
1400	269.32	55.65	186.29
Literature			
GGA-PBE [18]	322	63	227
GGA-PBE [19]	325	64	224
LDA [80]	342	67	235
GGA-WC [76]	375	75	337
GGA [77, 74]	325	63	221
GGA [67]	324	63	224
GGA-PBE [75]	333	67	227
GGA-PBE [79]	325	64	227

Table 3.2: Elastic constants calculated for different temperatures in our study and compared with other 0 K predicted values from the literature.

10^{-6} eV/Å respectively. The studies [80, 76] predicted the elastic constants higher than ours. Our largest difference is with the study by Kanoun *et al.* [76], where the elastic constants, C_{11}+C_{12}, C_{13} and C_{33}, where predicted 14%, 15% and 48% higher than ours respectively. The overestimation in the elastic constants can be partially explained by their choice of XC functional, where LDA, as used by Kanoun *et al.* , produces larger values than GGA, as used in this study. In general the elastic constants are underestimated when using GGA and overestimated using LDA functionals, resulting in larger predicted bond length and lower stiffness in the GGA case.

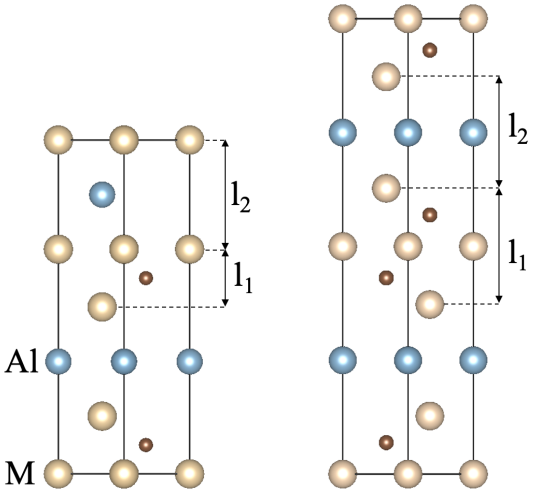

Figure 3.5: The [1 1 1] plane of the 211 and 312 structures. l_1 and l_2 denote the lengths of the carbide and Al layers in the MAX phases respectively, where M = Zr, Ti.

Because of the layered structure of the MAX phase, the strain ϵ_{33} will not be equally distributed between the atomic planes, and we might expect the strain to be lower within the carbide-like layers. To investigate this, we define ϵ_{MC} and ϵ_{MA} corresponding to the strains in the carbide and Al layers respectively, as illustrated in Fig. 3.5. Fig. 3.6 shows that the strains between the MAX phase layers are not uniformly distributed. Considering that the stress in the c direction, σ_{33}, is constant at every position between each pair of neighbouring planes, the crystal behaves as if it was composed of different local elastic constants along the c direction. These are soft regions corresponding to the Al layers and hard regions corresponding to the carbide layers, as shown for the Zr_2AlC phase in Fig. 3.6a where the linear change of ϵ_{MA} and ϵ_{MC} is shown as a function of ϵ_3, which varies from -0.025 to 0.025.

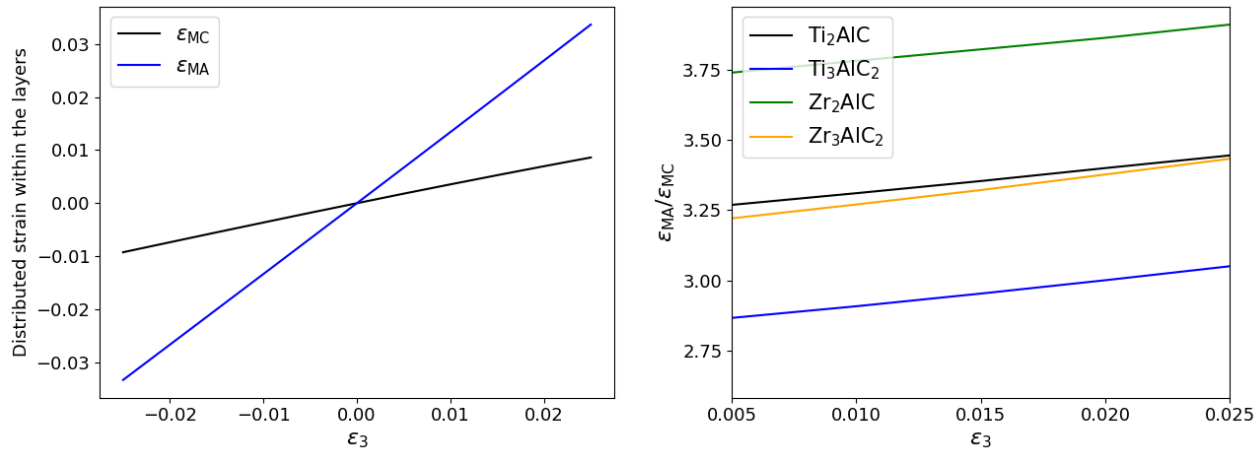

(a) (b)

Figure 3.6: Figure (a) shows how the applied ϵ_3 strain is distributed within the ZrC and Al layers of the Zr_2AlC phase. Figure (b) shows the $\epsilon_{MA}/\epsilon_{MC}$ as a function of ϵ_3 for the Zr and Ti MAX phases.

In Fig. 3.6b, the way $\epsilon_{MA}/\epsilon_{MC}$ varies with ϵ_3 for different MAX phases is shown. In this case we can see that as we go from 211 to 312 the ratio decreases, showing that the difference in the distributed strains between the layers is smaller in the case of 312. This correlates with the fact that the interlayer spacing in the carbide layer in 211 is smaller than the one in 312, indicating stronger binding within the carbide layers as is discussed in more detail in Chapter 5. For comparison reasons, the two closely related 211 and 312 Ti-based MAX phases are included in Fig. 3.6b. In general the Zr-based MAX phases were found to have a higher ratio than their corresponding Ti-based phases, with Zr_2AlC having the highest ratio overall.

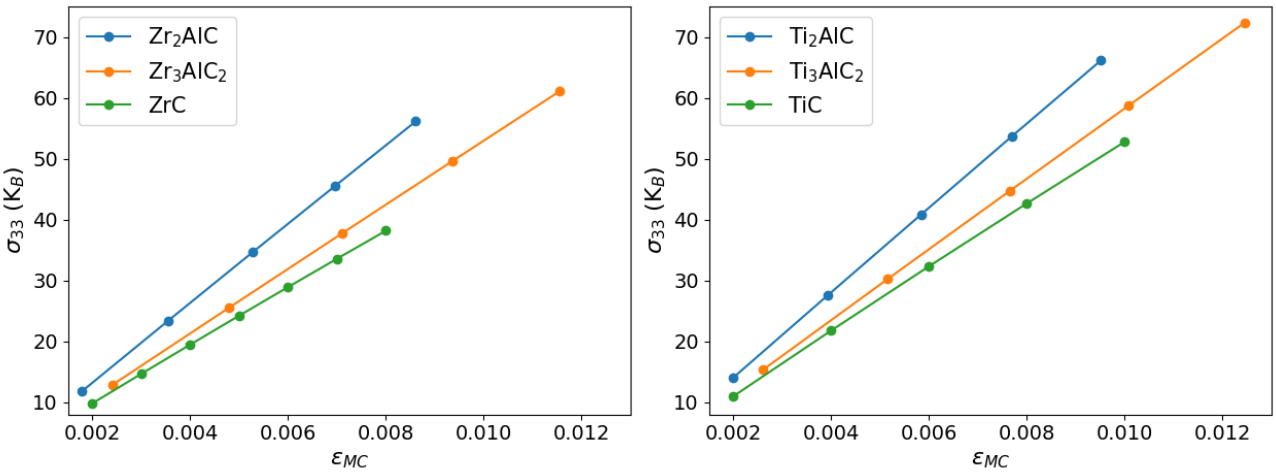

Figure 3.7: The two figures show the stress on the c axis (σ_{33}) as a function of the strain of the carbide layer, ϵ_{MC} for 211, 312 and pure carbide in the Zr and Ti systems.

The carbide layer in these MAX phases is a nanoscale slab of the metal carbide, which is bonded in a partially covalent, partially ionic way, and is a stiffer material than the nanolayer around the Al layer as is shown by their relative stiffness in Fig. 3.6. As the thickness of the carbide layer is increased then the elastic properties of the material would approach the elastic properties of a pure carbide. As shown in the metal carbide nanolayer stress-strain relation in Fig. 3.7, as the metal carbide proportion increases from the 211 to 312 MAX phase this stress-strain relation approaches that of the pure metal carbide for both Zr and Ti systems.

3.2.3 The c/a constraint

In general, crystals of hexagonal or tetragonal symmetry exhibit some degree of anisotropic thermal expansion, which changes the c/a ratio of a unit cell. It can be assumed, as it has been in many studies in the literature, that for crystals of hexagonal symmetry one can estimate the free energy as a function of temperature and volume sufficiently well by neglecting the change in c/a ratio. This approximation makes a large saving in computer time, since if c/a is held constant the scan of strains is only one dimensional, which is particularly useful when many compounds have to be scanned or when costly calculations such as the full phonon spectrum in the quasiharmonic approximation are required.

As was discussed previously for Zr_2AlC, free energy calculations were performed within the quasiharmonic approximation with respect to the two strains ϵ_1 and ϵ_3 taking into account the anisotropy that is introduced by the hexagonal symmetry of the MAX phases. Based on these calculations, thermal properties have been derived for Zr_2AlC, such as the thermal expansion coefficient and heat capacity. The resulting properties from both constrained and unconstrained free energy calculations were found to have negligible differences.

In Section 2.4.2 the expression of the error introduced to the free energy and volume was derived in terms of the equilibrium strains and elastic constants. Below, this error is evaluated using the derived equations, 2.73 and 2.74, for $Zr_{n+1}AlC_n$ and $Ti_{n+1}AlC_n$. For Zr_2AlC, using our calculated elastic constants and the equilibrium strains at 300 K resulted in errors of less than 2.5×10^{-4} meV/atom and 1.2×10^{-5} for the free energy and volume strain respectively.

Since calculations of strain dependent free energy and elastic constants were only conducted for Zr_2AlC, data from the literature, either experimental or theoretical, was applied to the error estimations for the other MAX phases considered. For the Ti_2AlC phase, the experimentally determined linear thermal expansion coefficients ($\epsilon_1 = 7.2 \times 10^{-6}$ and $\epsilon_3 = 9.3 \times 10^{-6}\,K^{-1}$) and predicted elastic constants ($C_{11} + C_{12} = 365$, $C_{13} = 59$ and $C_{33} = 272\,GPa$) were used from the study by Wang *et al.* [83], where high isotropy in thermal expansion was also noted. For Ti_3AlC_2, the predicted linear thermal expansion ($\epsilon_1 = 8.2 \times 10^{-6}$ and $\epsilon_3 = 11.6 \times 10^{-6}\,K^{-1}$) and elastic constants ($C_{11} + C_{12} = 440.08$, $C_{13} = 76.03$ and $C_{33} = 292.89\,GPa$) based on DFT calculations from the study by Son *et al.* [85] were used. For the Zr_3AlC_2 phase, the predicted isotropic volume thermal expansion coefficient ($1.34 \times 10^{-5}\,K^{-1}$ at $300\,K$) and the elastic constants ($C_{11} + C_{12} = 321.99$, $C_{13} = 63.07$ and $C_{33} = 226.77\,GPa$) based on DFT by applying the quasiharmonic Debye model were used from the study by Luo *et al.* [18]. In this case, by estimating the volume expansion to be isotropic, we consider ϵ_1 to be $1/3$ of the reported volume expansion coefficient. Since ϵ_1 has to be smaller than ϵ_3, we define an upper limit for the $(\epsilon_1 - \epsilon_3)$ term in the error expressions to be just ϵ_1. Based on the data described above, the error introduced by the c/a constraint on the free energy and volume strain for the Zr and Ti MAX phases is estimated to be negligible. Specifically, the error is estimated to be less than $10^{-7}\,meV/atom$ for the free energy and of the order of 10^{-7} for the volume strain.

In the following sections, where a larger number of phases are considered, the c/a constraint is therefore applied to the calculation of the thermophysical properties of the $Zr_{n+1}AlC_n$ and $Ti_{n+1}AlC_n$ MAX phases.

3.2.4 Thermal expansion of $Zr_{n+1}AlC_n$ and $Ti_{n+1}AlC_n$

This section focuses on the comparison of the volume thermal expansion coefficients between the different MAX phases in the two systems, Zr-Al-C and Ti-Al-C, under the approximation that their thermal expansion is isotropic. More detailed calculations though were conducted for Zr_2AlC, with anisotropy considered in the thermal expansion of a and c separately, and the electronic contribution to the free energy also being calculated. Comparison with the literature,

experimental and theoretical studies is given in Table 3.3.

The thermal expansion coefficient is a useful thermal property with a particular significance when interfaces in materials exist, as mismatches in the thermal expansion coefficient of the combined phases can result in mechanical failure during thermal cycling. In these cases the degree of anisotropy is also important, and although a lack of experimental studies is noted for Zr-based MAX phases, for the Ti-based MAX phases, Ti_2AlC and Ti_3AlC_2, a number of experimental studies are reported focusing on thermal expansion and anisotropy [93, 94, 95, 96, 97, 83, 98]. The two main experimental methods applied in those studies are dilatometry and high-temperature XRD measurements, which show a good agreement between themselves. The average linear thermal expansion, $\alpha_{\rm av} = (2\alpha_a + \alpha_c)/3$, given in these studies for their respective temperature ranges is presented in Table 3.3, after being converted to the volume thermal expansion coefficient, along with α_V from other theoretical studies. The different temperature ranges used in each study were all bounded between 300 and 1800 K. For Ti_2AlC, by comparing our results with the volume thermal expansion coefficient within the temperature ranges reported for each experimental study we find an agreement with a difference of 1–9% [83, 93, 98, 97]. The closest agreement between our predictions and experiment is noted with the study by Wang *et al.* [83] at about 1%, where the high-temperature XRD measurements were conducted within 300–800 K. For Ti_3AlC_2, a higher disagreement with the experimental studies compared to Ti_2AlC is noted, with differences being within the range of 14–25% [93, 94, 95, 96, 97]. Differences might occur due to the presence of other secondary phases as has been reported, to different levels, in all of the aforementioned studies. In most of these studies, even when high purity was achieved, the presence of secondary phases has been reported at around 4 vol%. In particular, in the study by Pang *et al.* [97] the final Ti_3AlC_2 sample was found to contain secondary phases, Ti_2AlC (2.7 wt.%) and TiC (0.2 wt.%), and an increase in Ti_2AlC and TiC_x contents was reported because of the decomposition of Ti_3AlC_2 as temperature increased from 1400 to 1550°C. In the study by Lane *et al.* [93] a multiphase sample consisting of a mixture of 38 wt.% $Ti_5Al_2C_3$, 32 wt.% Ti_2AlC, 18 wt.% Ti_3AlC_2, and 12 wt.% $(Ti_{0.5}Al_{0.5})Al$ was used. Although, as is reported in the study, by comparing the Ti_3AlC_2 phase's thermal expansion from the multiphase sample with this from a predominantly Ti_3AlC_2 sample, the difference is

comparable to their measurement uncertainty. Apart from the presence of other phases in the samples, the composition or the presence of impurities can also affect the thermal properties. Experimental research suggests that MAX phases have the tendency of forming vacancies in the C sublattice [138], which can also influence the thermal properties like thermal expansion and heat capacity [139]. In the study by Tzenov *et al.* [95], different $Ti_3Al_xC_y$ compositions were investigated within the window of $x = 0.8$–1.7 and $y = 1.8$–2.0, with the $Ti_3Al_{1.1}C_{1.8}$ composition being used for their thermal expansion measurements, as it was the only one found not to contain TiC_x, but only a 4 vol% of Al_2O_3. Apart from the above, anisotropy has been measured for the two Ti-based MAX phases in various studies [83, 93, 97, 96], where the α_c/α_a ratio was found to be between 1.13–1.34 for 312 and 0.8–1.3 for 211. Although ratios of up to around 1.3 are reported, we found the difference this anisotropy makes to the approximation of the constant ratio in the free energy and volume strain to be negligible, as examined for Ti_2AlC with thermal expansion values, α_c and α_a, from the study by Wang *et al.* [83] in Section 3.2.3.

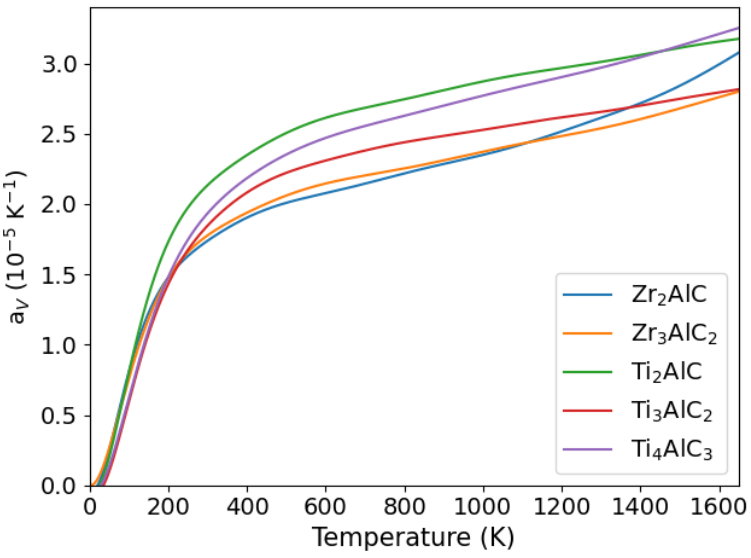

Figure 3.8: The thermal expansion coefficient for the $M_{n+1}AlC_n$, M = [Zr, Ti] MAX phases.

In Fig. 3.8 the thermal expansion coefficient is plotted as a function of temperature for the Zr and Ti MAX phases. In the temperature range 300–1000 K, the Zr-based MAX phases show lower thermal expansion coefficients compared to the Ti-based ones, with the Zr_2AlC phase showing the lowest. From the Ti-based phases the lowest thermal expansion is noted for Ti_3AlC_2 and the highest for Ti_2AlC. From around 400 K the Ti_4AlC_3 phase shows a high

rate of increase compared to the other MAX phases. However, after 1100 K, the greatest rate of increase is noted for Zr_2AlC compared to the rest of the MAX phases that show a rather more linear increase. This is probably due to the greater contribution of the Al layer in 211 compared to 312, recalling that the Al layers are softer than the ZrC layers.

Phase	α_V ($\times 10^{-5}$ K^{-1})			C_V (K_B)	C_P (K_B)		
	Calc.		Exp.	Calc.	Calc.		Exp.
	300 K	1000 K		300 K	300 K	1000 K	
Ti_4AlC_3	1.93	2.75			2.21	3.02	
Ti_3AlC_2	1.85	2.52	1.8[c] [93]	2.42	2.44	3.01	
	2.53 [90]	3.67[90]	2.298[d] [94]	2.21 [90]	2.24 [90]	3.12 [90]	
	2.19 [86]	2.99[86]	1.8[e] [95]	2.53 [7]	2.29 [86]	3.03 [86]	
	2.26 [85]	3.14[85]	2.76[f] [96]		2.30 [85]	3.17 [85]	
	2.31 [140]		2.76[g] [97]		2.59 [7]	3.03[j] [7]	
Ti_2AlC	2.13	2.9	2.37[h] [83]	2.34	2.36	3.04	2.60[a] [8]
	2.16 [83]	3.1[83]	2.76[c] [93]	2.35 [83]	2.39 [83]	3.05 [83]	2.37[b] [9]
	2.55[73]	3.2[73]	2.46[i] [98]	2.34[89]	2.4 [73]	3.06 [73]	
	1.40 [91]	1.6[91]	2.84[g] [97]		2.38 [89]	3.07 [89]	
	1.73 [89]	2.41 [89]	3.23 [89]				
Zr_3AlC_2	1.78	2.30		2.42	2.44	3.03	
				2.70 [7]	2.73 [7]	3.09[j] [7]	
Zr_2AlC	1.74	2.33		2.51	2.53	3.03	
	1.38 [18]	1.84 [18]			2.64 [19]	3.64 [19]	
	3.28 [19]	4.26 [19]					

Table 3.3: The volume thermal expansion (α_V) and heat capacity (C_P) for the $M_{n+1}AlC_n$, M = [Zr, Ti] MAX phases calculated in this study are compared to relevant experimental and theoretical values at 300 K and 1000 K. The theoretical calculation by Ouadha *et al.* [7], [j], is given at 600 K. The experimental C_P by Barsoum [a] [8] and Drulis [b] [9] are given at 400 K at 250 K respectively. The experimental measurements for α_V were conducted within the temperature ranges: [c]: 300–1273 K, [d]: 300 K, [e]: 300–1473 K, [f]: 300–1000 K, [g]: 300–1800 K, [h]: 300–800 K, [i]: 300–1600 K.

Apart from the experimental studies, a number of theoretical studies have been reported for Ti_2AlC [83, 73, 91, 89], Ti_3AlC_2 [90, 86, 85] and Zr_2AlC [18, 19]. Comparing these studies with experiment, as seen in Table 3.3, shows that the method used to approximate the lattice vibrations has an impact on the thermal expansion. As is also noted in the study by Wang *et al.* [83] for the MAX phases, quasiharmonic approximation resulted in better agreement with experimental studies compared to other approximations like the Debye–Grüneisen model, and the differences were more apparent for the thermal expansion coefficient than the heat capacities. This improvement with quasiharmonic approximation is due to its more accurate expression of the free energy by using the full phonon spectrum compared to the Debye approximation which does not take into account zero-point energy, nor the higher frequency optical phonons that can be associated with carbon atoms in the structure. This improvement can be seen for the Ti_2AlC phase since quasiharmonic approximation applied in our study and the study by Wang *et al.* [83] resulted in better agreement with the experimentally measured values by Wang *et al.* [83] compared to other studies using the quasiharmonic Debye model [91, 89].

This point is emphasised by comparing our thermal expansion coefficient with other theoretical studies, as shown in Table 3.3, the closest agreement is noted with studies also using the quasiharmonic approximation. In particular, in the study by Wang *et al.* [83] for Ti_2AlC at 300 K the thermal expansion coefficient was found to differ from our result by just 1.4%. However, in the study by Duong *et al.* [73], where the quasihamonic approximation was also used, the difference was found to be 20%. Part of this higher difference could be related to the contribution of electron excitations they included in the thermal expansion. Higher differences, within the range of 19–34%, were noted when the lattice vibrations were treated within the quasiharmonic Debye model [91, 89], with the difference increasing significantly at higher temperature for [91]. Similarly for the Ti_3AlC_2 phase, the closest agreement is noted with the study by Tongo *et al.* [86] where the thermal expansion coefficient was calculated using the quasiharmonic approximation, with a difference of 18%. A larger difference is noted with the study by Son *et al.* [85], where quasiharmonic approximation was used incorporating electron excitation and anharmonicity corrections to the free energy. The largest difference, at about 37% was noted with the study by Ali *et al.* [90] where the quasiharmonic Debye model was ap-

plied with the difference growing even larger as temperature increases. For the Ti_3AlC_2 phase it is also worth comparing our thermal expansion coefficient with one predicted by a recently developed bond-order potential [140]. Only a few interatomic potentials have been developed for MAX phases [140, 141] and these were mainly aimed at investigating specific MAX phase behaviour, such as plastic anisotropy and kinking nonlinear elasticity. In these studies, [141] uses a modified version of a previously developed bond order interatomic potential by [140] to better capture deformation behaviour. Although these interatomic potentials were not fitted based on thermal properties, in the earlier study [140] they reported a difference of 15% with experiment regarding their predicted thermal expansion coefficient, for which a difference of 25% was found when compared to our DFT calculations.

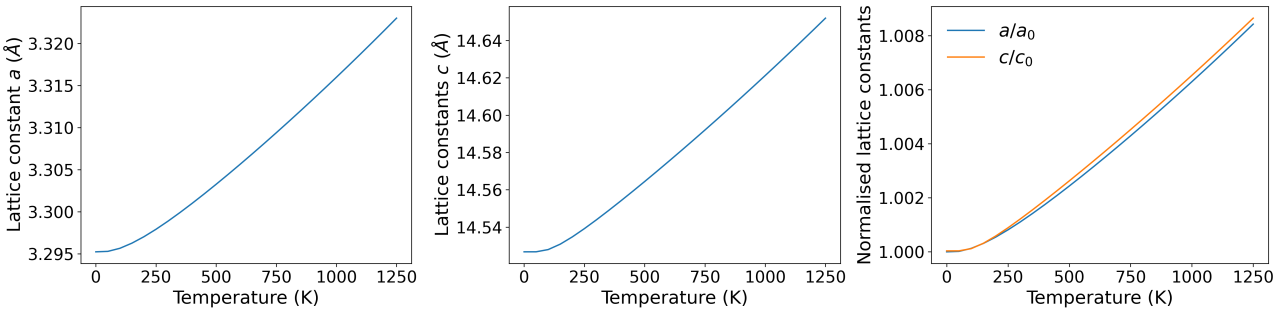

(a) (b) (c)

Figure 3.9: In (a) and (b) the calculated lattice constants a and c of Zr_2AlC are plotted as a function of temperature. In (c) the normalised lattice constants, a/a_0 and c/c_0 are shown as a function of temperature. In the three sub-figures the calculations included both the phonon and the electronic contributions.

Focusing on Zr_2AlC, in Fig. 3.9 the lattice constants, a and c, for this phase are shown as a function of temperature. The electronic contribution to the lattice constants was found to be negligible. At 1000 K an increase by around 0.01% with respect to the equilibrium values of the lattice constants is noted. The thermal expansion along the a and c axes is very similar, indicating an isotropic expansion. This is also described in sub-figure 3.9c where the two lattice parameters a and c are divided by their equilibrium values at 0 K and plotted as a function of temperature.

Harmonic phonons contribute the most to the temperature dependence of the Zr_2AlC free energy, as shown in Fig. 3.2, but the electronic term can make non-trivial contributions to the

derivatives such as the heat capacity at high-temperatures. The thermal expansion coefficient α_V compared to the literature is shown in Fig. 3.10. The electronic contribution to the thermal expansion is also plotted and found to be $0.09 \times 10^{-5}\mathrm{K}^{-1}$ at 1000 K. The thermal expansion coefficients compared to predictions by Luo *et al.* [18] and Nasir *et al.* [19] show considerable differences. For instance, at 1000 K we predicted α_V 2.8×10^{-5} K^{-1} compared to around 1.8×10^{-5} K^{-1} by Luo *et al.* and $4.27 \times 10^{-5}\mathrm{K}^{-1}$ by Nasir *et al.*. Both aforementioned studies used the quasiharmonic Debye model instead of the full normal modes spectrum in the quasiharmonic approximation applied in this study. Although both studies applied the same method, the difference between them is significant.

3.2.5 Heat capacity of $Zr_{n+1}AlC_n$ and $Ti_{n+1}AlC_n$

Heat capacity is an important thermal property, particularly useful for calculating phase diagrams. CALPHAD, a method for calculating phase diagrams, uses a database of both experimental and theoretical thermodynamic properties to fit the Gibbs free energy to polynomial expressions for each phase likely to contribute to stability in a system. Accurate calculations of heat capacities are therefore necessary, particularly in cases of a lack of experimental data, and are also important to be compared with available experimental data, as the reliability of

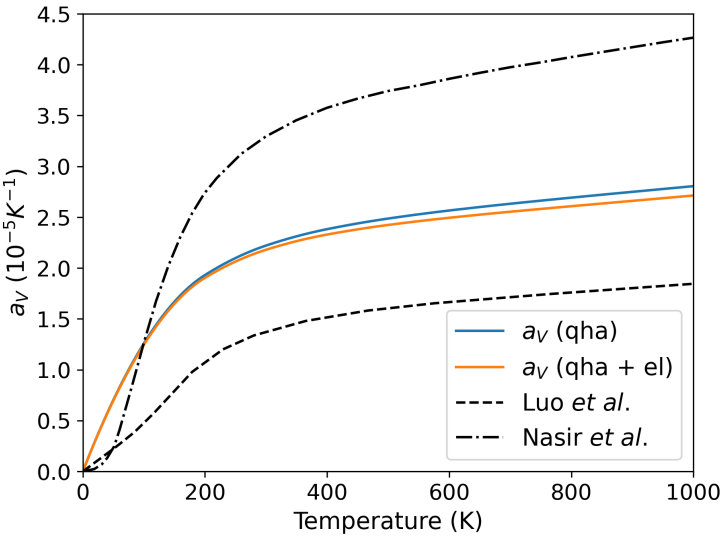

Figure 3.10: Thermal expansion coefficient for Zr_2AlC compared to studies by Luo *et al.* [18] and Nasir *et al.* [19].

the database used, and mainly of the heat capacities, determines the accuracy of the method.

In Fig. 3.11 the isobaric and isochoric heat capacity, C_P and C_V, are shown as a function of temperature for the Zr and Ti MAX phases. At low temperature the differences between C_P and C_V are small. After 800 K the difference increases, with C_P increasing linearly and deviating from C_V by 6–7% at 1600 K where C_V saturates to the classical limit of $3\,k_B$ at high temperature. From low temperatures up to around 1000 K the Ti MAX phases show lower heat capacities compared to Zr ones, which is the opposite trend noticed for the thermal expansion coefficients. The heat capacity increases as n decreases for both Ti-based and Zr-based phases, with Ti_4AlC_3 showing the lowest values overall.

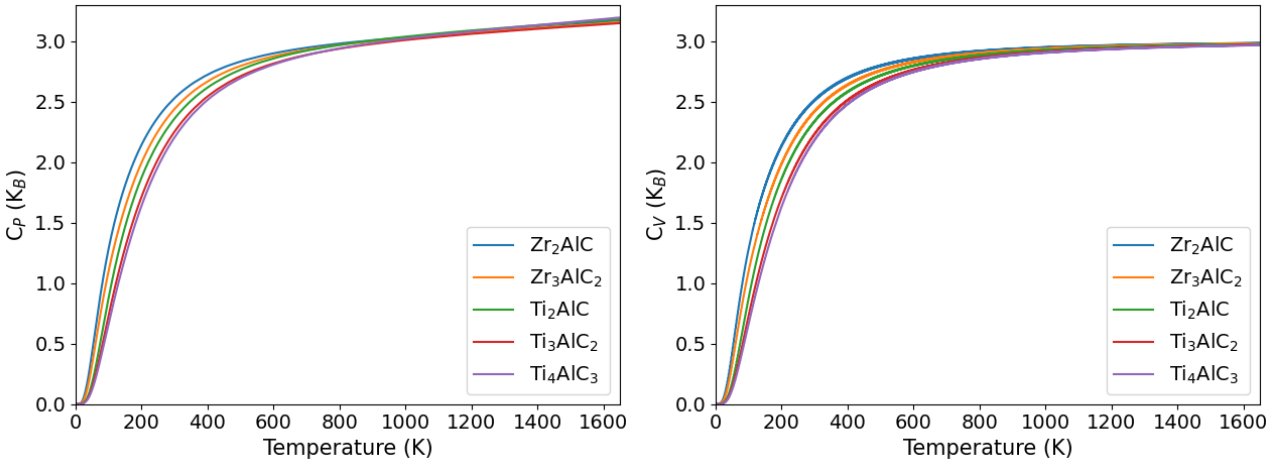

(a) (b)

Figure 3.11: The isobaric and isochoric heat capacity, C_P and C_V, for the $M_{n+1}AlC_n$, M = [Zr, Ti] MAX phases.

For the Ti_2AlC phase experimental studies measuring the heat capacity are reported by Drulis *et al.* [9] and Barsoum *et al.* [8]. The study by Drulis *et al.* [9] covers the temperature range from 3 to 260 K, with the heat capacity being proportional to T^3 at those low temperatures. At temperature 250 K our calculations underestimate their C_P by 19%. The study by Barsoum *et al.* [8] covers from 400 to 1400 K, from which the measured heat capacities up to 900 K were used to fit a Debye model. Our prediction is 11% lower than their experimental value at 400 K.

By comparing with other theoretical studies there is a good agreement and the choice of the method to approximate the lattice vibrations doesn't show as large an effect as in the case of the

thermal expansion. For Ti_2AlC the difference with our values are below 1% at 1000 K comparing with the theoretical studies [83, 73, 89]. In the studies by Wang *et al.* [83] and Duong *et al.* [73], electronic corrections to the C_P were also incorporated, showing an enhanced heat capacity by almost the same amount as the quasiharmonic contribution at high temperature, resulting in a better agreement with experiments [73]. For Ti_3AlC_2, by comparing with studies using the quasiharmonic approximation [90, 86], a difference below 4% was noted at 100 K, whereas for studies using the quasiharmonic Debye approximation a difference between 5% [85] and 8% [7] was noted, where in the former study electronic and anharmonic corrections were also applied. For Zr_3AlC_2, by comparing with the study by Ouadha *et al.* [7] using the quasiharmonic Debye approximation, a difference of 2% at 600 K is noted.

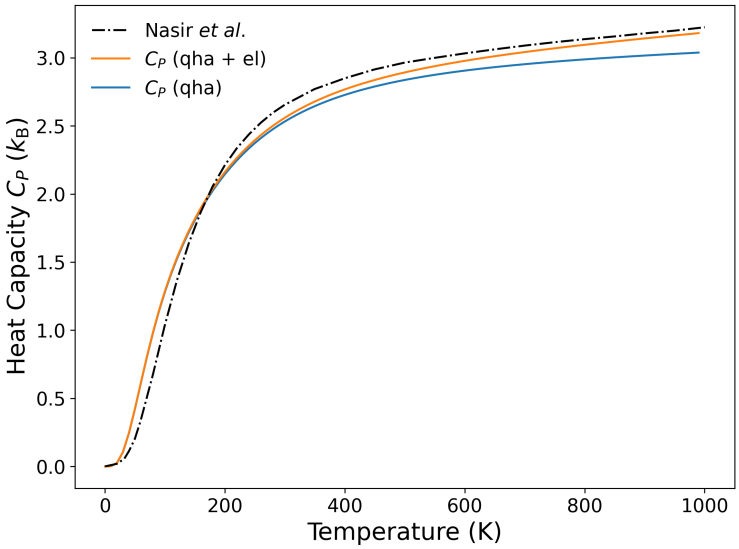

Figure 3.12: Heat capacity calculated taking into account the vibrational and electronic contribution and compared to calculated C_P by Nasir *et al.* [19].

For the Zr_2AlC phase, Fig. 3.12 shows the isobaric heat capacity, C_P, as a function of temperature along with predictions from study [19]. From our calculations the heat capacity including only C_P(qha) is 100.72 J/(mol K) at 1000 K. The electronic contribution to C_P is found to increase C_P(qha) by 4.6% at 1000 K. The calculated C_P by Nasir *et al.* [19] at high temperature shows only fair agreement with our results with the closest being with C_P(qha+el), e.g. at 1000 K Nasir *et al.* predicts C_P about 107 J/(mol K) which is close to our result of 105.56 J/(mol K). However there is a considerable disagreement at low temperatures which, as

will also be discussed later, could be a result of their use of the quasiharmonic Debye approximation instead of the quasiharmonic approximation that this study uses.

3.2.6 Bulk modulus of $Zr_{n+1}AlC_n$ and $Ti_{n+1}AlC_n$

In Fig. 3.13 the bulk modulus, B_T, is plotted for the Zr and Ti MAX phases with respect to the temperature. It is noted that the Zr-based phases have a lower bulk modulus than their corresponding Ti ones, indicating that the latter are more incompressible than their corresponding Zr phases. This is in agreement with the study by Cover *et al.* [67] where trends between 211 phases were studied. The bulk modulus increases with n, which is in agreement with the theoretical study by He *et al.* [68], where the 312 phases were predicted higher than the 211 ones. This trend is also shown by the experimental values [70, 71]. Both of the aforementioned trends are opposite to the trends noted for the heat capacities for the MAX phases. The highest B_T corresponds to Ti_4AlC_3, while the two lowest correspond to the 211 phases, with Zr_2AlC being the lowest overall. As temperature increases, the differences between Ti_4AlC_3 and Ti_3AlC_2 and between Ti_2AlC and Zr_3AlC_2 decrease. All the phases decrease their stiffness with temperature, with the greatest reduction noted for Zr_2AlC at 27% and the least for Ti_3AlC_2 at 16%.

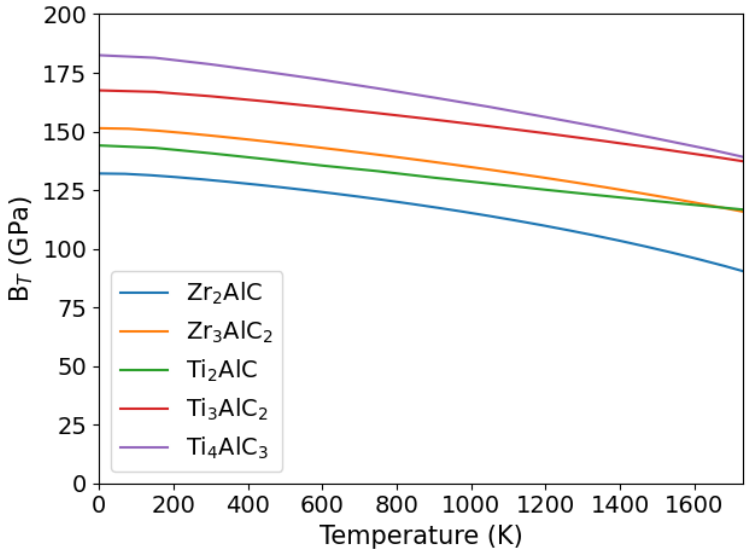

Figure 3.13: The isothermal bulk modulus for the $M_{n+1}AlC_n$, M = [Zr, Ti] MAX phases.

Other theoretical studies calculated the temperature dependence of the bulk modulus. The studies [89, 90, 91, 19] used the quasiharmonic Debye model while other studies treated the lattice vibrations within quasiharmonic approximation [83, 84, 73, 85, 86]. The study by Duong *et al.* [73] also considered the contribution due to electronic excitations while the study by Son *et al.* [85] also considered electronic and anharmonic corrections.

In Table 3.4 the bulk moduli calculated in this study are given for the Ti and Zr based MAX phases at 0 K along with other theoretical and experimental studies. In the reported theoretical studies, the isothermal bulk modulus, B_T was calculated under the c/a constraint using either Eq. 2.76 or similarly the second derivative Gibbs free energy with respect to the volume $V(\partial^2 G/\partial V^2)$. Other studies alternatively used the Voigt and/or Reuss approximations, or the average of those two bounds, the Voigt-Reuss-Hill (VRH) average, calculating them based on the elastic constants. The differences between the approximations were noted to be small.

Ti_4AlC_3	Ti_3AlC_2		Ti_2AlC		Zr_3AlC_2	Zr_2AlC
calc.	calc.	exp.	calc.	exp.	calc.	calc.
182.51	167.52	156 [70]	144.04	144 [71]	151.39	132.08
175.0 [69]	154 [86]		137 [72]	186 [142]	151 [68]	125 [19]
	161.9 [69]		138 [83]	139.6 [143]	167 [7]	134 [80]
	157 [90]		138.6 [69]		147.29 [84]	154 [76]
	168 [68]		161 [91]		148.04[75]	124 [77]
	160 [72]		141 [73]		158.2 [69]	125 [74]
	163 [85]		140 [89]			125 [67]
	184 [7]		138 [74]			176.28 [78]
			137 [67]			128.54 [75]
						133.7 [69]
						126 [79]

Table 3.4: B_T (GPa) for the $M_{n+1}AlC_n$, M = [Zr, Ti] MAX phases calculated in this study at 0 K and compared to experimental and theoretical values.

In general, a very good agreement is noted with most of the theoretical and experimental studies with differences from less than 1% to 8% compared to our calculations. For Ti_3AlC_2 the bulk modulus was found to be in close agreement with the experimental study by Zhang *et al.* [70] with only a 5% difference at 300 K. For Ti_2AlC, the predicted B_T shows the closest agreement with the experimental study [71], where we both agree on the same value of 144 GPa by comparing with our predictions for 0 K. At room temperature, our B_T prediction is less than 2% different to the experiments [71, 143] and a large difference of 32% is noted with the study [142].

Regarding the theoretical studies, the ones that showed the closest agreement to our values all treated the electronic XC energy within the Perdew–Wang generalised-gradient approximation (GGA-PW91). For Ti_3AlC_2, Zr_3AlC_2 and Zr_2AlC the studies that showed the closest agreement, with a difference less than 1%, were by He *et al.* [68] for the first two phases and Bai *et al.* [69] for the latter. Both these studies approximated the electron-ion interactions using the Vanderbilt-type ultrasoft pseudopotential. For Ti_2AlC, the closest agreement with the theoretical predictions, with a difference of 2%, was with the study by Duong *et al.* [73], which used the projector augmented-wave (PAW) pseudo-potentials approximation, similarly to this study.

The studies with the largest difference compared to our results, that exceed our values by more than 10%, used all-electron full-potential (linearised) augmented plane wave (FP-LAPW) pseudopotentials combined with a GGA type XC functional. In particular, for Ti_2AlC, Ti_3AlC_2 and Zr_3AlC_2, values around 10% greater than ours were noted with studies [91, 7] which used the FP-LAPW method with a GGA (PBE) functional. For Ti_3AlC_2 specifically, the study by Ouadha *et al.* [7] overestimates the experimental value [70] by 18%. In the case of Zr_2AlC, the predicted value by Kanoun *et al.* [76] was 16% higher than ours, where their study [76] used an all-electron full-potential (linearised) augmented plane wave plus local orbitals (FP-LAPW + lo) method with the XC potential estimated with the Wu and Cohen generalised gradient approximation (GGA-WC) [144]. The largest difference for Zr_2AlC, exceeding our results by 33%, is noted with the study by Yakoubi *et al.* [78] where apart from the pseudopotential difference the XC functional used also affected the predicted values. Specifically, the FP-LAPW method was used instead of PAW and instead of a GGA-type XC functional, and in particular PBEsol used in this study, LDA was used. It is generally known that LDA un-

derestimates the thermal expansion and lattice constants and GGA overestimates them. For the phonon frequencies and bulk modulus the opposite trend is noted with LDA overestimating these values.

3.2.7 Grüneisen parameters

The Grüneisen parameters describe the effect of temperature on the lattice dynamics of crystals by considering the volume dependence of the phonon frequencies. Based on this consideration, anharmonicity of phonon-phonon interactions and thermophysical properties such as thermal expansion can be predicted. In this section the average and mode Grüneisen parameters as defined in Section 2.4.3 have been calculated. The thermal Grüneisen parameter, γ_{th} defined in Eq. 2.81, was calculated as a function of temperature and compared for various phases in the Zr-Al-C and Ti-Al-C systems, including the MAX phases, their end member phases as well as other potentially competing phases. The mode Grüneiser parameters, $\gamma(qi)$ defined in Eq. 2.80, were also evaluated for the MAX phases to show the degree of change of each individual mode frequency with respect to changes in volume.

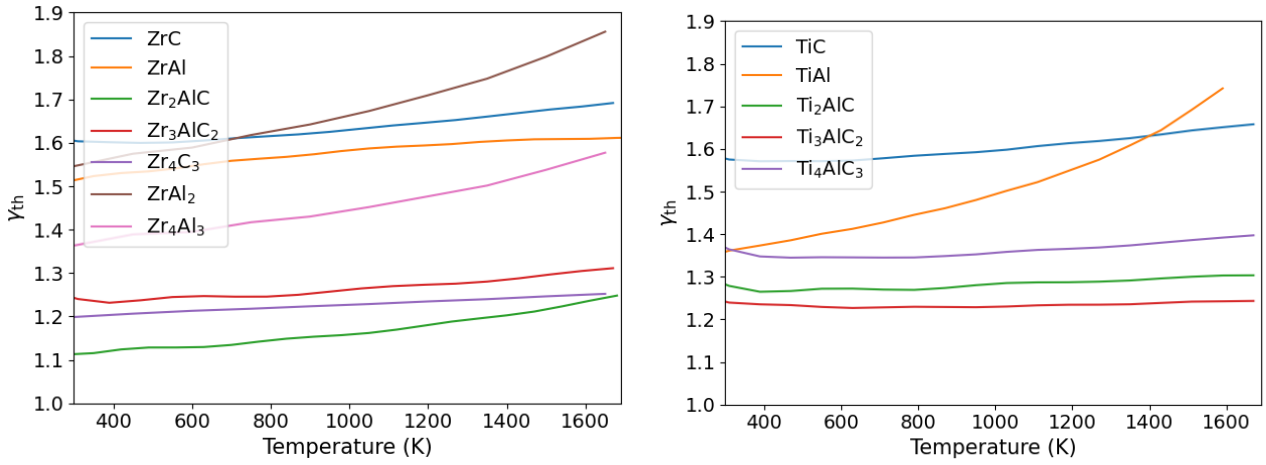

(a) Phases in Zr-Al-C system

(b) Phases in Ti-Al-C system

Figure 3.14: Thermal Grüneisen parameters, γ_{th}, with respect to the temperature for the MAX phases and their competing phases and end members in the two systems Zr-Al-C and Ti-Al-C.

In Fig. 3.14 the thermal Grüneisen parameters are shown for phases in the Zr-Al-C and Ti-Al-C systems. The Zr-based MAX phases have lower values overall than the corresponding Ti-based

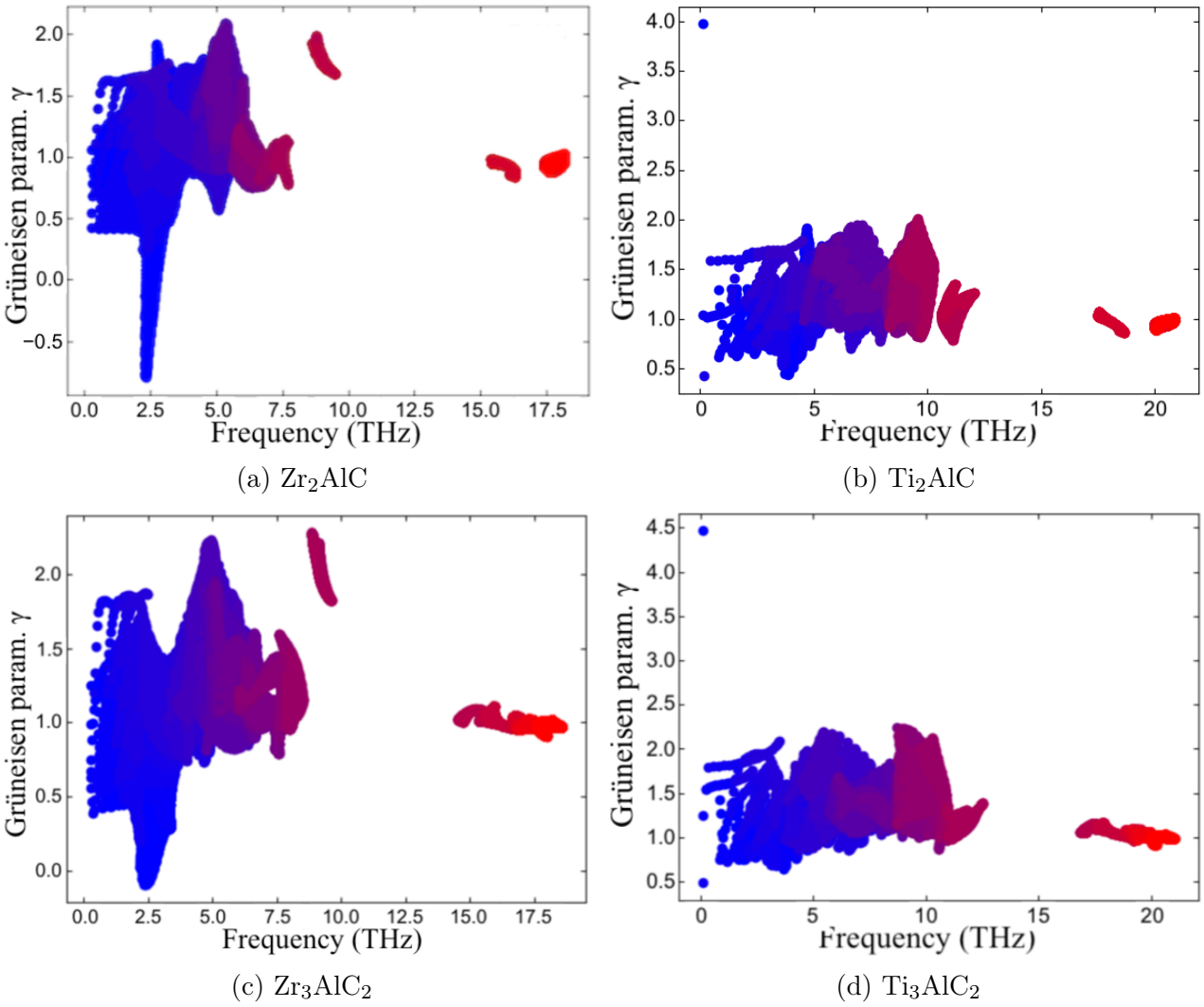

(a) Zr_2AlC (b) Ti_2AlC

(c) Zr_3AlC_2 (d) Ti_3AlC_2

Figure 3.15: Mode Grüneisen parameters calculations for Zr_2AlC (a), Ti_2AlC (b), Zr_3AlC_2 (c) and Ti_3AlC_2 (d). The colors of mode Grüneisen parameters are set for band indices with ascending order of phonon frequency.

ones and the difference between the end members and MAX phases is larger in the case of the Zr-Al-C system. The Zr-based 211 phase shows the lowest values overall, whereas for the Ti-based MAX phases the lowest values correspond to the 312 phase. In the Zr-Al-C system in particular, the Grüneisen parameter of Zr_3AlC_2 is in general higher than Zr_2AlC, so that its frequencies decrease faster with temperature, meaning that its free energy also decreases faster with temperature.

The lowest average Grüneisen parameters for the Zr_2AlC phase compared to the rest of the MAX phases can be explained by looking closer at the frequencies of individual phonons. In Fig. 3.15 the mode Grüneisen parameter $\gamma(qi)$, as defined in Eq. 2.80, is shown for the four MAX

phases. The Zr_2AlC and Zr_3AlC_2 phases show very similar patterns across the different phonon frequencies. Both of them show some negative modes at low frequencies close to 2.3 THz. The Zr_2AlC phase though shows the most negative values reaching -0.8 explaining the low average values in Fig. 3.14, whereas for Zr_3AlC_2 the most negative Grüneisen parameter is -0.098. On the other hand, the Ti_2AlC and Ti_3AlC_2 phases share a very similar pattern, without having negative values for any of their Grüneisen modes. In general, for the four MAX phases the mode Grüneisen parameters calculated show a significant degree of dispersion, with values ranging from around negative -0.8 to positive 4. This indicates that the thermophysical properties of such structures cannot be described accurately enough by the Debye model where only acoustic modes are considered, resulting in a linear dispersion curve that neglects important information about the full phonon dispersion spectra of the crystal.

3.3 Conclusions

Overall the thermophysical and structural properties of the $Zr_{n+1}AlC_n$ and $Ti_{n+1}AlC_n$ MAX phases were calculated based on DFT within the quasiharmonic approximation with a particular focus on Zr_2AlC. For the Zr_2AlC phase the free energy was expressed with respect to the temperature and strains and electronic corrections were applied. The choice of PBEsol over other XC functionals showed a close agreement with experiment with less than 1% difference in the lattice constants at room temperature. The temperature dependent elastic constants were predicted and the electronic contribution was found to be 2% at 1400 K. Further elastic property calculations predicted the slabs of metal carbide within the MAX phases to be stiffer than their alternating Al layers. Calculated stress-strain curves in both Zr and Ti-based systems further indicated that as this carbide slab thickened, the MAX phases' elastic properties approach those of the metal carbide, as would be expected. Deformability can be an important property requirement for candidate coating materials for nuclear fuel cladding, where coating materials may need to follow the deformation of substrate fuel cladding due to irradiation creep or swelling. By comparing the stress-strain curves for the two systems we found that Zr_2AlC is slightly softer than Ti_2AlC, though no significant difference was found, with the difference be-

ing less than 10%. Other than to the elastic properties, electronic excitations were also found to contribute to thermophysical properties, such as by 4.6% at 1000 K to the heat capacity. The anisotropy in the thermal expansion was found to be very weak for Zr_2AlC and the error introduced by neglecting it in the energy and volume strain was found to be negligible. Further comparisons of the thermophysical properties, thermal expansion, heat capacities, bulk moduli and Grüneisen parameters of the MAX phases in the Zr-Al-C and Ti-Al-C systems were performed under the approximation of the c/a constraint. The thermal expansion and bulk moduli were found to be higher for the Ti-based MAX phases than the Zr-based phases. The heat capacity was found to increase as n decreases, whereas the opposite trend was noted for the bulk modulus of the MAX phases in both systems. In general the predicted thermophysical properties were found to be in reasonable agreement with experimental data where it was available. The method applied to predict the lattice vibrations was however found to have an effect on thermal properties such as the heat capacity, as a significant discrepancy was noticed for Zr_2AlC at low temperatures between our results and the study by Luo *et al.* [18] where the quasiharmonic Debye method was used. This discrepancy can be explained by the significantly large degree of dispersion of the mode Grüneisen parameters we calculated for the MAX phases, indicating that for such phases the Debye theory may not be sufficient to describe the thermal effects.

Chapter 4

Thermodynamic stability of MAX phases in the Zr-Al-C and Ti-Al-C systems

One of the main objectives of this work was to predict the thermodynamic stability of MAX phases in the Zr-Al-C system against the formation of other secondary phases in the system. Thermodynamic stability was calculated via a convex hull construction for free energies, and the effect of temperature on stability was evaluated. For comparison purposes, the stability of the closely related $Ti_{n+1}AlC_n$ MAX phases was also calculated. The main results regarding the thermodynamic stability that follow have also been published in Poulou *et al.* [145].

The calculation of the convex hulls considered only fully ordered structures of intermetalics, carbides and ternary phases including the MAX phases in the system. The convex hull calculations were performed at 0 K (CH0), without zero point energy, and at finite temperature (CH(T)), with CH(T) being evaluated within the quasiharmonic approximation. The quantitative *ab initio* calculation of phase diagrams is notoriously problematic, since it generally requires the calculation of energy-differences that are similar to or smaller than the accuracy of the central approximation of applied DFT, which is the exchange-correlation (XC) functional. For this reason we give special attention to the robustness of our conclusions with respect to this approximation, by making selected calculations with four of the more commonly used XC functionals. Further to that the Zr-Al system is examined in detail and discrepancies between

various experiments and theoretical predictions are discussed. The thermodynamic prediction suggests Zr-based MAX phases are unstable at room temperature and below with respect to their decomposition to carbides and intermetallics, although with increasing temperature the Zr_3AlC_2 phase becomes stable. On the other hand, the pure Ti_2AlC phase is thermodynamically stable at room temperature, consistent with the success in its synthesis. This difference in stability between the Ti-based and Zr-based MAX phases is in alignment with the reported difficulty in synthesis of $Zr_{n+1}AlC_n$ and its low phase purity. Recent studies introduced techniques to improve the phase purity by means of partial site-substitutions and provided a link between phase purity and geometrical distortion in the MAX phases [3, 41]. Section 4.2.5 was motivated by these studies' findings and geometrical effects on the MAX phases for both systems were investigated by focusing on octahedral and Al layer distortion. Differences in the distortion effect are compared and discussed for the two systems.

4.1 Methodology

4.1.1 Computational details

The following calculations are based on Density Functional Theory (DFT) implemented in the Vienna Ab initio Simulation Package (VASP) [118, 119]. The electron-ion interactions have been treated using a projector augmented wave (PAW) [132] pseudopotential method. The exchange-correlation energy has been calculated using the PBEsol functional (Perdew-Burke-Ernzerhof revised for solids) [111]. The electrons treated as valence were the $4s$ $4p$ $5s^2$ $4d^2$ for Zr, the $3s$ $3p$ $4s^2$ $3d^2$ for Ti, the $2s$ $2p$ $3s^2$ $3p^1$ for Al, and the $2s$ $2p$ for C. The cut-off kinetic energy used was 760 eV for all phases in the two systems. At 760 eV, the convergence for each phase separately with respect to the total energy is better than 3.5 meV/atom, while the cancellation of errors brought the convergence of the standard formation energies to better than 0.14 meV/atom. The k-point convergence of total energy was tested separately for each phase to be better than 1 meV/atom. Accurate structural relaxation was conducted for each phase at a state of zero stress, setting the threshold for the total energy at 10^{-9} eV and for

the forces during the ionic relaxation at 10^{-5} eVÅ^{-1}. Phonon spectra were calculated using the small displacement supercell method implemented in PHONOPY [125] by applying finite displacements of 0.01 Å. The supercell for each phase was sufficiently large to converge the phonon free energy to 1 meV/atom, which was also the convergence criterion for the density of Brillouin zone mesh points for sampling the phonons.

4.1.2 Free energy of formation

The Helmholtz free energy is calculated in the quasiharmonic approximation, in which:

$$F(T,V) = U_0(V) + F_{\text{qha}}(T,V) \tag{4.1}$$

U_0 is the DFT energy at $T = 0$ K without including the zero point energy, and F_{qha} corresponds to the free energy due to atomic vibrations, computed within the harmonic approximation with fixed dimensions of the unit cell. In the case of a crystal of hexagonal or tetragonal symmetry, F is also a function of the c/a ratio of the conventional unit cell, however for the calculations of free energy of all the compounds required we approximate the thermal expansion as isotropic. We have shown that this approximation, although necessitated by the computational cost, introduces an error in the calculated free energy of much less than 0.1 meV/atom. The estimation of this introduced error was justified in the methodology Section 2.4.2 and it was later evaluated in Section 3.2.3 for MAX phases in the Zr-Al-C and Ti-Al-C systems by applying Eq. 2.73. We have not included here electronic excitations (except for test purposes), or anharmonicity and the impact of lattice vibrations on electronic free energy, of which anharmonicity in particular would be much more expensive to compute. These omissions are reasonable, since we are not concerned here with properties at above about half the melting point, where these contributions would start to become important [129].

The free energy was expressed in terms of volume and temperature by fitting the harmonic free energy calculated at temperature intervals of two degrees from 0 to 2000 K, and the internal energy with a 3$^{\text{rd}}$ order polynomial in V at five volumes. The volume scaling factors used

to scale the lattice vectors and atomic coordinates were 0.98, 0.99, 1.0, 1.01, 1.025. For the Ti-based phases we used six volumes, scaling as 0.98, 0.99, 1.0, 1.005, 1.015, 1.025. For the $Zr_{n+1}AlC_n$ MAX phases and the phases that might compete with them, an estimate of the electronic contribution to the free energy, $F_{el}(T, V)$, was added to Eq. 4.1. The electronic term was expressed in terms of volume and temperature by fitting it to a 5^{th} order polynomial on a 2D mesh consisting of 5 volumes, the same ones used for the Zr-Al-C system, and a set of 15 temperatures between 116 and 2000 K.

By minimising $F + PV$ with respect to the volume, the Gibbs free energy is obtained:

$$G(T, P) = \min_{V}[F + PV] \tag{4.2}$$

We have examined the thermodynamic stability by comparison of the Gibbs formation energies of each phase against any linear combination of alternative phases by a convex hull construction in the Zr-Al-C and Ti-Al-C systems. The convex hulls defined in this study are explained in Section 2.4.3.2. As mentioned in the Methodology chapter, it is important to note that all the structures considered for the convex hull evaluations were fully ordered structures, meaning the arrangement of structural vacancies in the γ-phase [130, 131] are not associated with any configurational entropy.

4.1.3 The phases considered

Tables 4.2 and 4.3 include the phases considered in the Zr-Al-C and Ti-Al-C systems respectively. Of the binaries, the zirconium aluminides and Al_4C_3 ($hR7$) phase have been reported as synthesised, but not all of them as pure phases. In particular, ten reported stable intermetallics $ZrAl_3$ ($tI16$), $ZrAl_2$ ($hP12$), Zr_2Al_3 ($oF40$), ZrAl ($oC8$), Zr_5Al_4 ($hP18$), Zr_4Al_3 ($hP7$), Zr_3Al_2 ($tP20$), Zr_5Al_3 ($tI32$), Zr_2Al ($hP6$) and Zr_3Al ($cP4$) were considered. The published phase diagrams suggest that two out of the ten reported phases are thermodynamically stable at high temperatures, Zr_5Al_4 and Zr_5Al_3. These ten intermetallics are included in the phase diagrams reported in the literature, based on assessments of the Zr-Al system, some of

them initially by Saunders *et al.* [146], followed by Murray *et al.* [23], Wang *et al.*, and a recent reassessment by Tamim *et al.* [147]. For the Ti-Al system, in cases where a published phase diagram included multiple phases at a given composition, dependent on the temperature, we have only included the lower temperature one. We have considered five stable Ti-Al intermetallics $TiAl_3$ ($tI8$), $TiAl_2$ ($tI24$), Ti_3Al_5 ($tI32$), TiAl ($tP2$) and Ti_3Al ($hP8$) whose synthesis has been reported many times, and they appear in the Ti-Al phase diagrams [148, 149, 150, 151]. We have discovered no reports of synthesis of Ti_2Al_3 ($oF40$), Ti_5Al_4 ($hP18$), Ti_4Al_3 ($hP7$) and Ti_3Al_2 ($tP20$) for which, as prototype structures, we have assigned those of the corresponding Zr aluminides. For both the zirconium and titanium carbides, the predicted structures which have ordered sublattices of carbon vacancies were considered [130, 131]. Regarding the zirconium ternary phases, all the phases considered, $Zr_2Al_4C_5$, $ZrAlC_2$, $Zr_3Al_4C_6$ $Zr_4Al_3C_6$, $Zr_3Al_3C_5$, $Zr_2Al_3C_4$, including the two MAX phases Zr_2AlC and Zr_3AlC_2, have been reported as synthesised [4, 5, 75, 152, 153]. For the MAX phases and especially the Zr_2AlC phase the presence of secondary phases, mainly ZrC and some aluminides (e.g $ZrAl_2$) was observed [4, 5]. Similarly all the titanium ternary phases considered, including the three MAX phases Ti_2AlC, Ti_3AlC_2, and Ti_4AlC_3 have been reported as synthesised, with the 211 and 312 MAX phases appearing with higher phase purity than the corresponding Zr ones.

4.2 Results

4.2.1 Results for phase diagrams in Zr-Al-C: 0 K

4.2.1.1 CH0 in the Zr-Al-C system

In Fig. 4.1 the stoichiometric phase diagram is shown at 0 K and 0 atm, calculated from the internal energies, without including the zero point energy. For this and subsequent convex hull constructions we have introduced the convention that compounds in red are on the convex hull, while those in black are above it. As shown, the two MAX phases, Zr_2AlC and Zr_3AlC_2 are predicted unstable with reference to CH0, their closest competing phases being Zr_4Al_3, Zr_4C_3,

$ZrAl_2$ and Zr_4C_3, Zr_7C_6, $ZrAl_2$ respectively. These are the 'red' phases that mark the corners of the bounding triangle closest to the MAX phase in question. Of the remaining ternary phases, $ZrAlC_2$, $Zr_2Al_4C_5$ and $Zr_3Al_4C_6$ are above the hull and only the $(ZrC)_nAl_3C_2$ $(n = 2, 3, 4)$ phases appear stable with reference to CH0.

Other phases appearing thermodynamically stable include Al_4C_3 and the following zirconium carbides: ZrC, Zr_2C, Zr_3C_2, Zr_4C_3 and Zr_7C_6. The predicted ordered carbides on CH0 are in agreement with the ground state carbides in the studies by Yu *et al.* [154] and Xie *et al.* [130]. The study by Zhang *et al.* [155] predicts the Zr_8C_7, Zr_6C_5, Zr_4C_3, Zr_3C_2 and Zr_2C ordered phases as stable, this difference with our CH0 could be because they did not include the Zr_7C_6 phase, which may have otherwise made the Zr_6C_5 and Zr_8C_7 stoichiometries unstable, as seen in our CH0.

As a by-product of our procedure, we find our stability prediction in the binary Zr-Al system disagrees with the published Zr-Al phase diagram [156], as we shall discuss in Section 4.2.2. For example of the ten phases reported as synthesised in this system, we predict four phases, Zr_3Al, Zr_4Al_3, $ZrAl_2$ and $ZrAl_3$, to be thermodynamically stable.

4.2.1.2 Sensitivity to exchange-correlation functional

The main uncertainty in the numerical results of these DFT calculations is in the approximation of the XC functional. An estimation of the error that might be introduced in the formation energies is important, since the phase stability sometimes depends on energy differences of a few meV/atom. The LDA [109] and GGA (Perdew-Wang) [133] functionals are generally believed to bracket the exact value [134] and our choice of PBEsol is a recommended GGA-type functional for solids with improved treatment of the exchange energy [111, 134], which we expect to return values within the range between standard LDA and GGA. This is our reference XC functional, with which all the phase diagrams were calculated. We have also included in our tests a recommended functional of the type that includes van der Waals dispersion, namely optPBE-vdW [157, 158]. In the phase diagrams of Fig. 4.2, regions of the CH0 around the MAX phases for the LDA, GGA, optPBE-vdW and PBEsol functionals are shown, with only a number of

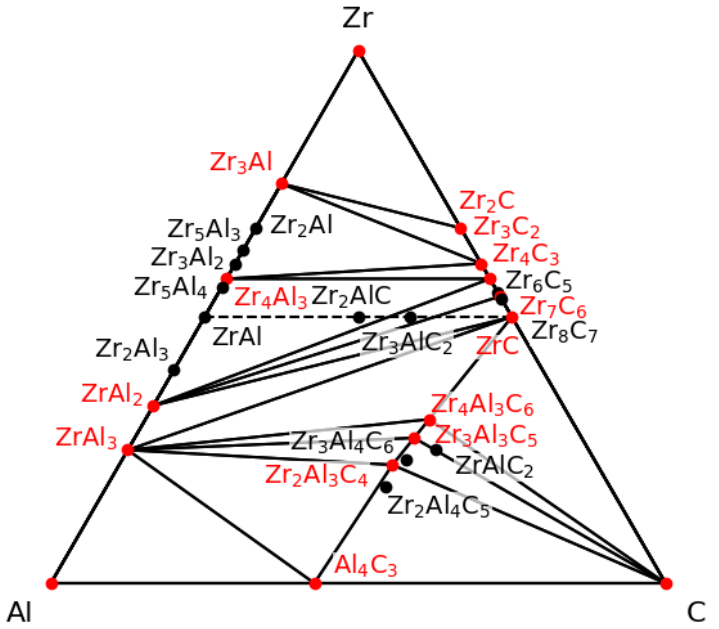

Figure 4.1: Zr-Al-C phase diagram at 0 K without zero point energy. The red and black points are located on and above the corresponding convex hull CH0 respectively. The MAX phases in the system appear along the dashed line.

intermetallics and carbides included out of the total binary phases considered. Those included were chosen based on the most competing phases for the two MAX phases as they appear in Fig. 4.1 as well as other potentially competing phases located closely around these two MAX phases, with the stability of most of those selected depending on no more than 5 meV/atom. The actual formation energies for these phases are shown in Table 4.1 and presented graphically in Fig. 4.3, and they show differences of up to 50 meV/atom between PBEsol and the other three tested functionals. As expected, the values calculated with PBEsol lie between those of LDA and GGA. Fig. 4.3 shows that the biggest differences in formation energy are in the carbon-containing compounds, where the formation energy with optPBE-vdW is consistently and increasingly lower, as the proportion of carbon increases.

The levels of stability and instability of these phases is evaluated by their vertical distances from the CH0 convex hull, and values are given in Table 4.1. The negative values represent compounds that are on the convex hull, and the distances are then measured from where the convex hull would be without them. These distances might be expected to be less sensitive

to the choice of XC functional than the formation energies. However, this is not generally true, although it is clearly the case for the MAX phases. All four functionals predict both MAX phases to be unstable by a margin of 19–30 meV/atom for Zr_2AlC and a reduced margin of 2–9 meV/atom for Zr_3AlC_2. The lower end of the margin of instability for both phases is predicted by GGA.

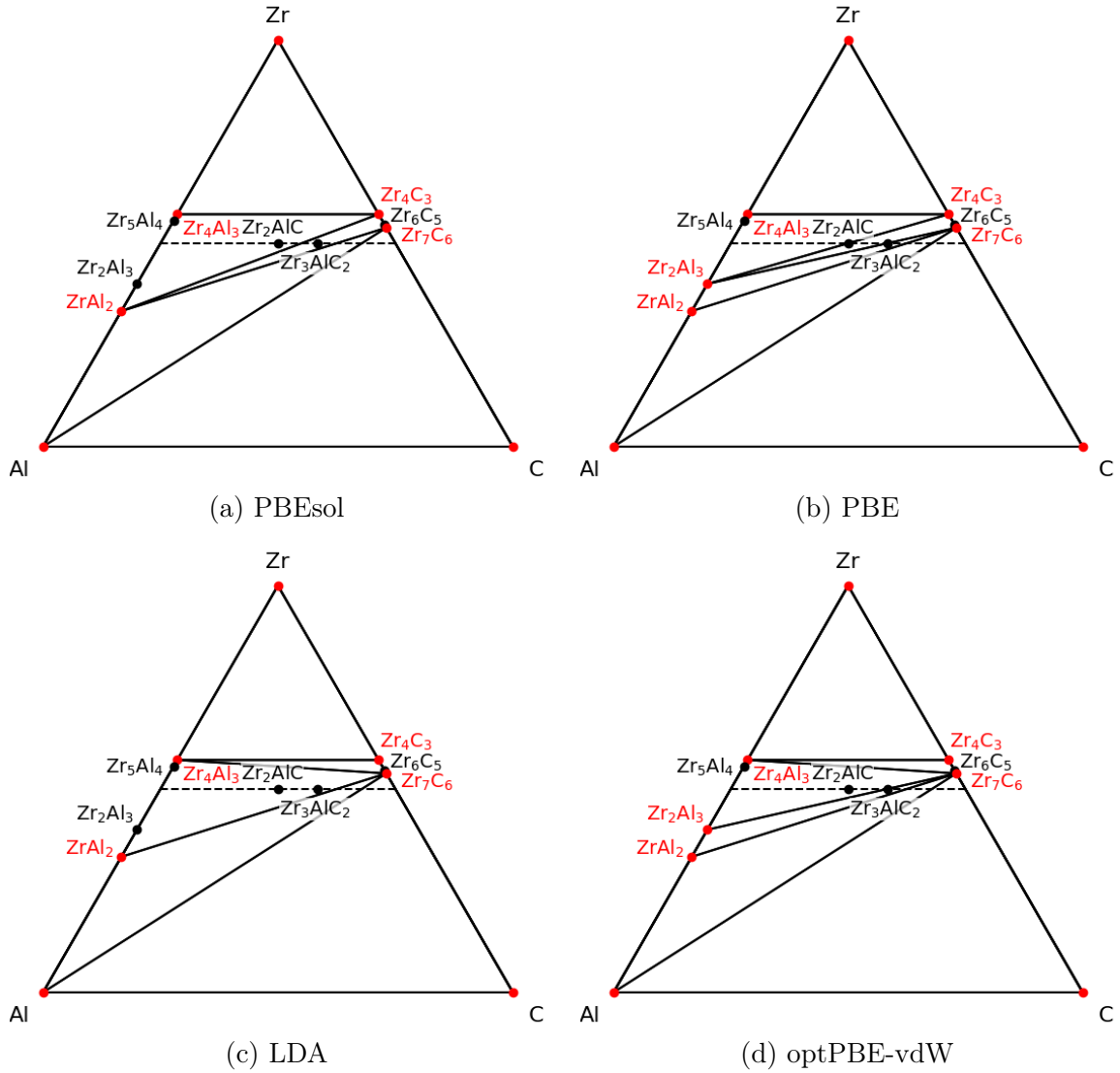

(a) PBEsol (b) PBE

(c) LDA (d) optPBE-vdW

Figure 4.2: Zr-Al-C phase diagrams ($T = 0$ K, no zero-point energy) for different XC functionals. Only the part of CH0 relevant to the stability of the MAX phases is shown. The red and black points are located on and above CH0 respectively. The MAX phases in the system are along the dashed line.

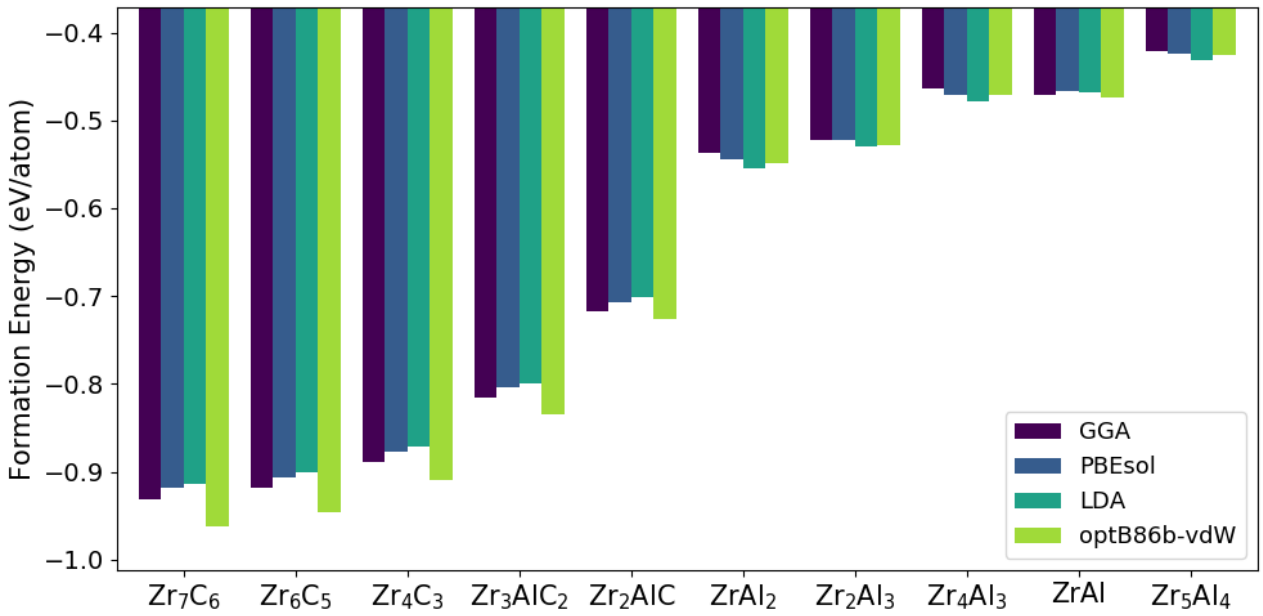

Figure 4.3: Gibbs energies of formation for the Zr_2AlC and Zr_3AlC_2 MAX phases and the phases that might compete with them, calculated using four different XC functionals.

Table 4.1: The formation energies ΔG_f and the distances from CH0 of the Zr_2AlC and Zr_3AlC_2 MAX phases and the phases that might compete with them, calculated with PBEsol, LDA, GGA and optPBE-vdW functionals. For these results CH0 is calculated without each compound in turn, so negative values indicate that the compound would be *on* the complete CH0.

Phase	ΔG_f and distance from CH0 (eV/atom)			
	PBEsol	LDA	GGA	optPBE-vdW
Zr_6C_5	−0.9062 +0.0039	−0.9007 +0.0043	−0.9189 +0.0036	−0.9467 +0.0040
Zr_4C_3	−0.8778 −0.0053	−0.8708 −0.0215	−0.8882 −0.0218	−0.9102 −0.0173
Zr_3AlC_2	−0.8039 +0.0035	−0.7999 +0.0085	−0.8161 +0.0020	−0.8353 +0.0060
Zr_2AlC	−0.7072 +0.0231	−0.7016 +0.0300	−0.7170 +0.0189	−0.7266 +0.0281
ZrAl	−0.4666 +0.0267	−0.4689 +0.0325	−0.4705 +0.0174	−0.4733 +0.0215
$ZrAl_2$	−0.5440 −0.0318	−0.5544 −0.0311	−0.5368 −0.0284	−0.5483 −0.0334
Zr_2Al_3	−0.5219 +0.0018	−0.5299 +0.0033	−0.5224 −0.0063	−0.5284 −0.0018
Zr_4Al_3	−0.4715 −0.0475	−0.4786 −0.0457	−0.4631 −0.0392	−0.4709 −0.0431
Zr_5Al_4	−0.4243 +0.0520	−0.4315 +0.0522	−0.4214 +0.0472	−0.4256 +0.0507
Zr_7C_6	−0.9188 −0.0069	−0.9142 −0.0250	−0.9318 −0.0246	−0.9616 −0.0270

Compared to the other functionals, optPBE-vdW consistently predicts greater stability of com-

pounds with a higher proportion of carbon, as we see in Fig. 4.3. We attribute this to lack of any van der Waals attractions in diamond, the reference end-member we have used in our formation energy calculations, whereas the metal atoms involved all have some degree of van der Waals interactions.

4.2.2 The Zr-Al intermetallics

Zr-Al exhibits the most complex phase diagram of any binary intermetallic system. During synthesis of the MAX phases, in the resulting polycrystals some Zr-Al intermetallics seem always to accompany the grains of the MAX phase, and the intermetallics would naturally also be products if the MAX phase were to decompose. We have compared our calculations of the formation energies of the known intermetallics, using the four different exchange-correlation functionals, with a range of experimental and theoretical data. A comparison with a previous theoretical study of the Zr-Al system, based on ultrasoft pseudopotentials and GGA, is shown in Fig. 4.4a. The energy differences are less than 0.02 eV/atom between those reported values and the current PBEsol ones. Besides the choice of exchange-correlation functional and pseudopotentials, these differences may be due to computational parameters, such as k-points and cut-off energy. All these calculations agree on the stability of the four phases that always appear on the convex hull, as in Fig. 4.1. More surprisingly, they also agree on predicting that ZrAl is *above* the convex hull, although ZrAl has been observed experimentally, and is taken to be thermodynamically stable at low temperature according to all recent assessments [20, 159].

There are large differences between experimental results for the heats of formation of the ten observed intermetallic phases reported by different authors, which makes it difficult to verify the accuracy of our DFT enthalpies of formation by comparison with published experimental data. We have included experimental data for enthalpy of formation that we could find that covers a range of compositions in Fig. 4.4, together with two sets of DFT calculations, including our own, and a thermodynamic assessment. The data of Wang *et al.* [20], also appearing in [156], are the outcome of their thermodynamic assessment, and are significantly below the theoretical predictions. The greatest difference we note is for the ZrAl phase, whose heat of

formation is assessed at $\sim 0.2\,\mathrm{eV/atom}$ (~ 20 kJ/mol) more negative than any DFT calculations. Furthermore, in contrast to this assessment, every DFT calculation places ZrAl clearly above CH(0) and CH(T). We suggest this discrepancy arises because the values reported by Wang *et al.* are the result of a CALPHAD optimisation of parameters, including heats of formation. In particular, their value for the ZrAl phase does not *directly* reflect experimental calorimetric measurements of that energy. Rather it is a consequence of fitting data that will reproduce the observed appearance of ZrAl on the phase diagram, on the assumption that it is actually an equilibrium phase. By contrast, the results of recent calorimetric measurements of Kematick *et al.* [22] give formation enthalpies slightly above the DFT values, but these data were reinterpreted by Murray [23], which shifts the results downwards to values that lie *below* DFT, although within 0.1 eV/atom. Both sets of data are shown in Fig. 4.4. Interestingly, these experimental data do indicate that the ZrAl phase lies slightly above the convex hull, confirm-

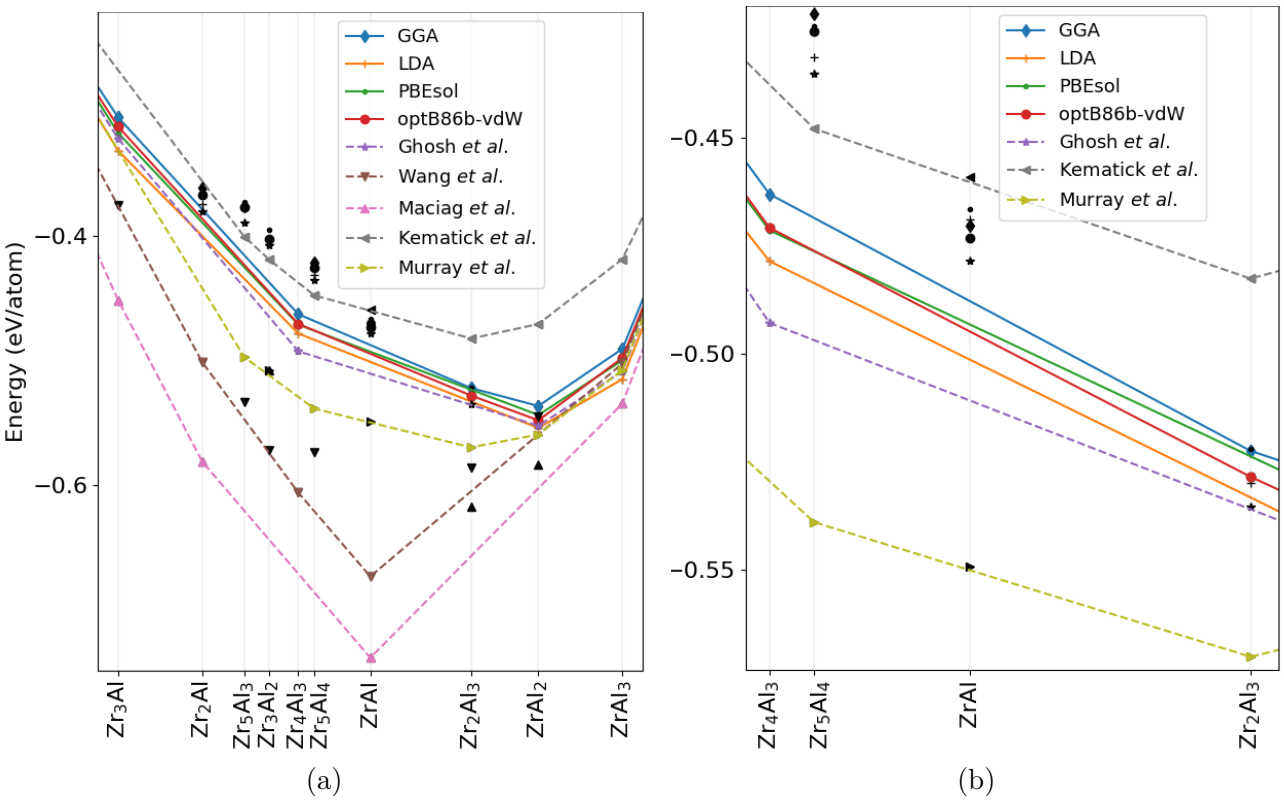

Figure 4.4: The CH0 for different functionals in this study are compared to experimental values by Wang *et al.* [20], Maciąg *et al.* [21], Kematick *et al.* [22] and Murray *et al.* [23] and calculations by Ghosh *et al.* [24]. The energies of formation for the Zr-Al intermetallics are with respect to their pure elements. Our calculations are shown on a continuous line, data from the literature are shown on a dashed line. The black symbols denote that the phase is above the hull. (a) the CH0 for the ten intermetallics (b) the CH0 zoomed in around the ZrAl phase.

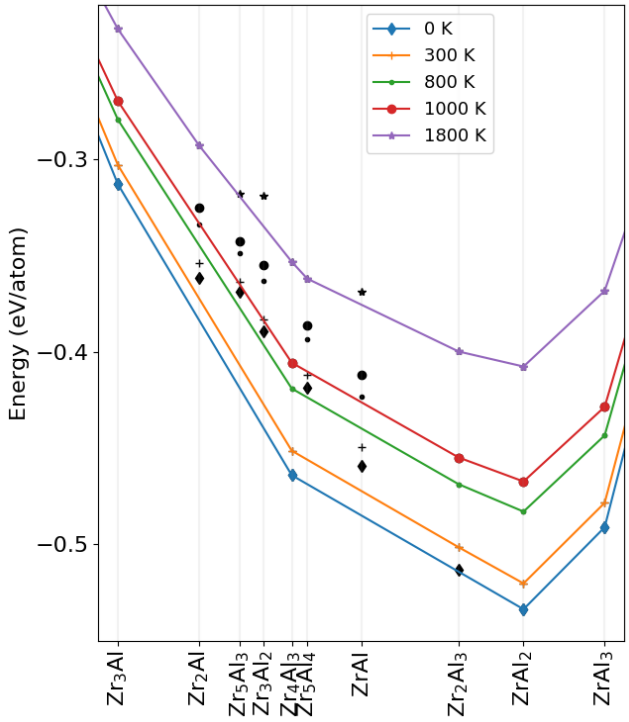

Figure 4.5: CH(T) calculated with PBEsol at different temperatures. The formation energies of the Zr-Al intermetallics are with respect to their pure elements. The black symbols denote that the phase is above the hull.

ing the DFT predictions that the ZrAl phase is thermodynamically unstable. Our calculated temperature-dependance of the enthalpies of formation, shown in Fig. 4.5, indicates a trend for the thermodynamically unstable phases to approach CH(T) as the temperature increases, and they all reach the convex hull except ZrAl, Zr_3Al_2 and Zr_5Al_3, albeit at an unrealistically high-temperature for the quantitative validity of the quasiharmonic model. In summary, our predicted instability of these three phases, which is robust to uncertainties in the DFT exchange-correlation parameters, agrees qualitatively with the experimental data of refs. [23] and [22], but not with the CALPHAD-assessed data of [20] or, more recently, [159].

Our final comment here on the comparison with experimental data concerns the biggest discrepancy of the DFT calculations, which is with the enthalpies of formation reported by Maciąg [21], and also plotted in Fig. 4.4a. These data all lie below the DFT values, the biggest discrepancy again being for ZrAl, with an enthalpy of formation about 0.3 eV/atom below DFT, which is low enough to place it as a stable compound on this experimental convex hull. The discrepancy is least, namely < 50 meV/atom, for the Al-rich phases, $ZrAl_2$ and $ZrAl_3$. The data of ref. [21]

were obtained from solution calorimetry, performed by preparing the phases, dissolving them in liquid Al, and measuring the temperature change with reference to that induced by dissolving the pure elements. There are two possible sources of error that have not been quantified. Firstly, a source of error suggested in the paper [21] is that, among the alloy phases prepared for these experiments, the least pure as measured by X-ray diffraction was ZrAl, which consisted of 92.72% ZrAl, with an admixture of Zr_2Al_3, Zr_4Al_3 and Zr_5Al_3. A second, perhaps greater source of error in solution calorimetry for this system, recently identified by Barachin *et al.* [160], is the likelihood of incomplete dissolution of Zr in liquid Al due to prior formation of $ZrAl_3$.

4.2.3 Results for phase diagrams in Zr-Al-C: $T > 0\,\mathrm{K}$

In Fig. 4.1 the stoichiometric phase diagram is shown at 0 K calculated from the internal energies, without including the zero point energy. Fig. 4.6 shows how the phase diagram changes with respect to the temperature by including the vibrational contribution to the free energy at atmospheric pressure. Four different temperatures are shown, 0, 300, 800, and 1800 K, where for 0 K the zero point energy is now included. On the Zr-Al side, the low-temperature phases, Zr_3Al, Zr_4Al_3, $ZrAl_2$ and $ZrAl_3$ remain thermodynamically stable and at 0 K the zero point energy doesn't change the stability of any intermetallic in the system (Fig. 4.6(a)).

The Zr_2Al_3 phase appears stable from 300 K, while the phases Zr_2Al and Zr_5Al_4 appear stable at temperature 1800 K in agreement with the reported Zr-Al phase diagram [156], in which the latter phase is also shown as a high temperature phase. The phases ZrAl, Zr_3Al_2 and Zr_5Al_3 are predicted to be unstable at all temperatures in marked contrast to the phase diagrams and experimental studies [20, 156]. However, their distances from the hull were decreasing with temperature as also shown in Table 4.2, with ZrAl being 0.0068 eV/atom above the hull at 1800 K, which is within the estimated error of the calculations. As also predicted by Ghosh *et al.* [24] ZrAl, Zr_3Al_2 and Zr_5Al_3 showed a significant discrepancy in formation energy obtained by *ab initio* and experiment reported in their study. This is consistent with earlier assertions [24] that these intermetallics may be stabilised by impurity effects. Regarding the carbides, raising

the temperatures above 300 K changes the stability of two phases compared to CH0 (Fig. 4.1). In particular, at 800 K Zr_2C has become unstable and at 1800 K Zr_8C_7 has become stable.

Regarding the MAX phases, Zr_3AlC_2 becomes stable by 800 K as the temperature increases, whereas Zr_2AlC remains unstable over the entire temperature range. The quantitative level of stability of these two MAX phases is evaluated based on their distances from the convex hull and the results are shown in Fig. 4.7. In the same plot, the contribution of the electronic free

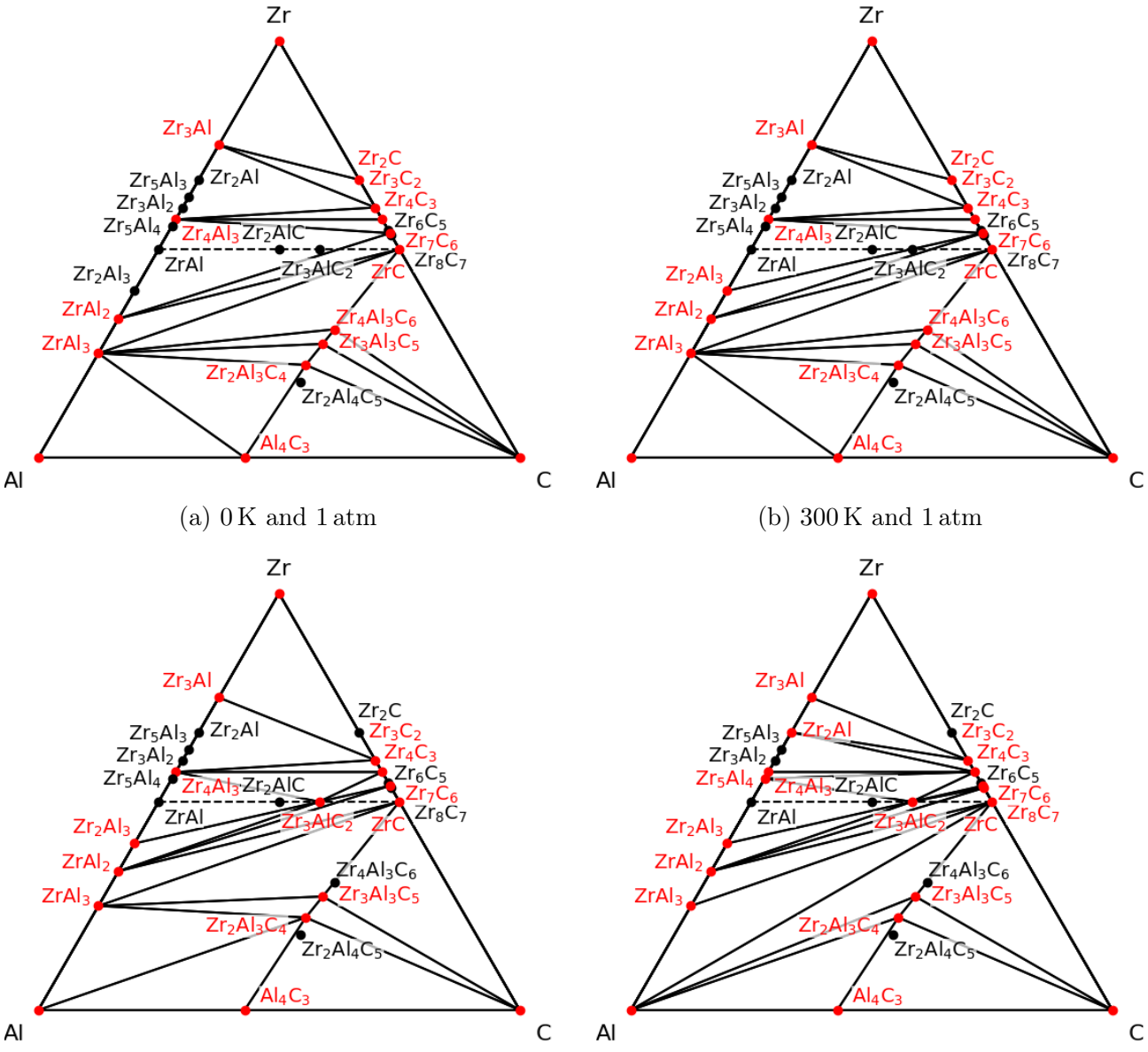

(a) 0 K and 1 atm

(b) 300 K and 1 atm

(c) 800 K and 1 atm

(d) 1800 K and 1 atm

Figure 4.6: Zr-Al-C phase diagrams at different temperatures. The red and black points are located on and above the convex hull respectively. The MAX phases in the system are shown along the dashed line.

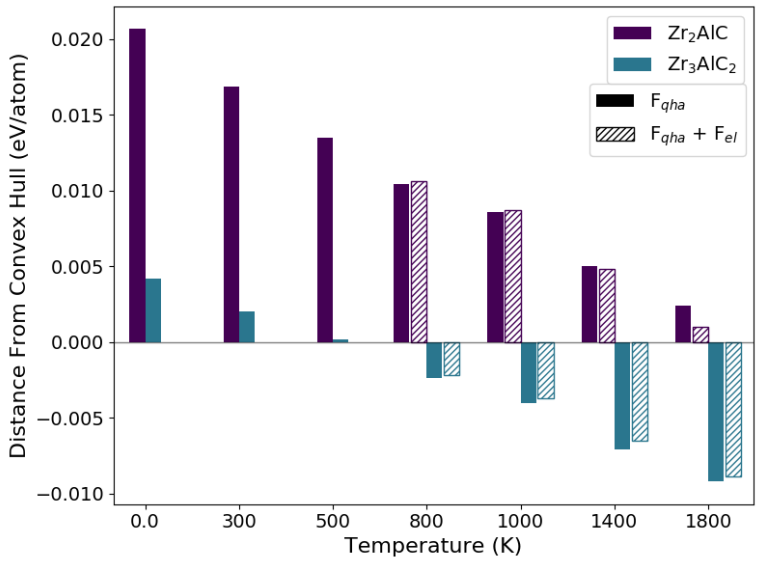

Figure 4.7: Distances in energy from the convex hull against temperature for the Zr_2AlC and Zr_3AlC phases. The electronic free energy contribution to the distance from the hull is shown from 800 K.

energy, F_{el}, to the distance from the hull for the two MAX phases is also shown for temperatures above 500 K. For temperatures below 500 K the contribution of F_{el} was found to be less than 2–3 meV/atom for the two MAX phases and their most competing phases, which is within the accuracy of the current calculations. The contributions of F_{el} to the the distances from the convex hull are relatively small and not monotonic with temperature. They don't affect the stability of either MAX phase. This is helped by some cancellation between the contributions of the F_{el} to the MAX phases and to their competing phases.

Due to the hexagonal structure of the MAX phases the error that is introduced by the constraint of fixed c/a has been estimated for different temperatures. This estimate is based on the Zr_2AlC phase whose free energy was expressed in terms of the two independent strains ϵ_1 and ϵ_3 and the temperature. The effect on the formation energies was < 1 meV/atom, which is less than the uncertainty introduced by the XC functional.

4.2.4 Comparison with the Ti-Al-C system

In Fig. 4.8 the convex hulls CH0 and CH(300) are shown for the Ti-Al-C system. These convex hulls are identical except for the status of the carbides, of which only Ti_2C is unstable at 300 K.

This convex hull remains the same at higher temperatures.

The predicted stable Ti-Al intermetallics are the five synthesised ones, Ti_3Al, TiAl, Ti_3Al_5, $TiAl_2$, and $TiAl_3$, in agreement with the Ti-Al phase diagram. The rest, Ti_2Al_3, Ti_4Al_3, Ti_5Al_4 and Ti_3Al_2, whose synthesis hasn't been reported yet and whose structures we included based on corresponding Zr-Al ones, are predicted unstable for both CH0 and CH(T) at standard conditions. This is in agreement with previous 0 K DFT energy calculations by Ghosh *et al.* [24] apart from Ti_4Al_3, which they predicted stable, suggesting a possible transformation into TiAl ($tP4$) and Ti_3Al ($hP8$) at low temperatures.

To better visualise the thermodynamic stability of the MAX phases, cross-sections of the convex hull between the end members ZrAl and ZrC for the Zr-based MAX phases and TiAl and TiC for the Ti-based MAX phases are plotted together at different temperatures in Fig. 4.9. On this diagram the Ti-based MAX phases clearly show their greater stability. Note that for this comparison we have added a calculation of the hypothetical Zr_4AlC_3 MAX phase, to check that the trend with $n > 2$ is similar to that observed in the $Ti_{n+1}AlC_n$ MAX phases, to be discussed below. We also note that calculations at 1800 K are expected to be less accurate, since full anharmonicity is not included. For the Zr-based MAX phases there is a tendency to higher stability as n increases, whereas the opposite trend is observed for the Ti-based phases, with Ti_2AlC and Ti_4AlC_3 appearing the most and least stable respectively. For the Ti-based MAX phases this tendency is also in agreement with a previous study, where Ti_2AlC was reported more stable than Ti_3AlC_2 [33], and is further indicated by the fact that the 211 phase was synthesised before 312. The effect of temperature on stability is also shown in Fig. 4.9. The Zr_2AlC phase approaches the convex hull as temperature increases as was also shown in Fig. 4.7, whereas in the Ti-based system there are no significant differences since the phases Ti_2AlC and Ti_3AlC_2 remain stable and Ti_4AlC_3 remains just above the hull. In the case of Ti_4AlC_3 the distance above the hull was about 0.5 meV/atom, a value smaller than the uncertainty of these calculations. In general we found that the vibrational free energy contribution affects stability in the Zr-Al-C system more than in the Ti-Al-C system, especially for the MAX phases. In fact, for the Ti-based MAX phases there is no change in stability and distance from the hull as a function of temperature.

A theoretical study by Dahlqvist *et al.* [43] calculated the formation energies of the three MAX phases, Ti_2AlC, Ti_3AlC_2 and Ti_4AlC_3, with respect to their decomposition into their closest competing phases. These formation energies are equivalent to the distance from the hull as defined in this study. For Ti_4AlC_3, in [43] the energy of formation with respect to its most competing phases, Ti_3AlC_2 and TiC, is considered zero, as it is within the error margin of their calculations, which is also the case with our study. Based on Fig. 4.8 where the Ti-Al-C CH0 is shown, the Ti_2AlC phase's distance from the hull is -29 meV/atom with most competitive phases TiAl and Ti_3AlC_2, whereas, for Ti_3AlC_2 the most competitive phases are Ti_2AlC and Ti_4AlC_3 with a smaller distance from the hull of -13 meV/atom. This description is in agreement with Dahlqvist *et al.*, with the same most competitive phases reported for each MAX phase, and energies of formation with respect to their competing phases being -27 and -12 meV/atom for 211 and 312 respectively. A different study by Keast *et al.* [161] also studied the thermodynamic stability of the three MAX phases in the Ti-Al-C system by comparing their formation energy against some considered competing phases in the system, namely TiAl, $TiAl_3$, TiC, Ti_3AlC and Al_4C_3. For Ti_2AlC, the competing phases considered were either TiAl and TiC or Ti_3AlC, $TiAl_3$ and TiC, resulting in formation energies of -135 and -91 meV/atom respectively. Neither of these reactions, however, involve the most competing phases for Ti_2AlC as identified by Dahlqvist *et al.* [43] or our study via convex hull construction. For the 312 and 413 MAX phases both Keast *et al.* [161] and our study agree on the most competing phases, with their study giving formation energies of -21 and 5 meV/atom respectively, with the latter formation energy also agreeing with the negligible distance from the hull mentioned earlier for the 413 phase.

Another study by Thore *et al.* [162], examined the effect of temperature on the stability of the Ti-Al-C system by considering the electronic free energy and including the vibrational energy within the quasiharmonic approximation. In agreement with our findings, their study showed that the quasiharmonic free energy did not affect the MAX phase stability trends. From 0 to 2000 K the most competing phases for the 3 MAX phases remained unchanged and the formation energy of Ti_4AlC_3 with respect to its most competing phases remained close to zero within their calculation uncertainty.

In agreement with these previous calculations, our formation energy per atom of the MAX phases with respect to MA and MX, as illustrated by Fig. 4.9, shows that for $n \geq 2$ the convex hulls are practically linear in the composition variable. This can be explained as follows from the description of a MAX phase as a multilayer structure of MA monolayers sandwiched between slabs of MX. The mole fraction x_{MA} of MA on this line is $1/(n+1)$, so we can write the total energy per atom of a mole of MAX phase in terms of the energy of pure MX and MA as:

$$E_n = \frac{n}{2n+2}E_{\mathrm{MX}} + \frac{1}{2n+2}E_{\mathrm{MA}} + \frac{1}{2n+2}\gamma_n \tag{4.3}$$

This point of view introduces an excess energy γ_n associated with the interfaces that separate each stoichiometric slab of MX from a thin layer of MA, the 'A' being a monotonic layer. With increasing n, γ_n should tend to a negative constant, as the mutual interaction of the single-atom A-layers vanishes. Taking the first two terms on the right-hand side of (4.3) over to the left of this equation, it becomes an expression for the formation energy per atom of the MAX phase with respect to these binaries, which we can write as:

$$E_{\mathrm{f}} = x_{\mathrm{MA}}\gamma_n/2 \tag{4.4}$$

Hence the linear behaviour in x_{MA} that we see in the calculations shows us that γ_n is already nearly constant for $n \geq 2$. The $n = 3$ and higher-order MAX phases can only be very marginally more stable than $n = 2$, by an amount too small to calculate reliably with the available methods.

The assumption of a constant value for the excess interfacial free energy γ_n would allow the rapid calculation of enthalpy and energy of other MAX-like phases, e.g. those with a mixture of thicknesses of the MX slabs. This could be further simplified to parameterise a model of the Ising type, such as the axial next-nearest-neighbour Ising (ANNNI) model, which is familiar for modelling the energy of different stacking sequences in close-packed metals and alloys. An ANNNI model was fitted to the total energy of some other MAX phases, including X = N besides carbon, by Ouisse and Chaussende [163], who observed the linear behaviour of energy with n that it predicts is a general feature of these structures. Since we completed the present

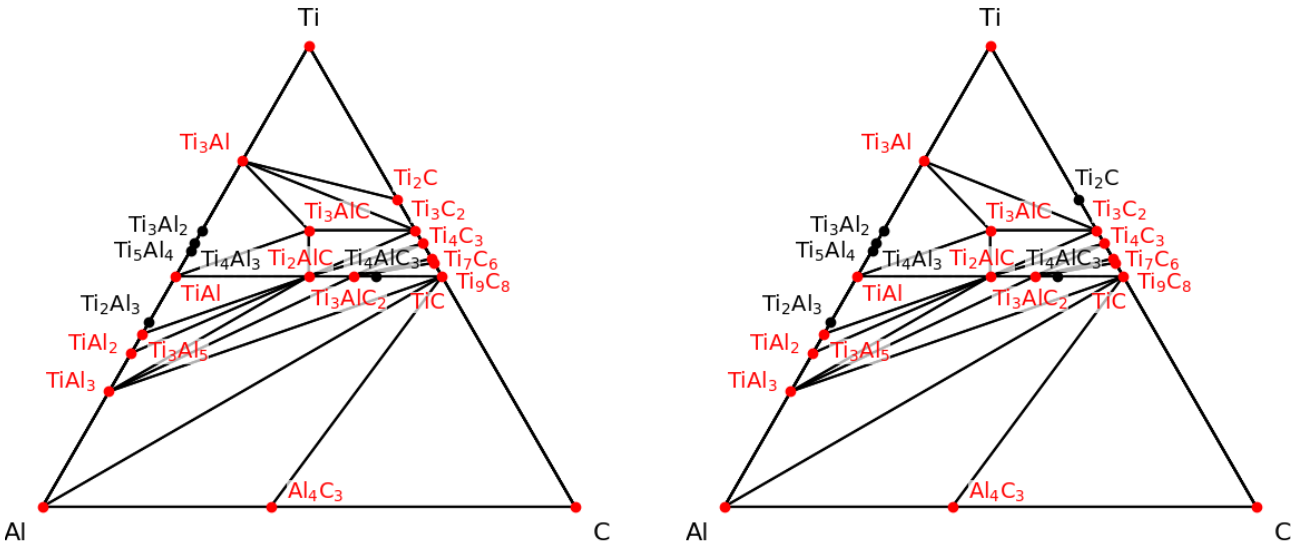

(a) 0 K (b) 300 K

Figure 4.8: Ti-Al-C phase diagrams (a) at 0 K and 0 atm without including the zero point energy and (b) at standard conditions. The red and black points are located on and above the convex hull respectively.

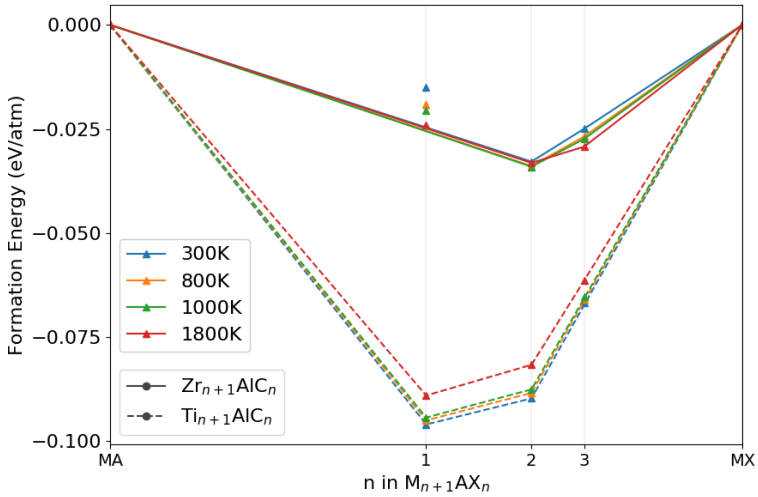

Figure 4.9: Convex-hull cross-section MA-MX for the Zr-Al-C and Ti-Al-C systems plotted for different temperatures.

calculations our attention was drawn to a paper by Lane *et al.*[42], who report on a MAX-like phase $Ti_5Al_2C_3$. These authors show convincingly that the $Ti_5Al_2C_3$ structure is composed of alternating layers of Ti_2AlC and Ti_3AlC_2, just as the stoichiometry suggests. Inspection of Fig. 3d in [42], scaling the energies per atom to estimate their calculated energies per formula unit, indicates that the energy of $Ti_5Al_2C_3$ is indeed very close to the combined energy of Ti_2AlC + Ti_3AlC_2, as our constant γ_n model, or the short-ranged ANNNI model of [163], would predict.

Table 4.2: Structures of phases considered in the Zr-Al-C system, the space group, the calculated lattice parameters, the formation energy ΔG_f with respect to the pure elements and the distance from the convex hull are presented for this study. ΔG_f values marked with * are at zero pressure without including vibrations, while unmarked values in this study include vibrations at 1 atm. These formation energies are compared with values from the literature where the calculations are at zero temperature (without the zero point effect). The values marked with † are from CALPHAD assessments. The values that correspond to the study by Alatalo *et al.* [10] are marked with ^{a} and ^{b} referring to LASTO and PWPP calculations respectively. The values that correspond to the study by Pisch [11] are marked by ^{c} and ^{d} referring to calculations using the SCAN functional at 298 K and the PBE functional at 0 K respectively.

Phase	Space group (#)	Lattice parameters (Å)	ΔG_f & Distance from the hull (eV/atom)	ΔF_f Literature	
			This study	Calculations	Experiment
Binary - Zr-Al					
$ZrAl_3$ [164]	I4/mmm (139)	$a = 3.9778$	−0.5001 −0.0921 (0 K)*	−0.509 [24]	−0.53 [21]
		$c = 17.1440$	−0.4912 −0.0909 (0 K)	-0.47^a [10]	−0.42 [22]
			−0.4785 −0.0882 (300 K)	-0.50^b [10]	−0.51 [23]
			−0.4435 −0.0812 (800 K)	−0.48 [165]	−0.502 [166]
			−0.3684 −0.0626 (1800 K)	−0.554 [167]	$-0.503^\dagger$ [20]
				−0.493 [168]	$-0.421^\dagger$ [169]
				−0.485 [170]	
$ZrAl_2$ [164]	$P6_3/mmc$ (194)	$a = 5.2459$	−0.5440 −0.0318 (0 K)*	−0.553 [24]	−0.58 [21]
		$c = 8.6818$	−0.5337 −0.0303 (0 K)	-0.56^a [10]	−0.47 [22]
			−0.5203 −0.0290 (300 K)	-0.57^b [10]	−0.56 [23]
			−0.4830 −0.0255 (800 K)	−0.535 [170]	−0.540 [166]
			−0.4077 −0.0218 (1800 K)		−0.532 [171]
					$-0.545^\dagger$ [20]
					$-0.475^\dagger$ [169]
Zr_2Al_3 [164]	Fdd2 (43)	$a = 9.5395$	−0.5219 +0.0018 (0 K)*	−0.535 [24]	−0.62 [21]
		$b = 13.8024$	−0.5132 +0.0011 (0 K)	-0.50^a [10]	−0.48 [22]
		$c = 5.5316$	−0.5016 −0.0005 (300 K)	-0.53^b [10]	−0.57 [23]
			−0.4688 −0.0037 (800 K)	−0.517 [170]	$-0.587^\dagger$ [20]
			−0.4000 −0.0059 (1800 K)		$-0.486^\dagger$ [169]
ZrAl [164]	Cmcm (63)	$a = 3.3121$	−0.4666 +0.0267 (0 K)*	−0.478 [24]	−0.74 [21]
		$b = 10.8395$	−0.4591 +0.0259 (0 K)	-0.45^a [10]	−0.46 [22]
		$c = 4.2639$	−0.4498 +0.0226 (300 K)	-0.46^b [10]	−0.55 [23]
			−0.4233 +0.0165 (800 K)	−0.49 [172]	$-0.674^\dagger$ [20]
			−0.3688 +0.0068 (1800 K)	−0.465 [170]	$-0.461^\dagger$ [169]

(TABLE 4.2 continued)

Phase	Space group (#)	Lattice parameters (Å)	ΔG_f & Distance from the hull (eV/atom)	ΔF_f Literature	
			This study	Calculations	Experiment
Zr_5Al_4 [164]	$P6_3/mcm$ (193)	$a = 8.3680$	−0.4243 +0.0520 (0 K)*	−0.435 [24]	−0.45 [22]
		$c = 5.7218$	−0.4189 +0.0499 (0 K)	−0.40[a] [10]	−0.54 [23]
			−0.4122 +0.0439 (300 K)	−0.42[b] [10]	−0.574† [20]
			−0.3938 +0.0300 (800 K)	−0.416 [170]	−0.425† [169]
			−0.3621 −0.0044 (1800 K)		
Zr_4Al_3 [164]	$P6/mmm$ (191)	$a = 5.3910$	−0.4715 −0.0475 (0 K)*	−0.493 [24]	−0.606† [20]
		$c = 5.3302$	−0.4642 −0.0467 (0 K)	−0.45[a] [10]	
			−0.4514 −0.0427 (300 K)	−0.47[b] [10]	
			−0.4192 −0.0339 (800 K)		
			−0.3534 −0.0011 (1800 K)		
Zr_3Al_2 [164]	$P4_2/mnm$ (136)	$a = 7.5853$	−0.3957 +0.0512 (0 K)*	−0.407 [24]	−0.51 [21]
		$c = 6.9056$	−0.3897 +0.0503 (0 K)	−0.40[b] [10]	−0.42 [22]
			−0.3831 +0.0446 (300 K)	−0.397 [170]	−0.51 [23]
			−0.3634 +0.0335 (800 K)		−0.572† [20]
			−0.3194 +0.0159 (1800 K)		−0.398† [169]
Zr_5Al_3 [164]	$I4/mcm$ (140)	$a = 10.9578$	−0.3733 +0.0521 (0 K)*	−0.390 [24]	−0.40 [22]
		$c = 5.3208$	−0.3691 +0.0498 (0 K)	−0.35[a] [10]	−0.50 [23]
			−0.3639 +0.0430 (300 K)	−0.37[b] [10]	−0.534† [20]
			−0.3489 +0.0284 (800 K)	−0.366 [170]	−0.376† [169]
			−0.3183 +0.0011 (1800 K)		
Zr_2Al [164]	$P6_3/mmc$ (194)	$a = 4.8552$	−0.3667 +0.0228 (0 K)*	−0.381 [24]	−0.58 [21]
		$c = 5.8486$	−0.3617 +0.0219 (0 K)	−0.35[a] [10]	−0.502† [20]
			−0.3540 +0.0183 (300 K)	−0.37[b] [10]	−0.346† [169]
			−0.3339 +0.0109 (800 K)	−0.355 [170]	
			−0.2930 −0.0032 (1800 K)		
Zr_3Al [164]	$Pm\text{-}3m$ (221)	$a = 4.3254$	−0.3177 −0.0427 (0 K)*	−0.322 [24]	−0.45 [21]
			−0.3131 −0.0419 (0 K)	−0.301 [170]	−0.375† [20]
			−0.3032 −0.0376 (300 K)	−0.30[a] [10]	−0.280† [169]
			−0.2796 −0.0292 (800 K)	−0.31[b] [10]	
			−0.2326 −0.0129 (1800 K)	−0.369 [167]	

(TABLE 4.2 continued)

Phase	Space group (#)	Lattice parameters (Å)	ΔG_f & Distance from the hull (eV/atom)	ΔF_f Literature	
			This study	Calculations	Experiment
Binary - Al-C					
Al_4C_3 [164]	R-3m (166)	$a = 3.3327$	−0.0945 −0.0945 (0 K)*	−0.102 [173]	−0.326† [174]
		$c = 24.9414$	−0.1087 −0.1087 (0 K)	−0.250[c] [11]	−0.286† [175]
			−0.1007 −0.1007 (300 K)	−0.092[d] [11]	−0.306† [176]
			−0.0836 −0.0836 (800 K)	−0.167 [177]	−0.307 [178]
			−0.0549 −0.0549 (1800 K)		−0.190 [179]
					−0.308 [180]
					−0.277 [181]
Binary - Zr-C					
Zr_2C [130]	Fd-3m (227)	$a = 9.3295$	−0.7024 −0.0087 (0 K)*	−0.62 [154]	
			−0.7204 −0.0067 (0 K)		
			−0.7069 −0.0043 (300 K)		
			−0.6870 +0.0017 (800 K)		
			−0.6578 +0.0150 (1800 K)		
Zr_3C_2 [130]	Fddd (70)	$a = 6.5875$	−0.8325 −0.0073 (0 K)*		
		$b = 9.3723$	−0.8564 −0.0074 (0 K)		
		$c = 19.7998$	−0.8431 −0.0075 (300 K)		
			−0.8264 −0.0079 (800 K)		
			−0.8074 −0.0052 (1800 K)		
Zr_4C_3 [130]	C2/c (15)	$a = 6.5964$	−0.8778 −0.0053 (0 K)*	−0.78 [154]	
		$b = 13.2348$	−0.9041 −0.0054 (0 K)		
		$c = 5.7285$	−0.8907 −0.0052 (300 K)		
			−0.8749 −0.0050 (800 K)		
			−0.8595 −0.0044 (1800 K)		
Zr_6C_5 [130]	C2/m (12)	$a = 5.7288$	−0.9062 +0.0039 (0 K)*	−0.80 [154]	
		$b = 9.9109$	−0.9349 +0.0035 (0 K)		
		$c = 6.6102$	−0.9217 +0.0034 (300 K)		
			−0.9078 +0.0028 (800 K)		
			−0.8979 +0.0014 (1800 K)		
Zr_7C_6 [130]	R-3 (148)	$a = 8.7349$	−0.9188 −0.0069 (0 K)*	−0.82 [154]	
		$c = 8.1232$	−0.9476 −0.0063 (0 K)		
			−0.9344 −0.0060 (300 K)		
			−0.9201 −0.0050 (800 K)		
			−0.9100 −0.0026 (1800 K)		

(TABLE 4.2 continued)

Phase	Space group (#)	Lattice parameters (Å)	ΔG_f & Distance from the hull (eV/atom)	ΔF_f Literature	
			This study	Calculations	Experiment
Zr_8C_7 [182]	$P4_332$ (212)	$a = 9.3539$	−0.9162 +0.0034 (0 K)*	−0.81 [154]	
			−0.9460 +0.0029 (0 K)		
			−0.9332 +0.0025 (300 K)		
			−0.9206 +0.0013 (800 K)		
			−0.9143 −0.0013 (1800 K)		
ZrC [130]	Fm-3m (225)	$a = 4.6686$	−0.9246 −0.0657 (0 K)*	−0.82 [154]	
			−0.9566 −0.0697 (0 K)		
			−0.9441 −0.0693 (300 K)		
			−0.9333 −0.0702 (800 K)		
			−0.9330 −0.0759 (1800 K)		
Ternary					
Zr_2AlC [164]	$P6_3/mmc$ (194)	$a = 3.2897$	−0.7072 +0.0231 (0 K)*	−0.68284 [45]	
		$c = 14.5060$	−0.7211 +0.0206 (0 K)	−0.700 [136]	
			−0.7118 +0.0168 (300 K)	−0.726 [76]	
			−0.6974 +0.0104 (800 K)		
			−0.6751 +0.0024 (1800 K)		
Zr_3AlC_2 [164]	$P6_3/mmc$ (194)	$a = 3.3067$	−0.8039 +0.0053 (0 K)*	−0.136[e] [7]	
		$c = 19.7747$	−0.8231 +0.0042 (0 K)		
			−0.8121 +0.0020 (300 K)		
			−0.7972 −0.0024 (800 K)		
			−0.7781 −0.0092 (1800 K)		
Zr_4AlC_3 [164]	$P6_3/mmc$ (194)	$a = 3.3119$	−0.8338 +0.0147 (0 K)*		
		$c = 25.0849$	−0.8562 +0.0138 (0 K)		
			−0.8455 +0.0113 (300 K)		
			−0.8326 +0.0056 (800 K)		
			−0.8212 −0.0043 (1800 K)		
$Zr_3Al_3C_5$ [164]	$P6_3/mmc$ (194)	$a = 3.3314$	−0.5935 −0.0030 (0 K)*	−0.556 [183]	
		$c = 27.4442$	−0.6157 −0.0029 (0 K)		
			−0.6052 −0.0030 (300 K)		
			−0.5879 −0.0036 (800 K)		
			−0.5642 −0.0057 (1800 K)		
$Zr_2Al_3C_4$ [164]	$P6_3mc$ (186)	$a = 3.3342$	−0.5122 −0.0117 (0 K)*		
		$c = 22.0921$	−0.5326 −0.0117 (0 K)		
			−0.5224 −0.0116 (300 K)		
			−0.5027 −0.0093 (800 K)		
			−0.4706 −0.0014 (1800 K)		

(TABLE 4.2 continued)

Phase	Space group (#)	Lattice parameters (Å)	ΔG_f & Distance from the hull (eV/atom)	ΔF_f Literature	
			This study	Calculations	Experiment
$Zr_4Al_3C_6$ [184]	$P6_3/mmc$ (194)	$a = 3.3291$	−0.6447 −0.0003 (0 K)*		
		$c = 32.7976$	−0.6685 −0.0003 (0 K)		
			−0.6575 −0.0002 (300 K)		
			−0.6407 +0.0003 (800 K)		
			−0.6194 +0.0015 (1800 K)		
$Zr_2Al_4C_5$ [164]	R3m (160)	$a = 3.3283$	−0.3959 +0.0382 (0 K)*		
		$c = 40.7833$	−0.4173 +0.0358 (0 K)		
			−0.4081 +0.0353 (300 K)		
			−0.3947 +0.0299 (800 K)		
			−0.3795 +0.0142 (1800 K)		
$Zr_3Al_4C_6$ [164]	R3m (160)	$a = 3.3232$	−0.4789 +0.0431 (0 K)*		
		$c = 48.8827$			
$ZrAlC_2$	$P6_3/mmc$ (194)	$a = 3.2385$	−0.2663 +0.2777 (0 K)*		
		$c = 29.7380$			

Table 4.3: Structures of phases considered in the Ti-Al-C system, the space group, the calculated lattice parameters, the formation energy ΔG_f with respect to the pure elements and the distance from the convex hull are given for this study. ΔG_f values marked with * are at zero pressure without including vibrations, while unmarked values in this study are given including vibrations at 1 atm. These formation energies are compared with values from the literature where the calculations are at zero temperature (without the zero point effect). The values marked with † are from CALPHAD assessments. The values that correspond to the study by Hong *et al.* [12] are marked with ^{a} and ^{b} referring to FLAPW and LMTO calculations respectively.

Phase	Space group (#)	Lattice parameters (Å)	ΔG_f & Distance from the hull (eV/atom)	ΔF_f Literature	
			This study	Calculations	Experiment
Binary - Ti-Al					
$TiAl_3$ [164]	I4/mmm (139)	$a = 3.8070$	−0.4045 −0.0785 (0 K)*	−0.403 [24]	−0.4619† [185]
		$c = 8.5375$	−0.3942 −0.0735 (0 K)	−0.42 [186, 187]	−0.406 [188]
			−0.3822 −0.0710 (300 K)	−0.42 [165]	−0.369 [189]
			−0.3470 −0.0632 (800 K)	−0.43 [190, 191]	−0.375† [192]
			−0.3177 −0.0566 (1200 K)	−0.41 [193, 194, 195]	−0.379 [196]
				−0.397 [173]	−0.379 [197]
				−0.396 [198]	
$TiAl_2$ [164]	Cmmm (65)	$a = 3.8931$	−0.4347 −0.0114 (0 K)*	−0.435 [24]	−0.4529† [185]
		$b = 12.0326$	−0.4276 −0.0145 (0 K)	−0.426 [198]	−0.385 [188]
		$c = 3.9637$	−0.4150 −0.0140 (300 K)		
			−0.3784 −0.0122 (800 K)		
			−0.3481 −0.0112 (1200 K)		
Ti_3Al_5 [164]	P4/mbm (127)	$a = 11.1764$	−0.4327 −0.0038 (0 K)*	−0.432 [24]	
			−0.4225 −0.0010 (0 K)		
		$c = 3.9844$	−0.4104 −0.0010 (300 K)		
			−0.3757 −0.0010 (800 K)		
			−0.3465 −0.0006 (1200 K)		
Ti_2Al_3 [164]	Fdd2 (43)	$a = 9.1883$	−0.3814 +0.0470 (0 K)*	−0.382 [24]	
		$b = 13.0683$	−0.3715 +0.0471 (0 K)		
		$c = 5.2440$	−0.3615 +0.0454 (300 K)		
			−0.3310 +0.0423 (800 K)		
			−0.3054 +0.0397 (1200 K)		

(TABLE 4.3 continued)

Phase	Space group (#)	Lattice parameters (Å)	ΔG_f & Distance from the hull (eV/atom)	ΔF_f Literature	
			This study	Calculations	Experiment
TiAl [164]	P4/mmm (123)	$a = 2.7905$	−0.4112 −0.0249 (0 K)*	−0.412 [24]	−0.4494† [185]
		$c = 4.0341$	−0.4029 −0.0260 (0 K)	−0.44 [190]	−0.364 [188]
			−0.3927 −0.0266 (300 K)	−0.42 [193, 199]	−0.377 [189]
			−0.3637 −0.0285 (800 K)	−0.41 [194]	−0.413† [192]
			−0.3394 −0.0301 (1200 K)	−0.40 [43]	−0.416 [196]
				−0.405 [173]	
				−0.39 [172]	
				−0.404 [198]	
				−0.401 [200]	
Ti_4Al_3 [164]	P6/mmm (191)	$a = 5.1211$	−0.3598 +0.0154 (0 K)*	−0.386 [24]	
		$c = 4.8810$	−0.3509 +0.0164 (0 K)		
			−0.3408 +0.0166 (300 K)		
			−0.3120 +0.0174 (800 K)		
			−0.2880 +0.0181 (1200 K)		
Ti_5Al_4 [164]	$P6_3/mcm$ (193)	$a = 7.8238$	−0.3393 +0.0439 (0 K)*	−0.332 [24]	
		$c = 5.3825$	−0.3319 +0.0433 (0 K)		
			−0.3248 +0.0404 (300 K)		
			−0.3037 +0.0333 (800 K)		
			−0.2868 +0.0267 (1200 K)		
Ti_3Al_2 [164]	$P4_2/mnm$ (136)	$a = 7.1615$	−0.2533 +0.1075 (0 K)*	−0.257 [24]	
		$c = 6.3876$	−0.2469 +0.1062 (0 K)		
			−0.2428 +0.1004 (300 K)		
			−0.2234 +0.0922 (800 K)		
			−0.2042 +0.0885 (1200 K)		
Ti_3Al [164]	$P6_3/mmc$ (194)	$a = 5.6812$	−0.2852 −0.0753 (0 K)*	−0.284 [24]	−0.2948† [185]
		$c = 4.6053$	−0.2783 −0.0736 (0 K)	−0.30 [190]	−0.260 [189]
			−0.2689 −0.0701 (300 K)	−0.28 [193, 194]	−0.285† [192]
			−0.2436 −0.0616 (800 K)	−0.28[a] [12]	−0.256 [196]
			−0.2227 −0.0530 (1200 K)	−0.29[b] [12]	
				−0.281 [173]	
				−0.279 [198, 200]	
				−0.295 [201]	
				−0.331 [202]	

(TABLE 4.3 continued)

Phase	Space group (#)	Lattice parameters (Å)	ΔG_f & Distance from the hull (eV/atom)	ΔF_f Literature	
			This study	Calculations	Experiment
Binary - Ti-C					
Ti_2C [131]	Fd-3m (227)	$a = 6.0436$	−0.7221 −0.0025 (0 K)*	−0.615 [173]	
			−0.7332 −0.0002 (0 K)	−0.656 [203]	
			−0.7230 +0.0010 (300 K)	−0.676 [204]	
			−0.7032 +0.0052 (800 K)	−0.720 [205]	
			−0.6897 +0.0091 (1200 K)	−0.60 [154]	
				−0.691 [206]	
Ti_3C_2 [131]	C2/m (12)	$a = 5.2645$	−0.8635 −0.0134 (0 K)*	−0.73 [154]	
		$b = 5.2580$	−0.8796 −0.0137 (0 K)		
		$c = 5.2440$	−0.8688 −0.0136 (300 K)		
			−0.8501 −0.0135 (800 K)		
			−0.8386 −0.0135 (1200 K)		
Ti_4C_3 [131]	C2/c (15)	$a = 5.2702$	−0.9049 −0.0068 (0 K)*	−0.70 [154]	
		$b = 5.2562$	−0.9227 −0.0068 (0 K)		
		$c = 6.7910$	−0.9119 −0.0068 (300 K)		
			−0.8937 −0.0066 (800 K)		
			−0.8831 −0.0063 (1200 K)		
Ti_7C_6 [131]	R-3 (148)	$a = 5.2623$	−0.9380 −0.0052 (0 K)*	−0.79 [154]	
			−0.9579 −0.0051 (0 K)		
			−0.9471 −0.0050 (300 K)		
			−0.9300 −0.0046 (800 K)		
			−0.9209 −0.0043 (1200 K)		
Ti_9C_8 [131]	R-3 (148)	$a = 5.2669$	−0.9404 −0.0059 (0 K)*		
		$c = 8.0370$	−0.9610 −0.0060 (0 K)		
			−0.9504 −0.0060 (300 K)		
			−0.9340 −0.0059 (800 K)		
			−0.9257 −0.0059 (1200 K)		
TiC [131]	Fm-3m (225)	$a = 4.2920$	−0.9230 −0.0348 (0 K)*	−0.780 [43]	
			−0.9458 −0.0382 (0 K)	−0.776 [173]	
			−0.9358 −0.0381 (300 K)	−0.76 [154]	
			−0.9219 −0.0397 (800 K)	−0.8473 [207]	
			−0.9163 −0.0420 (1200 K)	−0.849 [208]	
				−0.877 [206]	

(TABLE 4.3 continued)

Phase	Space group (#)	Lattice parameters (Å)	ΔG_f & Distance from the hull (eV/atom)	ΔF_f Literature	
			This study	Calculations	Experiment
Ternary					
Ti_2AlC [164]	$P6_3/mmc$ (194)	$a = 3.0357$	−0.7642 −0.0289 (0 K)*	−0.73 [43]	−0.692† [150]
		$c = 13.6224$	−0.7213 −0.0279 (0 K)	−0.68 [173]	
			−0.7602 −0.0287 (300 K)	−0.68168 [45]	
			−0.7378 −0.0287 (800 K)	−0.71 [209]	
			−0.7213 −0.0279 (1200 K)	−0.693 [136]	
Ti_3AlC_2 [164]	$P6_3/mmc$ (194)	$a = 3.0491$	−0.8434 −0.0134 (0 K)*	−0.74 [173]	−0.722† [150]
		$c = 18.4833$	−0.8547 −0.0132 (0 K)	−0.75 [43]	
			−0.8444 −0.0132 (300 K)	−0.138[e] [7]	
			−0.8242 −0.0128 (800 K)		
			−0.8105 −0.0123 (1200 K)		
Ti_4AlC_3 [164]	$P6_3/mmc$ (194)	$a = 3.0526$	−0.8628 +0.005 (0 K)*	−0.75 [173]	
		$c = 23.3616$	−0.8770 +0.0005 (0 K)	−0.76 [43]	
			−0.8668 +0.0005 (300 K)		
			−0.8482 +0.0005 (800 K)		
			−0.8366 +0.0003 (1200 K)		
Ti_3AlC [164]	Pm-3m (221)	$a = 4.1375$	−0.6440 −0.0132 (0 K)*	−0.57 [173]	−0.574† [150]
			−0.6495 −0.0148 (0 K)		
			−0.6432 −0.0185 (300 K)		
			−0.6294 −0.0274 (800 K)		
			−0.6195 −0.0343 (1200 K)		

[e] It looks as if perhaps the units were actually eV/atom rather than eV/f.u. in the paper cited [7]

4.2.5 Geometrical distortion effect

As was shown in the previous section and illustrated in Fig. 4.9, the Ti-based MAX phases are more thermodynamically stable than the Zr-based ones. This is in accordance with the earlier successful synthesis with higher achieved phase purity of Ti-based MAX phases compared to Zr-based ones. Recent studies [3, 41] regarding stability and phase purity of 211 MAX phase

solid solutions have nevertheless reported up to 98% phase purity. Such high levels of purity were achieved via the synthesis of double solid solutions, namely (Zr, Ti)$_2$(Al, Sn)C [3] and (Zr, Nb)$_2$(Al, Sn)C [41]. In these studies a link was established between the geometric distortion and the level of phase purity, with the distortion involving the octahedra around C atoms and the trigonal prisms around Al atoms in the MAX phase's carbide and aluminide layers. Quantitative measures of these distortions were defined and their values were calculated based on experimentally defined lattice parameters for the whole considered range of solutions between the end-member MAX phases. The degree of distortion for the various solutions within the limits of the end-member MAX phases was found to display a linear trend.

Based on the findings of these studies, this section discusses calculations that try to correlate the lower stability of the Zr-based phases with the level of geometrical distortion. In particular, the stability trend between Zr_2AlC and Ti_2AlC is studied in terms of the geometrical distortion of the carbon centered octahedra [CM_6] that make up the carbide slabs of the MAX phases for the two systems. We have included this subsection for completion, although in the end no clear correlation has emerged from our calculations. Octahedral distortion is defined with respect to the ideal octahedra in the carbide bulk structures as described in Fig. 4.10. The distortion of the octahedra in the MAX phases was additionally compared to the distortion of the octahedra in a carbide slab geometry. A "carbide slab" refers here to a sequence of atomic layers M-X-M in the 211 structure, or M-X-M-X-M in the 312 structure. There are two such slabs in the unit cell of either MAX phase. In this section, carbide slab calculations refer to calculations for 211 MAX phases where just a single carbide slab is retained from their unit cell, removing all other atoms.

The octahedral geometry is described with respect to the two variables h and d, which denote the distance between the Zr (or Ti) layers and the bond length between Zr-Zr (or Ti-Ti) respectively. The ideal h and d are expressed in the carbides as $h_{\text{ideal}} = a/\sqrt{3}$ and $d_{\text{ideal}} = a/\sqrt{2}$ respectively. Therefore, the ideal ratio $r_{\text{ideal}} = d_{\text{ideal}}/h_{\text{ideal}}$ equals $\sqrt{3/2}$. The octahedal distortion n can then be defined as:

$$n = \frac{\frac{d}{h} - r_{\text{ideal}}}{r_{\text{ideal}}} \tag{4.5}$$

The volume of the octahedron is given as $V = \frac{1}{\sqrt{3}} h d^2$ and for the carbide case is $V_{\text{ideal}} = \frac{1}{3} a^3$. The volume difference of an octahedron with respect to the ideal one is given as:

$$\frac{\delta V}{V} = \frac{V - V_{\text{ideal}}}{V_{\text{ideal}}} = \frac{h d^2 - h_{\text{ideal}} d_{\text{ideal}}^2}{h_{\text{ideal}} d_{\text{ideal}}^2} \tag{4.6}$$

In order to relate the equilibrium d and h values in the MAX phase, carbide slab and bulk carbide structures, as shown in Fig. 4.10, sets of strains are defined. Strain sets (ϵ_d(s), ϵ_h(s)), and (ϵ_d(b), ϵ_h(b)) correspond to the strains required to get from the slab and carbide to the MAX phase respectively, while (ϵ_d(bs), ϵ_h(bs)) corresponds to the strains required to get from the carbide to the slab structure. These strains are expressed as:

$$(\epsilon_d(\text{b}), \epsilon_h(\text{b})) = \left(\frac{d_{\text{M}} - d_{\text{b}}}{d_{\text{b}}}, \frac{h_{\text{M}} - h_{\text{b}}}{h_{\text{b}}} \right) \tag{4.7a}$$

$$(\epsilon_d(\text{s}), \epsilon_h(\text{s})) = \left(\frac{d_{\text{M}} - d_{\text{s}}}{d_{\text{s}}}, \frac{h_{\text{M}} - h_{\text{s}}}{h_{\text{s}}} \right) \tag{4.7b}$$

$$(\epsilon_d(\text{bs}), \epsilon_h(\text{bs})) = \left(\frac{d_{\text{s}} - d_{\text{b}}}{d_{\text{b}}}, \frac{h_{\text{s}} - h_{\text{b}}}{h_{\text{b}}} \right) \tag{4.7c}$$

where (d_{M}, h_{M}), (d_{s}, h_{s}) and (d_{b}, h_{b}) are the equilibrium values for the octahedra in the MAX phase, slab and bulk structures respectively.

	d_{M}, h_{M} (Å)	d_{b}, h_{b} (Å)	d_{s},h_{s} (Å)	ϵ_d(b), ϵ_h(b)	ϵ_d(s), ϵ_h(s)	ϵ_d(bs), ϵ_h(bs)
Zr	(3.290, 2.506)	(3.301, 2.695)	(3.231, 2.526)	(−0.0035, −0.0701)	(0.0180, −0.0078)	(−0.0211, −0.0627)
Ti	(3.036, 2.271)	(3.035, 2.478)	(2.999, 2.293)	(0.0003, −0.0836)	(0.0121, −0.0097)	(−0.0117, −0.0745)

Table 4.4: Equilibrium d and h values of the octahedra in the carbides, MAX phases and carbide slab and their strain relations.

	n(M)	n(s)	$\delta V/V$(M)	$\delta V/V$(s)
Zr	0.072	0.044	−0.077	−0.102
Ti	0.092	0.068	−0.083	−0.096

Table 4.5: The distortion n and volume change $\delta V/V$ for the slab (n(s), $\delta V/V$(s)) and MAX phase (n(M), $\delta V/V$(M)) structures with respect to the ideal r_{ideal} ratio of the bulk structure.

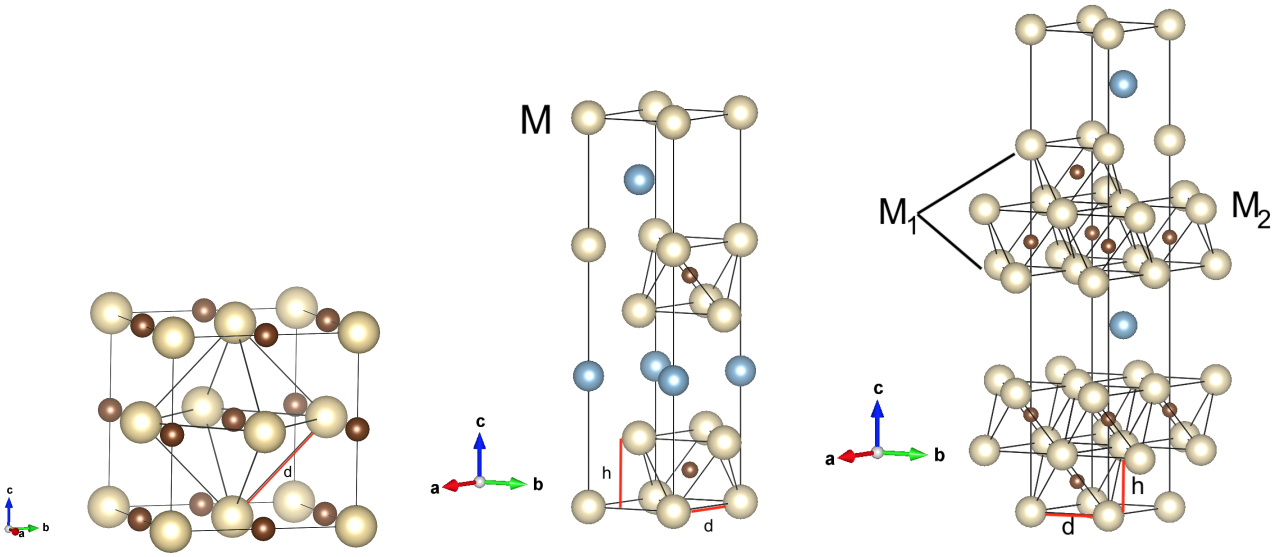

(a) The ideal octahedron in the carbide structure (MC).

(b) The distorted octahedra in M_2AlC.

(c) The distorted octahedra in M_3AlC_2.

Figure 4.10: The C centered octahedra, described by d and h values in the MC, M_2AlC and M_3AlC_2 structures, where M is either Zr or Ti. M_1 corresponds to the outer layer of the MC slab located next to the Al layer in the 312 MAX phase. M_2 corresponds to the M atoms in the MC slab of the 312 MAX phase.

In Table 4.4 the equilibrium d and h values for the three geometries are shown, both are smaller for the Ti-based case. The strains applied on d for the three different cases are larger in the Zr case than the corresponding Ti ones. Strain ϵ_d(s) is the largest of the strains applied to d for the Ti system, whereas for Zr, ϵ_d(bs) is largest. The smallest strain on d for both systems is ϵ_d(b). In particular in the case of Ti, this strain can be considered negligible. Unlike for d, the strains on the h value in the three examined cases are larger in the Ti system compared to the corresponding Zr ones. The largest h strain required for both systems is ϵ_h(b) from the bulk to the MAX phase geometry, and the smallest is ϵ_h(s) from the slab to the MAX phase geometry.

Table 4.5 shows the octahedral distortion and the volume change for the slab and MAX phase geometries with respect to the ideal octahedron as described by Equations 4.5 and 4.6. The distortion for both of these geometries was found to be larger for the Ti case. The change in volume for the MAX phase was found larger for the Ti case, whereas for the slab geometry it was found larger for the Zr case.

The described distortions and strains were next examined with respect to their associated energies. As a first step the carbide slab was relaxed with respect to the internal coordinates

for different d values for the Zr and Ti systems. Fig. 4.11 displays the equilibrium d values for the bulk carbides and the MAX phases as well as for each of the slab cases. For Ti, d_{b} and d_{M} are almost the same with the two corresponding vertical lines almost overlapping each other, whereas for the Zr case they are further apart. This is also described by the strains on d, $\epsilon_d(\mathrm{b})$ being -0.0035 and 0.0003 for Zr and Ti respectively. Additionally, d_{b} is closer to d_{s} for Ti, with $\epsilon_d(\mathrm{bs})$ being -0.0117, than for Zr where $\epsilon_d(\mathrm{bs})$ is almost two times larger. This larger difference for Zr is associated with an energy of 0.016 eV/octahedron. Further to that the energy that is required to distort the equillibrium octahedra in the ZrC slab to the carbide octahedra, having d_{ideal} and h_{ideal}, without relaxing the internal coordinates of the slab geometry, is 0.258 eV/octahedron (Fig. 4.12). This is comparable to the energy difference between the free energies of formation of Ti_2AlC and Zr_2AlC with respect to their binaries, which is around 0.324 eV/octahedron, as shown in Fig. 4.9.

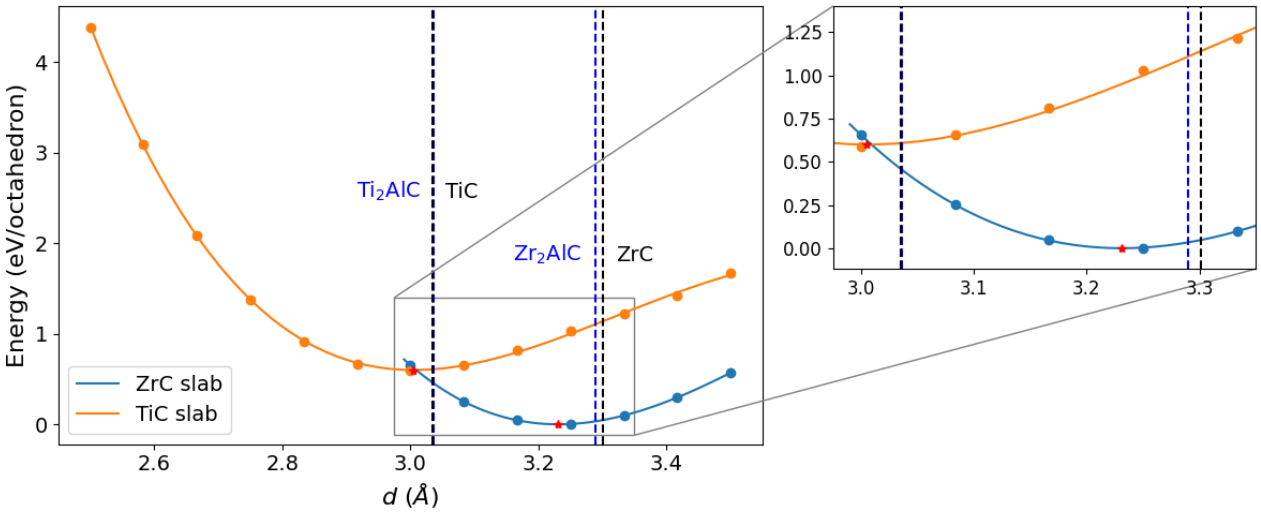

Figure 4.11: Energy as a function of d for ZrC and TiC slab structures. For each d configuration the internal coordinates have been relaxed. The dashed black and blue vertical lines correspond to the d equilibrium values of the carbide and the MAX phase for the two systems. The equilibrium d_{s} values for the slabs are denoted with the red stars.

In Fig. 4.13, the total energy of M_2AlC, where M is either Zr or Ti, is shown against the mixing parameter λ, corresponding to the different octahedral distortions between the ideal octahedra and the equilibrium ones in M_2AlC. For the energy evaluation of these different distortions no degree of lattice relaxation was involved. Fig. 4.13 shows that the differences in energy for both distortions of the octahedra are quite small. The d distortions are about 10 times smaller than

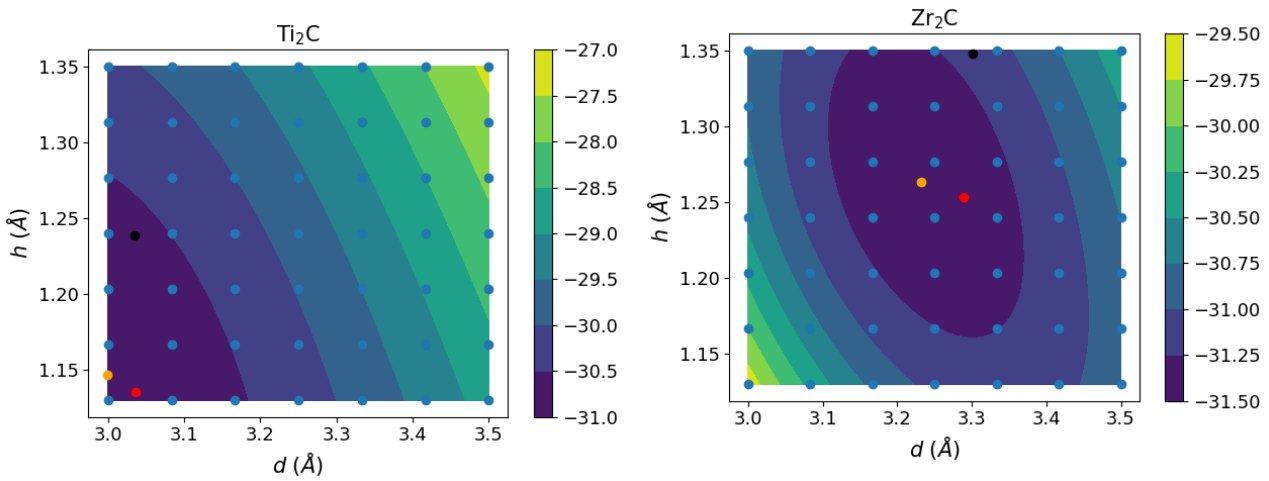

(a) (b)

Figure 4.12: Contour energy plots for the Zr_2C and Ti_2C carbide slabs as a function of h and d. The orange points correspond to the equillibrium values (h, d) for the slab geometries. The red and black points correspond to the MAX phase and bulk carbide structures respectively. The energy is given in eV/octahedron.

those of h. In the case of the d distortions, the change for Ti_2AlC is almost negligible, while for Zr_2AlC the change in total energy is about 0.40 meV/atom at the level of ZrC. For the h distortions, the differences in energy are larger and comparable to each other for the two MAX phases, with Ti_2AlC having a larger change than Zr_2AlC of about 0.01 eV/atom at the level of their respective carbides.

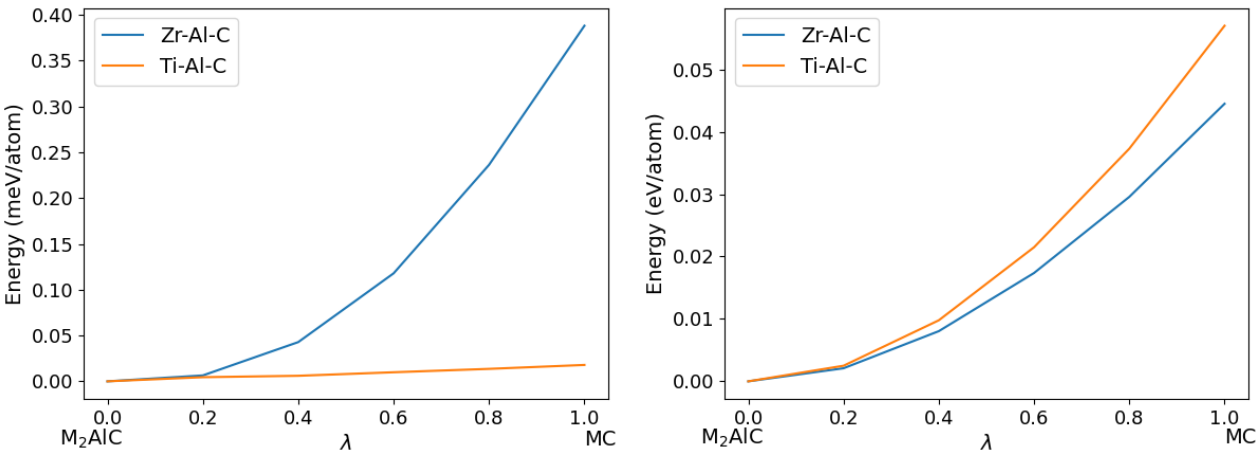

(a) Octahedral distortions along d. (b) Octahedral distortions along h.

Figure 4.13: Distortions of d and h values the octahedra in the Zr_2AlC and Ti_2AlC phases.

Additionally, the stability was examined against the distortion of the Al layers in the 211 MAX

phases. In Fig. 4.14a the total energy with respect to the different distortions of the Al layer are shown. The energy change associated with the difference between Zr_2AlC and Ti_2AlC is about 0.4 eV/atom and the lattice distances from the equilibrium a of the Al layer indicate that the latter phase has higher stability. The energy difference associated with the Al layer distortion is larger than the one corresponding to the C centered octahedral distortion.

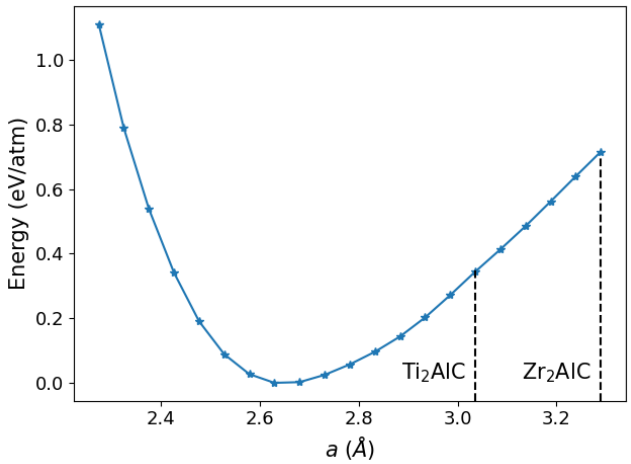

(a) Energy with respect to the different distortions of the a lattice of Al layers.

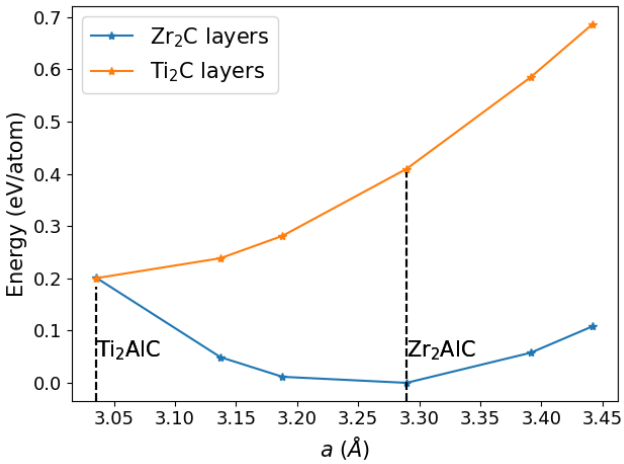

(b) Energy with respect to the different distortions of the a lattice of M_2C layers.

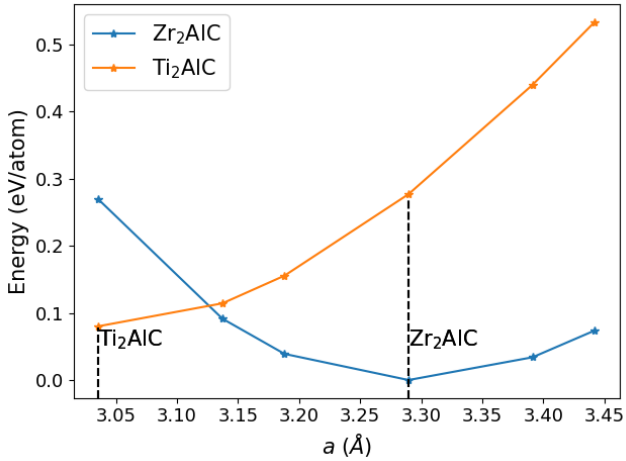

(c) Energy with respect to the different distortions of the a lattice of the MAX phases M_2AlC.

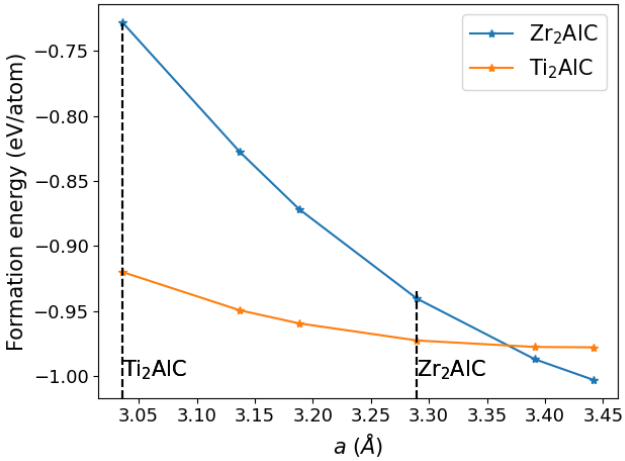

(d) MAX phases formation energy with respect to the Al layers and the MC layers against the different a lattice distortions.

Figure 4.14: Energy change with respect to the a lattice distortion.

Further to that, the binding energy between the Al and carbide layers is examined with respect to the a lattice distortions of the 211 MAX phases, Fig. 4.14d. The formation energy is given by:

$$E_f = E_{M_2AlC} - E_{M_2C} - E_{Al} \tag{4.8}$$

where E_{M_2AlC}, E_M and E_{Al} are the total energies of the MAX phase structure, the MAX phase structure without the Al atoms and the hexagonal Al layers respectively. In this figure, the formation energy for Ti_2AlC is lower than the corresponding Zr_2AlC phase for most of the a lattices, as well as having less energy change. However, by comparing the Ti_2AlC and Zr_2AlC phases at their equilibrium a lattices, Ti_2AlC is slightly above Zr_2AlC by 0.02 eV/atom. Therefore we can see that the formation energies of the MAX phases are about the same, with the Al layer being stretched to the appropriate lattice parameters, which are not metallic Al, though in the Ti case the Al layer is less stretched. The carbides do not appear stretched in the MAX phase structures.

The two Figures, 4.14b and 4.14c, show how the energies change with respect to the a lattice distortion for the carbide layers and the MAX phases structures respectively. The carbide layers in the Zr_2AlC phase have lower energies than the ones in the case of Ti. Similarly for the total structural distortion, the Zr_2AlC total energy is shown lower than that of Ti_2AlC at their equilibrium structures.

Up to this point, our geometric distortion analysis has focused on the octahedral distortions in the MAX phases compared to the ideal carbide lattice and the slab geometry, as well as on the Al lattice distortions and the energy associated with those. For completion of our analysis however, it is also worth calculating octahedral and prismatic distortions for the two MAX phases of interest as these distortions are defined in previous research [3, 41] and comparing them with values from the literature.

The expressions used in the two studies [3, 41] and in our calculations presented in Table 4.6 for the octahedral distortion, O_d, and the trigonal prism distortion, P_d, are given by:

$$O_d = \frac{\sqrt{3}}{2\sqrt{4Z_M^2(c/a)^2 + \frac{1}{12}}} \tag{4.9a}$$

$$P_d = \frac{1}{\sqrt{\frac{1}{3} + (\frac{1}{4} - Z_M)^2(c/a)^2}} \tag{4.9b}$$

where a, c, and Z_M correspond to the two lattice constants and the fractional z-coordinate of

the M-atom which determines the distance between the M atoms and the C layer atoms. For the ideal octahedral and trigonal prism, O_d and P_d equal 1, as does the ratio between them, O_d/P_d.

As was mentioned at the start of this section, in the studies by Lapauw *et al.* [3] and Tunca *et al.* [41] a link has been made between geometrical distortion and phase purity in terms of double partial substitutions in the M and A sites of the 211 MAX phases. An indicator of phase purity was noted in [41] to be the ratio of the two distortions, where a maximum purity was achieved with the ratio approaching 1 when both Ti and Si were alloyed in the form of the $(Zr,Ti)_2(Al,Sn)C$ MAX phase. In these studies however, particular attention was also paid to the prismatic distortion M_6A which could be interpreted as the level of the steric mismatch due to the difference between the size of the M and A atoms, with its value approaching 1 when their sizes are the same. In particular in [41], Zr_2AlC had the highest prismatic distortion of the study's considered phases. In the study by Lapauw *et al.* [3] as well, the prismatic distortion was identified as the main geometrical indicator for the high phase purity achieved with the $(Zr, Nb)_2AlC$ and $Zr_2(Al, Sn)C$ double solution. Although these two geometric distortions were used as stability criteria to mainly explain trends in solutions of MAX phases, for example to investigate how these distortion parameters change with the solute content in their M and A sites, our calculations involve only two of the end members of these double solutions, Zr_2AlC and Ti_2AlC.

In Table 4.6, our calculated values for O_d and P_d are presented alongside those by other theoretical and experimental studies, most of which were included in the study by Lapauw *et al.* [3] where the lattice parameters used were based on experimental measurements [4] and [25]. Based on our calculated lattice parameters the octahedral distortion, O_d, is predicted larger in Ti_2AlC by 1.6% compared to that of Zr_2AlC, whereas the prismatic distortion, P_d, is predicted smaller in Ti_2AlC by 2.2%, with both trends being in agreement with the study by Lapauw *et al.* [41]. O_d/P_d on the other hand, diverges from the ideal ratio in our calculations by 2.05% for Ti_2AlC compared to 1.78% for Zr_2AlC, which is the opposite trend to that noted in the experimental values and in the study by Lapauw *et al.* [41]. Compared with experiment, the values based on our calculations show the largest differences in the case of Ti_2AlC, while compared to other theoretical studies, our results show better agreement with some differences remaining for P_d, the

largest of which being less than 1% with the study by Tan *et al.* [210]. For O_d in Ti_2AlC our calculated values are all between 1.080–1.081 in contrast to the experimental value at 1.0707. For both distortions in Zr_2AlC, our calculations show less than 1% difference with the experimental values measured by Lapauw *et al.* [4].

Phase	O_d	P_d	O_d/P_d	$\lvert(O_d/P_d)-1\rvert$%	
Ti_2AlC	1.0801	1.0584	1.0205	2.05	calc. (this work)
	1.0809	1.0608	1.0189	1.89	Hug *et al.* (calc.) [25]
	1.0805	1.0630	1.0165	1.65	Tan *et al.*(calc.) [210]
	1.0707	1.0714	0.9993	0.07	Hug *et al.* (exp.) [25]
Zr_2AlC	1.0629	1.0822	0.9822	1.78	calc. (this work)
	1.0607	1.0889	0.9741	2.59	Lapauw *et al.* (exp.) [4]

Table 4.6: The distortion of the octahedral around the C atoms, the trigonal prism around the Al atoms and their ratio O_d, P_d and O_d/P_d are shown. These values for other theoretical and experimental studies are also shown.

4.3 Conclusions

A detailed computational study of the thermodynamic stability of the MAX phases in the Zr-Al-C system was made and was compared with the Ti-Al-C system, in which MAX phases were synthesised much earlier. For this purpose we have made free energy calculations at the level of density functional theory within the quasiharmonic approximation and constructed isothermal sections of the ternary phase diagrams in which the MAX phases are competing with known binary and ternary phases.

The concluding assessment is that at 0 K, neglecting zero-point energy, the PBEsol functional (the default choice) predicts that both observed phases, $Zr_{n+1}AlC_n$ for $n = 1$ and $n = 2$, are marginally unstable with respect to decomposition into carbides and aluminides of Zr, lying 23 meV/atom and 4 meV/atom respectively above the convex hull. Results with other functionals are similar, with all of them predicting the two MAX phases above the hull. The

inclusion of vibrational contributions has the effect of moving both MAX phases down in relative free energy. Zr_3AlC_2 is thereby predicted to be stable by $\sim 500\,\mathrm{K}$, but Zr_2AlC never quite becomes stable, although its distance above the convex hull is reduced to $< 5\,\mathrm{meV/atom}$.

A comparison with the analogous phases in Ti-Al-C shows that both MAX phases in that system are much more stable at all temperatures, in accordance with their earlier discovery. This is consistent with the practical experience that MAX phases in the Zr-Al-C system are more difficult to synthesise and that they can be obtained in a more phase-pure form when substitutional impurities such as Si are incorporated. A quantitative explanation of this effect remains as future research. Meanwhile, we predict there is no reason to expect that a pure $Zr_{n+1}AlC_n$ MAX phase can be synthesised. Despite this prediction, it is recognised that the two Zr-based MAX phases have been synthesised with over 60% phase purity, however our results indicate that these phases are actually metastable and perhaps appear for kinetic reasons. The synthesis for both phases took place at high temperature, specifically at 1500 °C for Zr_3AlC_2 and at a very narrow temperature window 1475–1575 °C for Zr_2AlC [4, 5]. As mentioned, in our predictions MAX phase stability shows a tendency to increase as temperature increases, therefore it could be possible that these phases are more stable at higher temperatures and their structure is kinetically stabilised if they are cooled down without the time to decompose. In that case it would be interesting to anneal them at an intermediate temperature between room temperature and their synthesis temperature window to investigate whether they remain stable or whether they decompose into intermetallics and carbides as the calculations predict. Another possible explanation for the experimental observation of these Zr-based MAX phases could be their stabilisation due to the hydrogen used in their synthesis procedure, since such a stabilisation mechanism has been shown to increase the percentage of phase purity and to facilitate the synthesis for other Ti-based MAX phases [211]. Incorporation of hydrogen in the crystalographic voids in the MAX phases could provide another possible variation on their composition that could lead to higher phase purity in addition to the previously mentioned impurity incorporations into their M and A sites. It would be interesting to investigate if hydrogen incorporation leads to increased vulnerability to decomposition or oxidation at high temperature.

We have explained the linear behaviour of the formation energy of $M_{n+1}AX_n$ with respect to n for $n > 2$, and that $n >= 3$ is only marginally more stable than $n = 2$, by introducing a model that treats the energy of the MAX phase as the sum of a metal carbide part, an aluminium layer part, and a constant excess energy corresponding to each aluminium layer.

Particular attention was paid in our study to the stability of compounds in the binary Zr-Al system, since there are large discrepancies between published thermodynamic data. The accepted published phase diagrams show ZrAl to be a stable line compound at low temperature. Our calculations reported here, in agreement with other published DFT calculations, suggest that on the contrary, ZrAl is thermodynamically unstable.

The last section of this chapter included an analysis of the degree of geometrical distortion of the octahedra in the Zr_2AlC and Ti_2AlC MAX phases compared to the ideal equilibrium values in the pure carbide structure. Comparisons for the d and h geometrical values of the octahedra were made between the MAX phase, carbide and solely carbide slab structures. The energies involved in distortions of the octahedra were determined for these different structures and comparison was made between them. The energies involved by varying the distortion of the Al layers in the MAX phases were also examined. In the last part of our geometrical distortion analysis, we calculated the prismatic distortion in addition to the octahedral distortion and compared our results to the literature. Prismatic distortion was calculated to be greater for Zr_2AlC compared to Ti_2AlC, in agreement with previous research. The opposite trend was noticed for the octahedral distortion as well as for the ratio of the two distortions which was found to show higher divergence from its ideal value for Ti_2AlC compared to Zr_2AlC. Although the prismatic distortion was predicted higher in Zr_2AlC than in Ti_2AlC, in agreement with previous research, the rest of our geometric analysis outlined above did not provide a clear and consistent link between geometrical distortion and the higher instability of Zr_2AlC compared to Ti_2AlC.

Chapter 5

Electronic structure and bonding analysis

The total energy of the MAX phases in our two systems, $Zr_{n+1}AlC_n$ and $Ti_{n+1}AlC_n$, as calculated within the DFT approximations, has demonstrated that, compared to the stable, Ti-based MAX phases, the Zr-based ones are either thermodynamically unstable, or metastable. However, it is worthwhile to explore whether a deeper explanation of the difference might be available, more explicitly within the electronic structures of the MAX phases or their competing compounds, for example encoded within the charge densities or the Kohn-Sham single-electron energies of the compounds involved. After all, although similar, Ti and Zr are not chemically identical. For example, their stable oxides have different structures (fluorite for ZrO, rutile or anatase for TiO), a slightly smaller metallic atomic radius (147pm versus 160pm) and slightly higher Pauling electronegativity (1.5 versus 1.4) are associated with Ti [13]. Therefore in order to understand this difference in stability, the electronic structure was studied in this chapter in terms of total and partial density of states as calculated for the MAX phases and their parent carbides and aluminides. Chemical bonding was also investigated based on charge density difference and calculations of charge transfer in the two systems by applying three different methods, Bader, Mulliken and DDEC. In order to further compare and understand the covalent bonding of the MAX phases in the Zr and Ti systems, bond orders as defined in the DDEC6 [14, 15, 16] methodology and ICOHP [122] energy values indicating the bond strength were calculated. The different methodologies applied for the charge transfer and covalent bond

strength are discussed and compared with literature.

5.1 Computational details

Calculations in this chapter were done within the DFT framework, using VASP and setting the same computational details for all phases considered as in the previous chapter, as defined in Section 4.1.1. In addition to these computational details, to perform an accurate charge density calculation in VASP a fine fast Fourier transform (FFT) grid density was used. This charge density was used for Bader analysis calculations conducted by using the Bader Charge Analysis code [212, 213, 214]. Other partitioning concepts applied in this chapter are the COOP and COHP [115], implemented in the LOBSTER software [122, 120, 121] where these local orbital based concepts are applied to outputs from planewave DFT codes such as VASP using projection schemes, resulting in the projected COHP and COOP, pCOHP and pCOOP. Another partitioning method applied uses the Density Derived Electrostatic and Chemical (DDEC) approach and in particular the DDEC6 version [15] implemented in the CHARGEMOL program [123]. By applying this method, overlap populations, atomic net charges, bond orders (BOs), and sum of bond orders (SBOs) can be calculated [14, 16]. The required charge density inputs for the DDEC method were computed using the fine FFT grid in VASP.

5.2 Results

5.2.1 Electronic structure

Electronic structure was studied in terms of the total and the atom projected density of states (DOS and pDOS) of the Zr and Ti based 211 and 312 MAX phases as well as of their corresponding carbide and aluminide binaries. Mainly, we focused on the comparison between the Zr and Ti systems in terms of the energies at which peaks in the pDOS on different atomic orbitals coincide, indicating a covalent bond. In particular, by examining the degree of hybridisation,

e.g. the magnitudes of the coinciding peaks in the Zr and Ti based MAX phases, we were seeking an indication of the relative strength of the corresponding bonds in these systems. The DOS and pDOS results for the two systems are presented in Figures 5.1 and 5.2 for the MAX phases and binaries respectively. In these figures, the Fermi energy was shifted to zero when plotted.

Before comparing the relative strength of the corresponding bonds in the two systems, we note that all MAX phases were found to have a non-zero density of states value at the Fermi level, verifying their metallic nature, as has also been reported for these systems in the literature [77, 74, 100]. We found the DOS that correspond to the Fermi level (the Fermi level is in parentheses and in eV) for the MAX phases Zr_2AlC, Zr_3AlC_2, Ti_2AlC and Ti_3AlC_2 to be 2.41 (7.7266), 3.27 (8.272), 2.51 (8.7349), and 3.51 (9.2989) states/eV (unit cell) respectively. DOS at the Fermi level for these MAX phases have also been reported in other theoretical studies, such as 2.67 [215] and 2.81 [100] for Ti_2AlC, 3.45 [100] for Ti_3AlC and 2.72 [77] for Zr_2AlC; these values have a 2–13% difference from our results. In our results, the DOS at the Fermi level between the Zr-based and Ti-based MAX phases were generally similar, with values for the Ti 211 and 312 MAX phases being only around 4% and 6% higher than their respective Zr counterparts. For Ti-based MAX phases, the DOS at the Fermi level for Ti_3AlC_2 was found to be 40% higher than Ti_2AlC. From Fig. 5.2, the main contribution to the DOS at the Fermi level for the four MAX phases is from the d orbitals forming the delocalised states, which are expected to dominate each compound's conductivity. To examine whether DOS at the Fermi level could be a good guide to the conductivity of these MAX phases, we compare trends in our DOS results and measured conductivities from the experimental literature. Unlike the 40% difference in the DOS at the Fermi level for the two Ti phases, experimentally measured electrical conductivities for Ti_2AlC [98] and $Ti_3Al_{1.1}C_{1.8}$ [216] were very similar: $2.7 \times 10^6\,\Omega^{-1}m^{-1}$ and $2.6 \times 10^6\,\Omega^{-1}m^{-1}$ respectively. Comparison of the electrical conductivities between Zr-based and Ti-based MAX phases with our calculated DOS at the Fermi level results has not been made, since no experimental measurements of electrical conductivities were found in the literature for the Zr_2AlC and Zr_3AlC_2 phases. For comparison reasons, we look into the link between electrical conductivities and DOS at the Fermi level for the two carbides, ZrC and TiC,

whose DOS at the Fermi level we calculated to be very similar at 1.15 and 1.16 states/eV (unit cell) respectively. Measured values available in the literature of electrical conductivity for the binary ZrC and TiC carbides, however, have been reported at 2.3×10^6 and 1.5×10^6 $\Omega^{-1}\mathrm{m}^{-1}$ respectively [217], resulting in ZrC conductivity being around 50% higher than in TiC. For TiC though, it is worth noting that a range of values, from 4×10^5–1.7×10^6 $\Omega^{-1}\mathrm{m}^{-1}$, have been reported in experimental studies [218]. This range of reported values of conductivity for TiC could suggest that stoichiometry may considerably affect the measured values. Thus from the above, no clear link between DOS at the Fermi level and electrical conductivity for the four MAX phases could be made.

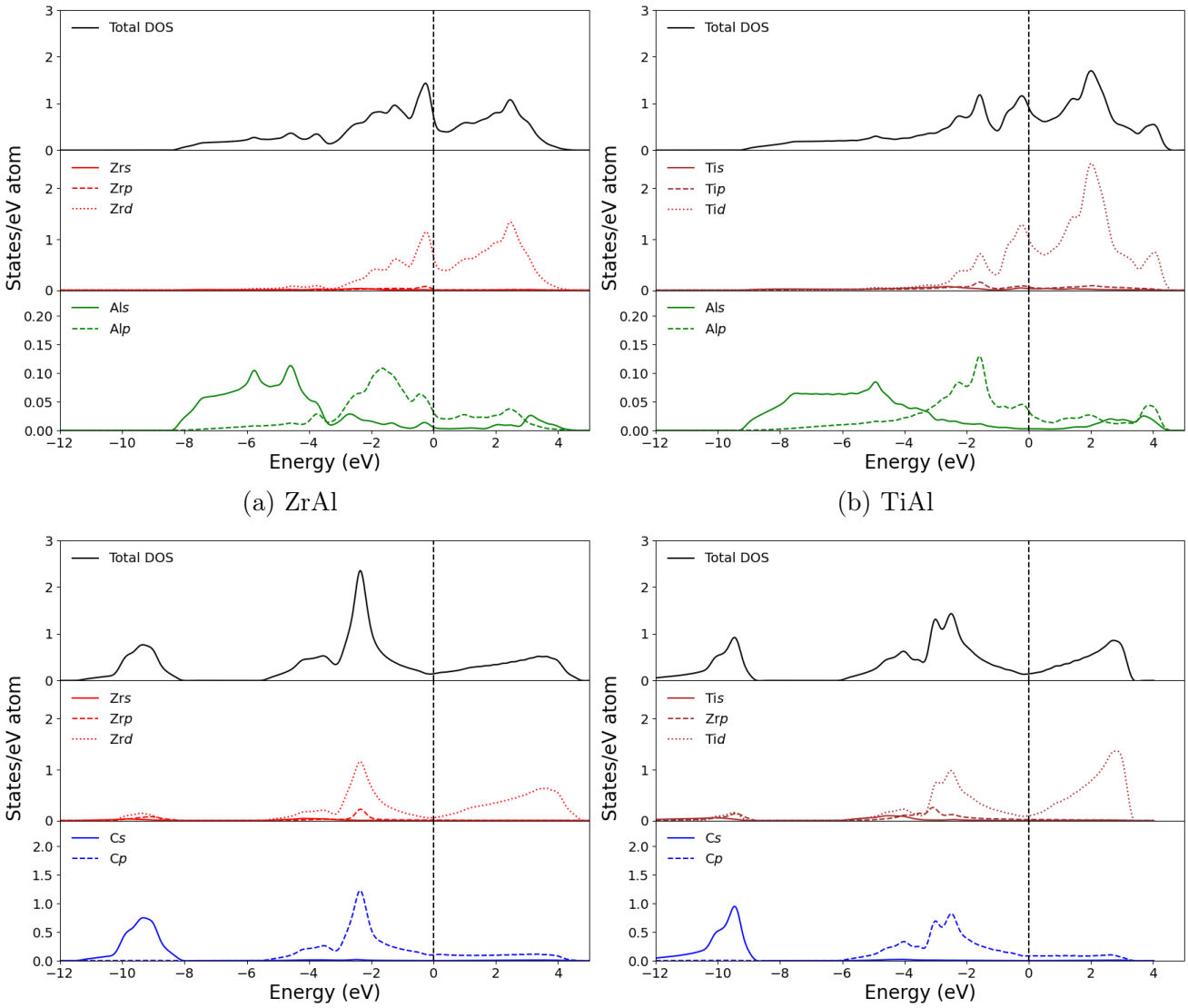

(a) ZrAl (b) TiAl

(c) ZrC (d) TiC

Figure 5.1: Atom and orbital projected DOS for the binary carbides and aluminides.

We begin the bond strength comparison by looking into overlapping pDOS peaks between atomic orbitals in the binary end members of the MAX phases (Fig. 5.1). Starting with the carbide structures, which are simpler than the MAX phases, we note that in the energies between −4.5 and −1.5 eV an overlap between the Md and Cp pDOS peaks occurs, suggesting strong hybridisation between these atoms for both ZrC and TiC. For the aluminides, hybridisation between Md and Alp occurs at a higher energy window compared to the carbides, from around −2.5 eV up to just after the Fermi energy. Specifically, the highest degree of overlap between Md and Alp occurs at around −1.6 eV for both aluminides where a sharp Alp peak in TiAl compared to a broader one for ZrAl are observed. Overall, the pDOS peaks for the binary carbides and aluminides show a high level of similarity between the two systems.

Moving on to the MAX phases, we see that their pDOS in Fig. 5.2 show some common attributes with those of their aforementioned end members. Specifically, the pDOS between the MAX phases and carbides are very similar if we exclude the Al peaks in the MAX phases. The M-C and M-Al covalent bonds in the MAX phases also occur at around the same energy windows with the carbides and aluminides respectively. In more detail, for the 211 MAX phases, the pDOS overlapping, which indicates bonding, is noticed mainly in the energy window between −4 to −2 eV where hybridisation between Md and Cp occurs, and to a much lesser degree between Md and Als. At a higher energy window between −2.2 eV and just after the Fermi level, hybridisation occurs mainly between Md and Alp. This suggests that the strongest bonding effects exist between the Md-Cp and Md-Alp atomic orbital interactions. Comparing the 211 and 312 Zr and Ti based MAX phases we find the energy windows are very similar, indicating no clear differences in the energies at which the Md-Cp and Md-Alp bonding occurs. As such, the strongest interactions for 312 MAX phases are noted in the same energy range as 211 and also stem from hybridisation of the Md-Cp and Md-Alp orbital pairs. 312 MAX phases have two types of M atoms, M_1 and M_2, in their carbide layer, corresponding to atoms in the outer and inner part of the layer respectively, with the outer layer being in contact with the Al atoms. Hybridisation for both $M_1$$d$-Al$p$ and $M_2$$d$-Al$p$ occurs between −2 eV and up to the Fermi level, where Md-Alp also occurs in 211. Similarly, $M_1$$d$-C$p$ and $M_2$$d$-C$p$ hybridisations occur where Md-Cp is found for 211, between −4 to −2 eV.

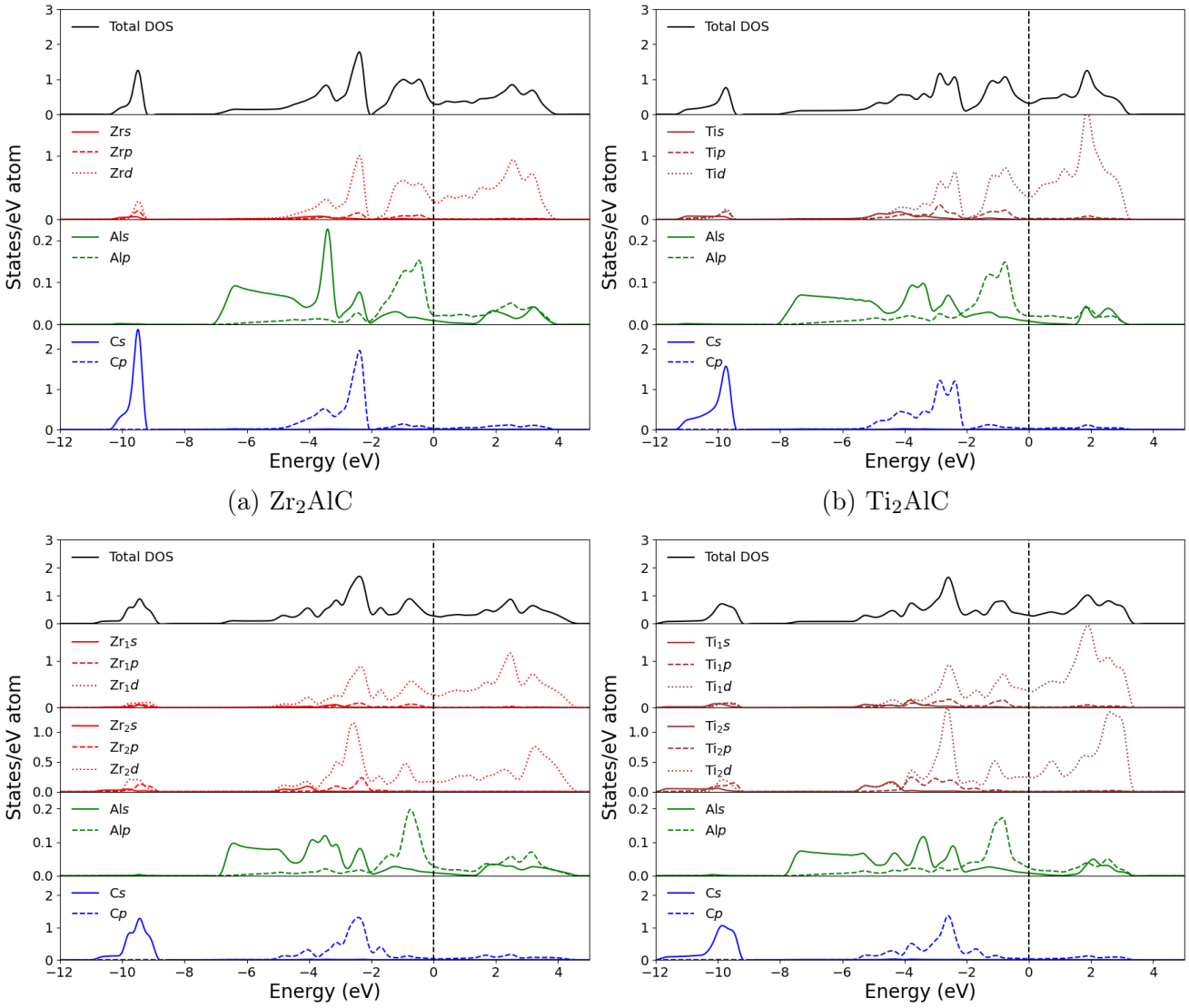

(a) Zr_2AlC (b) Ti_2AlC

(c) Zr_3AlC_2 (d) Ti_3AlC_2

Figure 5.2: Atom and orbital projected DOS for the $Zr_{n+1}AlC_n$ and $Ti_{n+1}AlC_n$ MAX phases.

These observations regarding the prominent M-C and then M-Al covalent interactions in the MAX phases confirm some of the typical bonding characteristics of MAX phases described in the literature. As a general observation from the above analysis, the DOS for both Zr and Ti based phases show a high resemblance, having their peaks in very similar energy ranges, and no clear distinguishing factors between Zr and Ti based MAX phases that could explain their difference in thermodynamic stability were found. As mentioned in the literature review, in the study by Bai *et al.* [102] a number of $M_{n+1}AlC_n$ phases with $n = 1$–3 and M including Zr and Ti, were examined based on their pDOS in order to identify trends in the strength of hybridisation between Md-Cp and Md-Alp with respect to the valence electron concentration (VEC) and

d-electron shell number of the M atoms. In the study by Bai *et al.*, although these indicated bonds were shown to have a tendency towards lower energies with increasing VEC, for VEC = 4 specifically, which includes Zr and Ti, no difference in the energy ranges or trends with respect to the *d*-electron shell number was noted, which is in agreement with our comparison findings for the Zr and Ti based MAX phases. To potentially explain the bonding differences and gain a more quantitative description of the relative bond strength between the corresponding bonds in the MAX phases of the two systems of interest, in the following sections, we will examine their chemical bonding with the tools of charge density difference and charge transfer, for the latter of which different methods such as Mulliken, COOP, COHP and DDEC were applied and discussed.

5.2.2 Charge density difference and charge transfer

To further understand the atomic interactions within the two types of MAX phases, $Zr_{n+1}AlC_n$ and $Ti_{n+1}AlC_n$, the charge density difference and the charge transfer have been calculated. The charge density difference can be useful in visualising the local chemical bonding with respect to the parent carbide systems. For the calculation of the charge density difference between the Al and Zr-C layers the following expression was used:

$$\Delta\rho_{\mathrm{Al}} = \rho_{\mathrm{M_2AlC}} - \rho_{\mathrm{M_2C}} - \rho_{\mathrm{Al}} \tag{5.1}$$

where M is either Zr or Ti and $\rho_{\mathrm{M_2AlC}}$, $\rho_{\mathrm{M_2C}}$ and ρ_{Al} are respectively the charge densities of the M_2AlC structure, of the 211 structure without the Al atoms and of the 211 structure with only the Al atoms present.

In Fig. 5.3 the 3D charge density difference in electrons per cubic Angstrom based on Eq. 5.1 is shown for Zr_2AlC and for Ti_2AlC. The yellow and blue colours represent electron accumulation and loss respectively. The isosurface around the Al atoms indicates a loss of electrons whereas electron accumulation exists in between the Ti or Zr and Al layers indicating the formation of a covalent bond. The charges are shown for the same isosurface value, 0.004 electrons $Å^{-3}$, for

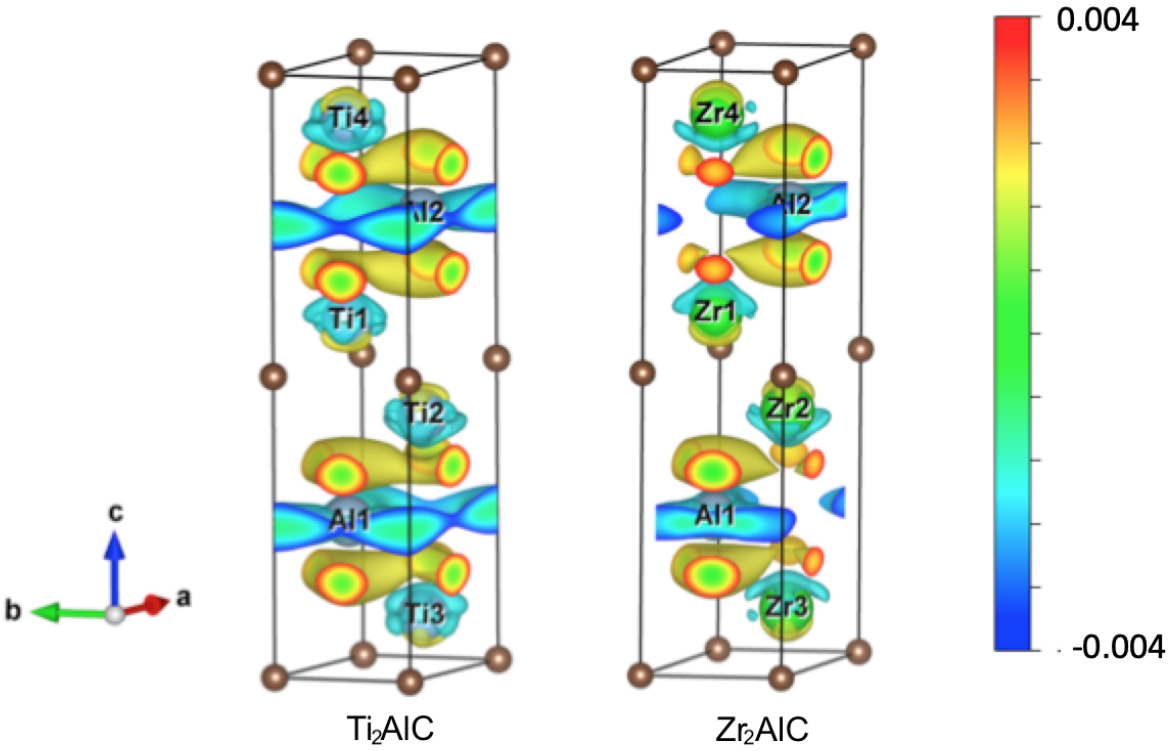

Figure 5.3: Charge density difference at isosurface level 0.004 electrons $Å^{-3}$ for Ti_2AlC and Zr_2AlC.

the two MAX phases and although it is qualitative, it seems that there are more electrons piled up between Ti and Al than Zr and Al. The isosurface around Zr or Ti has a positive and a negative charge, which could suggest polarisation of the M-M atoms that can be caused by electron movement between the M and Al atoms, as also noticed in the study by Magnuson *et al.* [219]. The C atoms seem to have no charge in both phases, indicating a very weak bonding between C and Al, as the Al layer appears to only have a local effect. This is confirmed below by the calculation of the bond order and strength using two different methods (DDEC and pCOHP). The weak Al-C bonds that are evidenced for both Zr_2AlC and Ti_2AlC have also been confirmed for Ti_2AlC in the study by Magnuson *et al.* [219]. Specifically, in their study, Magnuson *et al.* verified the weaker Al-C bonds for Ti_2AlC both experimentally, based on soft X-ray emission interpreted in terms of pDOS to give information about the hybridisation between the constituent atoms and particular orbitals involved, and theoretically, by calculating the balanced crystal orbital overlap population (BCOOP) [220] for the system. Similarly with COOP, BCOOP is an energy resolved quantity used as an indicator for bonding, with positive and negative values

corresponding to bonding and antibonding states respectively, with BCOOP being to a lesser degree basis set dependant. BCOOP performs better for highly non-orthogonal basis sets such

Phase	**Zr_2AlC**	**Zr_3AlC_2**	**Ti_2AlC**	**Ti_3AlC_2**
M_1	10.890 (+1.110)^a	10.798 (+1.202)^a	10.917 (+1.083)^a	10.838 (+1.162)^a
	10.960 (+1.04)^b	10.985 (+1.02)^b	10.995 (+1.01)^b	10.66 (+1.34)^b
	11.09 (+0.91)^c	11.06 (+0.94)^c	10.99 (+1.01)^c	10.95 (+1.05)^c
M_2		10.397 (+1.603)^a		10.562 (+1.438)
		10.65 (+1.35)^b		10.45 (+1.55)^b
		11.01 (+0.99)^c		10.97 (+1.03)^c
Al($2s2p3s^23p^1$)	11.551 (−0.551)^a	11.511 (−0.511)^a	11.518 (−0.518)^a	11.499 (−0.499)^a
	11.655 (−0.65)^b	11.560 (−0.56)^b	11.420 (−0.42)^b	11.75 (−0.75)^b
	11.78 (−0.78)^c	11.78 (−0.78)^c	11.91 (−0.91)^c	11.88 (−0.88)^c
C($2s^22p^2$)	5.669 (−1.669)^a	5.748 (−1.748)^a	5.648 (−1.648)^a	5.632 (−1.632)^a
	5.445 (−1.44)^b	5.420 (−1.42)^b	5.605 (−1.60)^b	5.77 (−1.74)^b
	5.02 (−1.02)^c	5.04 (−1.04)^c	5.11 (−1.11)^c	5.12 (−1.12)^c
Phase	**ZrAl**	**ZrC**	**TiAl**	**TiC**
M	11.665 (+0.336)^a	10.179 (+1.821)^a	11.400 (+0.600)^a	10.368 (+1.632)^a
	11.81 (+0.19)^b	10.57 (+1.43)^b	11.84 (+0.16)^b	10.39 (+1.61)^b
	11.24 (+0.76)^c	10.96 (+1.04)^c	11.14 (+0.86)^c	10.90 (+1.10)^c
Al($2s2p3s^23p^1$)	11.336 (−0.336)^a		11.600 (−0.600)^a	
	11.19 (−0.19)^b		11.16 (−0.16)^b	
	11.76 (−0.76)^c		11.86 (−0.86)^c	
C($2s^22p^2$)		5.821 (−1.821)^a		5.632 (−1.632)^a
		5.43 (−1.43)^b		5.61 (−1.61)^b
		5.04 (−1.04)^c		5.10 (−1.10)^c

Table 5.1: The number of electrons associated with atom I, N_I, and in the brackets the net atomic charge q_I is shown. These values are calculated by Bader analysis denoted with a, the DDEC method, b and Mulliken analysis, c. M refers to either Zr($4s4p5s^24d^2$) or Ti($3s3p4s^23d^2$) and M_1 and M_2 are defined as shown in Fig. 4.10.

as in full potential linearised muffin tin orbital (FP-LMTO) calculations, though for minimal basis sets such as in linear combination of atomic orbitals (LCAO) calculations, COOP and COHP are preferable [220].

Zr	Ti	Al	C
1.33	1.54	1.61	2.55

Table 5.2: Pauling electronegativity for the elements in the $Zr_{n+1}AlC_n$ and $Ti_{n+1}AlC_n$ MAX phases [13]

For further understanding of the bonding nature and level of ionicity in the phases, the charge transfer between the atoms in the 211 and 312 MAX phases has been calculated and compared with the charge transfer for their end members. The total number of electrons assigned to the atoms, N_I, and the net atomic charge, q_I, (related by Eq. 2.36) are shown in the Table 5.1 calculated based on three different methodologies. These methodologies consist of Bader, DDEC and Mulliken analysis, with each of these being based on different electron partitions. In the case of Mulliken analysis, the total number of electrons assigned to the atoms, Mulliken's gross population, contains the onsite atomic charge, as well as half of the corresponding overlap populations with the neighbouring atoms. Similarly, the DDEC N_I represents the number of assigned electrons incorporating the atomic and bonding charges as described in Eq. 2.37. These values are calculated for the four MAX phases and their corresponding binary aluminides and carbides. The electron transfer, q_I, shows the oxidation, quantifying the loss of electrons of each atom. This value does not always match the Pauling electronegativity of Zr, Ti, Al and C, where C is the most electronegative and Zr the least, as shown in Table 5.2 where although the electronegativity of Ti is greater than that of Zr, the charge transferred to Ti in the MAX phases is more or less than the charge transferred to Zr depending on which of the three definitions of charge transfer is chosen.

Based on the three applied methods in Table 5.1, the M_1 and M_2 atoms in the MAX phases show a loss of electrons while Al and C atoms show a gain. Compared to the study by Dahlqvist *et al.* [221], which applied Bader analysis to M_3AlC_2 MAX phases with the M atom in groups IV–VI, this trend is in agreement with their findings for groups IV and V which include

Zr and Ti, where Bader charge values for the atoms in Zr_3AlC_2 were found to be around +1.77 for M_2, +1.48 for M_1, −0.82 for Al and −1.98 for C and for Ti_3AlC_2 to be around +1.45 for M_2, +1.2 for M_1, −0.63 for Al and −1.64 for C. Focusing only on our results again, we note that the Al electron gain indicated by the different methods we used, as shown in Table 5.1, seems to not align with our charge difference results shown in Fig. 5.3, which indicate a loss of electrons around the Al atoms. This disagreement between our findings can be explained by the fact that partition methods like Mulliken and Bader assign all the charge to atoms and none to bonds e.g. in Bader, the partitioning of electrons is into space filling regions, whereas in Figure 5.3 the charge density difference clearly shows the charge that has been lost from Al appearing in bonds between Al and M atoms.

In general, it is expected that charge transfer values differ depending on the method applied, therefore differences and similarities in overall trends in the charge transfer between the methods were examined instead, focusing on trends between Zr and Ti MAX phases and binaries, and in the $M_{n+1}AX_n$ phases as n increases. As is discussed below, many inconsistencies between the methods were noted in these trends, however, indicating their strong dependence on the definition of charge transfer used.

From the results in Table 5.1, there is a complete disagreement between Bader and Mulliken analysis about whether Ti or Zr MAX phases show greater charge transfers. Based on the Mulliken analysis, the M, Al and C atoms in the Ti-based MAX phases show a greater charge transfer compared to their corresponding Zr-based ones. The opposite trend is noted in the Bader analysis, where the atoms in the Zr-based MAX phases have higher charge transfer, in agreement with the study by Dahlqvist *et al.* [221] where Bader analysis was also applied for atoms in the Zr and Ti systems. Regarding this trend, the DDEC method agrees with Mulliken analysis for all atoms only in 312 MAX phases. DDEC and Mulliken also agree that Ti binary carbides show greater charge transfers than Zr ones, but with the aluminides that are more metallic, they disagree.

Regarding whether 211 or 312 MAX phases show greater charge transfers, no overall agreement is apparent between any of the methods in Table 5.1, some partial agreement is noted however,

with the Bader and Mulliken methods showing the most similarities. In particular, according to Bader and Mulliken analysis the M_1 atom has lower charge in 211 than in 312 phases. The DDEC method agrees with this trend only for the Ti system, whereas a decrease of charge is noted from Zr_2AlC to Zr_3AlC_2. For the Al atoms Bader shows that in both systems the Al atom charge density is lower in 312 than 211, this trend is in agreement with Mulliken only for the Ti system, while for Zr Mulliken predicts no change. Results from the DDEC method for Al show no agreement with Bader or Mulliken for any of the systems. Regarding the charge transfer for the C atoms in the MAX phases, a trend is noted based on the Mulliken analysis where C atoms in the 211 phases have slightly lower charge, -1.02 (Zr_2AlC) and -1.11 (Ti_2AlC), compared to their corresponding 312, -1.04 (Zr_3AlC_2) and -1.12 (Ti_3AlC_2). This trend, however, is not verified with the Bader or DDEC methods as no consistent trend on the C atom oxidation is noticed for both Zr and Ti based MAX phases from 211 to 312.

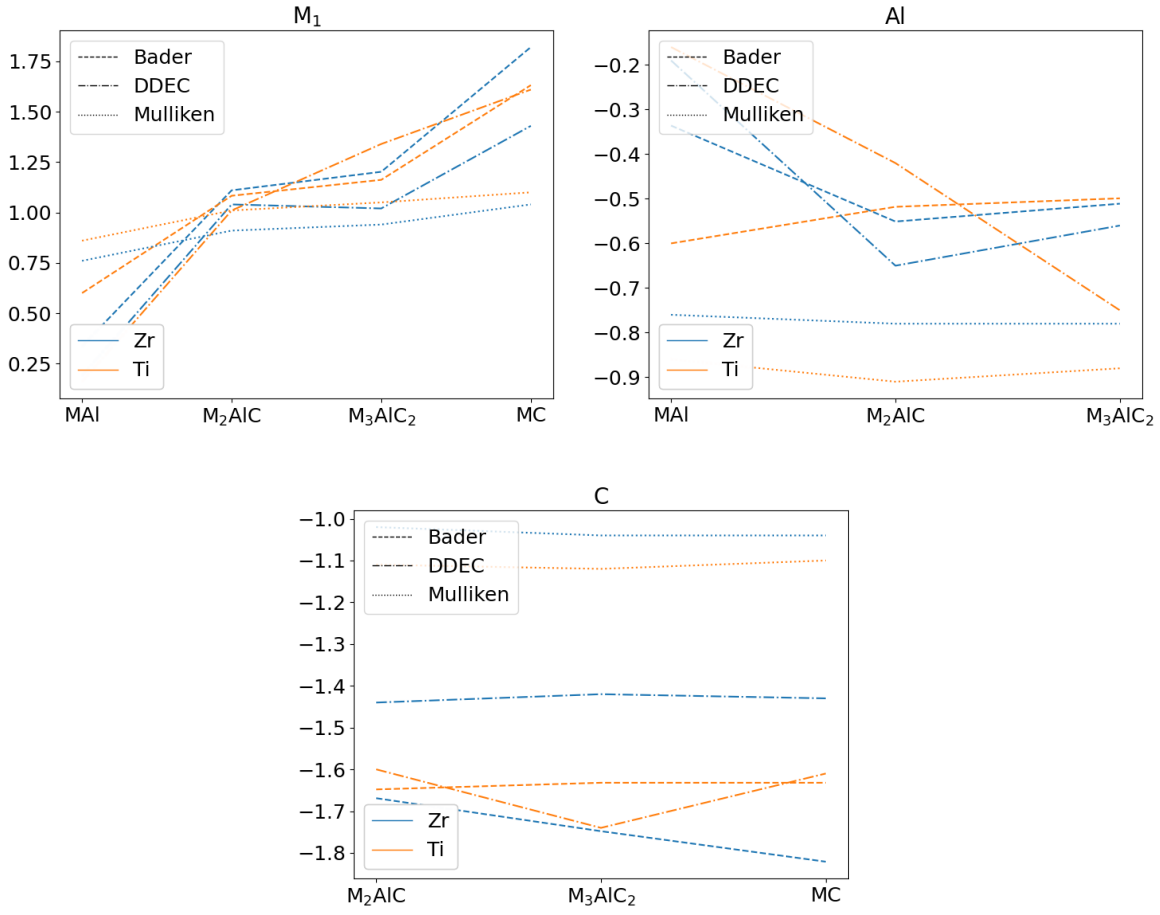

Figure 5.4: The atomic charges for the four MAX phases and their end members in the Zr-Al-C and Ti-Al-C systems calculated for the different methods as included in Table 5.1.

The above trends are better illustrated in Fig. 5.4, where the trends of the charge transfer for each atom in the end members and MAX phases are shown and compared as calculated by Bader and Mulliken analysis and the DDEC method. As n in the MAX phases increases, the charge transfer for the M atom increases and approaches the oxidation value of M in the carbide based on Bader and Mulliken analysis. This trend is true only for Ti-based phases according to the DDEC method. The three methods agree that the M atoms in the carbides have higher charge transfer than the M atoms in the corresponding MAX phases, with the lowest occurring in the alluminides for both systems.

5.2.3 Overlap population and bond order: DDEC method

Quantifying the covalent bond strength between neighbouring pairs of atoms can provide more detail into bonding differences between the chemically very similar $Zr_{n+1}AlC_n$ and $Ti_{n+1}AlC_n$ phases, as they were proven to be in sections 5.2.1 and 5.2.2. Based on the density derived electrostatic and chemical (DDEC) method [14, 15, 16], bond orders (BOs) and sum of bond orders (SBOs) can be defined, as is explained in the methodology section 2.2.3. Such values can reflect the bond strength and can be used to quantify similarity between phases. The DDEC method was employed to analyse 7 and 9 different interactions of neighboring atoms in the 211 and 312 MAX phases respectively, as well as equivalent interactions in their carbide and aluminide binary phases.

In Table 5.3, the DDEC bond orders for pairs of neighbouring atoms and their corresponding bond lengths are given. In the carbides and alluminides, the bond order is higher for Zr-C and Zr-Al than their corresponding Ti-C and Ti-Al. In the case of the 211 MAX phases the Zr-C bond order (0.68) is slightly stronger than Ti-C (0.67), whereas a larger difference is shown for Zr-Al (0.34) compared to Ti-Al (0.26). Regarding the 312 phases, Ti_1-C (0.75) is just slightly higher than Zr_1-C (0.74), whereas for M_2-C, Zr_2-C (0.51) is higher than Ti_2-C (0.48). For the M-Al bonds, Zr_1-Al (0.32) has a higher bond order than Ti_1-Al (0.29). Regarding the Al layer, the bond orders are higher for Ti_2AlC compared to Zr_2AlC where the bonds are more stretched, the same is true for the C-C bonding. The Al-Al and C-C bond lengths are smaller in Ti_2AlC

at 3.036 Å compared to 3.290 Å in Zr_2AlC.

As a general characteristic, indicated by the bond order values in Table 5.3 and common for the $Zr_{n+1}AlC_n$ and $Ti_{n+1}AlC_n$ MAX phases, the M-C bonds show the highest bond orders, followed by the M-Al and then by the Al-Al. The smallest bond orders are noted for the C-C and Al-C interactions. This sequence has also been noted in terms of bond strength quantified by ICOHP analysis for 211 MAX phases, including Ti_2AlC, in the study by Music *et al.* [222]. The Al-C bonds show a very small bond order for both Zr_2AlC and Ti_2AlC as there is a large distance between them, with M atoms in between resulting in bond lengths 4.094 Å in Zr_2AlC and 3.830 Å in Ti_2AlC. This weak interaction is in agreement with the density charge difference data discussed in Section 5.2.2 and other calculations based on total and partial DOS for the Zr-based MAX phases [75] as well as with BCOOP calculations for Ti_3AlC_2 [99]. BCOOP, as noted in the previous section, is a modified version of COOP that performs more robustly for highly non-orthogonal basis functions. The higher bond orders we predict for M-C compared to M-Al, e.g. 0.68 (Zr-C) and 0.34 (Zr-Al) for Zr_2AlC, suggest that the M-C bonds are stronger than the M-Al bonds, as we might also expect from the results of our pDOS analysis in Section 5.2.1. Other studies based on the total and partial density of states for Zr-based MAX phases [75, 76] and a number of other M_3AlC_2 MAX phases, with M varying from $3d$ to $5d$ [68], have also confirmed this characteristic. This has also been verified for the Ti system by Magnuson *et al.* [219], who, as mentioned previously, studied the system both experimentally, using soft X-ray emission, and theoretically, using the BCOOP method, finding that the M atoms are bonded stronger to the C atoms than the Al ones.

Recall that the two types of Zr or Ti atoms in the 312 phase are labelled M_1 and M_2, involving the outer and inner M atoms of the MC layer respectively. In general, M_1-C exhibits higher bond order compared to M_2-C, which is also confirmed by BCOOP calculations for Ti_3AlC_2 [99]. By comparing the M_1-C and M_2-C bonds in Zr_3AlC_2 to the M-C bonds in the carbide, the Zr_1-C bond order is increased by 0.2 compared to the binary ZrC, whereas for Zr_2-C it is decreased by 0.03. Similarly in Ti_3AlC_2, the Ti_1-C bond order is increased by 0.27 compared to TiC, whereas for Ti_2-C it remains the same. For the 211 structures the bond orders of Zr-C and Ti-C increase compared to the corresponding carbide structures by 0.14 for Zr and by 0.19 for

Zr_2AlC	OP	BO	BL (Å)	**Ti_2AlC**	OP	BO	BL (Å)
Zr - Al	0.27	0.34	3.040	**Ti - Al**	0.22	0.26	2.868
Zr - Zr^a	0.12	0.14/0.13	3.290	**Ti - Ti**^{a}	0.08	0.09	3.036
Zr - Zr^b	0.12	0.14	3.145	**Ti - Ti**^{b}	0.08	0.09	2.869
Al - Al	0.18	0.22	3.290	**Al - Al**	0.21	0.24	3.036
Zr - C	0.53	0.68	2.276	**Ti - C**	0.52	0.67	2.088
C - C	0.03	0.03	3.290	**C - C**	0.06	0.06	3.036
Al - C	0.01	0.01	4.094	**Al - C**	0.02	0.02	3.830
Zr_3AlC_2	OP	BO	BL (Å)	**Ti_3AlC_2**	OP	BO	BL (Å)
Zr_1 - Al	0.26	0.32	3.042	**Ti_1 - Al**	0.23	0.29	2.876
Zr_1 - Zr_1	0.10	0.12	3.307	**Ti_1 - Ti_1**	0.07	0.07	3.049
Zr_1 - Zr_2	0.10	0.10	3.206	**Ti_1 - Ti_2**	0.06	0.06	2.933
Zr_2 - Zr_2	0.07	0.07	3.307	**Ti_2 - Ti_2**	0.04	0.04	3.049
Zr_1 - C	0.56	0.74	2.242	**Ti_1 - C**	0.57	0.75	2.059
Zr_2 - C	0.41	0.51	2.367	**Ti_2 - C**	0.39	0.48	2.176
Al - Al	0.17	0.21	3.307	**Al - Al**	0.27	0.345/0.344	3.049
C - C^a	0.03	0.02	3.307	**C - C**^{a}	0.07	0.07	3.049
C - C^b	0.03	0.03	3.389	**C - C**^{b}	0.07	0.07	3.106
ZrAl	OP	BO	BL (Å)	**TiAl**	OP	BO	BL (Å)
Zr - Al	0.34	0.42	2.910	**Ti - Al**	0.23	0.27	2.822
Zr - Al	0.25	0.31	3.007				
Al - Al	0.34	0.43	2.633	**Al - Al**	0.24	0.28	2.791
Al - Al	0.13	0.15	3.312				
Zr - Zr	0.23	0.29	3.312	**Ti - Ti**	0.25	0.30	2.791
ZrC	OP	BO	BL (Å)	**TiC**	OP	BO	BL (Å)
Zr - C	0.42	0.54	2.334	**Ti - C**	0.39	0.48	2.146
C - C	0.03	0.03	3.301	**C - C**	0.07	0.07	3.035
Zr - Zr	0.06	0.06	3.301	**Ti - Ti**	0.03	0.03	3.035

Table 5.3: DDEC6 [14, 15, 16] bond orders (BO) and overlap population (OP) between different atomic interactions and their corresponding bond lengths (BL). Where ^{a} and ^{b} correspond to M-M bonds within M layers and between M layers respectively. When two values are given for the bond order of an atomic interaction they correspond to symmetrically equivalent bonds.

the Ti case. The above show that the bond order of M_1-C is higher in 312 than in 211 and lowest overall in the carbides, whereas M_2-C in 312 is lower than the M_1-C bond in 211 and compared to the carbide is the same for Ti and lower for Zr. This implies that the bonds in the carbide slabs of the MAX phases are stronger than in their corresponding binaries. This can be due to the weaker M-Al bonds which transfer charge to the M-C bonds. Specifically, in Zr_2AlC and Ti_2AlC the bond orders of Zr-C and Ti-C are around 2 and 2.6 times larger than Zr-Al and Ti-Al respectively. BCOOP calculations also confirm that the Ti_1-C bond strength in Ti_2AlC is higher than the carbide, however the Ti-C bond shows stronger bonding in Ti_2AlC than Ti_3AlC_2 [219], which is not aligned with our DDEC Ti_1-C comparisons between 211 and 312.

Zr_2AlC	SBOs	$B_{I,I}$	$z_I - B_{I,I}$	**Ti_2AlC**	SBOs	$B_{I,I}$	$z_I - B_{I,I}$
Zr	4.38	8.77	3.23	**Ti**	3.67	9.16	2.84
Al	3.51	9.90	1.11	**Al**	3.26	9.79	1.21
C	4.45	3.22	0.79	**C**	4.63	3.29	0.71
Zr_3AlC_2	SBOs	$B_{I,I}$	$z_I - B_{I,I}$	**Ti_3AlC_2**	SBOs	$B_{I,I}$	$z_I - B_{I,I}$
Zr_1	4.29	8.84	3.16	**Ti_1**	3.86	8.73	3.27
Zr_2	4.12	8.59	3.41	**Ti_2**	3.58	8.66	3.34
Al	3.34	9.89	1.11	**Al**	4.08	9.71	1.29
C	4.14	3.35	0.65	**C**	4.56	3.46	0.54
ZrAl	SBOs	$B_{I,I}$	$z_I - B_{I,I}$	**TiAl**	SBOs	$B_{I,I}$	$z_I - B_{I,I}$
Zr	4.46	9.58	2.42	**Ti**	3.47	10.10	1.90
Al	3.99	9.20	1.81	**Al**	3.38	9.47	1.53
ZrC	SBOs	$B_{I,I}$	$z_I - B_{I,I}$	**TiC**	SBOs	$B_{I,I}$	$z_I - B_{I,I}$
Zr	4.06	8.54	3.46	**Ti**	3.35	8.72	3.28
C	3.68	3.59	0.41	**C**	3.80	3.71	0.30

Table 5.4: Sum of bond orders (SBOs), localisation index ($B_{I,I}$) and $z_I - B_{I,I}$ for each atom calculated with the DDEC method [14, 15, 16].

Regarding the bond order between C-C and Al-Al, it does not seem to be affected as n in the

MAX phases increases. The Zr-Al bond becomes weaker from Zr_2AlC to Zr_3AlC_2, whereas the opposite trend is noticed for the Ti system. This Ti system trend is confirmed in the next section where bond strength is quantified with the integrated crystal orbital Hamilton population (IpCOHP). This has also been confirmed experimentally using X-ray emission spectroscopy

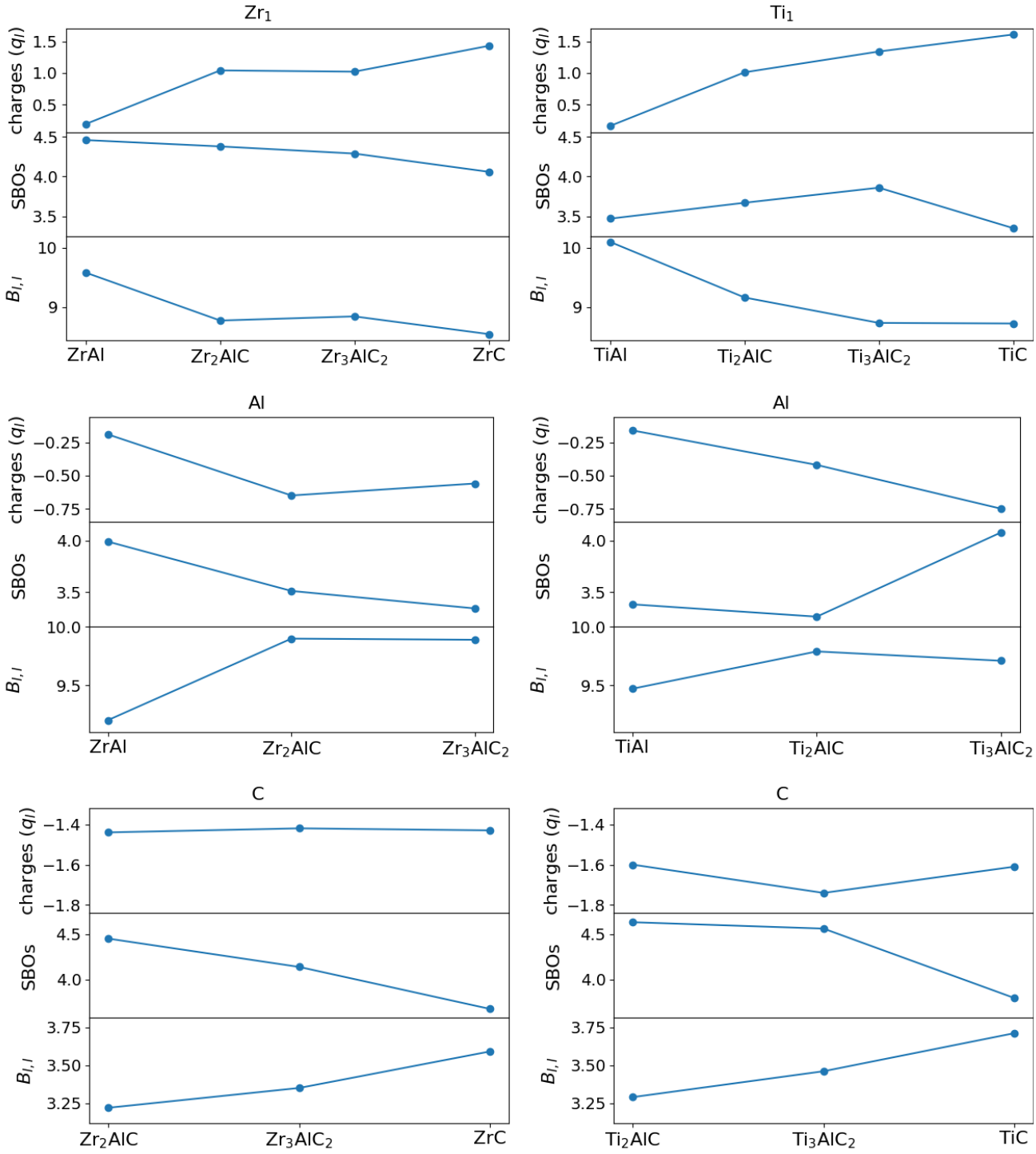

Figure 5.5: The atomic charge (q_I), SBOs and $B_{I,I}$ for each element (M, Al and C) for the phases in the Zr and Ti systems.

and theoretically using the BCOOP in the study by Magnuson *et al.* [219].

Table 5.4 shows the sum of bond orders (SBOs) on each atom as defined in Eq. 2.38, the localisation index ($B_{I,I}$) as defined in Eq. 2.34 and $z_I - B_{I,I}$ described in the methodology, Section 2.2.3, for $Zr_{n+1}AlC_n$, $Ti_{n+1}AlC_n$ and their end members. The SBOs, $B_{I,I}$ and q_I are also presented graphically in Fig. 5.5. $z_I - B_{I,I}$ shows the number of electrons that are shared in bonds formed by atom I or transferred to other atoms. In Fig. 5.5 there is a general downwards trend for $B_{I,I}$ on M_1 atoms in the sequence from the aluminide to 211, 312 and the carbide. The SBO on M_1 decreases from the aluminide to 211 and 312, whereas the opposite trend is noted for the Ti phases, with the SBO on Ti_1 increasing from TiAl to Ti_2AlC and Ti_3AlC_2. The charges on M_1 atoms are lower in the aluminides compared to the carbides in both systems. For C atoms the charge seems almost unchanged between 211, 312 and ZrC, whereas in the Ti system the 312 phases seems to have a lower charge. In general, apart from the Zr_1 atom, the opposite trend is noted between SBOs and $B_{I,I}$ on each atom for the different phases that are compared.

5.2.4 Crystal Orbital Hamilton Populations (COHP)

Apart from the DDEC method to gain insight into the strength and nature of bonds between atoms, the projected Crystal Orbital Hamilton Populations (pCOHP) analysis [122, 120, 121] can also be used to quantify the bond strength of atomic interactions. pCOHP quantifies the local contribution to the total band energy from a bond between a particular atomic pair at a given energy. This results in bonding and antibonding regions, indicated by the difference in sign of the pCOHP values at different energies. The COOP and COHP partitioning concepts are explained in more detail in the methodology Section 2.2.1. The integral of pCOHP up to the Fermi level results in an energy value, instead of a number of electrons as in COOP or the Mulliken scheme, and is therefore a more quantitative indicator of bond strength. The integrals of pCOHP and COOP, IpCOHP and ICOOP, were calculated for 6 and 9 different atomic interactions in the 211 and 312 MAX phases respectively as well as for pair interactions in their end member aluminides and carbides as presented in Table 5.5. The negative values

of IpCOHP in the table correspond to bonding and the positive to antibonding, whereas the opposite is true for the IpCOOP values.

By comparing the IpCOHP values between the Zr and Ti based MAX phases it is noted that the bond strength between the neighboring atoms is higher in the $Zr_{n+1}AlC_n$ phases than the $Ti_{n+1}AlC_n$ ones with the exception of the Al-Al interaction which is stronger in the Ti-based phases. This trend in bond strength is consistent with DDEC calculations of the bond orders in Section 5.2.3, apart from the bond orders of M_1-C, C-C and Al-C which are higher in the Ti-based MAX phases; although the values of the latter two are considered negligible.

As a general result from the IpCOHP values in Table 5.5 and in agreement with the DDEC and pDOS calculations, the M-C bonds are always strongest, followed by the relatively weaker M-Al and Al-Al and the weakest overall C-C and Al-C bonds. This trend is also indicated by similar ICOHP calculations on M_2AlC (M = Ti, V, Cr) MAX phases in the study by Music *et al.* [222] which found the following sequence for Ti_2AlC −3.48 (Ti-C), −0.92 (Ti-Al), −0.57 (Al-Al), −0.55 (Ti-Ti) and almost zero for the C–C and Al–C bond interactions. The M atoms are attached more strongly to the C atoms than to the Al atoms and it is further noted that M_1-C strength increases from 211 to 312. As was discussed in the DDEC section these are evident in both Zr and Ti systems and have been verified for other systems in the literature [75, 76, 219, 68].

Comparison between M-C bonds in the MAX phases and their corresponding carbides indicates that the M_1-C bond is stronger in the MAX phases, while the M_2-C bond in the 312 MAX phases was found to be weaker than in the carbides. This trend is mostly in agreement with the DDEC bond order results, with the difference that for Ti_2-C the bond order was found to match that of Ti-C in the TiC carbide.

The M-M^a and M-M^b interactions correspond to M-M bonds in the carbide slab within M layers and between M layers respectively. Based on the DDEC method these two M-M interactions have the same bond order. On the other hand based on the IpCOHP values the M-M bonds between the different basal layers are stronger than the ones within the same layers which also agrees with the bond lengths being shorter between the M atoms at different layers.

Zr_2AlC	Bond Lengths (Å)	IpCOHP	IpCOOP	**Ti_2AlC**	Bond Lengths (Å)	IpCOHP	IpCOOP
Zr - Al	3.040	−1.69	0.02	**Ti - Al**	2.868	−1.41	−0.03
Zr - Zr^a	3.290	−0.82	−0.11	**Ti - Ti**^{a}	3.036	−0.53	−0.10
Zr - Zr^b	3.145	−1.18	−0.10	**Ti - Ti**^{b}	2.868	−0.81	−0.09
Al - Al	3.290	−1.34	0.05	**Al - Al**	3.036	−1.75	0.02
Zr - C	2.276	−3.57	0.17	**Ti - C**	2.088	−3.42	0.15
C - C	2.290	−0.01	−0.01	**C - C**	3.036	−0.10	−0.02
Zr_3AlC_2	Bond Lengths (Å)	IpCOHP	IpCOOP	**Ti_3AlC_2**	Bond Lengths (Å)	IpCOHP	IpCOOP
Zr_1 - Al	3.042	−1.73	0.02	**Ti_1 - Al**	2.876	−1.42	−0.01
Zr_1 - Zr_1	3.307	−0.75	−0.10	**Ti_1 - Ti_1**	3.049	−0.49	−0.08
Zr_1 - Zr_2	3.206	−1.03	−0.12	**Ti_1 - Ti_2**	2.933	−0.70	−0.09
Zr_2 - Zr_2	3.307	−0.82	−0.11	**Ti_2 - Ti_2**	3.049	−0.57/−0.54	−0.10
Zr_1 - C	2.242	−3.99	0.19	**Ti_1 - C**	2.059	−3.79	0.17
Zr_2 - C	2.367	−3.04	0.13	**Ti_2 - C**	2.176	−2.94	0.12
Al - Al	3.307	−1.31	0.05	**Al - Al**	3.049	−1.73	0.02
C - C^a	3.307	−0.01	−0.01	**C - C**^{a}	3.049	−0.10	−0.02
C - C^b	3.389	−0.02	−0.01	**C - C**^{b}	3.106	−0.10	−0.01
ZrAl	Bond Lengths (Å)	IpCOHP	IpCOOP	**TiAl**	Bond Lengths (Å)	IpCOHP	IpCOOP
Zr - Al	2.867	−2.10	−0.02	**Ti - Al**	2.822	−1.33/-1.34	−0.02
Zr - Al	2.910	−2.44	0.14				
Zr - Al	3.000	−1.12	−0.08				
Al - Al	2.633	−3.38	0.20	**Al - Al**	2.791	−2.44/-2.41	0.14
Al - Al	3.312	−1.21	0.08				
Zr - Zr	3.312	−0.80	−0.13	**Ti - Ti**	2.791	−1.11	−0.06
Zr - Zr	3.327	−0.89	−0.08				
ZrC	Bond Lengths (Å)	IpCOHP	IpCOOP	**TiC**	Bond Lengths (Å)	IpCOHP	IpCOOP
Zr - C	2.334	−3.39/−3.38	0.15	**Ti - C**	2.146	−3.25/−3.26	0.14
C - C	3.301	−0.02	−0.01	**C - C**	3.035	−0.11	−0.02
Zr - Zr	3.301	−0.76/−0.78		**Ti - Ti**	3.035	−0.55	−0.09

Table 5.5: IpCOHP and IpCOOH for the four MAX phases M_2AlC and M_3AlC_2 and binaries MC and MAl (M = Zr or Ti) between different atomic pairs and their corresponding bond lengths. Where ^{a} and ^{b} correspond to M-M bonds within M layers and between M layers respectively. When two values are given for IpCOHP of an atomic interaction they correspond to symmetrically equivalent bonds.

The IpCOHP values for the M-Al and Al-Al bonds increase and decrease respectively from 211

to 312, whereas in the DDEC method for the Ti system, both Ti-C and Al-Al increase from 211 to 312 while for the Zr system, Zr-C and Al-Al decrease and increase respectively. Both of the aforementioned methodologies agree that the Ti-Al bond in the 211 phase is weaker than in 312. As was also discussed in the DDEC section, this is in agreement with the study by Magnuson *et al.* [219] were it was confirmed both experimentally and computationally. In this study [219] the role of Ti-Al and how it is affected by the order n of the MAX phase was found to be related to mechanical properties such as the shear modulus and Young's modulus, explaining the relative softness of Ti_2AlC compared to Ti_3AlC_2. A number of other studies have also made links between the elastic properties and electronic structure [104, 72, 103, 105, 76] underlining the effect of the M-Al bonding on the bulk modulus values, showing that increases of valence electrons involved in M-Al bonding result in increases in shear and bulk moduli. Based on the above and the IpCOHP bond energy values showing an increase for M-Al from 211 to 312, an agreement is noted with the trend in Section 3.2.6 where the bulk modulus increases with n for both systems, Zr and Ti MAX phases.

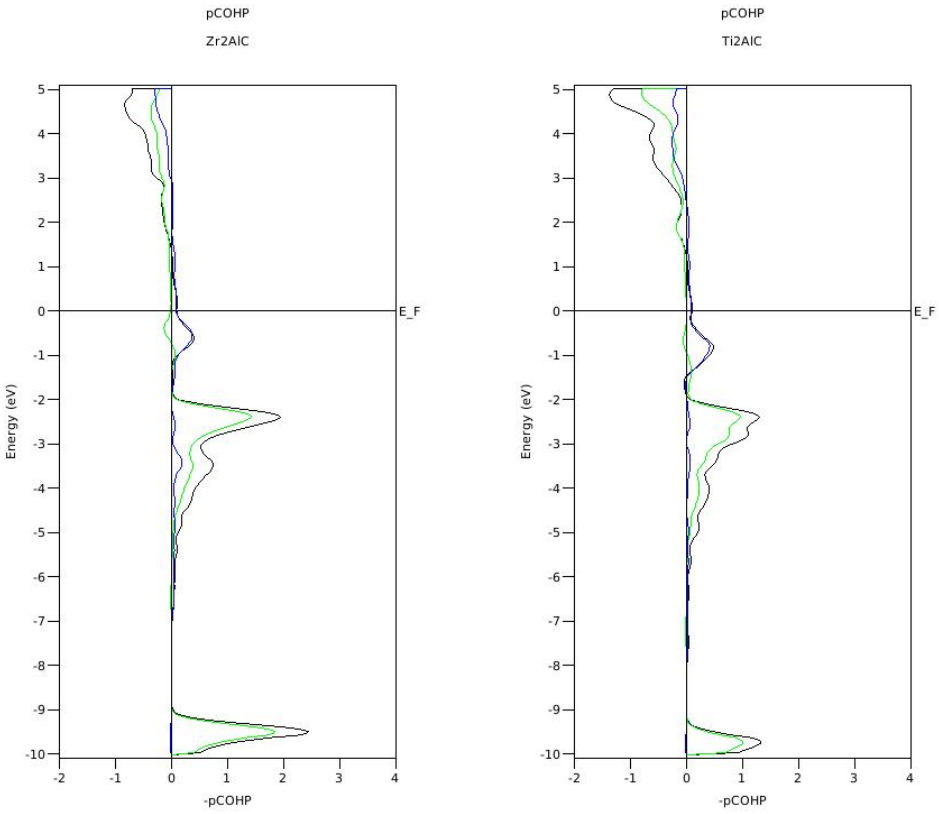

Figure 5.6: −pCOHP curve against energy for M_2AlC phases (M = Zr or Ti). Black: Total, Green: M-C, Blue: M-Al

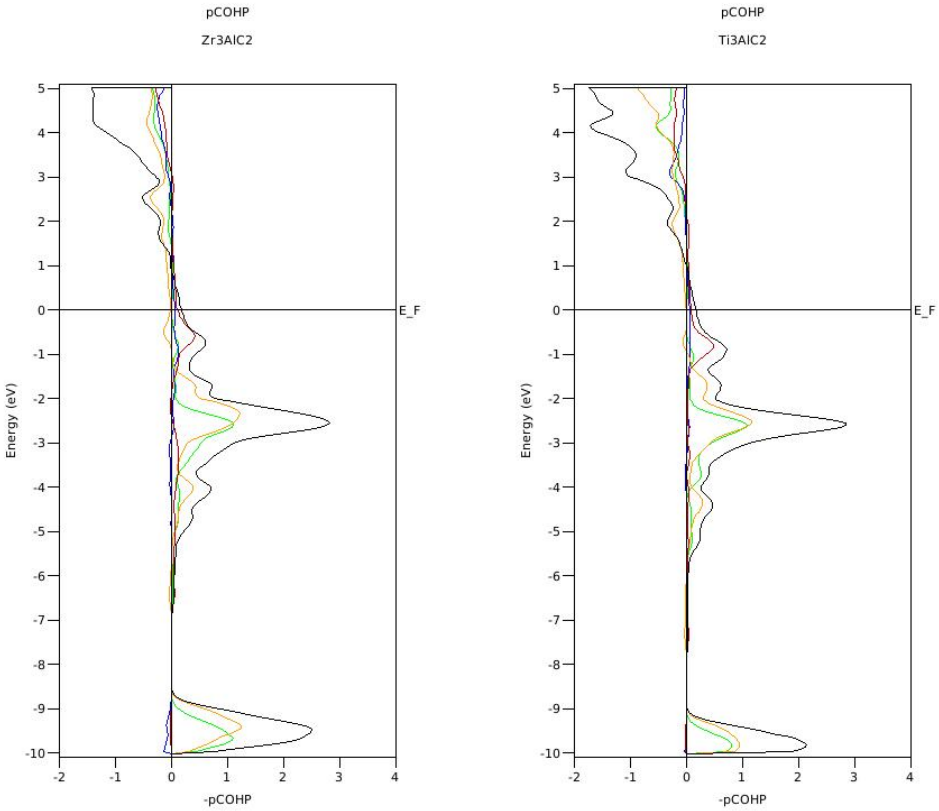

Figure 5.7: −pCOHP against energy for M_3AlC_2 phases (M = Zr or Ti). Black: Total, Red: M_1-Al, Blue: M_1-M_2, Yellow: M_1-C, Green: M_2-C

In Figures 5.6 and 5.7 the total and partial −pCOHP are plotted as a function of energy for the M_2AlC and M_3AlC_2 MAX phases respectively. The partial −pCOHP corresponds to 2 and 4 atomic interactions for the M_2AlC and M_3AlC_2 MAX phases respectively. The Fermi level is at zero pCOHP values for all the atomic pairs indicating stability. Unsurprisingly, the biggest contribution to the total corresponds to the M-C interaction, as it dominates the largest region below the Fermi energy for both systems. For the 312 phases the M_1-Al, M_2-C and M-M bonding orbitals are filled and antibonding orbitals are above E_F, whereas M_1-C shows a small antibonding peak just below E_F. Similarly for 211, the antibonding orbitals for M-Al are above E_F, whereas for M-C a small antibonding peak is again noticed just below E_F, which agrees with the pCOHP curve for Ti_2AlC phases calculated by Music *et al.* [222].

In order to facilitate comparison between Zr_2AlC and Ti_2AlC the pCOHP of M-Al and M-C are plotted in Figures 5.8 and 5.9 respectively. In these figures the M-C interaction contains a small antibonding peak for both phases, but with a larger peak for Zr_2AlC, although the

integrated value for the M-C bond energy is larger for the Zr case. In addition, it is noted that the M-Al bonding and M-C antibonding peaks right below the Fermi level are at lower energy for Ti than for Zr.

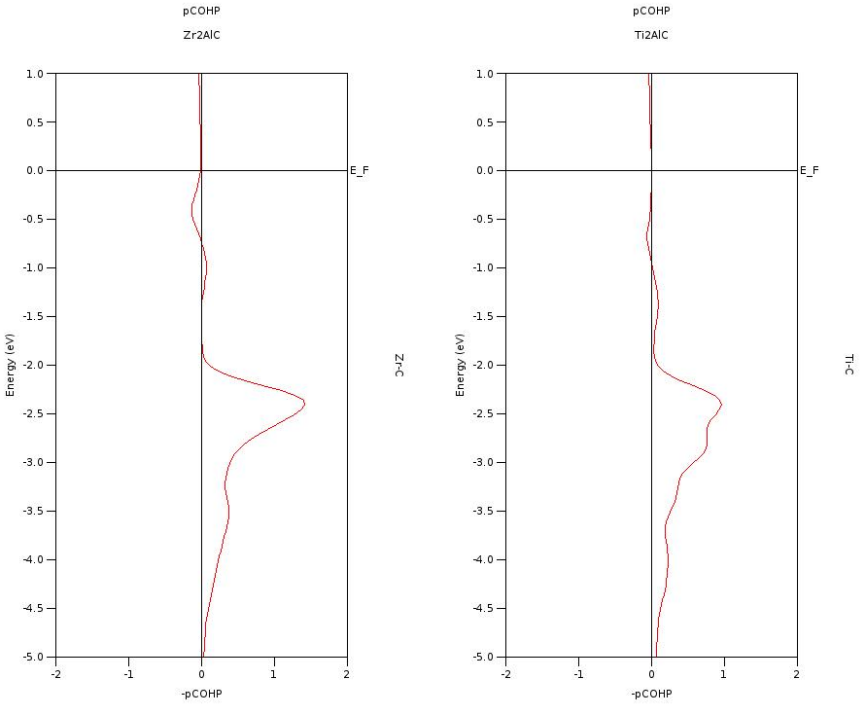

Figure 5.8: −pCOHP against energy for the M-C bond (M = Zr or Ti).

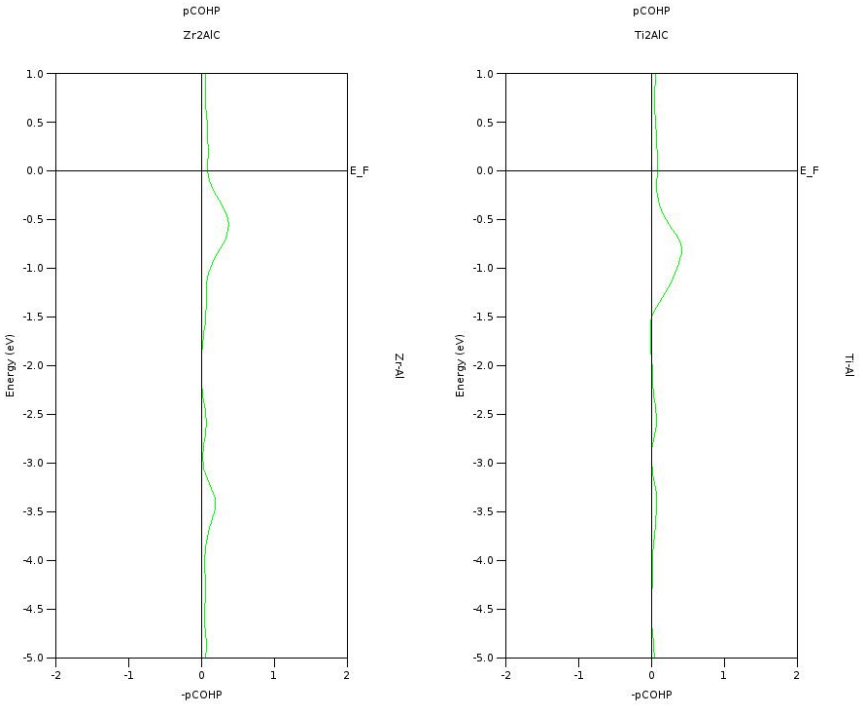

Figure 5.9: −pCOHP against energy for the M-Al bond (M = Zr or Ti).

5.3 Conclusions

The electronic structure was studied by calculating the total and partial DOS and a chemical bonding analysis was performed by calculating the charge density difference, charge transfer and bond orders. Different definitions of charge transfer were used by employing the Bader analysis, Mulliken analysis, and DDEC methodologies. To gain insight into the covalent bonds and quantify the different atomic interactions the DDEC bond orders were calculated and compared to pCOHP results. Based on the above analysis the different methods agreed on the general well-established chemical bonding characteristics of MAX phases. A mixed metallic-ionic-covalent bonding nature was identified. M atoms were found to be attached more strongly to the C atoms than the Al atoms. Generally, the M-C bonding in the carbide layer was found to be the strongest due to interactions of hybridised Md and Cp states followed by relatively weaker M-Al and even weaker Al-Al interactions. The weakest interactions were found to be the C-C and Al-C bonds. In the 312 phases the M_1-C bonds were found to be stronger than the M_2-C. It is further noted that M_1-C bond strength increases from 211 to 312 and that M_1-C bonds in the MAX phases are stronger than their corresponding M-C bonds in the carbides. For the atomic charges, q_I, the three methods applied, Bader, Mulliken and DDEC, agreed for both systems on the trend that the M atoms in the carbides have higher charge transfer than the M atoms in the corresponding MAX phases and that the lowest overall occurs in the alluminides. Apart from the above characteristics that show consistency between the methods, the charge values and some of the bond strength trends were found to strongly depend on the method used. Overall, a high chemical resemblance between the two MAX phases was noted and no clear differentiation was identified to address the main motivation of this chapter, to explain the lower thermodynamic stability of $Zr_{n+1}AlC_n$ compared to $Ti_{n+1}AlC_n$ and in particular the predicted thermodynamic instability of Zr_2AlC. In terms of their potential as coating materials for nuclear fuel cladding on the other hand, based on the above observations from our chemical bonding analysis, nothing stands out that would favour the Zr MAX phases over the Ti ones. For this use case, it is possibly other characteristics, such as the low neutron cross section, that could be considered important advantages of the Zr-based MAX phases.

Chapter 6

Phonon spectra and Raman spectroscopy

6.1 Introduction

Lattice-dynamics has been an important factor in understanding a number of physical properties such as heat capacity, thermal expansion, phase transitions, thermal conductivity as well as in understanding elastic neutron scattering, infrared and Raman spectra. From the phonon dispersion, the Γ point optical phonons are the best defined experimentally, as a number of them can be identified as Raman and infrared active. Raman and infrared spectroscopy are used as identification techniques based on the distinct vibrational characteristics of different materials. Raman spectroscopy, specifically, is associated with high energy photons from inelastic scattering of visible or near-infrared radiation which is often applied to measure stresses, identify compounds and the detection of defects. The association of the different vibrational modes to the specific frequencies (location of the peaks in the Raman spectra) is important and can contribute to understanding of how changes in Raman frequencies are connected to the stiffness of bonds between pairs of atoms and specifically in the case of MAX phases between the layers. Raman spectroscopy is the main technique that has been applied to understanding the vibrational behaviour of MAX phases in contrast to other methods such as neutron scattering or infrared spectroscopy [223].

Raman spectroscopy is important for identifying the presence or absence of particular phases

for which the 'fingerprint' of Raman-active modes and their frequencies is known from previous experiments or DFT calculations. There are a number of DFT studies on MAX phases focused on lattice dynamics and understanding the origin of Raman-active modes. Overall the Raman-active frequencies identified experimentally and theoretically show good agreement [224, 17, 225]. For 211 MAX phases all the four predicted Raman-active modes have been identified experimentally [17, 226, 227, 224], as is also shown in the study [224] where a number of phases, M_2AlC (M = Ti, V, Nb, Ta), were studied with the position of the spectra peaks being within ±15% of the corresponding predicted ones. On the other hand, for 312 phases, experimental studies on phases including Ti_3AlC_2, Ti_3SiC_2 and Cr_3AlC_2 have assigned up to 6 of the 7 total predicted Raman active modes [228, 229, 17, 230]. In the study by Amer *et al.* [228] the effect of carbon vacancies in the carbide layer of Ti_3SiC_2 was investigated by comparing the MAX phases's Raman spectra with the spectra of the non-stoichiometric $TiC_{0.67}$ carbide. The effect of carbon vacancies in TiC on Raman spectra has also been studied [229]. In the same study [229] the influence of secondary phases in MAX phase samples, such as of Ti_3SiC_2, on the Raman spectra was studied, indicating that in such multiphase systems prediction of the Raman frequencies that are the most commonly predicted in the literature, as well as of the height and broadening of the experimental peaks are important in understanding the spectra. Another study by Bai *et al.* [225] on the Raman and infrared spectra of $M_{n+1}AlC_n$ (n = 1–3 & M = Ti, Zr, Hf, V, Nb, Ta, Cr, Mo, and W) MAX phases, showed that the Raman wavenumbers decrease as the d-electron shell number of M atoms for 211, 312 and 413 increases. Phonon calculations and Raman spectra predictions were also conducted for Ti_3AlC_2 and Cr_3AlC_2 [231] with particular focus on how the Raman active modes of A_{1g} and E_{2g} could relate to the reduced mass of M-C and M-Al atomic pairs, suggesting that the M-C comparison of the bond strength between the two MAX phases was possible from the A_{1g} out of plane vibrations.

In the Ti-Al-C system there are a number of experimental [17, 226, 227] and theoretical [17, 226, 224, 227] studies focusing on understanding the Raman-active modes of MAX phases. For $Zr_{n+1}AlC_n$ MAX phases, phonon calculations and Raman-active modes analysis have been conducted for the three MAX phases in the system in the study by Bai *et al.* [225], however there are no reported experimental studies focusing on the Raman-active modes for Zr based

MAX phases.

In the current chapter harmonic phonon calculations were conducted for phases in the Zr-Al-C and Ti-Al-C systems focusing on the $Zr_{n+1}AlC_n$ and $Ti_{n+1}AlC_n$ MAX phases. The main characteristics of the phonon band structure and DOS of the MAX phases were identified and comparison with their competing phases, carbides and aluminides, was made. A particular aim was to identify secondary phases in the experimental samples of Zr_3AlC_2 that are studied in the group of Finn Giuliani (Materials Dept., Imperial College). The frequencies of the Raman-active modes were calculated for the MAX phases based on DFT calculations and identifying the appropriate mode symmetry. Specifically, analysis of the Raman spectra of the Zr_3AlC_2 phase based on calculations of the Raman-active frequencies and a comparison with the experimental data was conducted.

6.2 Computational details

DFT parameters and phonon calculation settings for all phases considered in this chapter were those defined in Section 4.1.1 of Chapter 4. For the Raman-active modes, separate convergence tests with respect to the cut-off and k-points were conducted on $1\times1\times1$ supercells, finding that the same values as those in Chapter 4 resulted in a convergence of the Raman active phonon frequencies to within $1\,\mathrm{cm}^{-1}$.

6.3 Results

6.3.1 Phonon band structure and DOS

The hexagonal Brillouin zone for the MAX phases belonging to the space group P63/mmc (194) is illustrated in Fig. 6.1, highlighting the high symmetry points along which the band structures have been calculated. Fig. 6.2 includes the band structure for the Zr_2AlC, Zr_3AlC_2,

Ti_2AlC and Ti_3AlC_2 MAX phases and Fig. 6.3 includes the phonon DOS for these four MAX phases and their binary end members.

In the band structures for the four different MAX phases in Fig. 6.2, the optical bands at the highest frequencies above 15 THz correspond to the C band where carbon vibrations dominate, as they are the lightest atoms with stiff bonds to the transition metal, whereas Al and Ti or Zr show overlapping frequencies mainly between 4.5–8 THz. For Zr MAX phases, vibrations of Al atoms typically couple to those of Zr or to a lesser degree to C, but there are still some modes mainly based on Al due to its lightness. These Al dominant modes are noted in Fig. 6.3 at low frequencies between 3–5 THz and at higher frequencies between 8.5–9.5 THZ. For Ti-based MAX phases, Al coupled more to Ti and C compared to the corresponding Zr-based phases resulting in less distinct Al peaks especially for the frequencies between 8.5–9.5 THz where a distinct Al peak is missing for the Ti-based MAX phases. The large atomic mass difference between Zr and Al which is almost double that of Ti and Al, could lead to this more decoupled Al peak in the Zr case. The bands at the lowest frequencies between 3–5 THz for Zr MAX phases and between 4–6 THz for Ti MAX phases correspond to vibrations mainly due to Al atoms. Those modes corresponding to the low energy distinct Al peaks are responsible for the

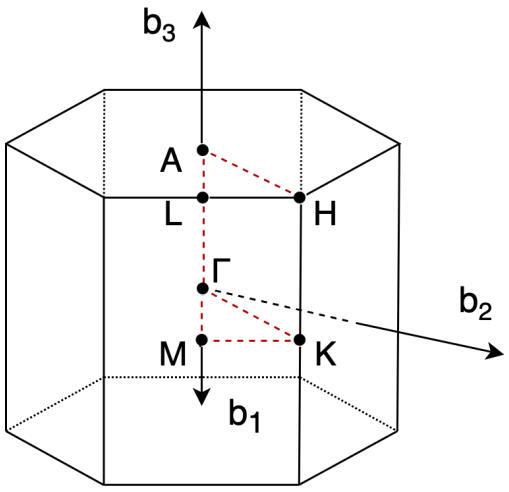

Figure 6.1: Hexagonal Brillouin zone, ($\boldsymbol{b_1}$, $\boldsymbol{b_2}$, $\boldsymbol{b_3}$) are the primitive reciprocal lattice vectors.

flat bands in Fig. 6.2 for the Zr case. Compared to Zr_2AlC where flat bands are mainly noticed between A and H, the projected DOS are narrower for Zr_3AlC_2 which is consistent with its lower band dispersion mostly along the A, H and K high symmetry directions. These bands

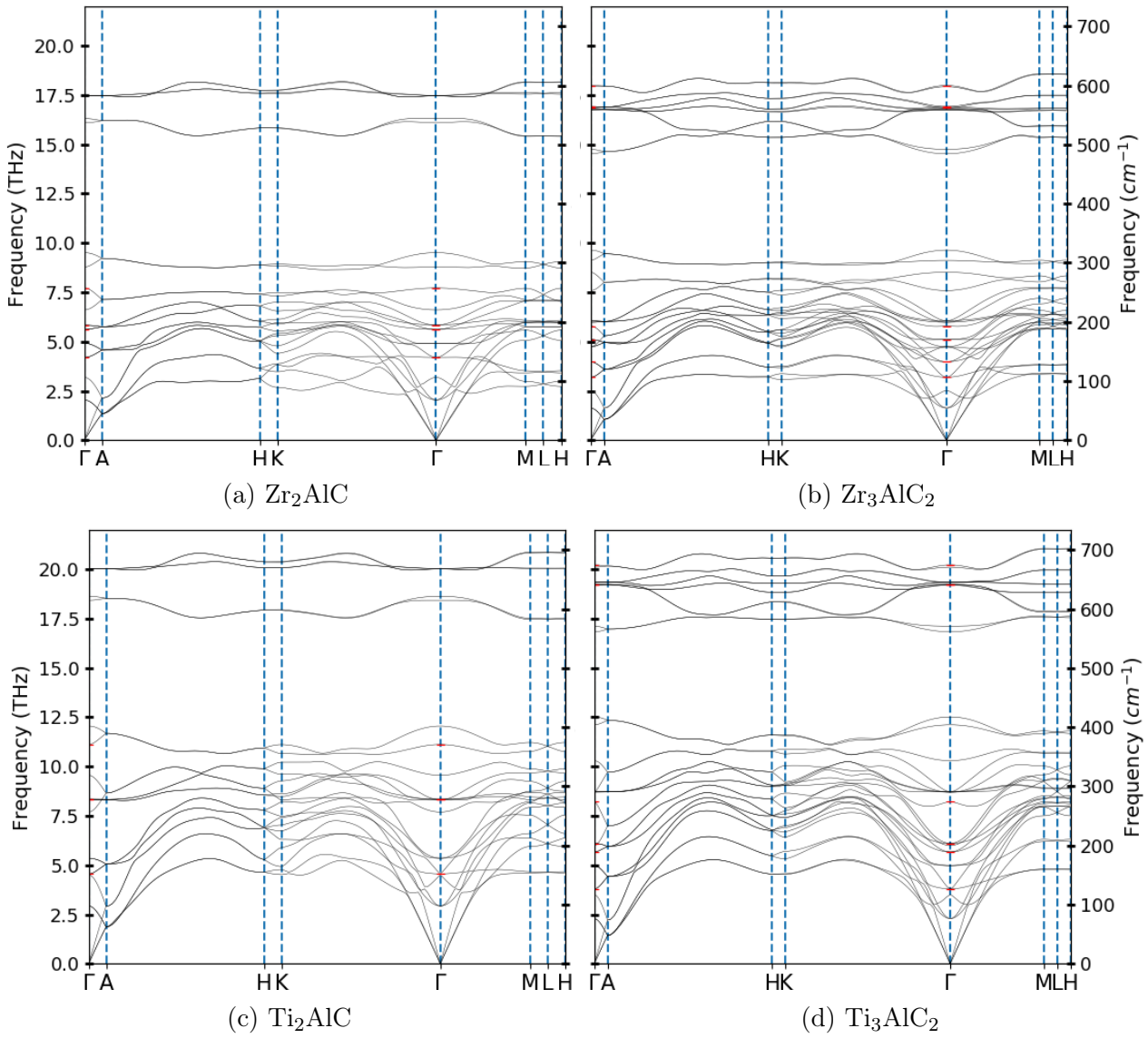

Figure 6.2: Phonon band structure for the 211 and 312 MAX phases. The Raman-active modes are highlighted with red markers on the Γ point.

are at slightly higher frequencies in Zr_3AlC_2 than in Zr_2AlC. For the modes with frequencies between 8.5–9.5 THz that correspond to the narrow Al peak for the Zr-based MAX phases, even lower band dispersion along all high symmetry directions can be noticed in Fig. 6.3.

For these phases there is also a small gap between the bands just under 10 THz and the bands just below them. This gap is larger for Zr_2AlC than Zr_3AlC_2 in agreement with the gap between Zr and Al in their projected DOS. For Ti_2AlC the modes between 10 and 12.5 THz involve much more Ti than Al and the gap at these frequencies in the projected DOS plots is not as clear as in the Zr case. A small gap is noticed in the Ti band structure for these frequencies however,

which could be due to the fact that the frequencies only appear in specific high symmetry directions. Specifically, in the Zr case there is a bigger gap compared to Ti, which never goes below 2 THz, with the closest approach being near the Γ point. In the Ti case, at the Γ point, the gap is bigger than the corresponding Zr one, at around 2.5 THz, but then the gap becomes considerably smaller or even vanishes along the other high symmetry points.

By comparing the projected DOS diagrams between the Ti and respective Zr phases in Fig. 6.3, the two aluminides, ZrAl and TiAl, show the largest differences in their phonon DOS patterns. This large difference is due to their different crystal structures, as TiAl has a tetragonal structure P4/mmm (123) and ZrAl has a more complicated structure Cmcm (63). For the TiAl case, there is overlapping of the projected phonon DOS of the Ti and Al atoms along all frequencies and there is no Al dominated band, whereas for ZrAl a distinct peak of solely Al vibrating atoms is noted at the higher end of its frequencies.

The mass difference effect between Zr and Ti as discussed so far seems to affect the DOS patterns in MAX phases as well as in the binary phases, however in the case of the aluminides no direct comparison could be made due to the difference in their structures. Assuming a harmonic oscillator, the vibrational frequency is given by $\omega = \sqrt{k/m}$, where k and m correspond to the bond stiffness and the mass respectively, showing how frequency differences between pairs of M, Al and C atoms depend on their differences in mass and bond stiffness. The frequencies of the Zr-based MAX phases generally appeared to be lower than of the Ti-based phases. The effect of the mass difference on the phonon frequencies in the 211 and 312 MAX phases is most pronounced for the lower frequency modes and in particular for modes governed by Zr or Ti atoms where the frequencies in the Zr phases are lower than those in Ti by a factor of about $\sqrt{1/2}$. This frequency difference is similar to what we would expect by assuming the spring constants for Zr and Ti were the same, resulting in their frequencies scaling with $\sqrt{1/m}$, and taking into account that Zr has about twice the atomic mass of Ti. In this low frequency region, we further focused on a comparison between the Zr_2AlC and Ti_2AlC phases by looking into the transverse mode, which is a 2-fold degenerate branch going from Γ to A. The frequencies at point A for Zr_2AlC and Ti_2AlC are 1.344 and 1.864 THz respectively, and by renormalising these by multiplying with their respective atomic masses, Zr (∼91.2 u) and Ti (∼47.8 u), we

have a point of comparison for the stiffness of their lattices to shears parallel to their basal plane. As also noted above, the mass effect dominates the difference in frequency at lower frequency modes, with the ratio of $m\omega^2$ between the two MAX phases being almost 1. This suggests that the Zr MAX phase lattice is not softer than the Ti one, at least for this shear mode. To further compare elastic properties such as deformability between these two MAX phases, a useful indicator could also be the ratio of the shear to the bulk modulus, i.e. the ratio of the shear constant to the longitudinal elastic constant in the c direction. This ratio expressed as the shear over the longitudinal frequency at point A for the Zr_2AlC and Ti_2AlC phases is 0.63 and 0.64 respectively, again suggesting no significant difference in deformability between the two phases. On the other hand, frequency differences between the Zr and Ti MAX phases at high frequencies, in the C band, can be mostly explained by bonding differences, since these modes are strongly decoupled from the rest of the atoms and correspond mainly to C atomic vibrations. The high frequency modes in Zr-based MAX phases are slightly reduced in frequency compared to their corresponding Ti ones, suggesting lower bond stiffness in Zr-based MAX phases for the C atoms, which is also consistent with the trend in calculated bond strengths from COHP noted in Section 5.2.4.

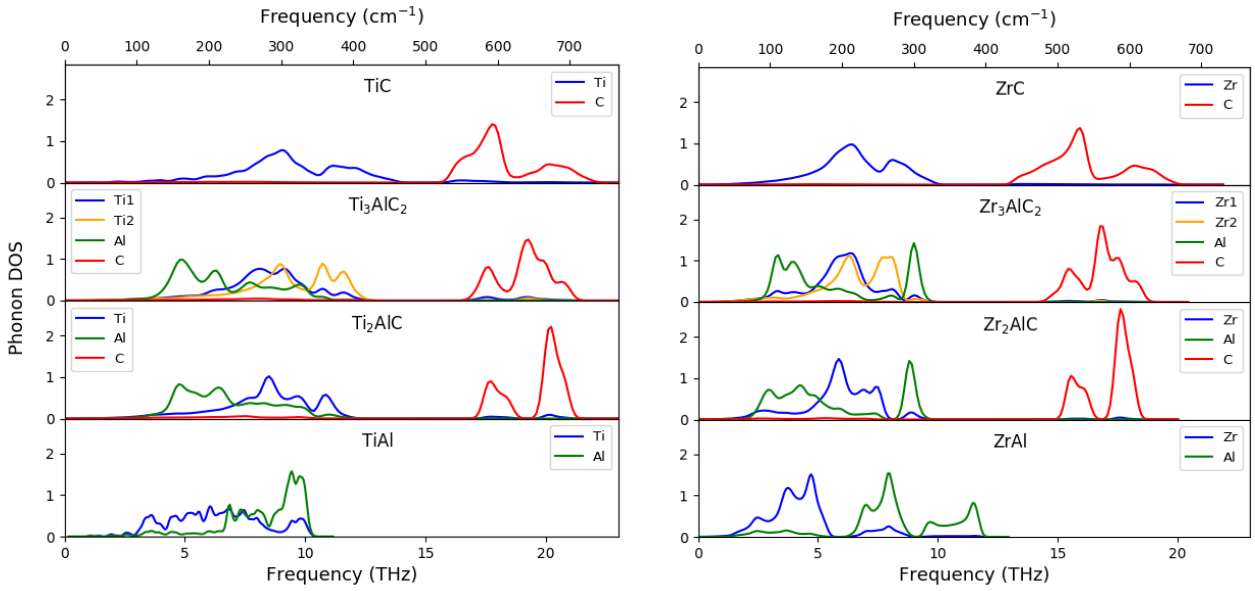

Figure 6.3: Projected phonon DOS for Zr and Ti based MAX phases and their end members.

For 312 and 211 there is a frequency, at about 4 THz for Zr and 7 THz for Ti, up to which

both unit cells have the same number of modes despite the 312 unit cell consisting of an extra Zr or Ti layer in its carbide slabs. This suggests that these carbide slabs are moving like rigid blocks in each of these compounds. These modes correspond to the lower optical modes, such as the two lower ones that are double degenerate at L and split between Γ and M resulting in four modes. At higher frequencies additional modes appear for 312 as the 3 layers of Zr in 312 allow an extra three degrees of freedom compared to the 2 layers of Zr in the 211 phases. For instance between the A and H directions at higher frequencies after the two first branches and below 13 THz, there are 7 modes in 211 and 10 in 312. Similarly, at frequencies above 13 THz there are 3 optical branches of carbon for 211 and 6 for 312.

The highest frequency at the Γ point for 211 phases is E_{2g} which is 2-fold degenerate, and corresponds to one mode frequency in two different directions in the x-y plane. There is also another nearly degenerate mode at a slightly lower frequency at the top of the band structure, in fact their difference is just 0.01 THz. This second highest frequency mode is again 2-fold degenerate, showing vibrations in the x-y plane. In the case of the highest frequency at the Γ point the Zr and C atoms are vibrating against each other, but the vibration of the C atoms is dominant. The C atoms in the two different Zr_2C slabs of a unit cell are vibrating out of phase, whereas for the mode just below the highest one the C atoms in the two slabs are vibrating in phase. The reason for this pair of very close frequencies can be explained by the layered crystal structure of the 211 phase as there is a very weak coupling between the C atoms in the separate slabs.

That is also the case for the highest band in the 312 phases, where there are two almost-degenerate modes, 17.992 and 17.930 THz for Zr_3AlC_2 and 20.225 and 20.111 THz for Ti_3AlC_2. In the 312 case the highest mode is not 2-fold degenerate as it is in 211. In these high frequency modes the M and C atoms, with C clearly dominating, are moving against each other in the z direction. The C atoms in the two Zr_3C_2 slabs are vibrating in antiphase for the highest mode and in phase for the mode just below it. Right after these two top frequency vibrations along the z axis, four 2-fold degenerate bands follow forming two pairs showing near-degeneracy in the x-y plane. Specifically, these two pairs are in the frequency window 16.8–16.9 THz, where the pair of modes with the highest frequency have frequencies 16.919 and 16.854 THz for Zr_3AlC_2

and 19.357 and 19.337 THz for Ti_3AlC_2 and the second pair at slighly lower frequency have 16.795 and 16.755 THz for Zr_3AlC_2 and 19.244 and 19.211 for Ti_3AlC_2. These pairs involve movements in the x-y plane, specifically the two layers of C atoms (or M atoms) in each slab are vibrating against each other for the pair with the highest frequency and in the same phase for the one right below it.

6.3.2 Calculation of Raman modes

In Table 6.1 the displacement contributions of the various atomic positions to the Raman active modes for the 211 and 312 MAX phases are shown. For 211 there are 24 modes in total, of which, apart from the 3 acoustic, the optical modes with symmetries defined as $\Gamma = A_{1g} + 2A_{2u} + 2B_{1g} + 2B_{2u} + 4E_{2u} + 4E_{2g} + 4E_{1u} + 2E_{1g}$ include 4 infrared ($2A_{2u}$+ $2E_u$) and 4 Raman (A_{1g} + $2E_{2g}$+ E_{1g}) active modes. Similarly for the 312 phases there are 36 phonon

$M_{n+1}AX_n$	Total modes	site (WP)	Raman active modes
211	24	M ($4f$)	A_{1g}+E_{2g}+E_{1g}
		A ($2d$)	E_{2g}
321	36	M_1 ($4f$)	A_{1g}+E_{2g}+E_{1g}
		M_2 ($2a$)	-
		A ($2b$)	E_{2g}
		X ($4f$)	A_{1g}+E_{2g}+E_{1g}

Table 6.1: Raman active modes for each site in the 211 and 312 MAX phases.

modes in total with optical modes $\Gamma = 2A_{1g} + 6E_{2g} + 4E_{1g} + 6E_{2u} + 3B_{1u} + 3B_{2g} + 3A_{2u} + 6E_{1u}$, of which 6 are infrared ($3A_{2u}$+$3E_{1u}$) and 7 Raman ($2A_{1g}$ + $2E_{1g}$ + $3E_{2g}$) active modes. It is noted that Raman active modes in 211 do not involve displacements in the C atoms ($2a$), unlike 312 for which all Raman active modes involve displacements of C atoms ($4f$), but which involve none for M_2 atoms ($2a$). The lack of involvement of C atoms in any of the Raman active modes in the 211 phases is because only one C atom exists in the carbide slab which cannot vibrate without creating a dipole, whereas in the 312 case the extra C layer in the carbide slab

enables three extra Raman active modes with the C atoms vibrating against each other in the x-y plane and the z direction.

In Figures 6.4 and 6.5 the schematics of the Raman active modes in the MAX phases are visualised. These Raman active modes are presented in ordered frequency from ω_1 to ω_4 and from ω_1 to ω_7 for 211 and 312 respectively. The 211 Raman active modes were found to correspond to vibrations involving only M and Al atoms along the z axis (longitudinal) and in the x-y plane (shear), as shown in Figure 6.4. Specifically, the E_{1g} and two E_{2g} modes involve vibrations in the basal plane with E_{1g} only corresponding to M atoms, whereas E_{2g} to both M and Al. The A_{1g} mode corresponds to longitudinal vibrations of the M atoms. The lowest frequency corresponds to the E_{2g} symmetry and the highest to A_{1g}. For 312, the predicted Raman modes with symmetry E_{2g} correspond to vibrations of M_1, Al and C atoms in the basal plane, whereas only the M_1 and C atoms are involved in the the A_{1g} and E_{1g} modes with their vibrations taking place along the z axis and in the basal plane respectively.

It is noted that between the frequencies of the first 4 and last 3 modes there is a relatively large gap, where in the former neighbouring M and C atoms are vibrating in the same direction, whereas in the latter in the opposite. These last 3 modes are in the C band, where the carbon vibrations dominate, showing a strong decoupling from the rest of the modes in the lower frequencies. The gap separating the C band from the rest of the modes, which is a general characteristic in 312 MAX phases also identified in the previous section in the phonon DOS and band structure of the MAX phases, is noted in Tables 6.2 and 6.3 for both Zr_3AlC_2 and Ti_3AlC_2. For both phases, this gap is related to the previously discussed large atomic mass difference between the M and C atoms, with Zr specifically, having over 7 times the atomic mass of a C atom. Comparison with Ti_3SiC_2 [227], where Raman spectra have been measured experimentally, also shows the clear decoupling of the carbon high frequency modes from the rest of the Raman active modes, but to a lower degree than Zr_3AlC_2, as the difference in frequency between the 4^{th} (A_{1g}) and 5^{th} (E_{2g}) mode is smaller in Ti_3SiC_2. The lowest mode, with symmetry E_{2g}, originates from shear vibrations involving M_1, Al and C atoms vibrating in the same direction. The highest mode involves only pairs of M and C atoms vibrating out of phase along the z axis. The 5^{th} and 6^{th} modes, E_{2g} and E_{1g}, are very close to each other, almost

at the same frequency, and as shown in their mode visualisation they differ only in that the M_1 atoms (or similarly the C atoms) in their separate slabs are in phase for E_{2g} and out of phase for E_{1g}. This indicates a weak coupling between the M_1 (or C atoms) atoms between the different slabs which has also been mentioned in the previous section to explain pairs of near-degenerate modes in the C band noted in the band structure. This is similar to the coupled pendulums analogy, described by two coupled harmonic oscillators vibrating in and out of phase, with the antiphase mode corresponding to higher frequency than the in-phase one, whereas if they were decoupled, both modes would vibrate in the same frequency. Due to this proximity of the two modes in the 312 phases, only 6 of the 7 predicted Raman modes have been verified experimentally for different 312 phases [225, 223, 100].

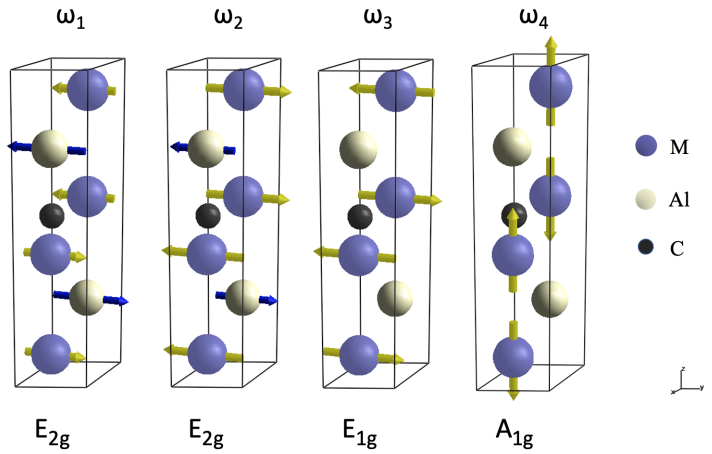

Figure 6.4: Visualisation of Raman active modes for the Zr_2AlC phase and its binary end members. The arrow lengths are proportional to the amplitude of the atomic motion.

For the Zr_3AlC_2 phase, the comparison between the experimental spectrum and the predicted peaks is shown in Fig 6.6. The sample used in this experiment consisted of roughly 50% Zr_3AlC_2, 40% ZrC and 5% $ZrAl_2$ defined based on XRD measurements. Due to the presence of coexisting phases in the sample, in addition to the Raman active modes for Zr_3AlC_2, the peaks of $ZrAl_2$ are plotted as well. No Raman-active modes are present for the pure ZrC phase due to its O_h symmetry, where each site in the crystal is a center of inversion symmetry. The predicted active modes for Zr_3AlC_2 and $ZrAl_2$ are marked as vertical lines identifying the frequency of each mode on the spectra plot.

Peaks ω_1, ω_2, ω_4 and ω_7 can be clearly identified on the experimental spectra giving sharp peaks

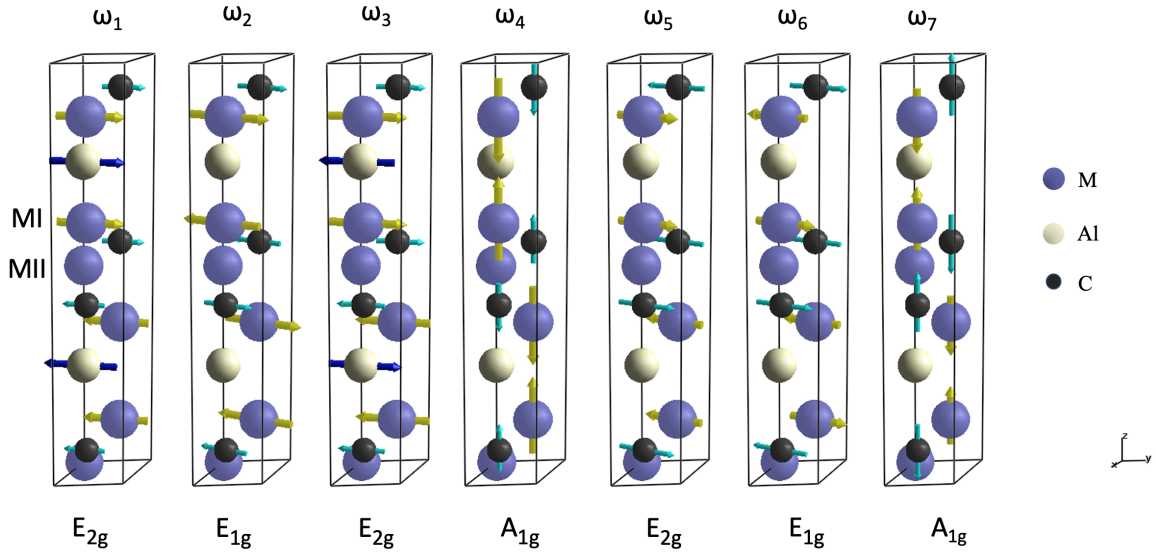

Figure 6.5: Visualisation of Raman active modes for the Zr_3AlC_2 phase. The arrow lengths are proportional to the amplitude of the atomic motion.

that closely match the predicted ones. However, some peaks in the calculated Raman spectra are not clearly visible in the experimental data, such as the predicted mode ω_3 at 170.33 (E_{2g}) due to the broad peak in the area around it and the nearly degenerate modes ω_5 at 564.37 (E_{1g}) and ω_6 at 562.20 (E_{2g}) which might correspond to the more widely split pair of peaks on either side, at about 560 and 570, or perhaps to one of these two that is too broadened to resolve the degeneracy. This discrepancy between experimental and predicted modes can be due to the proximity of their wavenumbers being too close for the experimental resolution, which is a characteristic that has also been observed in other 312 and 413 MAX phase studies [223]. Peaks matching phases other than Zr_3AlC_2 can also be seen on the spectra, in particular the predicted peak at 152.026 cm^{-1} (E_{2g}) of the $ZrAl_2$ phase is close to the peak at 154 cm^{-1} on the spectra, but this might be a coincidence, since there are no experimental peaks at frequencies anywhere close to two out of the other five predicted Raman frequencies for $ZrAl_2$.

The clarity of the Raman spectra, e.g. the number of peaks or their intensity, can also be affected by the presence of carbon vacancies [225, 223, 226, 228, 229] commonly found in synthesised MAX phases [138]. As stoichiometric ZrC has no Raman active modes, any Raman-induced peaks observed that might come from ZrC_x are due to carbon vacancies, and in particular, a study on TiC found that decreasing x in TiC_x resulted in increasing Raman peak widths

which was linked to vacancy clustering in the carbide layer [232]. Comparison between $TiC_{0.67}$ and the Ti_3SiC_2 MAX phase spectra by Amer *et al.* [228] found the presence of all observed Raman-induced peaks in $TiC_{0.67}$ in the MAX phase spectra, but with shifted positions [228].

Another factor affecting the clarity of the Raman spectra is the presence of impurities and secondary phases in the sample. It is common that MAX phase samples often contain other phases, as was also identified in the Zr_3AlC_2 sample analysed by Lyons [6], where the presence of other phases including $ZrAl_2$ was noted. For the Ti_3SiC_2 MAX phase, comparison between the mono-crystal and poly-crystal samples was made in the studies [229, 233], where in the latter Raman spectra were measured from Ti_3SiC_2 synthesised single crystals. In these studies difficulty in identifying the symmetries of the modes were explained based on the presence of secondary phases in the sample, as well as on the experimental conditions such as the laser beam wavelength. The secondary phases were found to affect the intensity, line-width and frequency of the modes [229].

The difficulty of identifying some predicted modes experimentally, as noticed for Ti_3SiC_2, occurs in both multiphase systems [229] and single crystals [233]. In both cases the low-intensity Raman peaks predicted on the perfect crystal can be obscured by the background noise, indicating the importance of the prediction of both the frequencies and intensities of the modes [229].

In the experimental Zr_3AlC_2 Raman spectra shown in Fig. 6.6, there are a number of unidentified peaks that do not align with the Raman active modes predicted for the two identified phases in the sample, Zr_3AlC_2 and $ZrAl_2$. These peaks include a quite sharp peak at around $90\,cm^{-1}$, two broad ones at around 276 and $380\,cm^{-1}$ and two broad peaks at high frequencies 553 and $576\,cm^{-1}$. In between of the latter two peaks the two closely degenerate modes of Zr_3AlC_2 are predicted. Due to these unidentified peaks Raman-active modes have also been predicted for some additional phases, possibly present in the sample. These additional phases include the Zr_2Al_3, Zr_4Al_3 besides the aforementioned $ZrAl_2$ aluminium intermetallics and the Zr_7C_6 non-stoichiometric carbide that were found to be the most competing phases of the two MAX phases in the Zr-Al-C system at standard conditions and at 0 K in Chapter 4. The

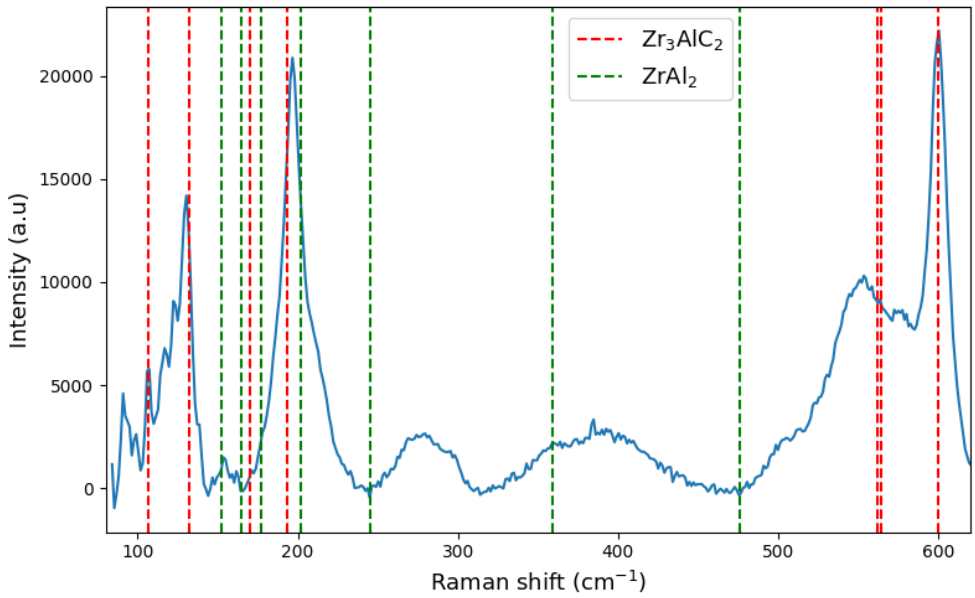

Figure 6.6: Raman spectra of Zr_3AlC_2 sample [6] with the predicted active modes for the Zr_3AlC_2 and Zr_2Al phases.

Raman-active modes for the Zr_2AlC MAX phase were also calculated.

Of particular interest are the Raman-active modes in the C band, showing a strong decoupling of the C atoms vibrations at high frequencies from the rest of the lower frequency modes. Due to the presence of the last broad split peaks at high frequencies, 553 and 576 cm^{-1}, which correspond to the upper modes in the C band resulting in three rather than two peaks, we calculated the Raman frequencies for 5 of the non-stoichiometric carbides that appear on the convex hull. In general, the presence of defects or disorder in the C sublattice would broaden the two peaks. Raman frequencies calculated for all the crystalline phases we have considered as possibly coexisting with the MAX phase are shown in Fig. 6.7. The experimental spectra of the Zr_3AlC_2 phase [6] are also shown again for comparison. From this figure, the Zr_4Al_3 and Zr_2AlC phases do not appear to align with any of the peaks. The Zr_2Al_3 phase matches the first unidentified peak at around 90 cm^{-1} and is present in the broader peak at 380 cm^{-1}. The Raman active modes of the non-stoichiometric zirconium carbides are present at high frequencies, as expected, as well as at some lower frequencies between 150 and 300 cm^{-1}. From these, the modes for Zr_3C_2, Zr_4C_3, Zr_7C_6 and Zr_8C_7 align or are close to the broad peaks at 276, 553 and 576 cm^{-1}. Zr_6C_5 does not closely match any of these broad peaks.

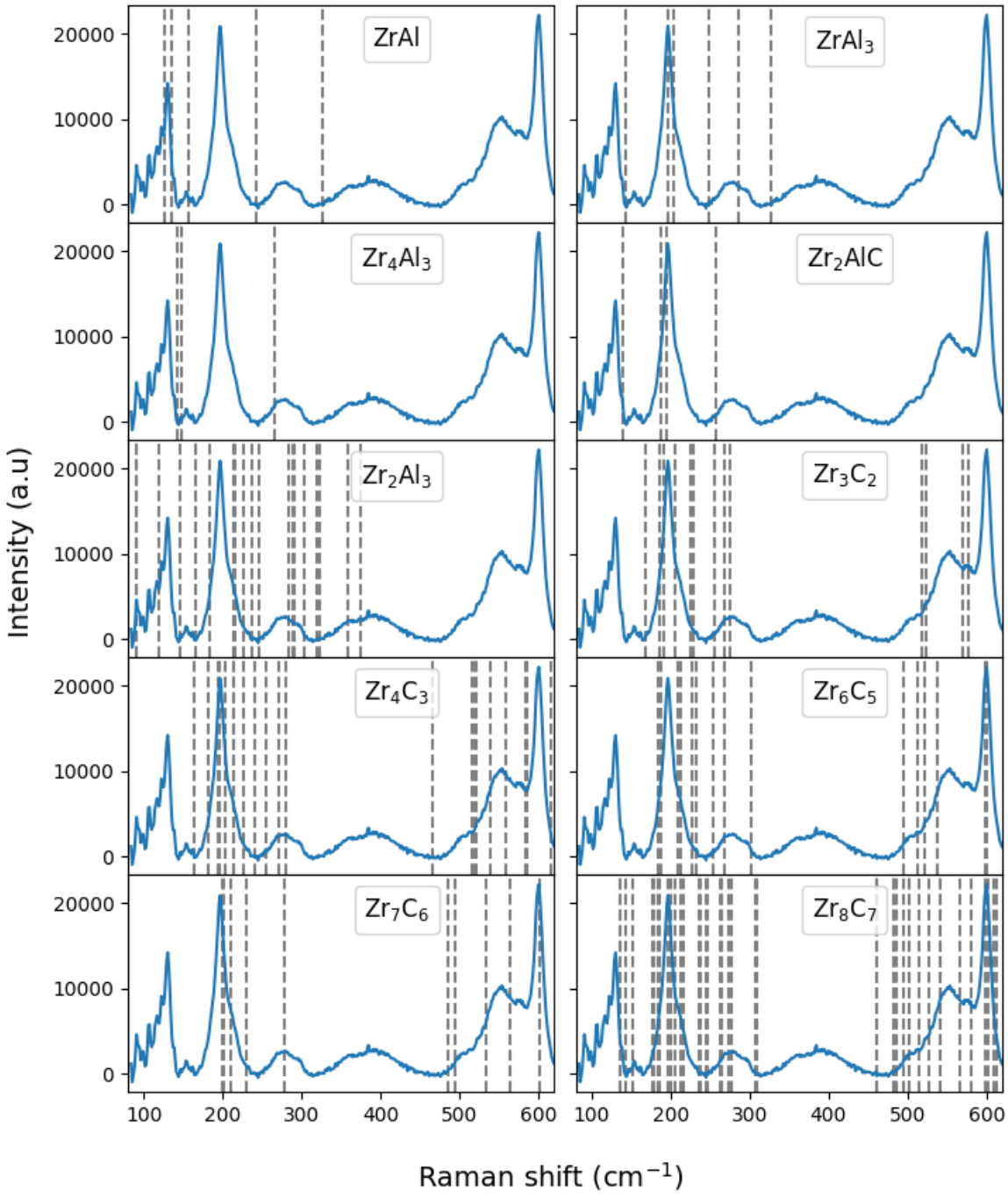

Figure 6.7: Raman spectra of Zr_3AlC_2 [6] with the predicted Raman-active modes of two intermetallics, the Zr_2AlC MAX phases and different ZrC_x carbides.

Apart from the possible existence of other defective ZrC phases discussed previously, the existence of this extra peak in the C band of the experimental spectra, close to the predicted

near-degeneracy peaks at 562.20 cm^{-1} (E_{2g}) and 564.37 cm^{-1} (E_{1g}) could be related to surface effects or to the splitting of this close degeneracy due to possible breaks in the symmetry of the phase. Surface effects can affect the selection criteria of particular bulk modes and the strength of the coupling between the surface excited modes and the bulk modes, depending on the penetration depth of the electromagnetic wave in the metal. Splitting of the degeneracy on the other hand, could be a result of vacancies in the C or Al sublattice of the 312 MAX phase which is common in MAX phases, as discussed before. This break in symmetry could also be due to interruptions of the stacking sequence along the z axis. For example the stability difference between 312 and 413 MAX phases is quite small, as shown in Chapter 4, with their formation energies having negligible differences from the convex hull. Another factor that could affect this degeneracy split, could be the grain orientation of Zr_3AlC_2 in the sample. Further research would be required to determine the importance and degree of the effect of each of the above possibilities on the existence of this extra peak in the C band.

Freq. (cm^{-1})	ω_1	ω_2	ω_3	ω_4	ω_5	ω_6	ω_7
Ti_2AlC	151.97 (E_{2g})	277.40 (E_{2g})	278.26 (E_{1g})	370.91 (A_{1g})			
exp.	153.3	260.9	270.3	358.7 [17]			
	-	266	266	359 [226]			
	149.9	262.1	268.1	365.1 [227]			
calc.	146	265	266	365 [17]			
	136	266	266	358 [226]			
	151	256	270	366 [224]			
	149	262	248	387 [227]			
Ti_3AlC_2	126.57 (E_{2g})	189.12 (E_{1g})	203.60 (E_{2g})	274.10 (A_{1g})	640.82 (E_{2g})	641.90 (E_{1g})	674.64 (A_{1g})
exp.	-	183.4	201.5	270.2	632.2	632.2	663.2 [17]
calc.	125	182	197	268	621 (E_{2g})	620 (E_{1g})	655 [17]
	128.5	185.1	202.7	277.2	622.2 (E_{2g})	617.8 (E_{1g})	664.8 [231]

Table 6.2: Predicted Raman frequencies for the Ti_2AlC and Ti_3AlC_2 MAX phases. The frequencies for the Ti-based MAX phases are compared with available theoretical and experimental data [17].

Tables 6.2 and 6.3 show the calculated Raman active modes compared with other theoretical and

experimental values for the Ti and Zr based MAX phases respectively. Table 6.4 contains the Raman active modes of Zr intermetallics considered competing phases for the Zr_3AlC_2 phase. For the Ti_2AlC phase our calculations overestimate the experimental values of ω_2–ω_4 by 2–6% compared to the three different studies [17, 226, 227], while the difference with other theoretical results is between 1–11% [17, 226, 224, 227]. Our calculations for Ti_3AlC_2 overestimate the experimental values by Presser *et al.* [17] by a maximum of 3% which corresponds to mode ω_2. The rest of the modes were found overestimated by less than 2% with a minimum of 1% for ω_3. The differences with other calculations [17, 231] is between 1–4%. For the phonon calculations, the methods used in the aforementioned literature were the direct method, used in our current study and the DFT studies [226, 224, 227], and the standard density functional perturbation theory, applied in the study by Li *et al.* [231].

For the Zr-based MAX phases, no experimental Raman analysis was found reported in the literature. Table 6.3 shows our calculations for Zr_2AlC and Zr_3AlC_2 with experimental measurements [6] for Zr_3AlC_2. Our calculations for Zr_3AlC_2 are in good agreement with the experimental values, with an underestimation of 0.55% and 1.9% for ω_1 and ω_4 and an overestimation of 0.38% and 0.023% for ω_2 and ω_7. The study by Bai *et al.* [225] shows a larger difference than our results with the experimental values between 1–6%, with the largest difference noted for ω_2.

Freq. (cm^{-1})	ω_1	ω_2	ω_3	ω_4	ω_5	ω_6	ω_7
Zr_2AlC	139.98 (E_{2g})	194.62 (E_{2g})	187.34 (E_{1g})	257.53 (A_{1g})			
calc.	129	186	179	238 [225]			
Zr_3AlC_2	106.41 (E_{2g})	132.51 (E_{1g})	170.33 (E_{2g})	193.16 (A_{1g})	562.20 (E_{2g})	564.37 (E_{1g})	600.14 (A_{1g})
exp.	107	132	-	197	-	-	600/605
calc.	109	140	16?	189	527	529	593 [225]

Table 6.3: Predicted Raman frequencies for the Zr_2AlC and Zr_3AlC_2 MAX phases. These frequencies are compared with experimental measurements [6].

Freq. (cm^{-1})	ω_1	ω_2	ω_3	ω_4	ω_5	ω_6	ω_7
$ZrAl_3$	143.44 (E_g)	197.47 (A_{1g})	203.20 (A_{1g})	248.76 (B_{1g})	285.77 (E_g)	328.01 (E_g)	
$ZrAl_2$	152.03 (E_{2g})	164.79 (E_{1g})	177.45 (A_{1g})	202.07 (E_{2g})	245.07 (E_{1g})	359.02 (E_{2g})	475.96 (A_{1g})
ZrAl	39.69 (B_{3g})	127.07 (B_{3g})	135.68 (B_{1g})	157.51 (A_g)	242.78 (B_{1g})	326.71 (A_g)	
Zr_4Al_3	143.15 (E_{1g})	147.57 (E_{2g})	264.99 (A_{1g})				

Table 6.4: Predicted frequencies of Raman active modes for possibly competing intermetallics.

Table 6.5: Predicted Raman-active frequencies for possibly competing binaries to the Zr-based MAX phases.

Freq. (cm^{-1})	Zr_2Al_3	Zr_3C_2	Zr_4C_3	Zr_6C_5	Zr_7C_6	Zr_8C_7
ω_1	90.72 (B_1)	110.52 (B_{3g})	164.75 (B_g)	184.96 (B_g)	198.95 (A_g)	136.02 (E)
ω_2	91.54 (A_2)	121.88 (B_{2g})	181.22 (B_g)	188.65 (A_g)	200.80 (E_g)	136.81 (A_1)
ω_3	119.68 (A_1)	168.59 (B_{1g})	194.16 (A_g)	209.20 (B_g)	210.93 (A_g)	144.19 (T_2)
ω_4	137.87 (B_2)	186.90 (B_{1g})	197.07 (A_g)	213.95 (A_g)	229.98 (E_g)	151.51 (E)
ω_5	146.94 (A_2)	187.80 (B_{2g})	203.55 (B_g)	228.17 (B_g)	249.35 (A_g)	177.08 (T_2)
ω_6	165.21 (A_2)	190.41 (B_{2g})	213.19 (B_g)	232.27 (A_g)	278.47 (E_g)	179.80 (E)
ω_7	165.89 (B_1)	191.03 (A_g)	214.56 (A_g)	253.43 (B_g)	486.12 (A_g)	184.59 (T_2)
ω_8	166.22 (B_2)	192.85 (B_{3g})	226.44 (B_g)	268.37 (A_g)	494.47 (E_g)	186.65 (E)
ω_9	184.48 (A_1)	199.35 (B_{3g})	240.03 (A_g)	302.16 (A_g)	534.04 (E_g)	196.84 (T_2)
ω_{10}	213.47 (A_2)	206.13 (B_{1g})	255.65 (B_g)	495.32 (B_g)	563.76 (A_g)	200.92 (E)
ω_{11}	215.00 (B_1)	215.51 (B_{3g})	271.00 (A_g)	513.90 (A_g)	602.45 (A_g)	205.25 (T_2)
ω_{12}	219.37 (B_2)	225.24 (A_g)	280.55 (A_g)	522.36 (B_g)	622.57 (E_g)	213.41 (A_1)
ω_{13}	227.08 (A_1)	228.34 (B_{1g})	466.56 (B_g)	537.58 (B_g)		217.24 (T_2)
ω_{14}	238.06 (B_1)	230.37 (B_{2g})	515.41 (A_g)	598.91 (B_g)		235.65 (T_2)
ω_{15}	246.59 (A_1)	246.83 (B_{2g})	519.05 (B_g)	600.21 (A_g)		238.67 (T_2)
ω_{16}	255.43 (B_2)	255.17 (A_g)	522.14 (A_g)			246.04 (T_2)
ω_{17}	283.52 (B_1)	268.75 (A_g)	539.64 (B_g)			246.29 (E)
ω_{18}	288.30 (A_1)	274.86 (B_{1g})	558.99 (B_g)			263.02 (T_2)

(TABLE 6.5 continued)

Freq. (cm^{-1})	Zr_2Al_3	Zr_3C_2	Zr_4C_3	Zr_6C_5	Zr_7C_6	Zr_8C_7
ω_{19}	290.41 (A_2)	485.52 (B_{3g})	583.72 (A_g)			264.29 (E)
ω_{20}	302.85 (B_1)	487.66 (B_{2g})	585.14 (B_g)			265.60 (A_1)
ω_{21}	304.48 (B_2)	506.62 (B_{2g})	615.63 (B_g)			274.43 (T_2)
ω_{22}	319.27 (A_2)	518.22 (B_{1g})				277.56 (E)
ω_{23}	323.12 (A_1)	524.70 (A_g)				308.33 (T_2)
ω_{24}	326.61 (B_2)	536.31 (B_{3g})				310.32 (A_1)
ω_{25}	359.25 (A_2)	571.20 (B_{1g})				460.87 (E)
ω_{26}	375.49 (B_1)	575.42 (B_{2g})				461.65 (T_2)
ω_{27}	389.09 (B_2)	576.98 (A_g)				482.10 (T_2)
ω_{28}		580.25 (B_{3g})				482.38 (A_1)
ω_{29}		594.77 (B_{3g})				486.26 (E)
ω_{30}		611.19 (B_{2g})				494.71 (T_2)
ω_{31}						502.67 (T_2)
ω_{32}						503.37 (E)
ω_{33}						514.31 (E)
ω_{34}						527.91 (T_2)
ω_{35}						541.04 (E)
ω_{36}						541.50 (T_2)
ω_{37}						566.88 (T_2)
ω_{38}						580.68 (E)
ω_{39}						599.08 (A_1)
ω_{40}						602.60 (T_2)
ω_{41}						609.13 (T_2)
ω_{42}						612.53 (E)

6.4 Conclusions

In this chapter phonon calculations were conducted, with analysis of the phonon band structure and DOS being performed for the $Ti_{n+1}AlC_n$ and $Zr_{n+1}AlC_n$ MAX phases and their end members. Characteristics of the MAX phase band structures and DOS were identified such as the low dispersion particularly at frequencies above 7.5 THz mostly observed for Zr-based phases, attributed to the relatively distinctive Al phonon DOS peak, especially at frequencies between 8.5–9.5 THz. Another characteristic noticed is the large band gap between the C band and the lower frequency modes, which is evidenced in both systems, indicating a strong decoupling between C dominated atomic vibrations and the rest of the vibrations. These characteristics were attributed to the large mass differences between Zr and Al for the first characteristic, and between M and C for the second, with Zr specifically having over 7 times the atomic mass of a C atom. Comparison of the band structures between the Zr and Ti MAX phases also showed that the mass effect dominated the difference in frequency at lower frequency modes. Specifically, this was the case for the difference in slope of the transverse branch between the Γ and A points for Zr_2AlC and Ti_2AlC. The elastic stiffness or deformability of these two MAX phases was further examined by comparing the ratios of their shear constant to their longitudinal elastic constant in the c direction. This comparison indicated that the Zr MAX phase lattice is not softer than the Ti one, though Zr_2AlC was found to have a slightly softer lattice based on their stress-strain curves in Chapter 3. As also noted in that chapter, stiffness or deformability can be an important property requirement for candidate coating materials for nuclear fuel cladding; our calculations, however, indicate no significant or systematic difference in the stiffness between Zr and Ti MAX phases, with their difference possibly being on the order of 10% either way.

Calculations of Raman-active phonon frequencies at the Γ point for these phases were conducted and assignment of their corresponding mode symmetry was made. For the Ti-based MAX phases the predicted Raman-active frequencies showed a good agreement of 2–6% compared to the experimental values reported in the literature. In the Zr-Al-C system the frequencies of Raman-active MAX phases and their possibly competing aluminides and carbides were calcu-

lated. In the Zr_3AlC_2 experimental spectra [6], 4 of the 7 theoretical Zr_3AlC_2 modes could be identified with a good agreement, with a difference of less than 2%, and the presence of $ZrAl_2$ was indicated but not conclusively proven, as two of the six theoretical Raman frequencies were not close to any experimental peak. Among the different competing phases considered, particular attention was paid to the presence of the ZrC phase reported in the sample by the XRD measurements [6] to possibly explain the two broad peaks observed in the C band at 553 and 576 cm^{-1}. For this reason the effect of vacancies in the carbide was examined by considering a number of non-stoichiometric Zr carbides. Overall though, no clear indication of the presence of any specific non-stoichiometric carbide and competing aluminide phases was found in the experimental spectra.

Chapter 7

Conclusions and future work

In this work, we set out to develop an improved understanding of the MAX phases in the Zr-Al-C and Ti-Al-C systems by predicting and comparing their structural, elastic, thermophysical and electronic properties as well as conducting phonon and bonding analysis and predicting their thermodynamic stability. Of particular importance in our study was the thermodynamic stability of the Zr-based MAX phases in the context of the M-A-X ternary phase diagrams with respect to their competing binary and ternary compounds, given their reported difficultly in synthesis and low phase purity levels. The theoretical framework chosen for this work was based on DFT with the lattice vibrations being treated within the quasiharmonic approximation.

This research first focused on, in Chapter 3, the prediction of structural and thermophysical properties for $Zr_{n+1}AlC_n$ phases and their end members and their comparison with the closely related and contrastingly well-studied phases in the Ti-Al-C system. During this process, it was found that the choice of PBEsol over other XC functionals, as tested for Zr_2AlC specifically, showed a close agreement with experiment with less than 1% difference in the lattice constants at room temperature. Particular attention was paid to Zr_2AlC, for which electronic excitations were considered in addition to the vibrational free energy, and the free energy was expressed as a function of the temperature and strains ($\epsilon_1 = \epsilon_2,\ \epsilon_3$). This also allowed for the prediction of three of Zr_2AlC's temperature dependant elastic constants, for which the electronic contribution was found to be around 2% at 1400 K and an agreement of better than 3.7% was found compared

to other predictions at $T = 0\,\mathrm{K}$. With regards to elastic properties in the MAX phases in general, calculations of the distribution of strain between the nanoscale layers of the phases showed the layers of metal carbide being stiffer than their alternating Al layers, as would be expected. As the thickness of this carbide layer increases, the MAX phases' elastic properties were also observed to approach those of the metal carbide, as indicated by the calculated MAX phase and metal carbide stress-strain curves in both Zr-Al-C and Ti-Al-C systems. For our calculations of equilibrium free energy in the quasiharmonic approximation we derived a simple criterion that allowed us to neglect the change in the c/a ratio of the unit cell with temperature, a common assumption in calculations of this kind, but not to our knowledge justified previously. Other thermophysical properties such as thermal expansion, heat capacity and temperature dependant bulk modulus were studied under the c/a constraint for $Zr_{n+1}AlC_n$ and $Ti_{n+1}AlC_n$ MAX phases and comparisons and trends were identified. Particularly, the Ti-based MAX phases show lower heat capacity than the Zr-based ones with the heat capacity increasing as n decreases. The opposite trend was noted for the bulk modulus, with its value increasing with n and the Zr-based MAX phases showing lower bulk moduli compared to their Ti-based counterparts. Comparison with the literature showed that heat capacity in particular was considerably different at low temperature between the quasiharmonic and quasiharmonic Debye methods, indicating the importance of considering the full phonon spectra in the free energy calculation for those phases.

As mentioned at the start of this chapter, synthesis of the Zr-based MAX phases, and in particular of Zr_2AlC, is reportedly challenging, and even when achieved, the presence of secondary phases has been unavoidable. Additionally, higher phase-purity of Zr_2AlC was only achieved with the presence of additional elements. These introduce uncertainty whether the phase composition would change in a component of such a material in service. This uncertainty was the motivation for the next focus of our study, in Chapter 4, on the prediction of the thermodynamic stability of MAX phases in the Zr-Al-C system and their comparison with those in the Ti-Al-C system. The thermodynamic stability was calculated against any competing binary and ternary known compounds in both systems via the construction of a convex hull as a function of temperature. By introducing these finite-temperature convex hulls in the ternary space

of compositions, we then could identify differences in the predicted thermodynamic stability of the MAX phases between the two systems and explain how certain small energy differences necessitated the very different options for their synthesis, despite their very close chemical and structural resemblance. At the starting point of our calculations, at 0 K, and neglecting the zero point energy, based on the predictions of our chosen functional in this study, PBEsol, the Zr_2AlC and Zr_3AlC_2 MAX phases were found to be thermodynamically unstable with respect to decomposition into carbides and aluminides in the Zr-Al-C system with their distances above the hull being 23 meV/atom and 4 meV/atom respectively. As a test of the robustness of our conclusions, the effect of other XC functionals was examined, finding that both phases remained unstable. The effect of temperature on the convex hull by the inclusion of vibrational and electronic excitations in the free energy was found to reduce the relative free energy of both Zr-based MAX phases. Thus in the 500–600 K temperature range, Zr_3AlC_2 becomes stable although Zr_2AlC remains unstable up to 1800 K where its distance reaches less than 5 meV/atom above the hull. Therefore our predictions find no reason to expect that a pure $Zr_{n+1}AlC_n$ MAX phase that would be stable at room temperature can be synthesised at all. Other research has shown that substitutional impurities e.g. Nb and Si included in these MAX phases can result in a higher level of phase-purity being achieved during synthesis, however the quantitative explanation of this impurity effect is an open question for future research. In a detailed comparison with corresponding phases in Ti-Al-C we found the 211 and 312 MAX phases in this system more stable than their competing phases at all temperatures. This is consistent with the earlier discovery of these Ti based MAX phases and the higher difficulty in synthesis experienced for MAX phases in Zr-Al-C. During this process, we introduced a simple model to explain the calculated linear behaviour of the formation energy of $M_{n+1}AX_n$ with respect to n for $n > 2$, which considers the MAX phases' energy to be the sum of a constant excess energy for each Al layer and a metal carbide part. This model demonstrates why as n increases above $n = 2$ in MAX phases, stability can at best only be marginally increased.

In our study, particular focus was given to the thermodynamic stability of phases in the Zr-Al system after large discrepancies were noted in the reported thermodynamic data, with studies mostly disagreeing on the stability of ZrAl. In point of fact, in published Zr-Al system phase

diagrams, ZrAl is shown to be a stable line-compound under around 1000 K, whereas our calculations on the other hand predict it unstable at any temperature, in agreement with other published $T = 0$ K predictions.

Having found the MAX phases in Zr-Al-C less thermodynamically stable than ones in Ti-Al-C, in the final section of this chapter we analysed their geometrical distortion as a possible explanation to these predicted differences. In particular, we examined the effect of the degree of geometrical distortion of the octahedra in the Zr_2AlC and Ti_2AlC MAX phases compared to the ideal equilibrium values in ZrC. Further to that the energy involved by varying the degree of distortion in the octahedra as well as in the Al layers of the MAX phases was calculated. No clear link was found with these areas, however, to explain the predicted differences in their stability. The Zr-based MAX phases are predicted either unstable or metastable, whereas the Ti-based ones are always predicted to be stable.

In an effort to further understand this difference in the thermodynamic stability between the two systems, we then attempted to provide a deeper explanation that explicitly links these differences with the electronic structure of the MAX phases or their competing compounds. As an initial step, the electronic structure was studied by calculating the total and partial DOS. Further chemical bonding analysis was performed by calculating the charge density difference and charge transfer, by employing different charge partition concepts, namely the Bader, Mulliken and DDEC methodologies. To gain insight into the covalent bonding and quantify the bond strength between different atomic pairs, bond orders based on the DDEC and pCOHP analysis were calculated and the results were compared. The different methods used in this chapter agreed on the general well-established chemical bonding characteristics of MAX phases, such as confirming their mixed metallic-ionic-covalent bonding nature. The M-C bonding in the carbide layer was also found to be the strongest followed by the relatively weaker M-Al and even weaker Al-Al interactions, with the weakest interactions overall being the C-C and Al-C bonds. In the 312 phases, the M_1-C bonds were found to be stronger than the M_2-C bonds and the M_1-C bond strength was found to increase from the 211 to the 312 phases. The different methods were further found to agree on certain trends between the MAX phases and their end members. For example, the M_1-C bond order was found to be higher in the MAX phases than in

their corresponding carbides. In terms of the atomic charge, q_I, the three methods consistently showed that the highest charge transfer on the M atoms occurs in the carbides and the lowest in the aluminides. Apart from the commonly agreed characteristics, and despite the overall high chemical resemblance of the $Zr_{n+1}AlC_n$ and $Ti_{n+1}AlC_n$ phases, the charge values and some of the bond strength trends were found to depend strongly on the method used. The chemical differences between the two systems of MAX phases that could possibly explain their difference in the thermodynamic stability might be masked by the details of these inconsistencies between the methods.

During the course of this work, experimentalists working within the project became keen to identify the phases they were finding while attempting the synthesis of Zr-based MAX phases, such as a Zr_3AlC_2 sample prepared by Lyons [6], with their main method of analysis being based on Raman spectroscopy. This provided an opportunity, in the context of this thesis, to put DFT into practice as a tool of analysis for experimental results. Phonon calculations conducted to assist in identifying what phases were present, showed that some of the Zr_3AlC_2 MAX phase frequencies were actually very clearly visible in the experimental results, whereas for other possibly competing phases in the sample no clear indication was found. Starting with this aim in Chapter 6, we first conducted phonon calculations for the $Zr_{n+1}AlC_n$ and $Ti_{n+1}AlC_n$ MAX phases and their end members and we analysed their phonon band structure and DOS, which were presented at the beginning of the chapter before our discussion of the predicted Raman active frequencies and comparison with the experimental spectra. One of the characteristics noticed in the band structures of these materials, was the low dispersion particularly at frequencies above 7.5 THz and mostly observed for Zr-based phases. This could be assigned to the relatively distinctive Al phonon DOS peak, especially at frequencies between 8.5–9.5 THz for the Zr-based phases, that can be explained by the large atomic mass difference between Zr and Al which is almost double that of Ti and Al, leading to this more decoupled Al vibrations from the rest of the atoms in the Zr case. Another band structure characteristic noticed for these phases was the large band gap between the C band and the rest of the lower frequency modes, indicating a strong decoupling between C dominated atomic vibrations and the rest of the vibrations. This is once more explained by the large mass difference between the

M and C atoms, with Zr specifically having over 7 times the atomic mass of a C atom. Because of the larger mass of Zr this decoupling is more pronounced for Zr-based MAX phases compared to phases from other systems e.g. compared with the Raman spectra of Ti_3SiC_2 [227]. Given the experimental analysis was done with Raman spectroscopy, Raman-active phonon frequencies for the $Zr_{n+1}AlC_n$ and $Ti_{n+1}AlC_n$ MAX phases were identified by their corresponding mode symmetry. From the Raman spectra, typical characteristics were identified, including the lack of C atom ($2a$) displacements in 211 Raman active modes, which are unlike those of 312 that do involve displacements in C atoms ($4f$) but not M_2 atoms ($2a$). Another typical characteristic observed in the spectra, were the two close, almost degenerate, Raman modes of the 312 MAX phases, which are also reported in the literature as a main reason experimental predictions have generally only measured up to 6 out of the 7 predicted Raman active modes. This proximity in the frequency of these two modes that correspond to the in and out of phase vibrations of the M or C atoms in the adjacent layers, can be explained by a very weak coupling of the atoms between the MAX phases' layers. For the Ti-based MAX phases our predicted Raman active frequencies showed a good agreement, between 2–6%, with the experimental values reported in the literature. Regarding the Zr_3AlC_2 sample prepared by Lyons [6], 4 of the 7 modes could be identified from the experimental Raman spectra based on the predicted Raman-active frequencies, with less than 2% difference to the experimental findings by Lyons [6], and the presence of a $ZrAl_2$ secondary phase was also indicated. Raman-active mode predictions were additionally made for a number of other possibly competing phases, aluminides and carbides mainly appearing stable on the convex hull, in order to explain the presence of yet unidentified peaks in the experimental spectra. Particular attention was paid to the presence of the ZrC phase reported in the sample by the XRD measurements [6]. Specifically, to possibly explain the two broad peaks in the experimental spectra in the C band at 553 and 576 cm^{-1}, the effect that vacancies might have on the Raman spectra was also investigated by calculating the Raman active frequencies for a number of different non-stoichiometric ZrC phases: Zr_3C_2, Zr_4C_3, Zr_6C_5, Zr_7C_6 and Zr_8C_7. No clear indication of the existence of any of these non-stoichiometric carbides was noticed however, therefore future research on other possibilities of explaining these unidentified peaks in the C band of the Raman spectra could be explored.

Such possible explanations could include symmetry breaks in the MAX phase structure, such as vacancies in C or Al sublattices or breaking of the stacking symmetry, e.g. by alternating 312 and 413 phases, or effects of grain orientation.

Bibliography

[1] Zapata-Solvas, E. *et al.* Synthesis and physical properties of $(Zr_{1-x},Ti_x)_3AlC_2$ MAX phases. *Journal of the American Ceramic Society* **100**, 3393–3401 (2017).

[2] Horlait, D., Grasso, S., Chroneos, A. & Lee, W. E. Attempts to synthesise quaternary MAX phases (Zr,M)$_2$AlC and Zr_2(Al,A)C as a way to approach Zr_2AlC. *Materials Research Letters* **4**, 137–144 (2016).

[3] Lapauw, T. *et al.* The double solid solution (Zr, Nb)$_2$(Al, Sn)C MAX phase: a steric stability approach. *Scientific Reports* **8**, 12801 (2018).

[4] Lapauw, T. *et al.* Synthesis of the new MAX phase Zr_2AlC. *Journal of the European Ceramic Society* **36**, 1847–1853 (2016).

[5] Lapauw, T. *et al.* Synthesis of the novel Zr_3AlC_2 MAX phase. *Journal of the European Ceramic Society* **36**, 943–947 (2016).

[6] Lyons, J. *To be published* (2021). Institution: Imperial College London.

[7] Ouadha, I., Rached, H., Azzouz-Rached, A., Reggad, A. & Rached, D. Study of the structural, mechanical and thermodynamic properties of the new MAX phase compounds $(Zr_{1-x}Ti_x)_3AlC_2$. *Computational Condensed Matter* **23**, e00468 (2020).

[8] Barsoum, M. W. *et al.* Thermal and electrical properties of Nb_2AlC, (Ti, Nb)$_2$AlC and Ti_2AlC. *Metallurgical and Materials Transactions A* **33**, 2775–2779 (2002).

[9] Drulis, M. K., Drulis, H., Gupta, S., Barsoum, M. W. & El-Raghy, T. On the heat capacities of M_2AlC (M = Ti, V, Cr) ternary carbides. *Journal of Applied Physics* **99**, 093502 (2006).

[10] Alatalo, M., Weinert, M. & Watson, R. E. Stability of Zr-Al alloys. *Physical Review B* **57**, R2009–R2012 (1998).

[11] Pisch, A. *et al.* Investigation of the thermodynamic properties of Al_4C_3: A combined DFT and DSC study. *Computational Materials Science* **171**, 109100 (2020).

[12] Hong, T. *et al.* Crystal structure, phase stability, and electronic structure of Ti-Al intermetallics: Ti_3Al. *Physical Review B* **43**, 1940–1947 (1991).

[13] Emsley, J. *Nature's building blocks: an AZ guide to the elements* (Oxford University Press, 2011).

[14] Manz, T. A. Introducing DDEC6 atomic population analysis: part 3. Comprehensive method to compute bond orders. *Royal Society of Chemistry Advances* **7**, 45552–45581 (2017).

[15] Manz, T. A. & Limas, N. G. Introducing DDEC6 atomic population analysis: part 1. Charge partitioning theory and methodology. *Royal Society of Chemistry Advances* **6**, 47771–47801 (2016).

[16] Limas, N. G. & Manz, T. A. Introducing DDEC6 atomic population analysis: part 4. Efficient parallel computation of net atomic charges, atomic spin moments, bond orders, and more. *Royal Society of Chemistry Advances* **8**, 2678–2707 (2018).

[17] Presser, V. *et al.* First-order Raman scattering of the MAX phases: Ti_2AlN, $Ti_2AlC_{0.5}N_{0.5}$, Ti_2AlC, $(Ti_{0.5}V_{0.5})_2AlC$, V_2AlC, Ti_3AlC_2, and Ti_3GeC_2. *Journal of Raman Spectroscopy* **43**, 168–172 (2012).

[18] Luo, F., Guo, Z.-c., Zhang, X.-l., Yuan, C.-y. & Cai, L.-c. *Ab initio* Predictions of Structural and Thermodynamic Properties of Zr_2AlC Under High Pressure and High Temperature. *Chinese Journal of Chemical Physics* **28**, 263–268 (2015).

[19] Nasir, M. T. *et al.* Zirconium metal-based MAX phases Zr_2AC (A = Al, Si, P and S): A first-principles study. *International Journal of Modern Physics B* **28**, 1550022 (2014).

[20] Wang, T., Jin, Z. & Zhao, J.-C. Thermodynamic assessment of the Al-Zr binary system. *Journal of Phase Equilibria* **22**, 544 (2001).

[21] Maciąg, T. Enthalpy of formation of intermetallic phases from Al–Zr system determined by calorimetric solution method. *Journal of Thermal Analysis and Calorimetry* **134**, 423–431 (2018).

[22] Kematick, R. J. & Franzen, H. F. Thermodynamic study of the zirconium-aluminum system. *Journal of Solid State Chemistry* **54**, 226–234 (1984).

[23] Murray, J., Peruzzi, A. & Abriata, J. P. The Al-Zr (aluminum-zirconium) system. *Journal of Phase Equilibria* **13**, 277–291 (1992).

[24] Ghosh, G. & Asta, M. First-principles calculation of structural energetics of Al–TM (TM=Ti, Zr, Hf) intermetallics. *Acta Materialia* **53**, 3225–3252 (2005).

[25] Hug, G., Jaouen, M. & Barsoum, M. W. X-ray absorption spectroscopy, EELS, and full-potential augmented plane wave study of the electronic structure of Ti_2AlC, Ti_2AlN, Nb_2AlC, and $(Ti_{0.5}Nb_{0.5})_2AlC$. *Physical Review B* **71**, 024105 (2005).

[26] Medvedeva, N. I., Novikov, D. L., Ivanovsky, A. L., Kuznetsov, M. V. & Freeman, A. J. Electronic properties of Ti_3SiC_2-based solid solutions. *Physical Review B* **58**, 16042–16050 (1998).

[27] Nowotny, V. H. Strukturchemie einiger Verbindungen der Übergangsmetalle mit den elementen C, Si, Ge, Sn. *Progress in Solid State Chemistry* **5**, 27–70 (1971).

[28] Ivchenko, V. I. & Kosolapova, T. Y. Conditions of preparation of ternary Ti-Al-C alloy powders. *Soviet Powder Metallurgy and Metal Ceramics* **14**, 431–433 (1975).

[29] Ivchenko, V. I., Lesnaya, M. I., Nemchenko, V. F. & Kosolapova, T. Y. Preparation and some properties of the ternary compound Ti_2AlN. *Soviet Powder Metallurgy and Metal Ceramics* **15**, 293–295 (1976).

[30] Jeitschko, W., Nowotny, H. & Benesovsky, F. Kohlenstoffhaltige ternäre Verbindungen (H-phase). *Monatshefte für Chemie und verwandte Teile anderer Wissenschaften* **94**, 672–676 (1963).

[31] Jeitschko, W. & Nowotny, H. Die Kristallstruktur von Ti_3SiC_2—ein neuer Komplexcarbid-Typ. *Monatshefte für Chemie-Chemical Monthly* **98**, 329–337 (1967).

[32] Wolfsgruber, H., Nowotny, H. & Benesovsky, F. Die Kristallstruktur von Ti_3GeC_2. *Monatshefte für Chemie und verwandte Teile anderer Wissenschaften* **98**, 2403–2405 (1967).

[33] Pietzka, M. A. & Schuster, J. C. Summary of constitutional data on the Aluminum-Carbon-Titanium system. *Journal of Phase Equilibria* **15**, 392–400 (1994).

[34] Barsoum, M. W. *et al.* High-Resolution Transmission Electron Microscopy of Ti_4AlN_3, or $Ti_3Al_2N_2$ Revisited. *Journal of the American Ceramic Society* **82**, 2545–2547 (1999).

[35] Manoun, B., Saxena, S. K., El-Raghy, T. & Barsoum, M. W. High-pressure x-ray diffraction study of Ta_4AlC_3. *Applied Physics Letters* **88**, 201902 (2006).

[36] Hu, C. *et al.* Nb_4AlC_3: A new compound belonging to the MAX phases. *Scripta Materialia* **57**, 893–896 (2007).

[37] Barsoum, M. W. & El-Raghy, T. Synthesis and characterization of a remarkable ceramic: Ti_3SiC_2. *Journal of the American Ceramic Society* **79**, 1953–1956 (1996).

[38] Barsoum, M. W., Brodkin, D. & El-Raghy, T. Layered machinable ceramics for high temperature applications. *Scripta Materialia* **36**, 535–541 (1997).

[39] Hu, C., Zhang, H., Li, F., Huang, Q. & Bao, Y. New phases' discovery in MAX family. *International Journal of Refractory Metals and Hard Materials* **36**, 300–312 (2013).

[40] Zhou, Y., Meng, F. & Zhang, J. New MAX-Phase Compounds in the V–Cr–Al–C System. *Journal of the American Ceramic Society* **91**, 1357–1360 (2008).

[41] Tunca, B. *et al.* Synthesis and Characterization of Double Solid Solution $(Zr,Ti)_2(Al,Sn)C$ MAX Phase Ceramics. *Inorganic Chemistry* **58**, 6669–6683 (2019).

[42] Lane, N. J., Naguib, M., Lu, J., Hultman, L. & Barsoum, M. W. Structure of a new bulk $Ti_5Al_2C_3$ MAX phase produced by the topotactic transformation of Ti_2AlC. *Journal of the European Ceramic Society* **32**, 3485–3491 (2012).

[43] Dahlqvist, M., Alling, B. & Rosén, J. Stability trends of MAX phases from first principles. *Physical Review B* **81**, 220102 (2010).

[44] Aryal, S., Sakidja, R., Barsoum, M. W. & Ching, W.-Y. A genomic approach to the stability, elastic, and electronic properties of the MAX phases. *Physica Status Solidi B* **251**, 1480–1497 (2014).

[45] Ohmer, D., Qiang, G., Opahle, I., Singh, H. K. & Zhang, H. High-throughput design of 211-M_2AX compounds. *Physical Review Materials* **3**, 053803 (2019).

[46] Pino, E. S., Abe, A. Y. & Giovedi, C. The quest for safe and reliable fuel cladding materials. *INAC 2015: international nuclear atlantic conference Brazilian nuclear program State policy for a sustainable world, Brazil* (2015).

[47] Duan, Z. *et al.* Current status of materials development of nuclear fuel cladding tubes for light water reactors. *Nuclear Engineering and Design* **316**, 131–150 (2017).

[48] Tallman, D. J. *et al.* Effects of neutron irradiation of Ti_3SiC_2 and Ti_3AlC_2 in the 121-1085℃ temperature range. *Journal of Nuclear Materials* **484**, 120–134 (2017).

[49] Wang, X. H. & Zhou, Y. C. Layered Machinable and Electrically Conductive Ti_2AlC and Ti_3AlC_2 Ceramics: a Review. *Journal of Materials Science & Technology* **26**, 385–416 (2010).

[50] Li, S., Song, G., Kwakernaak, K., van der Zwaag, S. & Sloof, W. G. Multiple crack healing of a Ti_2AlC ceramic. *Journal of the European Ceramic Society* **32**, 1813–1820 (2012).

[51] Lambrinou, K., Lapauw, T., Tunca, B. & Vleugels, J. *MAX Phase Materials for Nuclear Applications*, chap. 21, 223–233 (John Wiley & Sons, Ltd, 2017).

[52] Tunca, B. *et al.* Synthesis of MAX Phases in the Zr-Ti-Al-C System. *Inorganic Chemistry* **56**, 3489–3498 (2017).

[53] He, L. F. *et al.* Isothermal oxidation of bulk $Zr_2Al_3C_4$ at 500 to 1000℃ in air. *Journal of Materials Research* **23**, 359–366 (2008).

[54] Lu, X., Xiang, H., He, L.-F., Sun, L. & Zhou, Y. Effect of Ti Dopant on the Mechanical Properties and Oxidation Behavior of $Zr_2[Al(Si)]_4C_5$ Ceramics. *Journal of the American Ceramic Society* **94**, 1872–1877 (2011).

[55] Wan, D.-T. *et al.* A New Method to Improve the High-Temperature Mechanical Properties of Ti_3SiC_2 by Substituting Ti with Zr, Hf, or Nb. *Journal of the American Ceramic Society* **93**, 1749–1753 (2010).

[56] Adamaki, V., Minster, T., Thomas, T., Fourlaris, G. & Bowen, C. R. Study of the mechanical properties of Ti_2AlC after thermal shock. *Materials Science and Engineering: A* **667**, 9–15 (2016).

[57] Barsoum, M. W. & Radovic, M. Elastic and Mechanical Properties of the MAX Phases. *Annual Review of Materials Research* **41**, 195–227 (2011).

[58] Barsoum, M. W., Zhen, T., Kalidindi, S. R., Radovic, M. & Murugaiah, A. Fully reversible, dislocation-based compressive deformation of Ti_3SiC_2 to 1 GPa. *Nature Materials* **2**, 107–111 (2003).

[59] Radovic, M. & Barsoum, M. W. MAX phases: bridging the gap between metals and ceramics. *American Ceramics Society Bulletin* **92**, 20–27 (2013).

[60] Callister, W. *Materials Science and Engineering : An Introduction* (John Wiley & Sons, New York, 2007), 7^{th} edn.

[61] Ingason, A. S., Dahlqvist, M. & Rosen, J. Magnetic MAX phases from theory and experiments; a review. *Journal of Physics: Condensed Matter* **28**, 433003 (2016).

[62] Tallman, D. J., Anasori, B. & Barsoum, M. W. A Critical Review of the Oxidation of Ti_2AlC, Ti_3AlC_2 and Cr_2AlC in Air. *Materials Research Letters* **1**, 115–125 (2013).

[63] Lin, Z. J., Li, M. S., Wang, J. Y. & Zhou, Y. C. High-temperature oxidation and hot corrosion of Cr_2AlC. *Acta Materialia* **55**, 6182–6191 (2007).

[64] Lapauw, T. *et al.* Interaction of $M_{n+1}AX_n$ phases with oxygen-poor, static and fast-flowing liquid lead-bismuth eutectic. *Journal of Nuclear Materials* **520**, 258–272 (2019).

[65] Tunca, B. *et al.* Compatibility of Zr_2AlC MAX phase-based ceramics with oxygen-poor, static liquid lead–bismuth eutectic. *Corrosion Science* **171**, 108704 (2020).

[66] Lambrinou, K., Charalampopoulou, E., Van der Donck, T., Delville, R. & Schryvers, D. Dissolution corrosion of 316L austenitic stainless steels in contact with static liquid lead-bismuth eutectic (LBE) at 500 °C. *Journal of Nuclear Materials* **490**, 9–27 (2017).

[67] Cover, M. F., Warschkow, O., Bilek, M. M. M. & McKenzie, D. R. A comprehensive survey of M_2AX phase elastic properties. *Journal of Physics: Condensed Matter* **21**, 305403 (2009).

[68] He, X. *et al.* General trends in the structural, electronic and elastic properties of the M_3AlC_2 phases (M=transition metal): A first-principle study. *Computational Materials Science* **49**, 691–698 (2010).

[69] Bai, Y., He, X., Wang, R. & Zhu, C. An *ab initio* study on compressibility of Al-containing MAX-phase carbides. *Journal of Applied Physics* **114**, 173709 (2013).

[70] Zhang, H., Wu, X., Nickel, K. G., Chen, J. & Presser, V. High-pressure powder x-ray diffraction experiments and *ab initio* calculation of Ti_3AlC_2. *Journal of Applied Physics* **106**, 013519 (2009).

[71] Hettinger, J. D. *et al.* Electrical transport, thermal transport, and elastic properties of M_2AlC (M = Ti, Cr, Nb, and V). *Physical Review B* **72**, 115120 (2005).

[72] Wang, J. & Zhou, Y. Dependence of elastic stiffness on electronic band structure of nanolaminate M_2AlC ($M = \mathrm{Ti, V, Nb}$, and Cr) ceramics. *Physical Review B* **69**, 214111 (2004).

[73] Duong, T., Gibbons, S., Kinra, R. & Arróyave, R. *Ab-initio* aprroach to the electronic, structural, elastic, and finite-temperature thermodynamic properties of Ti_2AX (A = Al or Ga and X = C or N). *Journal of Applied Physics* **110**, 093504 (2011).

[74] Ali, M. A. *et al.* Recently synthesized $(Zr_{1-x}Ti_x)_2AlC$ ($0 \leq x \leq 1$) solid solutions: Theoretical study of the effects of M mixing on physical properties. *Journal of Alloys and Compounds* **743**, 146–154 (2018).

[75] Wang, C. *et al.* Elastic, mechanical, electronic, and defective properties of Zr–Al–C nanolaminates from first principles. *Journal of the American Ceramic Society* **101**, 756–772 (2017).

[76] Kanoun, M. B., Goumri-Said, S., Reshak, A. H. & Merad, A. E. Electro-structural correlations, elastic and optical properties among the nanolaminated ternary carbides Zr_2AC. *Solid State Sciences* **12**, 887–898 (2010). International Symposium on Structure-Property Relationships in Solid-State Materials.

[77] Ali, M. A., Hossain, M. M., Jahan, N., Islam, A. K. M. A. & Naqib, S. H. Newly synthesized Zr_2AlC, $Zr_2(Al_{0.58}Bi_{0.42})C$, $Zr_2(Al_{0.2}Sn_{0.8})C$, and $Zr_2(Al_{0.3}Sb_{0.7})C$ MAX phases: A DFT based first-principles study. *Computational Materials Science* **131**, 139–145 (2017).

[78] Yakoubi, A., Beldi, L., Bouhafs, B., Ferhat, M. & Ruterana, P. Full-relativistic calculation of electronic structure of Zr_2AlC and Zr_2AlN. *Solid State Communications* **139**, 485–489 (2006).

[79] Hadi, M. A. *et al.* Phase stability and physical properties of $(Zr_{1-x}Nb_x)_2AlC$ MAX phases. *Journal of Physics and Chemistry of Solids* **132**, 38–47 (2019).

[80] Bouhemadou, A., Khenata, R. & Chegaar, M. Structural and elastic properties of Zr_2AlX and Ti_2AlX (X = C and N) under pressure effect. *The European Physical Journal B* **56**, 209–215 (2007).

[81] Ali, M. A., Nasir, M. T., Khatun, M. R., Islam, A. K. M. A. & Naqib, S. H. An *ab initio* investigation of vibrational, thermodynamic, and optical properties of Sc_2AlC MAX compound. *Chinese Physics B* **25**, 103102 (2016).

[82] Li, X.-H., Cui, H.-L. & Zhang, R.-Z. Electronic, optical and thermal properties of Cr_3AlB_4 by first-principles calculations. *Vacuum* **145**, 234–240 (2017).

[83] Wang, J., Wang, J., Li, A., Li, J. & Zhou, Y. Theoretical Study on the Mechanism of Anisotropic Thermal Properties of Ti_2AlC and Cr_2AlC. *Journal of the American Ceramic Society* **97**, 1202–1208 (2014).

[84] Hadi, M. A. *et al.* Elastic and thermodynamic properties of new $(Zr_{3-x}Ti_x)AlC_2$ MAX-phase solid solutions. *Computational Materials Science* **137**, 318–326 (2017).

[85] Son, W. *et al. Ab-initio* investigation of the finite-temperatures structural, elastic, and thermodynamic properties of Ti_3AlC_2 and Ti_3SiC_2. *Computational Materials Science* **124**, 420–427 (2016).

[86] Togo, A., Chaput, L., Tanaka, I. & Hug, G. First-principles phonon calculations of thermal expansion in Ti_3SiC_2, Ti_3AlC_2, and Ti_3GeC_2. *Physical Review B* **81**, 174301 (2010).

[87] Razzak, M. A., Ali, M. S. & Hossain, M. A. First-principles study of structural, elastic, electronic, thermodynamic and optical properties of Sc_3SnX (X = B, C). *Computational Condensed Matter* **13**, 41–48 (2017).

[88] Li, X.-H., Cui, H.-L. & Zhang, R.-Z. Structural, optical, and thermal properties of MAX-phase Cr_2AlB_2. *Frontiers of Physics* **13**, 136501 (2018).

[89] Du, Y. L., Sun, Z. M., Hashimoto, H. & Tian, W. B. First-Principles Study on Thermodynamic Properties of Ti_2AlC and Ti_2SC. *Materials Transactions* **50**, 2173–2176 (2009).

[90] Ali, M. S., Islam, A. K. M. A., Hossain, M. M. & Parvin, F. Phase stability, elastic, electronic, thermal and optical properties of $Ti_3Al_{1-x}Si_xC_2$ ($0 \leq x \leq 1$): First principle study. *Physica B: Condensed Matter* **407**, 4221–4228 (2012).

[91] Djedid, A., Méçabih, S., Abbes, O. & Abbar, B. Theoretical investigations of structural, electronic and thermal properties of Ti_2Al_X(X=C,N). *Physica B: Condensed Matter* **404**, 3475–3482 (2009).

[92] Oganov, A. R., Brodholt, J. P. & Price, G. D. Comparative study of quasiharmonic lattice dynamics, molecular dynamics and Debye model applied to $MgSiO_3$ perovskite. *Physics of the Earth and Planetary Interiors* **122**, 277–288 (2000).

[93] Lane, N. J., Vogel, S. C., Caspi, E. N. & Barsoum, M. W. High-temperature neutron diffraction and first-principles study of temperature-dependent crystal structures and atomic vibrations in Ti_3AlC_2, Ti_2AlC, and $Ti_5Al_2C_3$. *Journal of Applied Physics* **113**, 183519 (2013).

[94] Gao, H., Benitez, R., Son, W., Arroyave, R. & Radovic, M. Structural, physical and mechanical properties of $Ti_3(Al_{1-x}Si_x)C_2$ solid solution with $x = 0$–1. *Materials Science and Engineering: A* **676**, 197–208 (2016).

[95] Tzenov, N. V. & Barsoum, M. W. Synthesis and Characterization of Ti_3AlC_2. *Journal of the American Ceramic Society* **83**, 825–832 (2000).

[96] Scabarozi, T. H. *et al.* Thermal expansion of select $M_{n+1}AX_n$ (M = early transition metal, A = A group element, X = C or N) phases measured by high temperature x-ray diffraction and dilatometry. *Journal of Applied Physics* **105**, 013543 (2009).

[97] Pang, W.-K., Low, I.-M. & Sun, Z.-M. *In Situ* High-Temperature Diffraction Study of the Thermal Dissociation of Ti_3AlC_2 in Vacuum. *Journal of the American Ceramic Society* **93**, 2871–2876 (2010).

[98] Barsoum, M. W., El-Raghy, T. & Ali, M. Processing and characterization of Ti_2AlC, Ti_2AlN, and $Ti_2AlC_{0.5}N_{0.5}$. *Metallurgical and Materials Transactions A* **31**, 1857–1865 (2000).

[99] Magnuson, M. *et al.* Electronic structure investigation of Ti_3AlC_2, Ti_3SiC_2, and Ti_3GeC_2 by soft x-ray emission spectroscopy. *Physical Review B* **72**, 245101 (2005).

[100] Magnuson, M. & Mattesini, M. Chemical bonding and electronic-structure in MAX phases as viewed by X-ray spectroscopy and density functional theory. *Thin Solid Films* **621**, 108–130 (2017).

[101] Emmerlich, J., Music, D., Houben, A., Dronskowski, R. & Schneider, J. M. Systematic study on the pressure dependence of M_2AlC phases (M = Ti, V, Cr, Zr, Nb, Mo, Hf, Ta, W). *Physical Review B* **76**, 224111 (2007).

[102] Bai, Y., He, X., Wang, R., Wang, S. & Kong, F. Effect of transition metal (M) and M–C slabs on equilibrium properties of Al-containing MAX carbides: An *ab initio* study. *Computational Materials Science* **91**, 28–37 (2014).

[103] Sun, Z., Music, D., Ahuja, R., Li, S. & Schneider, J. M. Bonding and classification of nanolayered ternary carbides. *Physical Review B* **70**, 092102 (2004).

[104] Sun, Z., Ahuja, R., Li, S. & Schneider, J. M. Structure and bulk modulus of M_2AlC (M = Ti, V, and Cr). *Applied Physics Letters* **83**, 899–901 (2003).

[105] Music, D., Sun, Z., Voevodin, A. A. & Schneider, J. M. Electronic structure and shearing in nanolaminated ternary carbides. *Solid State Communications* **139**, 139–143 (2006).

[106] Music, D., Emmerlich, J. & Schneider, J. M. Phase stability and elastic properties of $Ta_{n+1}AlC_n$ (n = 1-3) at high pressure and elevated temperature. *Journal of Physics: Condensed Matter* **19**, 136207 (2007).

[107] Hamilton, W. R. Second Essay on a General Method in Dynamics. *Philosophical Transactions of the Royal Society of London* **125**, 95–144 (1835).

[108] Slater, J. C. Atomic Shielding Constants. *Physical Review* **36**, 57–64 (1930).

[109] Perdew, J. P. & Zunger, A. Self-interaction correction to density-functional approximations for many-electron systems. *Physical Review B* **23**, 5048–5079 (1981).

[110] Ceperley, D. M. & Alder, B. J. Ground State of the Electron Gas by a Stochastic Method. *Physical Review Letters* **45**, 566–569 (1980).

[111] Csonka, G. I. *et al.* Assessing the performance of recent density functionals for bulk solids. *Physical Review B* **79**, 155107 (2009).

[112] Monkhorst, H. J. & Pack, J. D. Special points for Brillouin-zone integrations. *Physical Review B* **13**, 5188–5192 (1976).

[113] Bader, R. F. W. Molecular fragments or chemical bonds. *Accounts of Chemical Research* **8**, 34–40 (1975).

[114] Mulliken, R. S. Electronic Population Analysis on LCAO–MO Molecular Wave Functions. I. *The Journal of Chemical Physics* **23**, 1833–1840 (1955).

[115] Dronskowski, R. & Bloechl, P. E. Crystal orbital Hamilton populations (COHP): energy-resolved visualization of chemical bonding in solids based on density-functional calculations. *The Journal of Physical Chemistry* **97**, 8617–8624 (1993).

[116] Finnis, M. *Interatomic forces in condensed matter* (Oxford University Press, Oxford, 2010).

[117] Coulson, C. A. The electronic structure of some polyenes and aromatic molecules VII. Bonds of fractional order by the molecular orbital method. *Proceedings of the Royal Society of London A* **169**, 413–428 (1939).

[118] Kresse, G. & Furthmüller, J. Efficient iterative schemes for *ab initio* total-energy calculations using a plane-wave basis set. *Physical Review B* **54**, 11169–11186 (1996).

[119] Kresse, G. & Furthmüller, J. Efficiency of *ab-initio* total energy calculations for metals and semiconductors using a plane-wave basis set. *Computational Materials Science* **6**, 15–50 (1996).

[120] Maintz, S., Deringer, V. L., Tchougréeff, A. L. & Dronskowski, R. LOBSTER: A tool to extract chemical bonding from plane-wave based DFT. *Journal of Computational Chemistry* **37**, 1030–1035 (2016).

[121] Maintz, S., Deringer, V. L., Tchougréeff, A. L. & Dronskowski, R. Analytic projection from plane-wave and PAW wavefunctions and application to chemical-bonding analysis in solids. *Journal of Computational Chemistry* **34**, 2557–2567 (2013).

[122] Deringer, V. L., Tchougréeff, A. L. & Dronskowski, R. Crystal Orbital Hamilton Population (COHP) Analysis As Projected from Plane-Wave Basis Sets. *The Journal of Physical Chemistry A* **115**, 5461–5466 (2011).

[123] Manz, T. & Limas, N. G. CHARGEMOL program for performing DDEC analysis. *See the following:* http://ddec.sourceforge.net (2016).

[124] Wallace, D. C. *Thermodynamics of Crystals*. Dover books on physics (Dover Publications, 1998).

[125] Togo, A. & Tanaka, I. First principles phonon calculations in materials science. *Scripta Materialia* **108**, 1–5 (2015).

[126] Lehmann, G. & Taut, M. On the Numerical Calculation of the Density of States and Related Properties. *Physica Status Solidi B* **54**, 469–477 (1972).

[127] Baroni, S., de Gironcoli, S., Dal Corso, A. & Giannozzi, P. Phonons and related crystal properties from density-functional perturbation theory. *Reviews of Modern Physics* **73**, 515–562 (2001).

[128] Mermin, N. D. Thermal Properties of the Inhomogeneous Electron Gas. *Physical Review* **137**, A1441–A1443 (1965).

[129] Mellan, T. A., Duff, A. I. & Finnis, M. W. Spontaneous Frenkel pair formation in Zirconium Carbide. *Physical Review B* **98**, 174116 (2018).

[130] Xie, C. *et al.* Effects of carbon vacancies on the structures, mechanical properties, and chemical bonding of zirconium carbides: a first-principles study. *Physical Chemistry Chemical Physics* **18**, 12299–12306 (2016).

[131] Gunda, N. S. H. & Van der Ven, A. First-principles insights on phase stability of titanium interstitial alloys. *Physical Review Materials* **2**, 083602 (2018).

[132] Kresse, G. & Joubert, D. From ultrasoft pseudopotentials to the projector augmented-wave method. *Physical Review B* **59**, 1758–1775 (1999).

[133] Perdew, J. P. & Wang, Y. Accurate and simple analytic representation of the electron-gas correlation energy. *Physical Review B* **45**, 13244–13249 (1992).

[134] He, L. *et al.* Accuracy of generalized gradient approximation functionals for density-functional perturbation theory calculations. *Physical Review B* **89**, 064305 (2014).

[135] Zapata-Solvas, E. *et al.* Experimental synthesis and density functional theory investigation of radiation tolerance of $Zr_3(Al_{1-x}Si_x)C_2$ MAX phases. *Journal of the American Ceramic Society* **100**, 1377–1387 (2017).

[136] Shang, L., Music, D., to Baben, M. & Schneider, J. M. Phase stability predictions of $Cr_{1-x},M_x)_2(Al_{1-y},A_y)(C_{1-z},X_z)$ (M = Ti, Hf, Zr; A = Si, X= B). *Journal of Physics D: Applied Physics* **47**, 065308 (2014).

[137] Clark, S. J. *et al.* First principles methods using CASTE. *Zeitschrift für Kristallographie - Crystalline Materials* **220**, 567–570 (01 May. 2005).

[138] Sokol, M., Natu, V., Kota, S. & Barsoum, M. W. On the Chemical Diversity of the MAX Phases. *Trends in Chemistry* **1**, 210–223 (2019). Special Issue Part Two: Big Questions in Chemistry.

[139] Hehenkamp, T., Berger, W., Kluin, J.-E., Lüdecke, C. & Wolff, J. Equilibrium vacancy concentrations in copper investigated with the absolute technique. *Physical Review B* **45**, 1998–2003 (1992).

[140] Plummer, G. & Tucker, G. J. Bond-order potentials for the Ti_3AlC_2 and Ti_3SiC_2 MAX phases. *Physical Review B* **100**, 214114 (2019).

[141] Plummer, G. *et al.* On the origin of kinking in layered crystalline solids. *Materials Today* **43**, 45–52 (2021).

[142] Manoun, B. *et al.* Compression behavior of M_2AlC (M = Ti, V, Cr, Nb, and Ta) phases to above 50 GPa. *Physical Review B* **73**, 024110 (2006).

[143] Radovic, M. *et al.* On the elastic properties and mechanical damping of Ti_3SiC_2, Ti_3GeC_2, $Ti_3Si_{0.5}Al_{0.5}C_2$ and Ti_2AlC in the 300-1573 K temperature range. *Acta Materialia* **54**, 2757–2767 (2006).

[144] Wu, Z. & Cohen, R. E. More accurate generalized gradient approximation for solids. *Physical Review B* **73**, 235116 (2006).

[145] Poulou, A., Mellan, T. A. & Finnis, M. W. Stability of Zr-Al-C and Ti-Al-C MAX phases: A theoretical study. *Physical Review Materials* **5**, 033608 (2021).

[146] Saunders, N. & Rivlin, V. G. Thermodynamic characterization of Al–Cr, Al–Zr, and Al–Cr–Zr alloy systems. *Materials Science and Technology* **2**, 520–527 (1986).

[147] Tamim, R. & Mahdouk, K. Thermodynamic reassessment of the Al–Zr binary system. *Journal of Thermal Analysis and Calorimetry* **131**, 1187–1200 (2018).

[148] Kattner, U. R., Lin, J. C. & Chang, Y. A. Thermodynamic assessment and calculation of the Ti-Al system. *Metallurgical Transactions A (Physical Metallurgy and Materials Science)* **23 A**, 2081–2090 (1992).

[149] Zhang, F., Chen, S. L., Chang, Y. A. & Kattner, U. R. A thermodynamic description of the Ti-Al system. *Intermetallics* **5**, 471–482 (1997).

[150] Witusiewicz, V. T. *et al.* Thermodynamic description of the Al–C–Ti system. *Journal of Alloys and Compounds* **623**, 480–496 (2015).

[151] Witusiewicz, V. T., Bondar, A. A., Hecht, U., Rex, S. & Velikanova, T. Y. The Al-B-Nb-Ti system. III. Thermodynamic re-evaluation of the constituent binary system Al-Ti. *Journal of Alloys and Compounds* **465**, 64–77 (2008).

[152] He, L., Zhou, Y., Bao, Y., Lin, Z. & Wang, J. Synthesis, Physical, and Mechanical Properties of Bulk $Zr_3Al_3C_5$ Ceramic. *Journal of the American Ceramic Society* **90**, 1164–1170 (2007).

[153] Leela-adisorn, U. *et al.* $AlZrC_2$ synthesis. *Ceramics International* **32**, 431–439 (2006).

[154] Yu, X.-X., Weinberger, C. R. & Thompson, G. B. *Ab initio* investigations of the phase stability in group IVB and VB transition metal carbides. *Computational Materials Science* **112**, 318–326 (2016).

[155] Zhang, Y., Liu, B. & Wang, J. Self-assembly of Carbon Vacancies in Sub-stoichiometric ZrC_{1-x}. *Scientific Reports* **5**, 18098 (2015).

[156] Okamoto, H. Al-Zr (Aluminum-Zirconium). *Journal of Phase Equilibria* **23**, 455 (2002).

[157] Klimeš, J., Bowler, D. R. & Michaelides, A. Van der Waals density functionals applied to solids. *Physical Review B* **83**, 195131 (2011).

[158] Klimeš, J., Bowler, D. R. & Michaelides, A. Chemical accuracy for the van der Waals density functional. *Journal of Physics: Condensed Matter* **22**, 022201 (2010).

[159] Deng, Z.-X. *et al. Ab initio* and Calphad-type thermodynamic investigation of the Ti-Al-Zr system. *Journal of Mining and Metallurgy B* **55**, 427–437 (2019).

[160] Barrachin, M. *et al.* Critical evaluation of experimental data of solution enthalpy of zirconium in liquid aluminum. *Journal of Chemical Thermodynamics* **128**, 295–304 (2019).

[161] Keast, V. J., Harris, S. & Smith, D. K. Prediction of the stability of the $M_{n+1}AX_n$ phases from first principles. *Physical Review B* **80**, 214113 (2009).

[162] Thore, A., Dahlqvist, M., Alling, B. & Rosén, J. Temperature dependent phase stability of nanolaminated ternaries from first-principles calculations. *Computational Materials Science* **91**, 251–257 (2014).

[163] Ouisse, T. & Chaussende, D. Application of an axial next-nearest-neighbor Ising model to the description of $M_{n+1}AX_n$ phases. *Physical Review B* **85**, 104110 (2012).

[164] Datasheet from "PAULING FILE Multinaries Edition – 2012" in SpringerMaterials (2016). Copyright 2016 Springer-Verlag Berlin Heidelberg & Material Phases Data System (MPDS), Switzerland & National Institute for Materials Science (NIMS), Japan.

[165] Xu, J. & Freeman, A. J. Band filling and structural stability of trialuminides: YAl_3, $ZrAl_3$, and $NbAl_3$. *Journal of Materials Research* **6**, 1188–1199 (1991).

[166] Meschel, S. V. & Kleppa, O. J. Standard enthalpies of formation of 4d aluminides by direct synthesis calorimetry. *Journal of Alloys and Compounds* **191**, 111–116 (1993).

[167] Clouet, E., Sanchez, J. M. & Sigli, C. First-principles study of the solubility of Zr in Al. *Physical Review B* **65**, 094105 (2002).

[168] Colinet, C. & Pasturel, A. Phase stability and electronic structure in $ZrAl_3$ compound. *Journal of Alloys and Compounds* **319**, 154–161 (2001).

[169] Al-Zr. In *Binary Systems. Part 1 _ Elements and Binary Systems from Ag-Al to Au-Tl*, vol. 19B1 of *Landolt-Börnstein - Group IV Physical Chemistry* (Springer-Verlag Berlin Heidelberg). Datasheet - doi: 10.1007/10655491_58.

[170] Duan, Y. H., Huang, B., Sun, Y., Peng, M. J. & Zhou, S. G. Stability, elastic properties and electronic structures of the stable Zr–Al intermetallic compounds: A first-principles investigation. *Journal of Alloys and Compounds* **590**, 50–60 (2014).

[171] Klein, R., Jacob, I., O'Hare, P. A. G. & Goldberg, R. N. Solution-calorimetric determination of the standard molar enthalpies of formation of the pseudobinary compounds $Zr(Al_xFe_{1-x})_2$ at the temperature 298.15 K. *The Journal of Chemical Thermodynamics* **26**, 599–608 (1994).

[172] Nguyen-Manh, D. & Pettifor, D. G. Electronic structure, phase stability and elastic moduli of AB transition metal aluminides. *Intermetallics* **7**, 1095–1106 (1999).

[173] Dahlqvist, M., Alling, B., Abrikosov, I. A. & Rosén, J. Phase stability of Ti_2AlC upon oxygen incorporation: A first-principles investigation. *Physical Review B* **81**, 024111 (2010).

[174] Al-C. In *Binary Systems. Part 1 _ Elements and Binary Systems from Ag-Al to Au-Tl*, vol. 19B1 of *Landolt-Börnstein - Group IV Physical Chemistry* (Springer-Verlag Berlin Heidelberg). Datasheet - doi: 10.1007/10655491_29.

[175] Deffrennes, G. *et al.* Critical assessment and thermodynamic modeling of the Al–C system. *Calphad* **66**, 101648 (2019).

[176] Qiu, C. & Metselaar, R. Solubility of carbon in liquid Al and stability of Al_4C_3. *Journal of Alloys and Compounds* **216**, 55–60 (1994).

[177] Li, K., Sun, Z. G., Wang, F., Zhou, N. G. & Hu, X. W. First-principles calculations on Mg/Al_4C_3 interfaces. *Applied Surface Science* **270**, 584–589 (2013).

[178] Blachnik, R. O. G., Gross, P. & Hayman, C. Enthalpies of formation of the carbides of aluminium and beryllium. *Transactions of the Faraday Society* **66**, 1058–1064 (1970).

[179] Meschel, S. V. & Kleppa, O. J. Standard enthalpies of formation of AlB_{12} and Al_4C_3 by high temperature direct synthesis calorimetry. *Journal of Alloys and Compounds* **227**, 93–96 (1995).

[180] King, R. C. & Armstrong, G. T. Heat of combustion and heat of formation of aluminum carbide. *Journal of Research of the National Bureau of Standards Section A: Physics and Chemistry* **68A**, 661 (1964).

[181] Rinehart, G. H. & Behrens, R. G. Vaporization thermodynamics of aluminum carbide. *The Journal of Chemical Thermodynamics* **12**, 205–215 (1980).

[182] Rafaja, D., Lengauer, W., Ettmayer, P. & Lipatnikov, V. N. Rietveld analysis of the ordering in V_8C_7. *Journal of Alloys and Compounds* **269**, 60–62 (1998).

[183] Tian, H. *et al.* Predictions of the structures and properties of the substituted layered ternary compound series $(Zr_{1-x}T_x)_3Al_3C_5$ (T = Hf, Nb, and V) through first-principles studies. *Journal of Physics Condensed Matter* **31**, 12 (2019).

[184] Lin, Z. J., He, L. F., Li, M. S., Wang, J. Y. & Zhou, Y. C. Layered stacking characteristics of ternary zirconium aluminum carbides. *Journal of Materials Research* **22**, 3058–3066 (2007).

[185] Ohnuma, I. *et al.* Phase equilibria in the Ti–Al binary system. *Acta Materialia* **48**, 3113–3123 (2000).

[186] Hong, T., Watson-Yang, T. J., Freeman, A. J., Oguchi, T. & Xu, J.-h. Crystal structure, phase stability, and electronic structure of Ti-Al intermetallics: $TiAl_3$. *Physical Review B* **41**, 12462–12467 (1990).

[187] Hong, T. & Freeman, A. J. Effect of ternary additions on the structural stability and electronic structure of intermetallic compounds: Al_3Ti + Cu. *Journal of Materials Research* **6**, 330–338 (1991).

[188] Nassik, M., Chrifi-Alaoui, F. Z., Mahdouk, K. & Gachon, J. C. Calorimetric study of the aluminium–titanium syste. *Journal of Alloys and Compounds* **350**, 151–154 (2003).

[189] Kubaschewski, O. & Heymer, G. Heats of formation of transition-metal aluminides. *Transactions of the Faraday Society* **56**, 473–478 (1960).

[190] Asta, M., de Fontaine, D. & van Schilfgaarde, M. First-principles study of phase stability of Ti–Al intermetallic compounds. *Journal of Materials Research* **8**, 2554–2568 (1993).

[191] Fu, C. L. Electronic, elastic, and fracture properties of trialuminide alloys: Al_3Sc and Al_3Ti. *Journal of Materials Research* **5**, 971–979 (1990).

[192] Al-Ti. In *Binary Systems. Part 1 _ Elements and Binary Systems from Ag-Al to Au-Tl*, vol. 19B1 of *Landolt-Börnstein - Group IV Physical Chemistry* (Springer-Verlag Berlin Heidelberg). Datasheet - doi: 10.1007/10655491_53.

[193] Zou, J., Fu, C. L. & Yoo, M. H. Phase stability of intermetallics in the Al-Ti system: A first-principles total-energy investigation. *Intermetallics* **3**, 265–269 (1995).

[194] Watson, R. E. & Weinert, M. Transition-metal aluminide formation: Ti, V, Fe, and Ni aluminides. *Physical Review B* **58**, 5981–5988 (1998).

[195] Colinet, C. & Pasturel, A. Ab initio calculation of the formation energies of $L1_2$, $D0_{22}$, $D0_{23}$ and one dimensional long period structures in $TiAl_3$ compound. *Intermetallics* **10**, 751–764 (2002).

[196] Kubaschewski, O. & Dench, W. A. The heats of formation in the systems titanium-aluminium and titanium-iron. *Acta Metallurgica* **3**, 339–346 (1955).

[197] Meschel, S. V. & Kleppa, O. J. *The Standard Enthalpies of Formation of Some 3d Transition Metal Aluminides by High-Temperature Direct Synthesis Calorimetry*, 103–112 (Springer Netherlands, Dordrecht, 1994).

[198] Jian, Y. *et al.* Phase stability, mechanical properties and electronic structures of Ti-Al binary compounds by first principles calculations. *Materials Chemistry and Physics* **221**, 311–321 (2019).

[199] Zou, J. & Fu, C. L. Structural, electronic, and magnetic properties of 3d transition-metal aluminides with equiatomic composition. *Physical Review B* **51**, 2115–2121 (1995).

[200] Music, D. & Schneider, J. M. Effect of transition metal additives on electronic structure and elastic properties of TiAl and Ti_3Al. *Physical Review B* **74**, 174110 (2006).

[201] Wan, Y. *et al.* First-principles calculations of structural, elastic and electronic properties of second phases and solid solutions in Ti-Al-V alloys. *Physica B: Condensed Matter* **591**, 412241 (2020).

[202] Zhang, C., Hou, H., Zhao, Y., Yang, X. & Han, P. Effect of Zr, Hf, and Sn additives on elastic properties of α_2-Ti_3Al phase by first-principles calculations. *Journal of Wuhan University of Technology—Materials Science Edition* **32**, 944–950 (2017).

[203] Eibler, R. New aspects of the energetics of ordered Ti_2C and Ti_2N. *Journal of Physics: Condensed Matter* **19**, 196226 (2007).

[204] Hugosson, H. W., Korzhavyi, P., Jansson, U., Johansson, B. & Eriksson, O. Phase stabilities and structural relaxations in substoichiometric TiC_{1-x}. *Physical Review B* **63**, 165116 (2001).

[205] Eibler, R. Electronic structure and energetics of ordered titanium carbides of composition Ti_2C. *Journal of Physics: Condensed Matter* **14**, 4425–4444 (2002).

[206] Connétable, D. First-principles study of transition metal carbides. *Materials Research Express* **3**, 126502 (2016).

[207] Guo, F. *et al.* Structural, mechanical, electronic and thermodynamic properties of cubic TiC compounds under different pressures: A first-principles study. *Solid State Communications* **311**, 113856 (2020).

[208] Jang, J. H., Lee, C.-H., Heo, Y.-U. & Suh, D.-W. Stability of (Ti,M)C (M = Nb, V, Mo and W) carbide in steels using first-principles calculations. *Acta Materialia* **60**, 208–217 (2012).

[209] Hug, G. Electronic structures of and composition gaps among the ternary carbides Ti_2MC. *Physical Review B* **74**, 184113 (2006).

[210] Tan, J. *et al.* A comparative first-principles study of the electronic, mechanical, defect and acoustic properties of Ti_2AlC and Ti_3AlC. *Journal of Physics D: Applied Physics* **47**, 215301 (2014).

[211] Lu, Y. *et al.* Facile Synthesis of Ti_2AC (A = Zn, Al, In, and Ga) MAX Phases by Hydrogen Incorporation into Crystallographic Voids. *The Journal of Physical Chemistry Letters* **12**, 11245–11251 (2021).

[212] Henkelman, G., Arnaldsson, A. & Jónsson, H. A fast and robust algorithm for Bader decomposition of charge density. *Computational Materials Science* **36**, 354–360 (2006).

[213] Yu, M. & Trinkle, D. R. Accurate and efficient algorithm for Bader charge integration. *The Journal of Chemical Physics* **134**, 064111 (2011).

[214] Tang, W., Sanville, E. & Henkelman, G. A grid-based Bader analysis algorithm without lattice bias. *Journal of Physics: Condensed Matter* **21**, 084204 (2009).

[215] Hug, G. & Fries, E. Full-potential electronic structure of Ti_2AlC and Ti_2AlN. *Physical Review B* **65**, 113104 (2002).

[216] Barsoum, M. W. *et al.* Electrical conductivity, thermopower, and Hall effect of Ti_3AlC_2, Ti_4AlN_3, and Ti_3SiC_2. *Physical Review B* **62**, 10194–10198 (2000).

[217] Pierson, H. O. *Handbook of refractory carbides & nitrides: properties, characteristics, processing and applications* (William Andrew, 1996).

[218] Hollander, L. E. Electrical conductivity and thermoelectric effect in single-crystal tic. *Journal of Applied Physics* **32**, 996–997 (1961).

[219] Magnuson, M. *et al.* Electronic structure and chemical bonding in Ti_2AlC investigated by soft x-ray emission spectroscopy. *Physical Review B* **74**, 195108 (2006).

[220] Grechnev, A., Ahuja, R. & Eriksson, O. Balanced crystal orbital overlap population—a tool for analysing chemical bonds in solids. *Journal of Physics: Condensed Matter* **15**, 7751–7761 (2003).

[221] Dahlqvist, M. & Rosen, J. Order and disorder in quaternary atomic laminates from first-principles calculations. *Physical Chemistry Chemical Physics* **17**, 31810–31821 (2015).

[222] Music, D., Houben, A., Dronskowski, R. & Schneider, J. M. *Ab initio* study of ductility in M_2AlC (M = Ti, V, Cr). *Physical Review B* **75**, 174102 (2007).

[223] Bai, Y., Srikanth, N., Chua, C. K. & Zhou, K. Density Functional Theory Study of $M_{n+1}AX_n$ Phases: A Review. *Critical Reviews in Solid State and Materials Sciences* **44**, 56–107 (2019).

[224] Leaffer, O. D., Gupta, S., Barsoum, M. W. & Spanier, J. E. On the Raman Scattering from Selected M_2AC Compounds. *Journal of Materials Research* **22**, 2651–2654 (2007).

[225] Bai, Y., He, X. & Wang, R. Lattice dynamics of Al-containing MAX-phase carbides: a first-principle study. *Journal of Raman Spectroscopy* **46**, 784–794 (2015).

[226] Wang, J., Zhou, Y., Lin, Z., Meng, F. & Li, F. Raman active phonon modes and heat capacities of Ti_2AlC and Cr_2AlC ceramics: first-principles and experimental investigations. *Applied Physics Letters* **86**, 101902 (2005).

[227] Spanier, J. E., Gupta, S., Amer, M. & Barsoum, M. W. Vibrational behavior of the $M_{n+1}AX_n$ phases from first-order Raman scattering ($M = \mathrm{Ti, V, Cr}$, $A = \mathrm{Si}$, $X = \mathrm{C, N}$). *Physical Review B* **71**, 012103 (2005).

[228] Amer, M. *et al.* The Raman spectrum of Ti_3SiC_2. *Journal of Applied Physics* **84**, 5817–5819 (1998).

[229] Wdowik, U. D., Twardowska, A. & Mędala-Wąsik, M. Lattice dynamics of binary and ternary phases in Ti–Si–C system: A combined Raman spectroscopy and density functional theory study. *Materials Chemistry and Physics* **168**, 58–65 (2015).

[230] Liu, Z. *et al.* Crystal structure and formation mechanism of $(Cr_{2/3}Ti_{1/3})_3AlC_2$ MAX phase. *Acta Materialia* **73**, 186–193 (2014).

[231] Li, Y. F. *et al.* Phonon spectrum, IR and Raman modes, thermal expansion tensor and thermal physical properties of M_2TiAlC_2 (M = Cr, Mo, W). *Computational Materials Science* **134**, 67–83 (2017).

[232] Klein, M. V., Holy, J. A. & Williams, W. S. Raman scattering induced by carbon vacancies in TiC_x. *Physical Review B* **17**, 1546–1556 (1978).

[233] Mercier, F., Chaix-Pluchery, O., Ouisse, T. & Chaussende, D. Raman scattering from Ti_3SiC_2 single crystals. *Applied Physics Letters* **98**, 081912 (2011).